IFSC2019

THE 11th

INTERNATIONAL FUNDAMENTAL SCIENCE CONGRESS

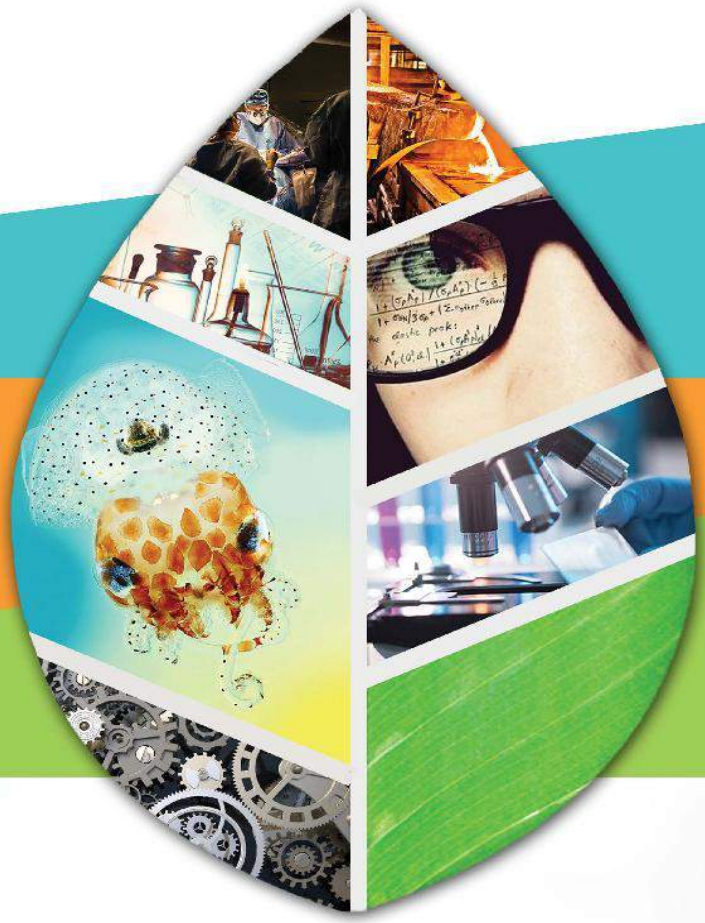

EXTENDED ABSTRACT BOOK

'Fortifying Fundamental Sciences for Translational Impact'

30th – 31st OCTOBER 2019

Palm Garden Hotel, IOI Resort City, Putrajaya, Malaysia

ORGANISED BY:
FACULTY OF SCIENCE
UPM

MAIN SPONSOR:
ROYAL SOCIETY OF CHEMISTRY

3 GOOD HEALTH AND WELL-BEING
6 CLEAN WATER AND SANITATION
7 AFFORDABLE AND CLEAN ENERGY
9 INDUSTRY, INNOVATION AND INFRASTRUCTURE
15 LIFE ON LAND

Scan me

e-ISBN ---------

Published by:
Faculty of Science
Universiti Putra Malaysia
43400 UPM Serdang, Selangor
Malaysia

UPM Press
Universiti Putra Malaysia
43400 UPM Serdang, Selangor
Malaysia

TABLE OF CONTENT

PLENARY LECTURES

PRINCIPLES OF MICROBIAL DEGRADATION: MOLECULAR AND PHYSIOLOGICAL APPROACHES TO UNDERSTANDING MICROBIAL DEGRADATION

Fahrul Zaman Huyop

Department of Biosciecnes, Faculty of Science, Universiti Teknologi Malaysia, 81310 UTM Johor Bahru, Johor, Malaysia

Abstract

Organic pollutants are mostly anthropogenic and microbial degradation plays an important role to reduce the build-up of toxic chemicals in the soil and water systems. Degradation of halogenated organic compounds are highlighted because carbon-halogen bonds are the most recalcitrant materials. There are four basic criteria for a given halogenated compound to be utilized by an organism as a sole carbon and energy source. First, the halogenated compound should not be toxic to the organism at intracellular concentrations. Secondly, entry of halogenated compound into the organism should be either through passive or active transport and trigger a specialized gene in the operon. Thirdly, the organism should be able to synthesize enzyme (dehalogenase) which can remove the substituent halogen(s) from the compound and finally, the product of dehalogenation should be non-toxic and easily converted to an intermediate which can readily be absorbed in the microorganisms via central metabolic pathways. There were many dehalogenase producing bacteria were isolated so far. Among all these microbes, only *Rhizobium* sp. RC1 produce three kinds of dehalogenase DehD, DehE and DehL. Current study will focus on all these 4 criteria that allow biodegradation to occur.

DESIGN, DIVERSITY AND DEFECTS IN FUNCTIONAL (Na,Bi)TiO_3 PEROVSKITES: ARE WE IN CONTROL

Derek Sinclair

Department of Materials Science and Engineering, University of Sheffield, UK

Abstract

Oxide-based perovskites (general formula ABO_3) are widely investigated by solid state chemists/physicists and materials scientists because they exhibit a diverse and impressive range of functional properties (eg superconductivity, ferroelectricity, fast-ion conductivity, mixed ionic-electronic conductivity) and find applications in many ceramic-based devices, eg multi-layer ceramic capacitors (MLCCs)/piezoelectric actuators and solid oxide fuel cells (SOFCs). Here we will review the range of electrical properties that can be displayed by (Na,Bi)TiO_3 (NBT) perosvkites, based on remarkably low levels of non-stoichiometry and/or aliovalent doping. This can span from polar-dielectric behaviour that can be used in applications such as dielectrics/piezoelectrics to solid electrolyte behaviour where the high levels of oxide-ion conduction make them potentially suitable for intermediate temperature SOFCs (see *Nature Materials,* 13, 31-35 (2014) & *Journal of Materials Chemistry* A, 6, 5243-5254 (2018)). The conductivity maximum achieved in NBT is in good agreement with an oxygen-vacancy diffusivity limit model in a perovskite lattice proposed by R. A. De Souza [*Advanced Functional Materials*, 25, 6326-6342 (2015).] and suggests that optimisation of the ionic conductivity in NBT may have been achieved.

OPTICAL GAS SENSOR BASED ON NANOSTRUCTURED MATERIALS

Muhammad Yahaya[1,2]

[1]School of Applied Physics, Faculty of Science and Technology, Universiti Kebangsaan Malaysia 43600 UKM Bangi, Selangor, Malaysia
[2]Institute of Microengineering and Nanoelectronics (IMEN), Universiti Kebangsaan Malaysia 43600 UKM Bangi, Selangor, Malaysia

Abstract

The accurate detection of harmful gases using their optical properties is highly important in industrial and environmental monitoring. The optical detection technique is considered as one of the accurate techniques for gas detection and has advanced very rapidly due to rapid progress in detectors and light sources. Basically, in optical methods, the optical absorption and scattering of gas at certain wavelength are measured. The output of measurement, distribution of absorption with wavelength provide information on the nature of gas and its concentration. This presentation will review some recent development of optical gas sensors, starting with detection material such as metal oxide nanowires and nanorods that have been synthesized by varieties of techniques such as vacuum evaporation, laser ablation, magnetron sputtering, sol-gel and detection in spectroscopic system. The application of sensor and integration with “big data” concept is the direction of future research.

Keywords: Metal oxide; ZnO; exciton; nanowires; nanorods; gas sensor; sol-gel, carbon monoxide; big data.

SOME OUTLIER DETECTION METHODS IN UNREPLICATED LINEAR FUNCTIONAL RELATIONSHIP MODEL FOR CIRCULAR VARIABLES

Abdul Ghapor Hussin[1]*

[1]*National Defence University of Malaysia, Kem Sungai Besi, 57000 Kuala Lumpur, Malaysia.*

*Corresponding author: ghapor@upnm.edu.my

Abstract

This study is on modelling circular data and proposed several methods of detecting outliers of the model considered. In particular, the linear functional relationship model is considered where the maximum likelihood parameters and the covariance matrix are derived for the case where the error concentration parameters are unequal since previous study only considered the parameter estimation for the case of equal error concentration. The parameter estimate of *x* variable is improved by applying the iterative procedure in which the incidental parameter stops accumulating after the values converge to a finite number. The parameter estimate of the concentration parameter is estimated by using modified Bessel function in which it is expanded to become a cubic function. Monte Carlo simulation study shows that the proposed parameter estimations give a small bias with mean resultant length near to 1 and small estimated root mean square errors that indicate an adequacy of the estimation. Next, some methods to detect the presence of outlier in circular data are discussed. Previous studies only considered outlier detection methods for equal error concentration case. Therefore, in this study, all outlier detection methods take into account of both equal and unequal error concentration parameters in the model. The first proposed method in outlier detection is by using the determinantal equation of the covariance matrix, called *covratio*, in which the covariance matrix is based on the one derived in the first part of the study. Another two proposed methods used to detect the outlier are by using the difference mean circular errors. The two trigonometric functions are the *cosine* (*FDMCEC*) and *sine* (*FDMCES*) functions. The cut-off equations are derived based on the 5% upper percentile of the simulation study for each method for 95% confident level. The feasibility of all of the methods is assessed by the power of performance in Monte Carlo simulation studies when outlier is planted in the data. The results from the simulation study suggest that the power of performance for all three outlier detection methods achieves the maximum percentage which is 100% as the level of contamination increases. Hence, this suggests the feasibility of the method used in outlier detection.

Keywords: Circular data, outlier detection

INVITED LECTURES

DRONE TECHNOLOGY FOR ENVIRONMENTAL APPLICATIONS

Amir Feisal Merican Aljunid Merican*, Zati Hakim Azizul Hasan, Mohamad Sofian Abu Talip, Zeeda Fatimah Mohamad, Hanis Badarudin

Institute of Biological Science, Faculty of Science, University of Malaya, Kuala Lumpur

*Corresponding author: merican@um.edu.my

Abstract

This talk will describe research being carried out in the University of Malaya, in using drone technology towards environmental applications.

Conventional ground-based surveying and remote sensing techniques (eg. collection of aerial photography from satellite or planes) for periodic monitoring of rivers and lakes are laborious, costly and time consuming. The rise of new digital industrial technology, known as Industry 4.0 (IR4.0) offer exciting new perspectives to measure and monitor water quality. Some of the advantages are: (i) an efficient tool in difficult-to-access environments and/or hostile conditions (ii) overcome problems associated with the use of traditional static sensors and probes, which require costly maintenance and personnel, and thus can only be deployed in limited numbers, and (iii) enable simultaneous, accurate and reliable mapping of a variety of different habitat parameters within rivers and lakes at very fine scales.

Our research involve the design and building a sensing platform with unique characteristics: a hydrone (UAV-drone platform with high navigational speed and maneuverability) and an intelligent water monitoring and communication system. Although data capture from these sensors is carried out from the sky (not satellite or planes), the resolution and accuracy has been reported to be comparable as ground surveying. Data communication system will be developed for real time data capture, transmission, processing, analysis and sharing information with end-users. This research encompases six out of the nine pillars of IR4.0 which are Autonomous robots, Internet of Things (IoT), Big data, Cloud computing, Simulation and System integration.

The outcome of this research shall paves the way towards novel observations of the environment, enabling development of efficient strategies to monitor water quality towards better management of river and lake ecosystems and biodiversity by government authorities or other stake holders.

C-F BOND: FROM CONSTRUCTION TO ACTIVATION

Norio Shibata*

Department of Nanopharmaceutical Sciences and Department of Life Science and Applied Chemistry, Nagoya Institute of Technology, Gokiso, Showa-ku, Nagoya, 466-8555, Japan

*Corresponding author: nozshiba@nitech.ac.jp

Abstract

C-F bond activation was achieved by under mild conditions. Direct activation of carbon–fluorine bonds (C–F) to introduce the silyl or boryl groups and generate valuable carbon–silicon (C–Si) or carbon–boron (C–B) bonds is important in the development of synthetically useful reactions, owing to the unique opportunities for further derivatization to achieve more complex molecules. Despite considerable progress of C–F bond activation to construct carbon–carbon (C–C) and carbon–heteroatom (C–X) bond formation, the defluorosilylation via C–F cleavage has been rarely demonstrated. Here, we report an ipso-silylation of aryl fluorides via cleavage of unactivated C–F bonds by a Ni catalyst under mild conditions and without the addition of any external ligand. Alkyl fluorides are also directly converted into the corresponding alkyl silanes under similar conditions, even in the absence of the Ni catalyst (Scheme 1). Applications of this protocol in late-stage defluorosilylation of potentially bioactive pharmaceuticals and in further derivatizations are also carried out [1]. More resent results are also discussed [2].

Keywords: fluorine; activation; Ni; catalysis; defluorosilylation

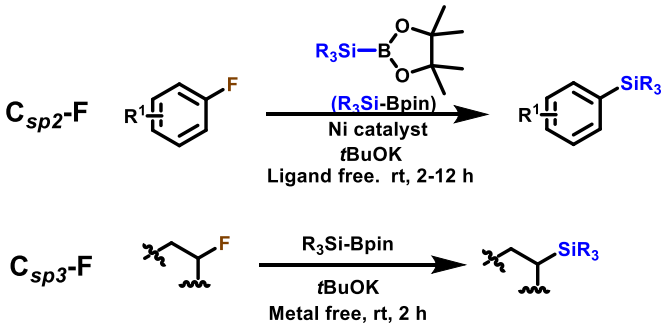

References

[1] Cui, B.; Jia, S.; Tokunaga, E.; Shibata, N. *Nat. Commun.* **2018**, *9*, 4393.
[2] Wang, J.; Ogawa, Y.; Shibata, N. *iScience* **2019**, *17*, 132.

SMALL MOLECULE ACTIVATION AND CATALYSIS USING HIGHLY UNSATURATED METAL COMPLEXES

Deborah L. Kays*

School of Chemistry, University of Nottingham, University Park, Nottingham, NG7 2RD, U.K.
*Corresponding author: deborah.kays@nottingham.ac.uk
http://www.nottingham.ac.uk/chemistry/people/deborah.kays

Abstract

The use of sterically demanding ligands affords the isolation of highly unsaturated complexes that show unusual reactivity towards small molecules.[1,2] Our research group are particularly interested in the use of *m*-terphenyl ligands (2,6-$Ar_2C_6H_3^-$) for this purpose, the steric bulk of which can be conveniently manipulated by changing the flanking Ar substituents. Low-coordinate iron(II) complexes featuring these ligands react with carbon monoxide, cleaving the C≡O bond to afford novel squaraines through selective homologation at ambient temperature and pressure.[3] Combined spectroscopic, structural and theoretical investigations have allowed us to postulate a mechanism for this reaction.

We are also interested in the use of these transition metal complexes as precatalysts for chemical reactions, such as cyclotrimerisation and hydrophosphination of isocyanates (Figure 1).[4,5] This reactivity affords phosphinodicarboxamide products through a combination of isocyanate coupling and P–H addition. Dehydrocoupling reactions between low-coordinate manganese(II) precatalysts and dimethylamine-borane highlight the importance of ligand choice, as small changes in the coordination environment around the metal centre can lead to significant differences in the reaction pathways.[6] These and other recent investigations of small molecule activation and catalysis using coordinatively unsaturated complexes will be described.

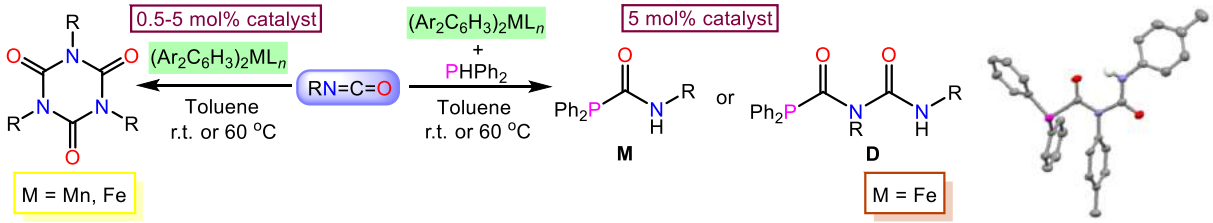

Figure 1. Cyclotrimerisation (left) and hydrophosphination of isocyanates (right) catalysed by *m*-terphenyl complexes. Far right: a phosphinodicarboxamide.

References

1. P. P. Power, *Chem. Rev.*, **2012**, *112*, 3482.
2. L. J. Taylor, D. L. Kays, *Dalton Trans.*, **2019**, *48*, 12365.
3. H. R. Sharpe, A. M. Geer, L. J. Taylor, B. M. Gridley, T. J. Blundell, A. J. Blake, E. S. Davies, W. Lewis, J. McMaster, D. Robinson, D. L. Kays, *Nat. Commun.*, **2018**, *9*, 3757.
4. H. R. Sharpe, A. M. Geer, H. E. L. Williams, W. Lewis, A. J. Blake, D. L. Kays, *Chem. Commun.*, **2017**, *53*, 937.
5. H. R. Sharpe, A. M. Geer, W. Lewis, A. J. Blake, D. L. Kays, *Angew. Chem. Int. Ed.*, **2017**, *56*, 4845.
6. H. R. Sharpe, A. M. Geer, T. J. Blundell, F. R. Hastings, M. W. Fay, G. A. Rance, W. Lewis, A. J. Blake, D. L. Kays, *Catal. Sci. Technol.*, **2018**, *8*, 229.

UNRAVELLING STRUCTURE-PROPERTY CORRELATIONS IN ADVANCED MATERIALS USING NEURON DIFFRACTION

Donna C. Arnold

School of physical sciences, University of Kent, Canterbury, Kent, CT2 7NH, UK

Abstract

Materials which exhibit electric and/or magnetic ordering are technologically important with application for example in renewable energy, memory devices, transducers and actuators. Extensive research is dedicated to increasing device functionality, lowering power consumption and moving away from the inclusion of toxic elements such as lead. However, in order to design improved functionality and develop the next generation of materials it is important to understand the correlations between the structure and properties. Our work centres on the use of neutron diffraction to understand the subtle perturbations in structure with stimuli such as temperature and pressure (both chemical and applied) and to correlate these with the properties a material exhibits. This talk will discuss some of our recent work on magnetic and ferroelectric materials and demonstrates the importance of using complementary techniques to understand structure-property correlations.

PRODUCTION OF LOW-DEFECT GRAPHENE SHEETS FOR THE ENHANCED PHOTOCATALYTIC PERFORMANCE OF GRAPHENE/ TiO_2 COMPOSITES

A. Tibodee[1], P. Pannak[1], K. Akkarachaneeyakorn[1], T. Thaweechai[2], W. Sirisaksoontorn[1]*

[1]Department of Chemistry and Centre of Excellence for Innovation in Chemistry, Faculty of Science, Kasetsart University, Chatuchak, Bangkok, Thailand.
[2]Knowledge of the Land for Sustainable Development, School of Integrated Science, Kasetsart University, Chatuchak, Bangkok 10900 Thailand

*Corresponding author: fsciwks@ku.ac.th

Abstract
A series of graphene-TiO_2 (GS/TiO_2) composites was successfully synthesized by the reaction of TiO_2 and low-defect graphene obtained from the exfoliation of a blue, stage-1 Na-ethylenediamine-GIC. The crystal structure of GS/TiO_2 exhibited both rutile and anatase. Low-defect graphene sheets dispersed in the composite were spectroscopically evaluated by XPS and Raman analyses. For the photocatalytic degradation of methylene blue (MB), GS/60TiO_2 could afford the superior performance with 92% degradation in comparison with rGO/TiO_2 and graphite/TiO_2.

Keywords: Graphite intercalation compound (GIC), Graphene, TiO_2, Photocatalyst

Introduction
TiO_2 has been extensively used as a photocatalyst during the past decades due to its low cost, high stability, and low environmental impact (Schneider et al. 2014). Anatase and rutile TiO_2 phases are broadly selected to study in photochemical processes. With the band gap of 3.0-3.2 eV, TiO_2 can be appropriately activated by the UV light, which leads to the promotion of electrons to the conduction band (CB), leaving behind a region of holes in the valence band (VB). Both photogenerated charges are able to mobilize to the surface of TiO_2 and react with the adsorbed organic dyes (Hoffmann et al. 1995). Unfortunately, the electron-hole recombination process happens faster than the surface reaction, causing a reduction of the photocatalytic performance. As a consequence, many researchers have placed numerous attempts to overcome this limitation (Leary et al. 2011). In this work, we introduced a low-defect graphene (GS) obtained from the exfoliation of stage-1 GIC into the TiO_2 matrix so as to improve the electron-hole-pair separation. We systematically studied the photocatalytic performance of the GS/TiO_2 composites in comparison with rGO/TiO_2 and graphite/TiO_2.

Methodology
A stage-1 GIC with $[Na(en)_x]^+$ as an intercalating complex was synthesized as reported previously (Sirisaksoontorn et al. 2011). The resulting GIC was exfoliated in dimethylsulfoxide (DMSO) with the concentration of 1 mg/ml, followed by centrifugation 5000 rpm for 15 min to obtain a stable suspension of graphene sheets. Then, TiO_2 was further mixed with graphene to obtain GS/TiO_2 composites with the variation of TiO_2 amounts (20, 40, and 60 mg) as denoted by GS/20TiO_2, GS/40TiO_2, and GS/60TiO_2. The structural characterization was studied by XRD, XPS, Raman, SEM, and TEM. For the photocatalytic study, GS/TiO_2 was applied for the photodegradation of MB under the 10 W UV-C light and its performance was compared with rGO/TiO_2, graphite/TiO_2, and pristine

TiO_2. The inorganic products from the photodegradation reaction was also investigated by ion chromatography.

Results and Discussion

A blue-colored stage-1 GIC was exfoliated in DMSO under prolonged sonication to produce a stable graphene suspension (Fig. 1). The as-obtained graphene was decorated by amide functional groups as confirmed by XPS. Raman results suggested the presence of low structural defect in graphene sheets as indicated by the small I_D/I_G ratio. As a result, a low-defect graphene could improve the photocatalytic performance of TiO_2 with 92% degradation of MB. The apparent kinetic rate constant was $1.20x10^{-2}$ min^{-1} which was superior to other photocatalysts; i.e. rGO/TiO_2, $graphite/TiO_2$ and pristine TiO_2 (Fig. 2). Moreover, three main inorganic products such as nitrate, sulphate, as well as ammonium ions were clearly detected.

Fig. 1 Synthesis route of the graphene suspension from a stage-1 GIC.

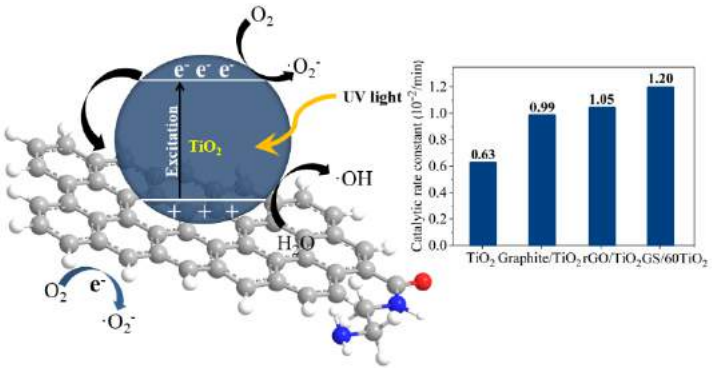

Fig. 2 Proposed photocatalytic mechanism of GS/TiO_2 and the comparative photocatalytic performance of different catalysts.

Conclusion

In summary, we successfully reported use of the stage-1 GIC as an alternative low-defect graphene source to prepare GS/TiO_2 composites. Low-defect graphene sheets with amide edge functionalization were homogeneously dispersed in the TiO_2 matrix. The electron-hole separation was greatly enhanced via the strong synergistic interaction of low-defect graphene and TiO_2, resulting in the enhanced photocatalytic performance in $GS/60TiO_2$ for MB degradation. Three main inorganic products (NH_4^+, SO_4^{2-} and NO_3^-) were detected as the photocatalytic products. Moreover, the structural stability and chemical reactivity of $GS/60TiO_2$ were maintained after five cycles of the photocatalytic reaction.

Acknowledgement

This research was financially supported by Kasetsart University Research and Development Institute (KURDI) (grant no. 73.59).

References

1. Schneider, J., Matsuoka, M., Takeuchi, M., Zhang, J., Horiuchi, Y., Anpo, M., and Bahnemann, D.W., 2014. Understanding TiO_2 Photocatalysis: Mechanisms and Materials. *Chem. Rev.* 114, 9919-9986.
2. Hoffmann, M.R., Martin, S.T., Choi, W., and Bahnemann, D.W., 1995. Environment Applications of Semiconductor Photocatalysis. *Chem. Rev.* 95, 69-96.
3. Leary, R., and Westwood, A., 2011. Carbonaceous Nanomaterials for the Enhancement of TiO_2 Photocatalysis. *Carbon.* 49, 741-772.
4. Sirisaksoontorn, W., Adenuga, A.A., Remcho, A.T., and Lerner, M.M., 2011. Preparation and Characterization of a Tetrabutylammonium Graphite Intercalation Compound. *J. Am. Chem. Soc.* 133, 12436-12438.

PRAZIQUANTEL-TOWARDS AN UNDERSTANDING OF THE MECHANISM

David J Timson

University of Brighton, UK

Abstract

Praziquantel (PZQ) is widely used in the treatment of schistosomiases and other infections by parasitic worms. Early observations suggested that the drug acts by dysregulating calcium homeostasis in the worm. However, the precise biochemical mechanism of action has never been elucidated. The consensus of opinion is that it acts on voltage-gated calcium channels. However, adenosine uptake, myosin light chains and host proteins have also been implicated.

This talk will summarise the various hypotheses for PZQ's mechanism of action and present data on calcium binding proteins from *Schistosoma mansoni* which have been shown to interact with the drug. Initially we hypothesised that PZQ might antagonise the interaction between calmodulin and the voltage-gated calcium channel. However, our experimental work showed that this is unlikely to be the case. Some members of the tegumental antigen-like (TAL) family of proteins interact with PZQ and one member, SmTAL1, also interacts with the voltage-gated calcium channel. PZQ disrupts this interaction leading to the intriguing hypothesis that this may play an important part in the drug's mechanism of action. The talk will conclude with some suggestions for investigating this attractive, but speculative, hypothesis.

HIERARCHIES BEYOND THE MOLECULE: INNOVATING MODERN FUNCTIONAL MATERIALS

Ian J Scowen,[a] Tasnim Munshi[a] and Stefan Wüttke[a,b]

[a] School of Chemistry, University of Lincoln, Lincoln LN6 7 DL, United Kingdom
[b] Basque Center for Materials, Applications and Nanostructures, 48940 Leioa, Spain

Abstract

The design of functional materials with properties at human-scales represents a frontier challenge for research in materials chemistry. Natural and man-made materials exhibit structure on more than one length scale and the hierarchy of such structural units can have considerable influence on bulk materials properties. Furthermore, consideration of structure at molecular (pm), supramolecular/nano (nm), micro (μm) and meso (mm and above) scales and the hierarchy of structural units offers the potential to 'design-in' desired properties leading to full 'bottom-up' design of functional materials.

The growing appreciation of structural principles 'beyond the molecule' has led to the explosive growth in supramolecular chemistry and, in the case of long-range ordering, crystal engineering in recent decades. In this perspective presentation, we will draw on examples of engineered solid state materials with differentiated physical property domains that engender properties (e.g. physical, optical, electronic) that are a function of the assembled materials in contrast to their molecular components. Offering a perspective to the future, we will also consider the emerging challenges that accompany extension of the concept of structural hierarchies that may facilitate materials design from molecule to functional products.

HIGH AND NEAR ROOM TEMPERATURE SUPERCONDUCTIVITY IN THE CUPRATES AND HYDRIDES

R. Abd-Shukor*

School of Applied Physics, Universiti Kebangsaan Malaysia, 43600 Bangi, Selangor, Malaysia

*corresponding author: ras@ukm.edu.my

Abstract

The interest on superconductivity is renewed recently following the discovery of near room temperature superconductivity in hydrogen sulfide (203 K) and hydride (250-280 K) under high pressure. In this paper we discuss the relation between the critical temperature T_c and coherence length ξ (Figure 1), electron-phonon coupling constant and other thermodynamic properties of these new superconductors. The possible role of phonons in the superconducting mechanism of hydrogen sulfide and hydrides are discussed. The relevance of conventional BCS theory to these new superconducting materials is also discussed. The similarities and differences between the hydride and cuprate superconductors will also be highlighted.

Keywords: near room temperature superconductivity; Bardeen Cooper Schrieffer theory, phonons; high pressure

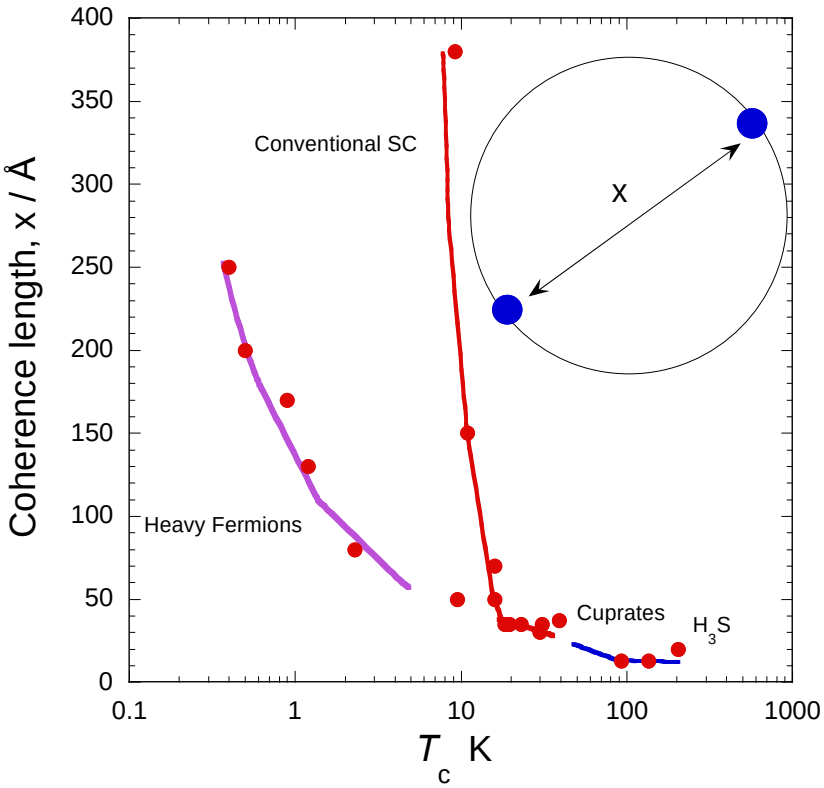

Figure 1. The relationship between coherence length and critical temperature of low, high and near room temperature superconductors

A GROUP ATTACK OF TWO PURSUERS AT ONE EVADER IN AN EVASION DIFFERENTIAL GAME WITH COORDINATE-WISE INTEGRAL CONSTRAINTS ON CONTROL FUNCTIONS OF PLAYERS

I. Arif Alias[1]*, Y. Salleh[2], G. Ibragimov[3]

[1,2,3]*Institute for Mathematical Research (INSPEM), Universiti Putra Malaysia, 43400 UPM Serdang, Selangor, Malaysia.*
[1,3]*Department of Mathematics, Universiti Putra Malaysia, 43400 UPM Serdang, Selangor, Malaysia.*

*Corresponding author: idham_aa@upm.edu.my

Abstract
We consider an evasion differential game of which evader is under a group attack of two pursuers in plane R^2. The control functions of players are subjected to coordinate-wise integral constraints. The evader maneuvers against a selected pursuer with nonnegative vertical speed in a small area of *y*-axis, based on a defined natural-valued step function. We say that evasion is possible if the position of the evader does not collide with that of any of the pursuer at all times and it is proved by using the constructed strategies and fictitious evaders.

Keywords: Evasion, strategy, coordinate-wise, integral constraints, fictitious evader

Introduction
The opposite parties in a differential game are called pursuer and evader respectively. The evader is to avoid being captured by the pursuer in an evasion differential game and the study was started by Isaacs (1967). Since then, several studies on evasion differential game were done by many including Azimov (1974), Zak (1978), Chodun (1989), Kuchkarov et al. (2002), Ibragimov et al. (2012) and Alias et al. (2013).

In the present paper, we investigate an evasion differential game for one evader to avoid being captured by two pursuers in a group attack. The study is based on coordinate-wise integral constraints on control functions of players. The objectives of the study is to find sufficient condition of evasion and construct an explicit strategy for the evader to ensure evasion are possible from any initial positions of players. We just consider $y_{10} \le x_{10}$, $y_{20} \le x_{20}$ and use fictitious evaders to estimate the distance between the real evader and each pursuer.

Methodology
The pattern of trajectory of the evader is decided to form its strategy. The strategy is then shown to be admissible. Evasion is possible is then proved by using the sufficient condition and the constructed strategy.

Result and Discussion

Theorem 3.1. If $\sigma_1^{\,2} \ge \rho_{11}^{\,2} + \rho_{21}^{\,2}$ and $\sigma_2^{\,2} \ge \rho_{12}^{\,2} + \rho_{22}^{\,2}$ then evasion is possible.

Proof. Let $d = \min\{|x_{10} - y_0|, |x_{20} - y_0|\}$ and specify a_1 to be any number satisfying $0 < a_1 < \min\{1, d\}$ and $a_2 = k a_1^{\,4}$ for $0 < k < 1$. Define τ_1 to be the first time when

$|x_1(\tau_1)-y(\tau_1)|=a_1>0$ and τ_2 to be the first time when $|x_2(\tau_2)-y(\tau_2)|=a_2>0$. Also let $\tau_1'=\tau_1+\frac{a_1}{\alpha}$, $\tau_2'=\tau_2+\frac{a_2}{\alpha}$ for $0<\alpha<1,\ a\alpha<\sigma_1^2,\ a\alpha<\sigma_2^2,\ \sqrt{2\alpha}\le\sigma_1-\rho_1,\ \sqrt{2\alpha}\le\sigma_2-\rho_2$ and $\tau^*=\max\{\tau_1',\tau_2'\}$ is the finishing time of the game. We consider both cases when $\tau^*=\tau_1'$ and $\tau^*=\tau_2'$ and define a natural-valued step function $r=r(t)=\max\left\{p\middle|\tau_p\le t<\tau_p',\ p\in\{1,2\}\right\}$ for $\tau_1\le t<\tau^*$ of which, x_r is the chosen pursuer.

Let, $V_{r1}(t)=\begin{cases}\alpha+|u_{r1}(t)|, x_{r1}(\tau_r)<y_1(\tau_r)\\ -(\alpha+|u_{r1}(t)|), x_{r1}(\tau_r)<y_1(\tau_r)\end{cases}$, and $V_{r2}(t)=\alpha+|u_{r2}(t)|$.

a) Construction of a Strategy for the Evader

For both cases, $v(t)=\begin{cases}(0,|u_{12}(t)|), 0\le t<\tau_1\\ (V_{11}(t),V_{12}(t)), \tau_1\le t<\tau_2\end{cases}$.

For case 1 ($\tau^*=\tau_1'$), $v(t)=\begin{cases}(-V_1(t),V_2(t)), \tau_2\le t\le\tau_2',\\ (V_1(t),V_2(t)), \tau_2'\le t\le\tau_1',\\ (0,V_{12}(t)), \tau_1'\le t\le\tau_1'+\frac{a_1}{\alpha},\\ (0,|u_{12}(t)|), t>\tau_1'+\frac{a_1}{\alpha}\end{cases}$ and

for case 2 ($\tau^*=\tau_2'$), $v(t)=\begin{cases}(-V_1(t),V_2(t)), \tau_2\le t\le\tau_1',\\ (-V_1(t),V_2(t)), \tau_1'\le t\le\tau_2',\\ (0,V_{22}(t)), \tau_2'\le t\le\tau_2'+\frac{a_2}{\alpha},\\ (0,|u_{22}(t)|), t>\tau_2'+\frac{a_2}{\alpha}\end{cases}$

b) Construction of Strategy for the Fictitious Evaders

$w_1(t)=(V_{11}(t),V_2(t)), \tau_1\le t<\tau_1'$ and $w_2(t)=(V_{12}(t),V_2(t)), \tau_2\le t<\tau_2'$.

c) Admissibility of the Strategy

$\int_0^\infty v_1^2(s)ds=0\le\sigma_1^2$ and $\int_0^\infty v_2^2(s)ds=\int_0^\infty|u_2(s)|^2ds\le\rho_2^2\le\sigma_2^2$ and similarly for $w_1(t)$ **and** $w_2(t)$**.**

d) Proof of Evasion is Possible

We estimate the distances between evader and each pursuer from above, on each time interval and use fictitious evaders. We conclude that, $y(t) \neq x(t), t \geq 0$ and proof is completed.

Conclusion

The sufficient conditions for evasion is possible are $\sigma_1^2 \geq \rho_{11}^2 + \rho_{21}^2$ and $\sigma_2^2 \geq \rho_{12}^2 + \rho_{22}^2$, and with each constructed strategy, it is shown that evasion is possible from any initial position of players.

Acknowledgement

This research was partially supported by the National Fundamental Research Grant Scheme (FRGS) of Malaysia, No. 01-01-16-1840FR.

References

1. Alias, I.A., Salleh, Y., Azamov, A., 2013. Evasion Differential Game of Two Evaders and One Pursuer with Integral Constraints. *AIP Conf. Proc.* 1557: 140-145.
2. Azimov, A.Y., 1974. A linear differential evasion game with integral constraints on the controls. *USSR Computational Mathematics and Mathematical Physics*. 14(6): 56-65.
3. Chodun, W., 1989. Differential games of evasion with many pursuers. *Journal of Mathematical Analysis and Applications*. 142(2), 370-389.
4. Ibragimov, G.I., Salimi, M., Amini, M., 2012. Evasion from many pursuers in simple motion differential game with integral constraints. *European Journal of Operational*. 218(2), 505-511.
5. Kuchkarov, A.S., Rikhsiyev, B.B., 2002. The possibility of avoiding an encounter in a linear differential game of evasion. *Journal of applied mathematics and mechanics*. *66*(2), 233-237.
6. Isaac, R., 1965. Differential Game. John Wiley and Sons. New York.
7. Zak, V.L., 1978. On a problem of evading many pursuers. *PMM*. 43(3): 456-465.

ROBUST AUGMENTED APPROACH TO DESIRABILITY FUNCTION FOR OPTIMIZING MUTIPLE RESPONSES AND ITS APPLICATION TO MANUFACTURING INDUSTRIES

Habshah Midi[1]*, Mohd Shafie Mustafa[1] and Nasuhar Ab. Aziz[2]

[1]Faculty of Science and Institute for Mathematical Research, Universiti Putra Malaysia, 43400 Serdang, Selangor, Malaysia.
[2]Univesiti Teknologi Mara, 185000, Kota Baru, Kelantan, Malaysia.

*Corresponding author: habshah@upm.edu.my

Abstract

Response Surface Methodology is widely used in manufacturing industry such as food and chemical industry for optimizing a process with the purpose of determining the optimum settings that give optimum yield over a certain region of interest, with minimum cost. In many experiments, usually more than one response is of interest and in this situation researchers have to deal with multiple response optimization. The desirability function approach is the commonly employed technique to handle the problem of optimizing multiple responses simultaneously. However, this approach has its shortcoming whereby it does not take into consideration for the variability in each predicted response. As a result, the actual response may fall outside the acceptable region even though the predicted response at the optimal solution has high overall desirability score. An augmented approach to the desirability function (AADF-OLS based) which can reduce the variances of all predicted responses resulting in narrower prediction intervals, is put forward to remedy this problem. Nonetheless, in the presence of outliers, the AADF-OLS is not reliable since its formulation is constructed based on the Ordinary Least Squares (OLS) and geometric mean estimates which are not resistant to outliers. As an alternative, we propose to incorporate robust MM-estimator and geometric median in the augmented approach framework and name it the Augmented Approach to the Desirability Function based on MM estimator and Geometric Median and denote as (AADF-MM based). The merit of our method is confirmed by real example and Monte Carlo simulation.

Keywords: Augmented approach, Desirability function, Geometric median, MM estimaror, Outliers

A MATHEMATICAL APPROACH IN FORECASTING

S. N. I. Ibrahim[1,2*]

[1]Department of Mathematics, Faculty of Science, Universiti Putra Malaysia, 43400 UPM Serdang, Selangor, Malaysia.
[2]Institute for Mathematical Research, Universiti Putra Malaysia, 43400 UPM Serdang, Selangor, Malaysia.

*Corresponding author: iqmal@upm.edu.my

Abstract

This study investigates the modelling of price paths under the dynamics of geometric Brownian motion (GBM). For calibration and simulation, we used daily historical prices which include non-trading days and public holidays. We also include jump-diffusion process and compare accuracy with GBM for the price simulation. Numerical results show that GBM and GBM with jumps produce accurate price prediction for a short-term period, with GBM with jumps produce a lower MAPE value.

Keywords: Price path, geometric Brownian motion, MAPE.

APPLICATIONS OF SEMISIMPLE GROUP ALGEBRA TO CRYPTOGRAPHY

Denis Wong Chee Keong[1]*

[1]Centre for Cyber Security, Universiti Tunku Abdul Rahman, Jalan Sungai Long, Bandar Sungai Long, 43000 Kajang, Selangor, Malaysia.

*Corresponding author: deniswong@utar.edu.my

Abstract
Almost all conventional cryptosystems are defined over large cyclic groups, commutative platforms, vector spaces over finite field and polynomial ring in a very natural way. However, not much works has been done on constructing cryptographic primitives by using a group algebra. By choosing an appropriate group algebra possess plenty of nice structures and properties might be suitable for cryptography purposes. In this talk, we will be investigating different types of applications for semisimple group algebra in constructing various cryptographic primitives.

Keywords: Cryptosystem, group algebra

ORAL PRESENTATION

BIOLOGY

COMPARISON OF DIFFERENT SOLVENTS (ACETONE, ETHANOL AND DMSO) ON LOCOMOTOR BEHAVIOUR OF ZEBRAFISH (*Danio rerio*) LARVAE

Anis Azman[1], Noraini Abu Bakar[1], Nurul Farhana Ramlan[1] and Wan Norhamidah Wan Ibrahim[1,2,3*]

[1] Department of Biology, Faculty of Science, Universiti Putra Malaysia, 43400 Serdang, Selangor, Malaysia
[2] Laboratory of Natural Product, Institute of Bioscience, Universiti Putra Malaysia, 43400 UPM Serdang, Selangor, Malaysia
[3]Integrated Chemical Biophysics Research Centre (i-CheBP), Universiti Putra Malaysia, 43400 UPM Serdang, Selangor, Malaysia

*Corresponding author: wnwi@upm.edu.my

Abstract

Solvent is fundamental vehicles that have been used in delivering insoluble chemicals to the zebrafish larvae during various types of chemical testing. However, information about toxicity effects for different types of solvents on zebrafish larvae's locomotor behavior is limited. Therefore, this study evaluated the effects of acetone, DMSO and ethanol on the larvae's locomotor behavior under different light illumination condition; continuous illumination and alternate light-dark illumination by using Zebrabox Viewpoint Technology. The larvae were exposed to different types of solvent in 24-well plate at 6 days post fertilization for 24 hours before subjected to behavioral recording. The concentrations were chosen according to the commonly used concentration based on literature. The control group received distilled water and was handled similarly with the treatment group. Exposure to 0.01% acetone and 1% ethanol for 24 hour incubation caused hypolocomotor activity (high or low total freezing count, shorter total distance travelled and slower swimming speed) in zebrafish larvae movement for both continuous illumination and alternate light-dark illumination. Whereas, 0.5% DMSO treated larvae showed almost similar locomotor responses as the control in both conditions. Therefore, DMSO is the most ideal carrier solvents since it gave no significant effect towards the zebrafish larvae's locomotor behavior in comparison to acetone and ethanol.

Keywords: Light and dark; Locomotor; Solvent; Zebrafish larvae

THE EFFECTS OF TOCOTRIENOL DERIVED FROM *Elaeis guineensis* ON OSTEOCYTE BIOMARKERS IN RATS WITH METABOLIC SYNDROME AND OSTEOPOROSIS

S.K. Wong[1], K.-Y. Chin[1], S. Ima-Nirwana[1]*

[1]*Department of Pharmacology, Faculty of Medicine, Universiti Kebangsaan Malaysia, Jalan Yaacob Latif, Bandar Tun Razak, 56000 Cheras, Kuala Lumpur, Malaysia.*

*Corresponding author: imasoel@ppukm.ukm.edu.my

Abstract
Osteocytes are cells residing within the mineralized bone matrix which function to sense mechanical stimuli and secrete various bone-related peptides to coordinate the osteoblast and osteoclast activities. This study highlighted the role of osteocyte in regulating bone homeostasis and the beneficial effects of palm tocotrienol on bone through modulation of osteocyte-derived molecules in a rat model of bone loss due to metabolic syndrome (MetS).

Keywords: Dyslipidaemia, Hyperglycaemia, Hypertension, Obesity, Vitamin E

Introduction
Osteoporosis is associated with metabolic syndrome (MetS) (Wong et al. 2018a; Wong et al. 2018b). Previous studies on the underlying mechanisms mediated by MetS in orchestrating bone remodelling have focused on the behaviour of mature osteoblast and osteoclast while neglecting the role of osteocytes. Herein, we evaluated the effects of tocotrienol on osteocyte-mediated bone remodelling through the levels of bone-related peptides [osteoprotegerin (OPG), parathyroid hormone (PTH), Dickkopf-related protein-1 (DKK-1), sclerostin (SOST), fibroblast growth factor-23 (FGF-23), and soluble receptor activator of nuclear factor-kappa B Ligand (sRANKL)] in an osteoporotic rat model induced by MetS.

Methodology
Male Wistar rats (n=30) aged 12-week-old were randomised into five experimental arms. The baseline group was sacrificed during the onset of experiment. Standard chow diet and tap water were given to the normal group. The remaining groups were supplied with high-carbohydrate high-fat (HCHF) diet and 25% fructose drinking water. Treatments were started at week 8. The normal animals were orally administered with normal saline. The HCHF animals were orally treated with three different regimens [corn oil (vehicle), 60 and 100 mg/kg palm tocotrienol] respectively. The rats were euthanized at week 20. Right tibias were excised, stripped off soft tissues and homogenised in protein extraction buffer. The supernatant was collected for the assessment of osteocyte-related biomarkers though magnetic multiplex immunoassay.

Results and Discussion
The vehicle-treated HCHF rats had higher levels of PTH, DKK-1, SOST, FGF-23 and sRANKL in the right tibias ($p<0.05$). After treatment with 60 and 100 mg/kg palm tocotrienol, the levels of FGF-23 and sRANKL decreased ($p<0.05$). Only 100 mg/kg palm tocotrienol reduced DKK-1 and SOST levels in tibias of the HCHF animals ($p<0.05$). Mature osteocytes secrete OPG, DKK-1, SOST, FGF-23 and RANKL that play important roles in the regulation of bone remodelling. DKK-1 and SOST are potent inhibitors of bone formation. Their binding to LRP5 and LRP6 prevents the activation of Wnt/β-catenin

signalling, which is an essential pathway in osteoblastogenesis (Bellido 2014). FGF-23 modulates serum phosphorus level by increasing renal phosphate excretion, thus high level of FGF-23 inhibits bone mineralization (Guo & Yuan 2015). Differential production of OPG and RANKL, characterized by low OPG:RANKL ratio, determines osteoclast formation and activity (Bellido 2014). On the other hand, PTH functions to inhibit osteoblast apoptosis, leading to increased osteocyte density. PTH also induces RANKL production by osteocytes, resulting in increased osteoclastogenesis and bone resorption (Ben-zwadh et al. 2014).

Conclusion

Osteocytes play a role in orchestrating bone metabolism in osteoporosis induced by MetS Palm-based tocotrienol exerts potential bone-protecting effects through regulating the osteocyte regulatory proteins. Hence, these findings suggested that osteocyte-driven bone remodelling may be targeted in developing new prophylactic or therapeutic intervention for the management of osteoporosis.

Acknowledgement

We thank Universiti Kebangsaan Malaysia for the financial support through MI-2019-006 and FF-2019-036/1 grants.

References

Bellido, T., 2014. Osteocyte-driven bone remodelling. *Calcif. Tissue Int.* 94, 25-34.

Ben-awadh, A.N., Delgado-Calle, J., Tu, X., Kuhlenschmidt, K., Allen, M.R., Plotkin, L.I., and Bellido, T., 2014. Parathyroid hormone receptor signaling induces bone resorption in the adult skeleton by directly regulating the RANKL gene in osteocytes. *Endocrinology* 155, 2797–2809.

Guo, Y.-C. and Yuan, Q., 2015. Fibroblast growth factor 23 and bone mineralization. *Int. J. Oral Sci.* 7, 8–13.

Wong, S.K., Chin, K.-Y., Suhaimi, F.H., Ahmad, F., Jamil, N.A., and Ima-Nirwana, S., 2018a. Osteoporosis is associated with metabolic syndrome induced by high-carbohydrate high-fat diet in a rat model. *Biomed. Pharmacother.* 98, 191–200.

Wong, S.K., Chin, K.-Y., Suhaimi, F.H., Ahmad, F., and Ima-Nirwana, S., 2018b. Effects of metabolic syndrome on bone mineral density, histomorphometry and remodelling markers in male rats. *Plos One* 13, e0192416.

THE EVALUATION OF ANTIPROLIFERATIVE POTENTIAL OF DOXYCYCLINE AND AZITHROMYCIN IN SINGLE AND COMBINATION TREATMENTS AGAINST HUMAN GLIOBLASTOMA CELLS

Siti Nazihahasma Hassan[1,3], Zamzuri Idris[1,3], Abdul Aziz Mohamed Yusoff[1,3], Norhanani Mohd Redzwan[2,3] & Farizan Ahmad[1,3*]

[1]Department of Neurosciences, School of Medical Sciences, Universiti Sains Malaysia, 16150 Kubang Kerian Kelantan, Malaysia.
[2]Department of Immunology, School of Medical Sciences, Universiti Sains Malaysia, 16150 Kubang Kerian Kelantan, Malaysia.
[3]Hospital Universiti Sains Malaysia, 16150 Kubang Kerian, Kelantan

*Corresponding author: farizan@usm.my

Abstract
Doxycycline (DOXY) and Azithromycin (AZI) have demonstrated antiproliferative activity against human glioblastoma (GBM) cells *in-vitro* in a time and concentration dependent fashion. Nevertheless, the combination of both antibiotics exerts antagonistic antiproliferative activity in human GBM cells.

Keywords: Doxycycline, Azithromycin, Combination interaction, Glioblastoma

Introduction
There is growing evidence showing that generic antibiotics such as DOXY and AZI own anticancer activities in various *in-vitro* and *in-vivo* cancer models by way of targeting mitochondria. Indeed, mitochondria biogenesis and oxidative metabolism are the main sources for cancer stem cells (CSCs) propagation. As chemo-radioresistance is a hallmark of CSCs, targeting mitochondria dysfunction using inducers like DOXY and AZI may have great potential in eradicating the CSCs and overcoming chemo-radioresistance (Fiorillo *et al.*, 2019; Lamb *et al.*, 2015). Although studies have shown that both antibiotics have anticancer activities, none is known about their combination against human GBM cells. The present study aims to evaluate the antiproliferative potential of DOXY, AZI and combinations thereof in human GBM U87 cells.

Methodology
Half-maximal inhibitory concentration (IC50) of DOXY and AZI was obtained from MTT viability derived dose-response curve. Antiproliferative activity of DOXY, AZI and combinations thereof in U87 cells was evaluated by MTT viability assay for 24, 48, 72 and 96 hours. Median-effect analysis of Chou-Talalay (Chou, 2006) was used to determine the *in-vitro* combination interaction (CI) of DOXY and AZI.

Results and Discussion
DOXY and AZI inhibited U87 cell proliferation in a time and concentration dependent fashion. However, only AZI treated group showed statistically significant difference of antiproliferative activity compared to TMZ, Figure 1 (a). For the combination groups, only DOXY+AZI (73.5+112.5 µg/ml) displayed statistically significant difference of antiproliferative activity as presented in Figure 1 (a). Nonetheless, the calculated CI value suggests that DOXY+AZI (73.5+112.5 µg/ml) combination was antagonistic for all four incubation periods, Figure 1 (b). There were several DOXY+AZI combinations fell into synergistic interaction yet were impotent to inhibit U87 cell proliferation. The DRI values for most of the DOXY+AZI combinations were more than one which indicated favourable dose reduction. This signifies that the toxicity of both drugs can be reduced by decreasing

the dose. Alternatively, the efficacy of both drugs can be increased by increasing the dose without increasing toxicity. Collectively, DOXY+AZI combinations does not works better than either drug alone against U87 cells.

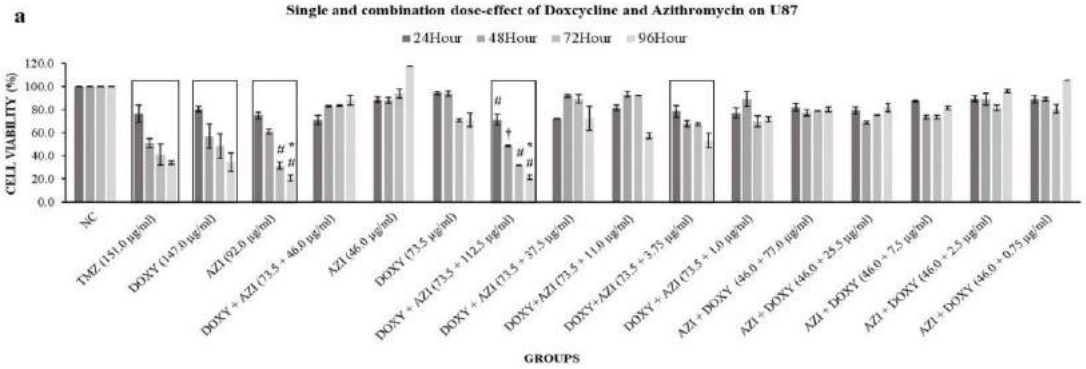

Figure 1 (a) Concentration-response profile of DOXY, AZI and combinations thereof. Dose-effect trend similar to TMZ was boxed with black. Quantitative analysis by repeated measures ANOVA, *significant compared to TMZ (IC50), #significant compared to DOXY (IC50) and †significant compared to AZI (IC50) with $p<0.05$. Error bars represent ± SD.

b

Fa(%) (CI) DRI Doxycycline DRI Azithromycin			Azithromycin (µg/ml)						Doxycycline (µg/ml)					Fa(%) (CI) DRI Doxycycline DRI Azithromycin		
			1.0	3.75	11.0	37.5	46.0	112.5	77.0	25.5	7.5	2.5	0.75			
Doxycycline (µg/ml)	24 hour	73.5	0.23 (0.45) 2.27 85.21	0.21 (0.52) 2.14 20.95	0.18 (0.68) 1.93 6.25	0.28 (0.75) 2.62 2.73	0.29 (0.81) 2.69 2.31	0.29 (1.43) 2.69 0.94	0.18 (1.44) 3.08 0.89	0.21 (0.62) 3.42 3.08	0.13 (0.54) 2.51 7.00	0.10 (0.52) 2.15 17.10	0.11 (0.46) 2.27 61.33	46.0	24 hour	Azithromycin (µg/ml)
	48 hour	73.5	0.11 (0.85) 1.20 44.02	0.32 (0.62) 1.75 21.38	0.07 (1.27) 1.05 3.20	0.08 (1.91) 1.09 1.00	0.17 (1.55) 1.39 1.20	0.51 (1.44) 2.19 1.02	0.23 (1.58) 2.50 0.85	0.31 (0.69) 2.76 3.08	0.26 (0.50) 2.58 9.40	0.11 (0.58) 1.92 17.60	0.11 (0.54) 1.92 58.70	46.0	48 hour	
	72 hour	73.5	0.30 (0.98) 1.03 67.03	0.33 (0.93) 1.14 18.37	0.07 (3.56) 0.30 4.32	0.10 (3.25) 0.40 1.37	0.17 (2.43) 3.23 1.26	0.68 (1.53) 0.61 0.82	0.21 (2.11) 1.18 0.79	0.24 (1.16) 1.33 2.47	0.26 (0.81) 1.44 8.60	0.19 (0.97) 1.08 23.80	0.19 (0.94) 1.08 79.34	46.0	72 hour	
	96 hour	73.5	0.28 (1.04) 0.98 70.53	0.47 (0.76) 1.41 20.71	0.42 (0.92) 1.29 6.90	0.28 (1.55) 0.98 1.88	0.12 (2.37) 0.61 1.36	0.78 (1.61) 2.61 0.81	0.20 (1.93) 1.28 0.87	0.18 (1.21) 1.21 2.59	0.18 (0.94) 1.21 8.80	0.04 (1.77) 0.58 21.72	0.00 (3.26) 0.31 61.33	46.0	96 hour	

Figure 1 (b) Summary table showing potency (Fa), CI and DRI values of DOXY and AZI combined at various concentrations. CI < 0.9, CI = 0.9-1.1 and CI > 1.1 means synergistic (marked with yellow), additive effect (marked with green) and antagonistic (marked with pink), respectively. Fa = 0 indicates no antiproliferative activity whereas Fa = 1 indicates 100% antiproliferative activity. DRI=1 shows no dose reduction, DRI<1 unfavourable dose reduction and DRI>1 favourable dose reduction.

Conclusion

DOXY and AZI possess antiproliferative activity against human GBM cells in a time and concentration dependent fashion. Nevertheless, the combination treatment using both antibiotics exerts antagonistic fashion of antiproliferative activity in human GBM cells.

Acknowledgement

FRGS (203/PPSP/6131203) and Universiti Sains Malaysia Fellowship.

References

Chou, T.-C. (2006). Theoretical basis, experimental design, and computerized simulation of synergism and antagonism in drug combination studies. *Pharmacological reviews,* **58(3)**, 621-681.

Fiorillo, M., Tóth, F., Sotgia, F. & Lisanti, M. P. (2019). Doxycycline, Azithromycin and Vitamin C (DAV): A potent combination therapy for targeting mitochondria and eradicating cancer stem cells (CSCs). *Aging (Albany NY),* **11(8)**, 2202.

Lamb, R., Ozsvari, B., Lisanti, C. L., Tanowitz, H. B., Howell, A., Martinez-Outschoorn, U. E., Sotgia, F. & Lisanti, M. P. (2015). Antibiotics that target mitochondria effectively eradicate cancer stem cells, across multiple tumor types: treating cancer like an infectious disease. *Oncotarget,* **6(7)**, 4569.

STUDENTS' PARTICIPATION IN BIOLOGY GARDEN PRACTICAL IN COLLEGES OF EDUCATION IN ANAMBRA STATE OF NIGERIA FOR SELF-RELIANCE

Egbunonu, Roseline N[1]*, Ugbaja J.N[2], Obiajulu A.N[3] and Emma-Adiole N.B[4].

Biology Education Department, School of Sciences, Federal College of Education (Technical), Umunze, Anambra State of Nigeria

*Corresponding author: egbunonuroseline@gmail.com

Abstract
This study investigated the biology students' participation in garden practical in colleges of education in Anambra state, Nigeria. Two research questions and one hypothesis guided the study. Population consist 598 biology students with sample size of 240. Data collected with questionnaire was analyzed with mean(x), standard deviation (SD) and T-test. The result showed that; students participated fully in some biology garden practical activities like watering of plants, sowing of seeds and transplanting of seedlings, some of the things that affect students' participation include: working in the garden is difficult and dirty, insufficient time for participation. Based on the findings, the study recommended that enough time should be allotted for garden activities and students should be oriented on the need to be involved in garden activities to acquire skills for self-reliance.

Keywords: Biology, Garden, Practical, Students, Self-reliance.

Introduction
Biology garden creates avenue of achieving training in functional education. It enhances students with suitable skills and knowledge that provides opportunity for self-employment. Acquiring gardening knowledge, skills and value in biology education will to some extent help to overcome the barriers unemployment imposed in the country. Despite the fact that biology garden plays vital role in education for self-reliance and creates employment opportunities, the students' participation in it has not been determined. Colleges of Education in Anambra state were chosen as a case study because both colleges have biology gardens and offer courses that involves gardening. To some students, working in the garden is like labouring them. Students may not like to soil their hand in the process of acquiring garden skills and may take it as punishment. The theoretical framework was extensively reviewed.

Methodology
This study adopted survey design. A survey research is the type in which a group of people or items is studied by collecting and analyzing data from only a few of items considered to be representative of the entire group (Anaekwe and Onunkwo 2016). Two research questions and one hypothesis used, filled the gap by identifying: garden practical activities students participate in biology garden; factors that affect students' participation in garden activities.

Population of the study
Population of the study consists of 598 biology students in Colleges of Education in Anambra State, Nigeria. Sample of 240 students were selected using Yaro Yamane. Structured questionnaire was used and validated by three experts in the related areas. The instrument was trial tested. To ensure the reliability coefficient, Cronbach Alpha was used

and the result yielded 0.87. Mean, standard deviation and t-test were used to analyze the data collected.

Results and Discussion

The findings of the study revealed that 8 students participated fully in some biology garden practical activities. This is in line with Okafor (2017) who stated that biology students are involved in garden activities. Also, the findings of the study showed that some factors affect students' participation in biology garden practical activities which include; insufficient time allotted to biology garden practical activities, students seeing garden activities as different and dirty activities but to mention a few. Finally, there is no significant difference on the mean scores of male and female students on the participation of biology garden practical activities.

Conclusion

The findings of the study revealed that students participate in some of the biology garden practical activities. Thus, the students should be encouraged to participate in all garden activities so as to acquire the skills that would aid them to be self-employed.

References

Anaekwe, M.C. and Onunkwo, G.I. (2016). Data Analysis; Inferential Statistics. In M.C, Anakwe(Ed). *Basic Research and Statistics in Education and Social Sciences* pages 195-228.

Okafor, N.M. (2017). Extent of student participation in biology garden practical, Federal College of Education, Eha-Amufu: Implication for entrepreneurship. *Journal of empirical research in science and technology education JERSTE 5(1)* 106-116

FACTORS INFLUENCING DENGUE KNOWLEDGE, ATTITUDE AND PRACTICES IN SELECTED AREAS OF SELANGOR, MALAYSIA

Alaba Ajibola Lamidi-Sarumoh[1, 3], Shamarina Shohaimi[1, 2]*, Mohd Bakri Adam[2], Mohd Noor Hisham Mohd Nadzir[1], Nurul Akmar Ghani[1]

[1]*Department of Biology, Faculty of Science, Universiti Putra Malaysia, Serdang, Selangor, Malaysia.*
[2]*Institute for Mathematical Research, Universiti Putra Malaysia, Serdang, Selangor, Malaysia.*
[3]*Department of Mathematics, Faculty of Science, Gombe State University, Gombe, Nigeria.*

*Corresponding author: shamarina@upm.edu.my

Abstract
Dengue epidemics are widespread in the tropical and sub-tropical regions of the world. Past studies had shown that the mitigation of dengue fever and virus is mostly subjected to human behaviour, preventive measures on vector control and case management. Examining knowledge, attitude, and practices (KAP) on dengue is one of the mitigation processes which is used to study the population of interest in order to create sustainable mediation strategies.

Keywords: Dengue; Knowledge; Attitude; Practices; Malaysia

Introduction
The absence of licensed chemoprophylaxis to suppress the dengue virus after episode and cost-effectiveness of dengvaxia affirm the importance of dengue KAP (Flasche et al., 2016). The objective of this study was to investigate the factors, including socio-demographic factors influencing KAP regarding dengue in selected areas of Selangor, Malaysia and the relationship between dengue KAP.

Methodology
A cross-sectional survey was conducted at a train station (Bandar Tasik Selatan) and IOI City Mall (Putrajaya) from May 2018 to October 2018. A structured validated bilingual questionnaire (Malay and English) was used to obtain information from 560 voluntary participants. The questionnaire has six sections: socio-demographic characteristics, medical history on dengue fever, the medium of information and participation in dengue campaigns, questions on knowledge about dengue, questions on attitude towards dengue and questions on practices against dengue. The latent constructs of dengue KAP have acceptable Cronbach's Alpha of 0.72, 0.70 and 0.61 respectively in the pilot study of 70 respondents. The status of KAP was assessed as poor and good. Logistic regression model is popularly used to evaluate the association between one dependent categorical variable and a set of multiple explanatory variables. It is sometimes used as a discriminant analysis to separate the most influencing factors from less influencing factors (NCSS Statistical Software, 2009). Simple and multiple logistic regression was adopted to predict the most influencing socio-demographic factors in each domain of dengue KAP in order to achieve the aim of the study. Recognizing the most influencing factor of dengue KAP could aid the mediation strategies in curtailing morbidity rates.

Results and Discussion
Among the respondents, 53.8% had good knowledge, 68.4% had good attitude and 56.6% had good preventive practices. The highest source of information was television (91.8%). There was a low but significant positive correlation between knowledge on dengue and

preventive practices shown in Table 1. This result is consistent with earlier dengue KAP studies conducted in Kuala Lumpur and Seremban (Al-Dubai et al., 2013; Naing et al., 2011). At multivariate level, type of residence and attendance of dengue-related programs influence knowledge on dengue. Gender, educational status, occupational status, and number of family living together influence attitude towards dengue. At univariate level, age and ethnicity influence preventive practices against dengue. Respondents who had attended dengue-related programs are 1.4 times more likely to have good knowledge on dengue than the respondents who had never attended dengue programs.

Table 1: Spearman's Correlations between the categories of dengue KAP

	Knowledge	**Attitude**	**Practices**
Knowledge	1.00	0.07	0.16**
Attitude	0.07	1.00	-0.30
Practices	0.16**	-0.30	1.00

**Correlation was significant at 0.05 level (2-tailed).

Conclusion

The results indicated that knowledge on dengue has a higher influence on preventive practices than the attitude towards dengue. This study suggests that more dengue campaign programs are needed to increase dengue KAP in the selected areas of Selangor.

Acknowledgement

Ministry of Higher Education under the Fundamental Research Grant Scheme (FRGS) (Project No: 02-02-14-1561 FR)

References

Al-Dubai, S. A. R., Ganasegeran, K., Alwan, M. R., Alshagga, M. A., & Saif-Ali, R. (2013). Factors affecting dengue fever knowledge, attitudes and practices among selected urban, semi-urban and rural communities in Malaysia. *Southeast Asian Journal of Tropical Medicine and Public Health*, *44*(1), 37–49.

Flasche, S., Jit, M., Rodríguez-Barraquer, I., Coudeville, L., Recker, M., Koelle, K., … Ferguson, N. (2016). The Long-Term Safety, Public Health Impact, and Cost-Effectiveness of Routine Vaccination with a Recombinant, Live-Attenuated Dengue Vaccine (Dengvaxia): A Model Comparison Study. *PLoS Medicine*, *13*(11), 1–19.

Gubler, D. J. (2011). Dengue, Urbanization and Globalization: The Unholy Trinity of the 21st Century. *Tropical Medicine and Health*, *39*(4SUPPLEMENT), S3–S11.

Ikhwan Zaini, Z. I., Othman, H., Karim, N., Abd Rashid, N. A., Hisham Abas, M. B., Sahani, M., … Nordin, S. A. (2019). Knowledge and practices regarding Aedes control amongst residents of dengue hotspot areas in Selangor: A cross-sectional study. *Sains Malaysiana*, *48*(4), 841–849.

Naing, C., Yih, W., Chan, R., Man, Y., Wong, C., & Ee, S. (2011). Awareness of Dengue and Practice of Dengue Control Among the Semi-Urban Community : A Cross Sectional Survey. *Journal of Community Health*, *36*, 1044–1049.

NCSS Statistical Software. (2009). Logistic regression: from introductory to advanced concepts and applications. *Choice Reviews Online*, *47*(01), 321–369.

Wong, L. P., & AbuBakar, S. (2013). Health Beliefs and Practices Related to Dengue Fever: A Focus Group Study. *PLoS Neglected Tropical Diseases*, *7*(7), e2310.

ORAL PRESENTATION

CHEMISTRY

IN VITRO AND *IN SILICO* STUDIES ON THE CYTOTOXICITY ACTIVITY OF GIRINIMBINE AND MAHANIMBINE FROM *Murraya koenigii* (L) AGAINST BREAST CANCER

R. C. Ng[1], N. K. Kassim[1]*, M. B. Abdul Rahman[1], L. Saiful Yazan[2]

[1]Department of Chemistry, Faculty of Science, Universiti Putra Malaysia, 43400 UPM Serdang, Selangor Darul Ehsan, Malaysia.
[2]Department of Biomedical Sciences, Faculty of Medicine and Health Sciences, 43400 UPM Serdang, Selangor Darul Ehsan, Malaysia.

*Corresponding author: kartinee@upm.edu.my

Abstract
Phytochemical isolation from *Murraya koenigii* had afforded two carbazole alkaloid; girinimbine and mahanimbine. Cytotoxicity study revealed girinimbine and mahanimbine exhibited potent cytotoxic activity toward breast cancer cell lines, MCF-7 with the IC_{50} values of 11.95 and 11.01 µg/mL respectively. Girinimbine also showed stronger cell growth inhibition against MDA-MB-231 cell line, with IC_{50} of 8.92µg/m. The *in silico* docking studies showed that mahanimbine exhibited higher binding energy with the values of -9.31 and -9.30 kcal/mol towards p38α MAPK and hER-α receptors respectively. Meanwhile, docking of girinimbine with p38α MAPK and hER-α receptors produced the binding energies of -8.60 and -8.83 kcal/mol respectively. The binding of both girinimbine and mahanimbine displayed mutual interactions with the amino acids that responsible for the p38α MAP kinase inhibition. The *in silico* studies of girinimbine and mahanimbine with p38α MAPK and hER-α were firstly reported.

Keywords: (carbazole alkaloid; cytotoxicity; *in silico*; *in vitro*; breast cancer)

Introduction
Murraya koenigii is used as an essential culinary ingredient for food flavoring. In Ayurvedic system, the plant has been used as tonic, stimulant and carminative (Handral and Shruthi, 2012). Carbazole alkaloid was found to be the major chemical constituent related to genera *Murraya*.

Breast cancer is the most common malignancy found in women population (Ghoncheh *et al*., 2016). The side effects and drawbacks from current breast cancer chemotherapy such as heart disease problem had promoted the discovery for new drug (Mitry and Edwards, 2015). Human p38 Mitogen-activated protein kinase (MAPK) belongs to the MAPK superfamily. The activation of p38 MAPK is important for cell migration, invasion and metastasis. Meanwhile, estrogen plays an important role in the growth and development of bone, breast and uterine pathology. There are two types of estrogen receptor (ER), namely ERα and ERβ. ERα is responsible in cell proliferation and has been found in the endometrial, breast cancer and ovarian stromal cell (Levin, 2005; Omoto & Hayashi, 2002).

The molecular docking studies provide an opportunity to enhance the development of drugs for a protein that has been directly implicated to a health issue; for example, Estrogen Receptor in the breast cancer. Virtual screening via docking studies is a fast, economic and effective way to study protein-drug interaction in atomic level. Thus, this study was intended for the isolation of carbazole alkaloid from *Murraya koenigii (L)* and to evaluate their cytotoxicity activities through in *vitro* and *in silico* approaches

Methodology

Isolation of pure compounds

Repeated glass column chromatographic(GCC) separation method on chloroform extracts from root and stem bark of *Murraya*, eluted with solvent mixture of hexane, ethyl acetate and methanol in increasing polarity afforded a white crystal of girinimbine and mahanimbine respectively.

Cell Culture and *determination of cytotoxicity*

The MCF-7, MDA-MB-231 and 3T3 cells were purchased form American Type and Culture Collection (Rockville, USA). Cells were cultured in RPMI-1640 medium supplemented with 10% (v/v) of Fetal Bovine Serum (FBS) and 1% (v/v) of penicillin-Streptomycin. The cells were incubated in a humidified atmosphere of 5% carbon dioxide (CO_2) and at temperature of 37 ^{O}C. The MTT colorimetric assay previously described by Mosmann (1983) was used to measure the cytotoxicity. The absorbances were measured with VersaMax Tunable microplate reader at wavelength 570 nm and 630.The cell viability were calculated by the following equation and expressed in percentage (%) = (OD$Treated$ − OD$blank$)/ (OD$Controll$ − OD$blank$) × 100

Molecular Docking

The molecular docking hardware was performed using Windows 8.1. Meanwhile, the software used AutoDockTools-MGL. The crystallography structure of p38α MAPK (PDB ID: 4FA2) and human estrogen receptor alpha, hER-α (PDB ID: 3ERT) were obtained from RSCB protein Data Bank.

Results and Discussion

Characterization of the compounds

The ^{1}H and ^{13}C NMR spectra data of the compounds were in agreement with the ^{1}H and ^{13}C NMR literature data (Abu Bakar *et al*., 2007).

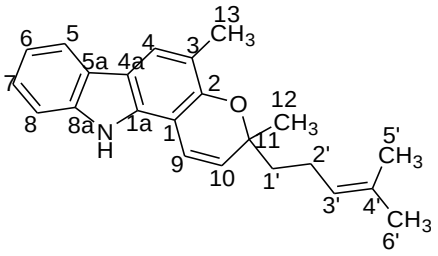

mahanimbine

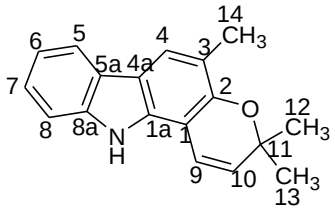

girinimbine

Cytotoxicity determination

Girinimbine significantly reduced the viability of both MCF-7 and MDA-MB-231. The IC_{50} values of girinimbine towards MCF-7 and MDA-MB-231 cell lines at 72 hours were 11.95 µg/mL and 8.92 µg/mL, respectively. From the cytotoxicity assay (IC_{50} value), girinimbine showed stronger inhibition to the cell growth of MDA-MB-231 cell as compared to MCF-7 cell. The finding indicated that MCF-7 cell exhibited higher resistance towards girinimbine than MDA-MB-231 cell. The IC_{50} values of mahanimbine towards MCF-7 and MDA-MB-231 at 72 hours of incubation were 11.01 µg/mL and 12.41 µg/mL respectively. The cytotoxicity of mahanimbine was in an agreement with previous finding reported by Sukari *et al*. (2014). The cytotoxicity of the compounds were tabulated in Table 1.

Table 1: Cytotoxicities of Two Carbazole Alkaloids as Measured by MTT Assay

Pure Compound	IC50 (µg/mL)*					
	MCF-7			MDA-MB-231		
	Incubation Period (hours)					
	24	48	72	24	48	72
Girinimbine	13.99	14.67	11.95	10.94	6.35	8.92
Mahanimbine	13.56	12.63	11.01	9.68	11.28	12.41

In silico docking study

Mahanimbine gave higher binding affinity (-9.30 kcal/mol) towards the p38a MAPK receptor through intermolecular activity with seventeen non-ligand residues. The high binding energy of mahanimbine might due to the extra four hydrophobic interactions near the tail of the isoprenyl unit. Meanwhile, girinimbine docked into the active site of p38a MAPK with the binding energy of -8.60 kcal/mol through thirteen van der Waals interactions.

Conclusion

The isolated compounds, girinimbine and mahanimbine were found to exhibit potent cytotoxic activities toward MCF-7 and MDA-MB-231.The *in silico* studies with Human P38 alpha Mitogen-Activated Kinase and Human Estrogen Receptor Alpha (hER-α) showed mahanimbine produced higher binding energy. The binding interactions of both girinimbine and mahanimbine showed mutual interactions with the amino acids. The binding of girinimbine and mahanimbine also showed anti-estrogenic properties. The *in silico* studies revealed that girinimbine and mahanimbine could be the potent drug nuclei as an anti-estrogen agent and p38α MAPK inhibitor for the treatment of breast cancer.

Acknowledgement

The authors thank Ministry of Education (MOE), Malaysia for Mybrain15 scholarship to one of the authors and IPS-Putra grant (Vot no. 9461100) for financial support in the study.

References

Abu Bakar, N.H., Sukari, M.A., Rahmani, M., Md. Sharifi, A., Khalid, K., and Yusuf, U.K., 2007. Chemical constituents from stem barks and roots of *Murraya koenigii* (rutaceae). *The Malaysian Journal of Analytical Sciences*. 11(1), 173-176.

Ghoncheh, M., Pournamdar, Z., and Salehiniya, H., 2016. Incidence and mortality and epidemiology of breast cancer in the world. *Asian Pacific Journal of Cancer Prevention*. 17(S3), 43-6.

Handral, H. K., Pandith, A., and Shruthi, S. D., 2012. A review on *Murraya koenigii*: multipotential medicinal plant. *Asian Journal of Pharmaceutical and Clinical Research*. 5(4), 5-14.

Levin, E. R., 2005. Integration of the extranuclear and nuclear actions of estrogen. *Molecular Endocrinolog.* 19(8), 1951-1959.

Mitry, M. A., and Edwards, J. G., 2015. Doxorubicin induced heart failure: Phenotype and molecular mechanisms*. International Journal of Cardiology: Heart & Vasculature*. 10, 17-24.

Mosmann, T., 1983. Rapid colorimetric assay for cellular growth and survival: application to proliferation and cytotoxicity assays. *Journal of Immunologica Methods.* 65, 55-63.

Omoto, Y., and Hayashi, S. I., 2002. A study of estrogen signaling using DNA microarray in human breast cancer. *Breast Cancer*. 9(4), 308-311.

Sukari, M. A., Ismail, N., Bakar, N. A., and Ithnin, N. L., 2014. Cytotoxic carbazole alkaloids from *Murraya koenigii* (Rutaceae). *Research Journal of Chemistry and Environment*. 18(11), 8-11.

IN VITRO STUDY OF FATTY ACID CONJUGATED TETRAPEPTIDE FOR WOUND TREATMENT

N.I.M. Fadilah[1], H. Ahmad[1,2*], M.B.A. Rahman[1,2], L.M. Yusof[3], S.L. Chia[4], S.F.Ng[5]

[1]Integrated Chemical Biophysics Research, Universiti Putra Malaysia, 43400 UPM Serdang, Selangor, Malaysia.
[2]Department of Chemistry, Faculty of Science, Universiti Putra Malaysia, 43400 UPM Serdang, Selangor, Malaysia.
[3]Department of Veterinary Clinical Studies, Faculty of Veterinary Medicine, Universiti Putra Malaysia, 43400 UPM Serdang, Selangor, Malaysia.
[4]Instistute of Bioscience, Universiti Putra Malaysia, 43400 UPM Serdang, Selangor, Malaysia.
[5]Centre for Drug Delivery Research, Faculty of Pharmacy, Universiti Kebangsaan Malaysia, Jalan Raja Muda Abdul Aziz, 50300 Kuala Lumpur, Malaysia.

*Corresponding author: haslina_ahmad@upm.edu.my

Keywords: Peptide, Cytotoxicity, Cell proliferation, Cell migration, Wound healing

Introduction

Current therapeutic drugs and delivery systems have been extensively investigated for wound healing [1], [2], [3]. Nevertheless, common drugs such as antibiotic creams and antiseptics were limited in terms of healing time, itching, irritation, dryness and scar formation [4]. Furthermore, by compared to those drugs with high cost, low activity and safety, bioactive peptide with high activity, stability and specificity have aroused considerable interest in the related field of research. It is generally preferred new therapeutic drug as well as to focus on increasing the efficacy while minimizing the side effects. In this study, we proposed a novel fatty acid conjugated tetrapeptide which is palmitic acid conjugated Gly-Asp-Pro-His (Palmitoyl-GDPH). It acts as a new biological active molecule specifically as a potential drug for wound treatment. The aim of this study was to synthesize and evaluate the *in-vitro* study of the Palmitoyl-GDPH on wound healing potential.

Methodology

Peptide Synthesis

Palmitoyl-GDPH (palmitic acid-Gly-Asp-Pro-His) was synthesized by solid phase peptide scheme (SPSS) method, and analyzed by HPLC and mass spectrometry to confirm high purity of 98%.

In-Vitro Cell Culture Assay

The cell proliferation assay was conducted as described by [5] with slight modifications. The percentage of cell viability was calculated using equation below:

% Cell viability = [(Absorbance of sample) / (Absorbance of control)] x 100

Wound Scratch Assay

The assay was conducted according to method described by [2] with minor modifications. The images were captured at the same site to observe the migration of the cells over time.

Results and Discussion

Palmitoyl-GDPH Enhanced Cell Proliferation

The Palmitoyl-GDPH promoted growth of normal human dermal fibroblasts (NHDF) cells after 24 hr and 48 hr, respectively. The cells did not show cytotoxicity up to 100 µg/ml and

the cell viability remained above 80% throughout the treatment (*p < 0.05). According to ISO 10993-5:2009 guidelines, cell viability above 80% is considered non-toxic to cells [6].

Palmitoyl-GDPH Enhanced Cell Migration

Treatment with Palmitoyl-GDPH significantly gives high percentage of NHDF migration in-vitro up to 98.4% compared to 95.6% of tetracycline at 100 µg/ml during 48 hr treatment (p <0.05). At 24 hr, cells cultured in plain medium (without treatment) migrated relatively less, with healing progression less than 20% whereas complete wound closure was found in the presence of 100 µg/ml Palmitoyl-GDPH.

Conclusion

Palmitoyl-GDPH was successfully synthesized by solid phase peptide scheme (SPPS) method. The *in-vitro* study showed that the Palmitoyl-GDPH was not toxic rather proliferated normal human fibroblast cells, hence it was found to be an effective drug in treating wound healing.

Acknowledgement

This research work was financially supported by Putra IPS Grant (GP-IPS/2017/9577800) from Universiti Putra Malaysia (UPM). The authors also would like to thank to MyBrain15 (Ministry of Higher Education) for educational scholarship scheme.

References

1. Ain, N. J., Diyana, A. S., Hazirah, N. R., Fathiah, N. A., Fairus, A., Teoh, S. L. Anum, Y. M. 2018. The Effect of Piper Betle on Wound Healing in Male Sprague Dawley Rats. *Medicine and Health-Kuala Lumpur* .13, 165-174.
2. Chin, C. Y., Jalil, J., Ng, P. Y. Ng, S. F. 2018. Development and Formulation of *Moringa Oleifera* Standardised Leaf Extract Film Dressing for Wound Healing Application. *J. Ethnopharmacol.* 212, 188-199.
3. Li, X., Fan, R., Tong, A., Yang, M., Deng, J., Zhou, L. Zhang, X. Guo, G. 2015. In Situ Gel-forming AP-57 Peptide Delivery System for Cutaneous Wound Healing. *Int. J. Pharm.* 495, 560-571.
4. Murphy, P. S. Evans, G. R. 2012. Advances in Wound Healing: A Review of Current Wound Healing Products. *Plas. Surg. Int.* 2012,1-8.
5. Tang, J., Liu, H., Gao, C., Mu, L., Yang, S., Rong, M. Zhang, Z. Liu, J., Ding, Q. Lai, R. 2014. A Small Peptide with Potential Ability to Promote Wound Healing. *Plos One. 9*, e92082.
6. Normalizacyjny, P.P.K. 2009. Biological Evaluation of Medical Devices - Part 5: Test for *In-Vitro* Cytotoxicity (ISO 10993-5:2009), 3rd ed. Polski Komitet Normalizacyjny . 30-37.

ISOLATION AND CHARACTERIZATION OF TRITERPENES FROM PETROLEUM ETHER AND ETHYL ACETATE EXTRACTS OF BARK OF *Ziziphus spina christi* (L) *Desf.*

I.Sadiq, I.S[1]

[1]*Department of Chemistry, Faculty of Science, Federal University Dutse, Jigawa State, P.M.B 7156, Nigeria.*

*****Corresponding author: shinasadiq2015@gmail.com

Abstract
Ziziphus spina christi (L) Desf. is a plant used in Nigerian folk medicine for the treatment of syphilis and cancer. It also has antihelmenthic and antidiarrhetic properties respectively. Through flash column chromatography (FCC) techniques, two compounds have been isolated from petroleum ether and ethyl acetate extracts of the bark of *Ziziphus spina christi.* These compounds obtained were characterized on the basis of ^{1}HNMR, ^{13}CNMR, HSQC and IR spectroscopic studies.

Keywords: *Ziziphus spina christi,* bark, isolation, ethyl acetate, triterpenes

Introduction
Natural products, including plants, animals and minerals have been the basis of treatment of human diseases. History of medicine dates back practically to the existence of human civilization by Patwardhanet *et al*., (2004).). Recently, terpenes have been used as a drug in the first-line treatment against malaria, especially artemisinin which is a diterpene (Bala, 2006; Halilu *et al*., 2013; Sadiq *et al*., 2015). *Ziziphus spina-christi* (L) Desf. or wild vernacular names in Hausa is *Kurna*, while in Yoruba as *Eakannase-adie.* belong to the Family Rhamnaceae (Bala, 2006; Sadiq *et al*., 2015). *Ziziphus spina-christi* is a plant used in Hausa traditional medicine in Northern Nigeria for treatment of cancer and different parts of the plant are used to remedy ailments and several other diseases (Mdidea, 2004: Bala, 2006). The aim of this paper is to report the isolation of pure compounds present in the bark extract of *Ziziphus spina christi (L) Desf* by chromatographic techniques, spectroscopic analysis so as to establish the presence of triterpenoids using nuclear magnetic resonance (NMR) and heteronuclear single quantum correlation (HSQC) experiment. Previous work have earlier reported the isolation of lupeol, betulin and betulinic acid from different plants species (Letidal *et al.,* 2009; Bulus 2011; Boligon *et al*., 2014; Halilu *et al*., 2013; Venter and Venter, 1996). This is a recent work and it will contribute to knowledge particularly in the field of natural product chemistry.

Methodology
Collection and Identification of Plant Material
The bark of the plant was collected from Sokoto State, Nigeria in December, 2009 and transported to the Herbarium Unit, Department of Biological Sciences, Faculty of Science, Usmanu Danfodiyo University, Sokoto State for identification (SK125NG).

Drying and Preservation of Plant Material
The bark of the plant was shade dried for one week and repeatedly weighed until a constant weight. It was powdered using mortar and pestle. The powder was stored in an air-tight plastic container until required for use.

Extraction
The powdered bark was extracted serially with petroleum ether and ethyl acetate. The plant material (1.5 kg) was extracted (defatted) with 4 L of petroleum ether with the aid of a Soxhlet extractor. The extract was allowed to dry and then extracted with 3 L of ethyl acetate. The extract was filtered and concentrated at reduced pressure on a rotary evaporator. Thin layer Chromatography; a mixture of chloroform / ethyl acetate (3:1) was used to determine the separation profile of the petroleum ether.

Column chromatography
A petroleum ether slurry of silica-gel powder (200 g) was packed in a glass column (30 x 35 cm). The extract (3g) in a fine powdered form was loaded onto the column and allowed to stabilize for 3 hours before elution commenced. The column was eluted in gradient profile. The elution began with petroleum ether 100% and chloroform was added gradiently from 0 to 100%. The elution continued with the addition of methanol from 0 to 100%. Several fractions (10 ml each) were collected and monitored by TLC (chloroform 100%) and sprayed with 5% sulphuric acid. Similar fractions were pooled and concentrated *in vacuo*. One major compound was obtained and designated as Z_1. Further purification of the compound was carried out by repeating column chromatography. Another compound Z_2, was isolated from the ethyl acetate extract using similar procedure as described above. NMR Sample Preparation/ Analysis; the isolated compounds were weighed (15 mg) and dissolved in 0.5 ml of deuterated.

Results and Discussion
Their masses of the extracts and the physical appearance are presented: Results of Proton NMR, Carbon NMR, HSQC, IR, Melting point (m.p) and TLC are summarized below. Column Chromatography of Petroleum Ether and Ethyl acetate Extracts; their masses obtained are Z_1 (45mg), Z_2 (37mg) and both were obtained as white powdery solids. From the NMR, HSQC data which compared well with the available literature, suggested structure of compound Z_1 is betulin (lup-20(29)-en-3β, 28-diol) and Structure of Compound Z_2 from the NMR, HSQC, suggested structure of compoundZ_2 is betulinic acid (3βhydroxy-lup-20(29)-en-28-oic acid).

Compound Z_1 was isolated as a white powder, soluble in chloroform, with a melting point of 255- 257^{o}C. Which biogenetically originates from the same precursor (biogenetic isoprene). The presence of methylene olefinic protons of the lupane triterpenes Ayotollahi *et al*. (2011) which are attached to carbon-29.

Conclusion
The isolation of the bark of *Ziziphus spina christi* and subsequent chromatographic separation led to the isolation of triterpenes compounds: betulin and betulinic acid which were compared with other previous work done.

Acknowledgement
Special thanks goes to the Tertiary Education Trust Fund (TETF AST&D) for financial support through Federal University Dutse, Jigawa State.

References
Ayatollahi A.M. Mastafa. G.SuleimanA.OmerM.A.Mehdi.M. and GbolamrezaA (2011).Pentacyclic Triterpenes in *Euphorbia Microcandela* with their T-cell Publication Activity. *Iranian Journal of Pharmaceutical Research,* **10** (2); 287-294.

Bala S.A. (2006). Some Ethnomedicinal plants of the Savannah Region of West Africa Description and Phytochemicals, First edition, Triumph Publishing company Ltd. Zungur Kano, Nigeria Vol, II, pp.1-266.

Bulus A. (2011). Structural Characterization of ZS – 2A: An Antiplasmodial Compound Isolated from *Ziziphus spina-christi* Root Bark. *Life Science Global.*1 (1):52-58.

Boligon A. A. Debrum T.F. Frolhich J.K. Froeder A. L and Athayde M. L (2012a). HPLC Profile and Determination of Total Phenolics, Flavonoids, Tannins and Alkaloids contents of *Scutia buxifolia* Reissek stem bark, *Research Journal of Phytochemistry*,**6:**84-91

Halilu M.E. October N. Balogun M. Agunu A. Abubakar A. and Abubakar M.S. (2013). Isolation and Characterization of Steroids, from petroleum Ether Extracts of Stem Bark of *Parinari curatellifolia* planch ex. Benth (Chrysobalanaceae). *Journal of Natural Sciences Research*, **3(6):**53-61.

Letidal E.M. Bushra E.L. Muhammad E.E. and Shamsun N.K. (2009). Bioactive Natural Products from Two Sudanese Medicinal Plants *Diospyros mespiliformis* and *Croton zambesicus Rec.Nat.Prod*.**3 (4**); 193-203.

Mdidea R. (2004). The Jujube Berries; A magic fruit for motion controlling, Central African. Spectrum Press Ltd. pp 12-36.

Patwardhan B., Ashok D.B. and Chorghade, M. (2004). Ayurveda and Natural Products Drug discovery*. Current*

Sadiq I.S**.**Dangoggo S.M .Hassan L.G.Manga S.B and Tahir M.T (2015).Isolation and Characterization of Triterpenes from Ethyl acetate Extract leaf of *Diospyros mespiliformis, Dutse Journal of Pure and Applied Sciences*,1(1);137-144, Faculty of Science(FUD).

Venter, F. and Venter, J.A. (1996). Making the Most of Indigenous Trees*.* Briza Publications, Pretoria. 56-79.

PUTATIVE METABOLITE PROFILING OF *Mitragyna speciosa* USING UHPLC-MS/MS

S. Abubakar Garba[1, 4*], K. Shaari[2], S. M. Mohd Faudzi[2], M. Rashid Abdul Manaf[2], S. Kumar Jayaram[3], S, Yee Lee[1]

[1]*Institute of Bioscience Universiti Putra Malaysia, 43400 UPM Serdang, Selangor Darul Ehsan, Malaysia.*
[2]*Department of Chemistry, Faculty of Science, Universiti Putra Malaysia, 43400 UPM Serdang, Selangor Darul Ehsan, Malaysia.*
[3]*Senior Forensic Scientist, Kimia Malaysia. JLN Sultan 46661, PJ.*
[4]*Sule Lamido University, PMB 048 Kafin Hausa, Jigawa State. Nigeria.*

*Corresponding Author: gs55018@student.upm.edu.my

Abstract
Mitragyna speciosa Koth, commonly known as *'Ketum'* or *'biak-biak'* in Malaysia, while in Thailand as '*kratom'* or *'kakuam'*. The plant is native to south eastern Asia and has been one of the most popular New Psychoactive Substances (NPSs) available online in Europe. Kratom contained various classes of natural products such as Poly-phenols and glycosides, while alkaloids are the major constituents of this plant with mitragynine and 7-hydroxymitragynine reported as biomarkers of this plant. In this study, putative metabolites identification of the crude leave extract of *M. speciosa* was reported. The separation of the crude extract was conducted by UHPLC-MS/MS and the gradient elution was performed at 0.4mL/min and 40 °C using water in 0.1% formic acid (A) and acetonitrile (ACN) in 0.1% formic acid (B) as mobile phases with a total run time of 38.5min. The mass spectra data of the compounds showed strong signal for both positive and negative mode $[M+H]^+$ and $[M-H]^-$. The MS data analysis was conducted using ThermoXcalibur 2.2 SP1.48 (Thermo Fisher Inc.) and literature data. A total number of 27 alkaloids and 22 poly-phenols were identified in this report. These include mitragynine, 7-hydroxymitragynine, rutin and epi-catechin with molecular ion m/z 399.2403, 415.2362, 609.1451 and 289.0714 respectively. In this study phytochemical constituents of *M. speciosa* have been successfully profiled using UHPLC-MS/MS and our findings indicated that the phenolic compound preferred to be ionized in negative mode while the alkaloids preferred positive ionization.

Keyword: Analgesic, Kratom, Mitragynine, Metabolites, Psychoactive.

Introduction
Mitragyna speciosa is non-seasonal, tropical evergreen, usually found in valley and swamps and grows richly in wet, humid areas rich with humus in Malaysia, Indonesia and Papua New Guinea, Borneo, Philippines (Shellard,1967). The Plant is cultivated mostly for its leaves (Beckett *el al.,* 1965). Kratom leaves traditionally known for its stimulant, analgesic, and treatment for opioid addiction, can be chewed or refined into powder and liquid extract form for different therapeutic purposes. *M. speciosa* plant can grow up to 20 m high with a girth of 1 m and its leaves are large measuring up to 15 cm long and 6 cm wide (Brown *et al,* 2017). An alkaloids mitragynine and 7-hydroxymitragynine are the main psychoactive components in the leaves both found only in *M. speciosa,* other analogues alkaloids have also been identified (speciogynine, paynantheine, and speciociliatine) (Ruck and Hoffman, 2011). Mitragynine in Kratom plant material has been detected using a number of chromatographic and mass spectrometric techniques, including liquid chromatography-mass spectrometry (LC-MS) (Kikura-Hanajiri *et al.,* 2009), ion mobility mass spectrometry (IMS) (Fuenffinger *et al.,* 2017), high-performance liquid chromatography (HPLC) (Kong *et al.,* 2017), gas chromatography-mass spectrometry

(GC-MS) (Oliveira et al., 2016), and direct analysis in real time-high-resolution mass spectrometry (DART-HRMS) (Lesiak *et al.,* 2015).Parthasarathy *et al.,* (2013) reported a quick, easy and reliable method for detection and routine quantification of mitragynine, alkaloids and ketum beverages using HPLC-DAD technique. Fowble *et al.,* (2019) validated method for the quantification of mitragynine by DART-HRMS, and its application for the determination of the mitragynine content in several commercially available Kratom products.

Methodology

Dried leaves of *M. speciosa* was collected from Chemistry Department, Malaysia and ground into fine powdered. 5g of the powdered leave was dissolved in 100mL of methanol and sonicated for 1hr at 53kHz, 25^{0}C and the procedure was repeated three times. The mixture was concentrated to dryness using a rotary evaporator and prepared for LC-MS analysis. Chromatographic separation was achieved using C18 Reversed-phase Hypersil GOLD column (100 mm x 2.1 mm, 1.9 µm) (Thermo, USA) at 40 ºC on Dionex Ultimate 3000 UHPLC with a diode-array DAD-3000 detector with gradient elution was performed at 0.4mL/min and 40 °C using water in 0.1% formic acid (A) and acetonitrile (ACN) in 0.1% formic acid (B) as mobile phases with a total run time of 38.5min.The injection volume of sample was 1 µL and the UV was set at 210, 254, 270 and 360nm respectively (Veeramohan *et al.*,2018).

Results

Table I: Metabolites Identification of Crude Methanol Leave Extract from *M. speciosa* plant positive mode ionization

S/N	RT (Min)	PDA (λ_{max})	m/z [M-H]$^-$	MS/MS Fragmentation	Putative Compound(s)	Elemental Composition	References
1	14.67	230.0 286.0	415.2362	110.1004, 190.0926 226.1514, 271.1526 383.2092	7-hydroxymitragyne	$C_{23}H_{29}N_2O_5$	Fu, 2016
2	15.46	222.0	399.2403	110.1003, 174.0971 226.1512, 238.1138	Mitragynine	$C_{23}H_{30}N_2O_4$	Avula *et al.,* 2015 Neng, *et al.,* 2015
3	16.49	228.0 332.0	399.2407	110.1003, 174.0971 226.1513, 238.1515	Mitraciliatine	$C_{23}H_{30}N_2O_4$	Basiliera *et al.,* 2018

Table II: Metabolites Identification of Crude Methanol Leave Extract from *M. speciosa* Plant in negative mode ionization

S/N	RT (Min)	PDA (λ_{max})	m/z [M-H]$^-$	MS/MS Fragmentation	Putative Compound(s)	Elemental Composition	References
1	5.05	202.0 282.0	289.0714	97.0281,109.0283, 125.0232,137.0233,151. 0281, 179.0341, 203.0706, 221.0814, 227.0706, 245.0816	Epi-catechin	$C_{15}H_{14}O_6$	Cai *et al.,* 2017
2	7.06	206.0 256.0 354.0	609.1451	151.0124, 178.9976, 255.0297, 271.0246, 300.0275	Rutin	$C_{27}H_{30}O_{16}$	Jiménez-Sánchez *et al.,* 2016
2	7.87	206.0 352.0		151.0027, 178.9977, 243.0297, 255.0297, 271.0247, 300.0275	Hyperoside	$C_{21}H_{20}O_{12}$	Chen *et al*., 2012; Deng et al., 2013

3	8.22	222.0 262.0 338.0	593.1505	151.0024, 227.0342, 255.0298, 284.0325	Kaempferol/luteolin-diglycoside	$C_{27}H_{30}O_{16}$	Bravo *et al.,* 2007

Conclusion

UHPLC-MS/MS has been applied to profile the constituents of *M. speciosa* with the advantage of avoiding time-consuming and tedious purification of compounds from the crude extracts. The characteristic fragmentation patterns observed in MS/MS spectra allowed the identification of the indole group and presence of other functional groups.

Reference

Parthasarathy, S., Ramanathan, S., Murugaiyah, V., Hamdan, M. R., Mohd Said, M. I., Lai, C. S., & Mansor, S. M. (2013). A simple HPLC-DAD method for the detection and quantification of psychotropic mitragynine in Mitragyna speciosa (ketum) and its products for the application in forensic investigation. *Forensic Science International*, *226*(1–3), 183–187.

THE EFFECT OF BASIS SET SIZE ON THE STATIC DIELECTRIC CONSTANT VALUES OF LOW DIELECTRIC ORGANIC LIQUIDS PREDICTED BY THE GENERAL AMBER FORCE FIELD (GAFF)

Mohd F. Ismail[1,2*], Mohd B. Abdul Rahman[1,2]

[1]Department of Chemistry, Faculty of Science, Universiti Putra Malaysia, 43400 UPM Serdang, Selangor Darul Ehsan, Malaysia.
[2]Integrated Chemical Biology, University Putra Malaysia, 43400 UPM Serdang Selangor Darul Ehsan, Malaysia

*Corresponding author: mohd_farid@upm.edu.my

Abstract
The static dielectric constant calculated from molecular dynamics simulation depends on the partial charges of the liquid constituents. For the General AMBER Force Field (GAFF), the partial charges are calculated using *ab-initio* methods employing the restricted Hartree-Fock method and the 6-31g* basis set. It has been shown that the static dielectric constant values calculated using the GAFF can be inferior compared to the values of static dielectric constant calculated by other methods that utilizes bigger basis set. However, to this date, there is no systematic study that investigates the relationship between the basis set size and the static dielectric constant values. This work focuses on investigating the relationship between the basis set size and the static dielectric constant for low dielectric solvents. Simulations of triethylamine and dimethylcarbonate were performed using the GAFF using partial charges derived from various basis sets. For both organic solvents, the addition of the diffuse function increases the values of the static dielectric constant. In addition, when the polarization function is added to the hydrogen atoms, the values of the static dielectric constant also increases. Finally, as the size of the basis set is increased, the values of the static dielectric constant are also increased. It is thus concluded that the values of the static dielectric constant vary according to the size of the basis set.

Keywords: GAFF, static dielectric constant, molecular simulation, basis set, organic solvents.

Introduction
In molecular dynamics simulation, the calculation of the static dielectric constant calculation involves the partial charges of the molecules. For the GAFF, the partial charges is calculated using *ab-initio* methods employing the restricted Hartree-Fock method and the 6-31g* basis set (Wang et al, 2004). Other force field like the Optimized Potentials for Liquid Simulation (OPLS) force field employs the Moller-Plesset perturbation theory method and the slightly bigger correlation consistent polarized valence triple zeta (cc-pVTZ) basis set (Jorgensen et. al. 1996).

It has been shown that the static dielectric constant calculated using the OPLS force field is slightly better compared to the GAFF (Caleman et al, 2011). In addition, it has been shown that other liquid properties predicted by the OPLS force field and the GAFF also favours the OPLS force field (Martin, 2006). However, to this date, there is no systematic study that shows the relationship between the basis set size and the static dielectric constant values. In this work, the performance of the GAFF in predicting the static dielectric constant as the basis set of the partial charges is varied is investigated. Simulations of triethylamine and dimethylcarbonate were performed using partial charges that were varied by varying the basis set used in their calculations. The resultant static

dielectric constant is evaluated from the trajectory from the simulations. The results suggest that the increase in the size of the basis set results in the increase of the static dielectric constant values.

Methodology

The AMBER 16 molecular dynamics package was used with the GAFF force field (Case et al, 2016). The Avogadro software was used to generate the molecules (Hanwell et al, 2012). The various partial charges for the molecules were generated with Antechamber and R.E.D. Tools (Dupradeau et al, 2010). The AMBER Tools 16 was used to generate the appropriate files to perform the simulation and to perform the analysis (Case et al, 2016). The molecular dipole moment was obtained via the 'vector' module of the cpptraj program. The values of the static dielectric constant were obtained by inserting the molecular dipole moment into a spreadsheet that uses the equation as described in the literature (Caleman et al, 2012).

Results and Discussion

Basis Set	TEA	DMC
6-31+	2.287 ± 0.025	1.882 ± 0.020
6-31++	2.293 ± 0.016	1.895 ± 0.039
6-31s (resp def)	1.794 ± 0.001	1.493 ± 0.001
6-31ss	1.796 ± 0.001	1.499 ± 0.008
ccpvdz	1.640 ± 0.001	1.505 ± 0.019
ccpvtz	1.672 ± 0.008	1.597 ± 0.032
ccpvqz	1.736 ± 0.028	1.596 ± 0.035
ccpv5z	1.744 ± 0.001	1.606 ± 0.031
Experimental	2.4	3.087

The table shows the experimental and the average calculated static dielectric constant values for each basis set. The results show that all calculated values deviate from the experimental values.

As the polarization basis set is increased (6-31g* to 6-31g**), and as the diffuse function is added to the basis set, (6-31g+ to 6-31g++), the values of the static dielectric constant also increases. Similarly, as the basis set size is increased (cc-pvdz to cc-pvtz to cc-pvqz to cc-pv5z) the value of static dielectric constant also increases.

Conclusion

From the experiment, the calculated values for both solvents are lower than the experimental values. However, as the basis set size is increased, the value of the calculated static dielectric constant increases approaching the experimental values. This suggests that when using the GAFF for low dielectric organic liquids simulation, bigger basis set size must be used to in order to get partial charges that will result in the static dielectric constant that is closer to the experimental values. More solvents should be included to support the results from this work. The results provide a general guide for performing molecular dynamics simulation with low dielectric solvents.

Acknowledgement
The authors would like to express their gratitude to the Department of Chemistry, Faculty of Science, UPM for providing the general facilities. This work was supported by the UPM via the Initiative Putra Malaysia (IPM) grant scheme (Reference Code: UPM/700-2/1/GP-IPM/2015/9455900, Project Code: GP-IPM/2015/9455900).

References

Wang, J. M., Wolf, R. M., Caldwell, J. W., Kollman, P. A., and Case, D. A., 2004. Development and testing of a general AMBER Force Field. *J. Comput. Chem.* 25(9), 1157-1174.

Caleman, C., van Maaren, P. J., Hong, M., Hub, J. S., Costa, L. T., and van der Spoel, D., 2012. Force Field benchmark of Organic Liquids: Density, Enthalpy of Vap., Heat Capacities, Surface Tension, Isothermal Comp., Vol. Expansion Coeff., and Die. Constant. *J. Chem. Theory Comput.* 8(1), 61-74.

Martin, M. G., 2006. Comparison of the AMBER, CHARMM, COMPASS, GROMOS, OPLS, TraPPE and UFF force fields for prediction of vapor–liquid coexistence curves and liquid densities. *Fluid Phase Equilibria*. 248, 50-55.

Case, D. A., Betz, R. M., Cerutti, D. S., Cheatham, III, T. E., Darden, T. A., Duke, R. E., Giese, T. J., Gohlke, H., Goetz, A., Homeyer, N., Izadi, S., Kaus, J., Kovalenko, A., Lee, T. S., S. LeGrand, P. Li, C. Lin, T. Luchko, R. Luo, B. Madej, D. Mermelstein, K. M. Merz, G. Monard, H. nguyen, H. T. Nguyen, I. Omelyan, A. Onufriev, D. R. Roe, A. Roitberg, C. Sagui, C. L. Simmerling, W. M. Botello-Smith, J. Swails, R. C. Walker, J. Wang, R. M. Wolf, X. Wu, L. Xiao and P. A. Kollman (2016), AMBER 2016, University of California, San Francisco.

M. D. Hanwell, D. E. Curtis, D. C. Lonie, T. Vandermeersch, E. Zurek, G. R, Hutchison, 2012. Avogadro: An advanced semantic chemical editor, visualization, and analysis platform. *Journal of Cheminformatics* 4(17), 1-17.

F.-Y. Dupradeau, A. Pigache, T. Zaffran, C. Savineau, R. Lelong, N. Grivel, D. Lelong, W. Rosanski & P. Cieplak, 2010. The R.E.D. tools: Advances in RESP and ESP charge derivation and force field library building. *Phys. Chem. Chem. Phys.* 12, 7821-7839.

COPPER METAL AND ACID PROPERTIES OF $CuCeZrO_x$ FOR GLYCEROL HYDROGENOLYSIS TO 1,2-PROPANEDIOL

R. Irmawati[1*]

[1]*Catalysis Science and Technology Research Centre (PutraCat), Department of Chemistry, Faculty of Science, Universiti Putra Malaysia, 43400 UPM Serdang, Selangor Darul Ehsan, Malaysia.*

*Corresponding author: irmawati@upm.edu.my

Abstract
In this study, a biomass derived glycerol is converted into 1,2-propanediol through hydrogenolysis process over $CuCeZrO_x$ catalyst. XRD analysis shows the formation of copper oxide, CuO of the calcined catalyst which was converted to copper metal when reduced in hydrogen. Although the calcined CuCeZrOx has high acid content as compared to the reduced one, but the reaction activity was incredibly low. However, when copper metal was present, the catalytic activity increased tremendously with virtually all 5 wt% glycerol were converted with 97.9 % selectivity towards 1,2-propanediol was achieved. Thus indicated the structurally sensitive of glycerol hydrogenolysis to copper metal along with super strong acid site.

Keywords: oxalate gel, $CuCeZrO_x$, glycerol, 1,2-propanediol, platform chemicals

Introduction
The hike in the amount of CO_2 in the air causes the earth's temperature to rise in alarming acceleration. In a conscious effort to reduce CO_2 emissions, an initiatives for investing on renewables has been called [1]. In this context, a bio-based platform chemicals with a focus on glycerol is the efficient alternatives to fossil fuel-based products. Glycerol could be transformed into valuable chemicals through various processes including hydrogenolysis to 1,2-propanediol (1,2PDO) and 1,3-propanediol (1,3PDO) which are used as monomers in polyester industry [2].

Copper-based catalysts are widely investigated for glycerol hydrogenolysis for its high selectivity for dehydration and C-O hydrogenation [2,3]. In most cases different supports (SiO_2, Al_2O_3, MgO) or a binary copper-based (CuCr) system have been used [3,4]. Unfortunately, there is limited study on ternary system has been reported. Therefore, in the present work, a mixed oxide of Cu, Ce and Zr was investigated in order to determine the surface properties of the catalyst involved in the reaction. The ternary catalyst system was synthesized by oxalate gel method. The catalyst surface properties and phase composition were investigated as a function of calcination and reduction temperatures. These properties were then related to the catalytic performances for glycerol hydrogenolysis to 1,2-propanediol.

Methodology
Catalyst preparation
The synthesis of bulk Cu:Ce:Zr at a molar ratio of 1:1:1 was done by using oxalate gel method using 7.60g Cu(II) nitrate, 13.67g Ce(III) nitrate and 7.84g Zr(IV) nitrate. The sol obtained was dried and calcined in air at 600 ºC. The catalyst was then reduced under 5%H_2/Ar at 180 ºC. All of the chemicals were obtained from Sigma-Aldrich.

Catalyst characterization

The catalyst phase composition was obtained by powder X-ray diffraction (XRD) on a PANalytical X'Pert Pro. Ammonia temperature programmed desorption (NH_3-TPD) was performed by using a Quantachrome Chembet. The performance of the catalysts for glycerol hydrogenolysiswas determined in a stainless steel PARR 5500 autocalve.

Results and Discussion

The XRD patterns of the CuCeZr systems are shown in Fig. 1. In both calcined and reduced conditions, the phase content for CeO_2-ZrO_2 is assigned to a cubic fluorite phase (JCPDS 38-1439) [5]. High temperature of calcination promotes the formation of CuO aggregates verified at 2θ = 35.6° and 38.6°. When the sample was reduced, a metallic copper (Cu^0) is established with the peak appears at 2θ value of 43.43°.

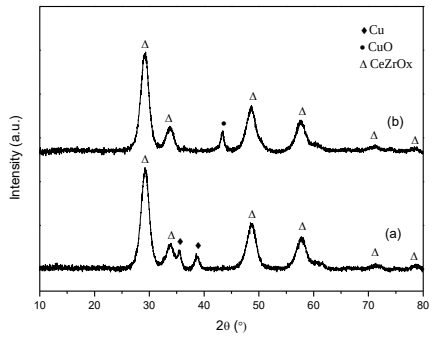

Fig. 1. XRD patterns of (a) calcined $CuCeZrO_x$ (b) reduced $CuCeZrO_x$

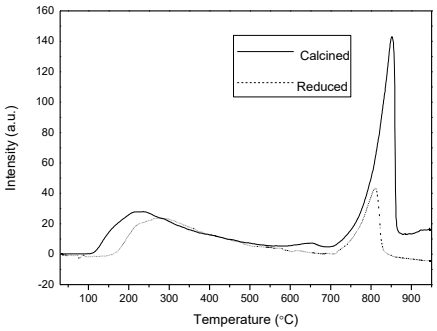

Fig. 2. NH_3-TPD of calcined and reduced CuCeZr samples.

The acid properties of calcined and reduced CuCeZrOx is shown in Fig. 2 with weak to strong acid sites appear in the range of < 450 °C. Interestingly, an intense peaks are observed at temperature above 700 °C which signify a super strong acid sites [2]. The profiles also show reducing the catalyst appears to a significant reduction in acid amount. Catalytic test reveals the reduced catalyst performed better with conversion of glycerol (5 wt%) reaches 100% and 1,2-propanediol selectivity achieved 97.9 %.

Conclusion

The CuCeZrOx catalyst prepared by oxalate gel method was calcined in air and reduced in hydrogen. The performance of these catalysts were carried out in glycerol hydrogenolysis. Although calcined sample contains high amount of super strong acid site but without copper metal present on the surface, the catalyst was unable to convert glycerol to the desired product. This was an opposite to the performance of the reduced catalyst with copper metal and a medium amount of strong acid site. Thus, both copper metal and acid properties of CuCeZrOx catalyst were conjointly needed for the effective reaction of glycerol to 1,2-propanediol.

References

1. Roberts, D.; Pidcock, R.; Chen, Y.; Connors, S.; Tignor, M. *Global Warming 1.5 C*; 2018;
2. Zhou, W.; Luo, J.; Wang, Y.; Liu, J.; Zhao, Y.; Wang, S.; Ma, X. Applied Catalysis B : Environmental WO x domain size , acid properties and mechanistic aspects of

glycerol hydrogenolysis over Pt / WO x / ZrO 2. *Appl. Catal. B Environ.* **2019**, *242*, 410–421.

3. Xiao, Z.; Wang, X.; Xiu, J.; Wang, Y.; Williams, C.T.; Liang, C. Synergetic effect between Cu0and Cu+in the Cu-Cr catalysts for hydrogenolysis of glycerol. *Catal. Today* **2014**, *234*, 200–207.
4. López, A.; Aragón, J.A.; Hernández-cortez, J.G.; Mosqueira, M.L.; Martínez-palou, R. Study of hydrotalcite-supported transition metals as catalysts for crude glycerol hydrogenolysis. *Mol. Catal.* **2019**, *468*, 9–18.
5. Huber, F.; Venvik, H.; Rønning, M.; Walmsley, J.; Holmen, A. Preparation and characterization of nanocrystalline , high-surface area Cu Ce Zr mixed oxide catalysts from homogeneous co-precipitation. **2008**, *137*, 686–702.

GLYCEROL ACETYLATION OVER SULFONATED CARBON CATALYST DERIVED FROM BIOMASS WASTE USING DIFFERENT CARBONIZATION METHODS: SYNTHESIS, CHARACTERIZATION AND SCREENING

U. I. Nda-Umar[1,3*] I. Ramli[1,2], E. N. Muhamad[1,2], Y. H. Taufiq-Yap[1,2]

[1]Department of Chemistry, Faculty of Science, Universiti Putra Malaysia, 43400 UPM Serdang, Selangor, Malaysia.
[2]Catalysis Science and Technology Research Centre, Faculty of Science, Universiti Putra Malaysia, 43400 UPM Serdang, Selangor, Malaysia.
[3]Department of Chemical Sciences, Federal Polytechnic, PMB 55, Bida, Niger State, Nigeria.

*Corresponding author: uindaumar@gmail.com

Abstract
Sulfonated carbon catalysts were synthesized using three different carbonization methods and characterized with advanced analytical techniques. The synthesized catalysts exhibited better acetylation activity when compared with earlier studies.

Keywords: Glycerol, acetylation, carbonization, sulfonation, biomass

Introduction
The recent increase in the production and utilization of biodiesel as an alternative fuel has led to the upsurge in the volume of glycerol produced globally (Quispe et al., 2013). Hence research is focused on the conversion of glycerol into high valued products such as acetin which is produced via catalytic glycerol acetylation. Though several solid catalysts such as amberlyst-15, K-montmorillonite, zeolites, etc have been utilized in glycerol acetylation with high conversion but characterized with low selectivity to triacetin and other limitations (Okoye et al., 2017). Therefore, the objective of this research is to synthesize carbon-based catalysts using palm kernel shell (PKS) via different carbonization techniques with a view to enhancing glycerol acetylation to triacetin.

Methodology
The PKS, after pretreatment was carbonized under CO_2 environment using three different carbonization methods namely direct, chemical and template methods at 400 and 800 °C respectively and later sulfonated with concentrated H_2SO_4 (96%). The carbonized materials and the catalysts were characterized using CHNS, XRD, FTIR, TPD, TGA, SEM, EDX, BET analyzer and acid-base titration and later evaluated in glycerol acetylation with acetic acid in a batch reaction. The components of the product were identified using GC-MS (Shimadzu QP2010 Plus) while the product distributions were analyzed with GC (Agilent 7890A) using 1,3-butanediol as the internal standard.

Results and Discussion
The results of the elemental analysis as shown in Table 1 indicate an increase in carbon content with increasing temperature from 400 to 800 °C which is also in line with the XRD results which showed broad diffraction peaks at 2θ=15-30^o and at 40-50^o attributable to amorphous carbon and are more pronounced at 800 °C. This observation is consistent with Geng et al. (2012). The sulphur content generally increased after sulfonation indicating that the sulfonic acid group was successfully incorporated onto the carbon material with the template carbonized material showing the highest. This is corroborated by the results of total acid sites and the presence of functional groups as obtained by TPD analysis (Table 2) as well as FTIR spectra. The highest total acidic site was exhibited by the catalysts

prepared using the template method carbonized at 800 °C indicating that the carbonization methods as well as the carbonization temperature played active roles in the synthesis.

Table 1: Elemental composition of PKS, carbonized and synthesized carbon catalysts

	Carbonized					Sulfonated carbon catalysts					
Sample	**C (%)**	**H (%)**	**O (%)**	**N (%)**	**S (%)**	**Catalyst**	**C (%)**	**H (%)**	**O (%)**	**N (%)**	**S (%)**
PKS	49.59	5.79	44	0.09	0.53						
CAC	65.57	3.23	31.15	0.01	0.04	CACS	59.78	3.00	34.96	0.01	2.25
P400	61.09	2.57	36.27	0.03	0.04	P400S	54.24	2.44	40.51	0.30	2.51
P800	73.22	0.70	25.62	0.45	0.01	P800S	64.41	1.44	31.22	0.36	2.57
PC400	64.88	3.72	30.29	0.92	0.14	PC400S	59.79	2.62	35.41	0.004	2.18
PC800	57.52	1.14	40.96	0.37	0.01	PC800S	57.45	1.42	40.64	0.38	0.11
PT400	58.93	2.91	37.71	0.29	0.16	PT400S	55.95	2.98	62.34	0.41	3.00
PT800	73.68	0.28	26.03	0.003	0.01	PT800S	65.31	1.24	30.07	0.35	3.03

Table 2: Textural and acidic properties of PKS and the synthesized carbon-based catalysts

Sample	**BET Surface area (m^2/g)**	**Pore volume (cm^3/g)**	**Average Pore size (Å)**	**Catalyst**	**BET Surface area (m2/g)**	**Pore volume (cm3/g)**	**Average Pore size (Å)**	**Acid density SO_3H (mmol/g)**	**Total acid sites (µmol NH3/g)**
PKS	2.1	0.0	83.6						
CAC	958.5	0.9	38.8	CACS	850.6	0.7	30.4	0.72	1574.7
P400	1.2	0.0	168.6	P400S	2.2	0.0	108.7	0.80	3820.1
P800	233.9	0.2	27.7	P800S	33.5	0.4	18.9	0.82	5203.5
PC400	388.6	0.3	26.7	PC400S	491.7	0.3	21.4	0.72	2927.9
PC800	429.4	0.3	23.2	PC800S	680.8	0.4	20.8	0.04	1447.1
PT400	2.9	0.0	95.7	PT400S	3.6	0.0	60.2	0.96	8064.6
PT800	483.5	0.3	27.1	PT800S	493.2	0.1	27.1	0.97	10246.6

The BET surface area of the material and catalysts (Table 2) carbonized at higher temperature are relatively very high when compared with those obtained at lower temperature. The N_2 adsorption isotherm and the pore size distribution indicate that the solid catalysts obtained at high 800 °C exhibit type IV isotherm with hysteresis loop which is evidence of mesoporous materials in line with IUPAC classification.

The GC results of the glycerol acetylation reaction with acetic acid indicate very high glycerol conversion for all the catalysts including the blank which is similar to earlier studies but differs in selectivity to mono, di and triacetin. The catalysts obtained from the template method gave the highest selectivity to triacetin (58.9%) within 3 h reaction time attributable to the presence of very high acidic sites.

Conclusion

Sulfonated carbon catalysts were successfully synthesized from PKS using direct, chemical and template methods of carbonization and they exhibited better acetylation activity when compared with earlier studies including the commercial amberlyst-15 catalyst.

Acknowledgement

UPM is hereby appreciated for the research grant (number 9658900). The sponsorship received from TETFund through the Fed Poly Bida, Nigeria is also hereby acknowledged.

References

Geng, L., Yu, G., Wang, Y., Zhu, Y. (2012). Ph-SO_3H-modified mesoporous carbon as an efficient catalyst for the esterification of Oleic acid. Applied catalysis A: General 427-428. 137 – 144.

Okoye, P., Abdullah, A., Hameed, B. (2017). Synthesis of oxygenated fuel additives via glycerol esterification with acetic acid over bio-derived carbon catalyst. Fuel, 209, 538-544.

Quispe, C. A., Coronado, C. J., Carvalho Jr, J. A. (2013). Glycerol: production, consumption, prices, characterization and new trends in combustion. Renewable and Sustainable Energy Reviews, 27, 475-493.

PRODUCTION OF BIODIESEL FROM PALM OIL USING K_2O DOPED DOLOMITE

M. Yahaya[1], I. Ramli[1,2], Y.H. Taufiq-Yap[1,2], E. Bt. Muhamad[1,2]

[1]Department of Chemistry, Faculty of Science, Universiti Puta Malaysia
[2]Catalysis Science and Technology Research Centre, Faculty of Science
Universiti Putra Malaysia

**Corresponding author: irmawati@upm.edu.my*

Abstract
Biodiesel (FAME) is one of the promising substitutes of conventional petroleum based-diesel due to it numerous benefits such as non-toxic, biodegradable and free from sulphur and aromatic compounds. K_2O doped dolomite was prepared by impregnation method. The catalyst was characterized by XRD, TPD-CO_2 and BET. The effect of reaction conditions such as Temperature, Time, Molar ratio and Catalyst load were investigated. The catalyst showed 92.3% conversion of biodiesel with Temperature 80^{O}C, Time 1hr, Methanol to oil ratio 20:1 and 10wt% catalyst load. The catalytic activity of the catalyst was found to be depending on the surface area as well as the basicity of the used catalyst.

Keywords: Biodiesel, Palm oil, Dolomite, Heterogeneous, catalyst, Transesterification

Introduction
Biodiesel is the best alternative to non-renewable fuel source. Which is made up of fatty acid methyl ester (FAME) obtained from vegetable oil and animal fats (Nur *et al.*, 2012). The renewable non carbon-based fuels has numerous advantages over conventional petroleum-based fuel which include; essentially free of sulphur content (Nur et al., 2014), aromatic compounds (Ngamcharussrivichai *et al.*, 2010), oxides of carbon and nitrogen that affect the greenhouse. (Nur *et al*., 2014). However, utilization of homogeneous catalyst in the production of biodiesel has numerous weaknesses such as unable to recover catalyst and generate greater amount of wastewater and effluents. However, to avoid these issues, the use of catalyst that is heterogeneous in nature paramount and this will survive most of the environmental and economic setbacks during homogeneous method. (Marques *et al.*, 2015) Dolomite is one of the cheapest and available heterogeneous basic catalyst support used in production of biodiesel. (Buasri *et al*.,2015). (Jindapon & Ngamcharussrivichai, 2018) reported that they have achieved 99.9% FAME yield using dolomite catalyst and reaction condition of molar ratio of 15:1, reaction time 3hr, amount of catalyst 3wt% at 60^{O}C.

Methodology
The 10wt% Catalyst was synthesized using impregnation method and calcined for 3hr at 850^{O}C. The catalyst was further characterized using analytical tools (XRD, TPD-CO2 and BET). Production of biodiesel was done by Transesterification reaction.

Results and Discussion
The XRD pattern of parent material (dolomite) and the synthesized 10wt% K_2O doped K_2O are depicted in fig 1 the activated parent material without active component exhibit peaks at 2θ = 32.4^O, 37.6^O, 54.2^O 64.6^O 67.9^O (JCPDS = 01-074-1226) which is attributed to quicklime (CaO) and at 2θ = 43.5^O and 62^O. (JCPDS = 01-075-1525) is attributed to periclase (MgO). Similar result revealed by (Nur et al., 2012) and (Buasri *et al.*, 2015). When K_2O was introduced onto the catalyst support, the peak intensities decreased and new phases are formed. At 2θ = 50.8^O (JCPDS: 01-076-066) is attributed to $Mg(OH)_2$ and

at 2θ= 34.2^{O} (JCPDS: 01-089-2779) is attributed to $Ca(OH)_2$. The measurement and strength of basic site were examined using Temperature Program Desorbed with CO_2 as probe molecule (TPD-CO_2), the results were summarized in table 1. According to the peaks presented by TPD-CO_2 in fig 2. 10K/D displayed peak at 968K with the amount of CO_2 desorption of 892.22µmol/g which showed high basicity of the catalyst. The BET surface area and pore volume of calcined dolomite and K_2O doped dolomite were presented in fig 2. The parent material calcined at 850^{O}C built a mesoporous structure with BET surface area of 19.1m^2/g higher than a specific surface area reported by (Buasri *et al.*, 2015). According to (Nur *et al.*, 2012), after activation of the dolomite, the specific surface area and morphology instantly change which allowed physical and chemical alteration. However, after adding the active component, there was a substantial decrease in pore volume and surface area. Precisely, when K_2O was introduced on the support, the surface area and pore volume of the catalyst decreased from 19.1m^2/g to 5.589m^2/g and from 0.045 to 0.020cc/g respectively.

Table 1. BET surface area, TPD-CO_2 and crystal size

Catalyst	Surface area m^2/g	Pore volume (cm^3/g)	Pore diameter (nm)	Tmax (^{O}C)	Amount of CO_2 Desorption (µmol/g)	Crystal size
Calcined D	19.08	0.03	7.03	-	-	36.70
10wt%	5.24	0.03	1.90	720	1692.5	31.90

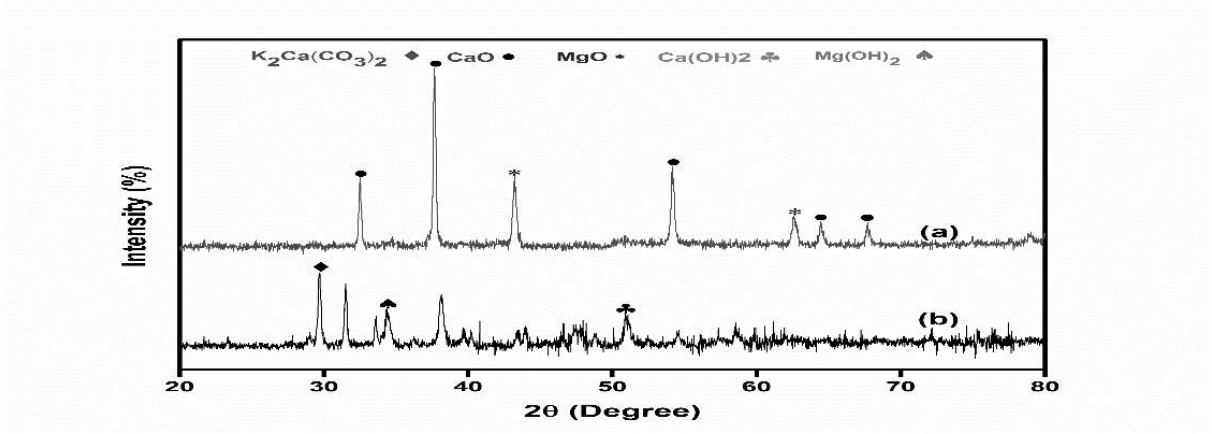

Fig 1. XRD pattern of (a) Activated Dolomite (AD). (b) 10wt% of K2O doped dolomite

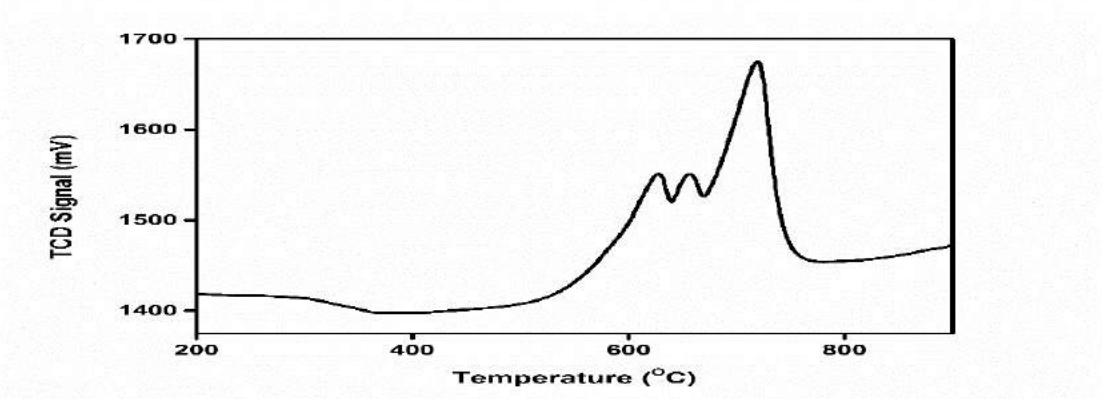

Fig 2. The TPD-CO_2 spectrum of 10wt% K_2O Doped Dolomite.

Conclusion

In this research, the 10wt% of K_2O doped dolomite gave a higher conversion of 99.4% due to its basicity and surface area. These factors affected the biodiesel production as well as the reaction parameters (Molar ratio, catalyst load, temperature and time). The catalytic activity of this catalyst was found to be depending on the basicity as well as the surface area of the catalyst used.

Acknowledgment

I am very grateful to Universiti Putra Malaysia for making this work possible by providing me with research grant 9658900.

References

1. Buasri, A., Rochanakit, K., & Wongvitvichot, W. (2015). *The Application of Calcium Oxide and Magnesium Oxide from Natural Dolomitic Rock for Biodiesel Synthesis*. *Energy Procedia* (Vol. 79). Elsevier B.V.
2. Jindapon, W., & Ngamcharussrivichai, C. (2018). Heterogeneously catalyzed transesterification of palm oil with methanol to produce biodiesel over calcined dolomite: The role of magnesium oxide. *Energy Conversion and Management*, *171*(April), 1311–1321.
3. Marques, L., Sousa, N. De, Sousa, D., Loureiro, C., Jr, C., Antonio, J., Silveira, R. (2015). Characterization and application of dolomite as catalytic precursor for canola and sunflower oils for biodiesel production. *Chemical Engineering Journal*, *269*, 35–43.
4. Ngamcharussrivichai, C., Nunthasanti, P., Tanachai, S., & Bunyakiat, K. (2010). Biodiesel production through transesteri fi cation over natural calciums. *Fuel Processing Technology*, *91*(11), 1409–1415.
5. Nur, Z. A. S., Nizah, M. F. R., Teo, S. H., Syazwani, O. N., & Islam, A. (2014). Production of biodiesel from palm oil using modified Malaysian natural dolomites. *Energy Conversion and Management*, *78*, 738–744.
6. Nur, Z. A. S., Taufiq-Yap, Y. H., & Hussein, M. Z. (2012). Tin Oxide Doped on Activated Dolomites as Efficient Catalyst for Biodiesel Production. *Advanced Materials Research*, *620*, 378–383.

STUDY OF THE Pd(II) COMPLEXES WITH THIAZOLYLAZO DERIVATIVES APPLIED ON PEPSIN AND PAPAIN INHIBITION

N. Phiromphu[1], A. Piyasaengthong[2], A. Songsasen[2]*

[1] Department of Chemistry, Faculty of Science, Kasetsart University, Chatuchak, Bangkok 10900, Thailand
[2] Department of Chemistry and center of Excellence for Innovation in Chemistry (PERCH-CIC), Faculty of Science, Kasetsart University, Chatuchak, Bangkok 10900, Thailand

**E-mail address: fsciass@ku.ac.th*

Abstract
3-[2-(1,3-thiazol-2-yl)diazen-1-yl]pyridine-2,6-diol(TADHP),aminothiazolylazo,2-(2'-thiazolylazo)-5-aminoanisole (*p*-amino TAA) and 4-(2'-thiazolylazo)-3-aminoanisole (*o*-amino TAA) have been synthesized and characterized by basic techniques. The spectrochemical properties of these compounds were obviously appeared in UV-Vis spectroscopy and presented the azine-hydrazone tautomeric form of TADHP in various pH solutions, including the two isomeric structures of TAA. The stoichiometric ratio of Pd(II) and ligands which is 1:1 for TADHP and 1:2 for *o*-amino TAA. The stability constants of two complexes are 4.00×10^4 and 4.50×10^3 of TADHP complex and 2×10^9 and 1.75×10^9 of *o*-amino TAA complex at pH 4 and 7, respectively. The TADHP complex has the biological inhibited efficiency for pepsin activity higher than the free Pd(II) or ligands because of the specific structure of TADHP ligand suitable for binding to allosteric site of pepsin enzyme. The IC_{50} of this complex is 12.09 ± 0.03 µM.

Keywords: Tautomeric form of TADHP, TADHP complex, *o*-amino TAA complex, Pd (II) complex, Proteases enzyme inhibitor

Introduction
Many types of thiazole dye have strong colour because of a chromophoric azo bond (-N=N-) and thiazole ring in the structure. The strong donor atom of dyes can bind to the protein cell adhesive and some of the azo schiff bases exhibited the antibiotic activities that were utilized for the pharmaceutical field in terms of the drug transferability. In this research, not only the tautomeric or isomeric form of ligands in the various pH but also the complexation with Pd(II) are studied and investigated their phenomena, including their application of enzyme inhibitors tested on pepsin and papain inhibition.

Methodology
1. Synthesis of TADHP, *p*-amino TAA and *o*-amino TAA
In the first step, 2-aminothiazole and $NaNO_3$ were mixed in an ice bath to produce the diazonium salt. After that, TADHP was synthesized by the coupling reaction of 2,6-dihydroxypyridine while the two isomeric TAA used *m*-anisidine instead following in **Figure 1**. In order to identify the molecular structures of three thiazolylazo derivatives, many techniques such as the ^{1}H-NMR, FT-IR, ESI-MS and X-ray crystallography were cooperatively used to analyst, especially UV-Vis spectroscopy.

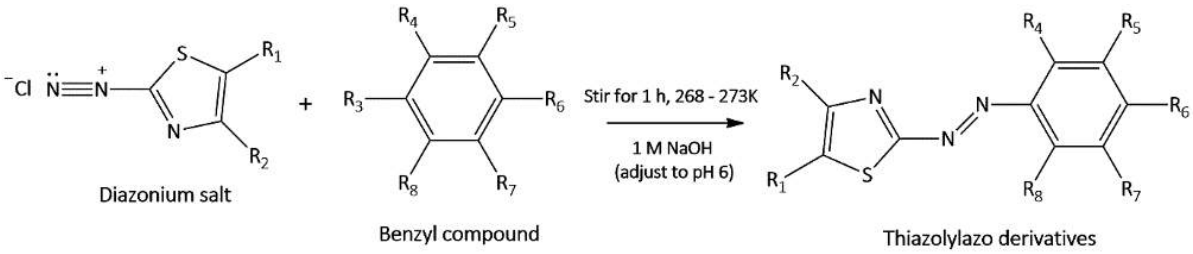

Figure 1 The pictorial representation of the major coupling step to synthesize thiazolylazo ligands

2. Study of the complexation with Pd(II) and stability of their complexes

TADHP and *o*-amino TAA ligand were bound to Pd(II) and these complexation were measured by the chemical absorption. The appropriate pH and reaction time led to the highest stability of thiazolylazo complex with Pd(II) were regarded and then the stoichiometric ratio of complexes was determined by Job's method and mole ratio. The stability constants of complexes were observed by Benesi-Hildebrand's equation.

3. Study on pepsin and papain protease inhibition

The IC_{50} of the thiazolylazo complexes with Pd (II) were performed by the process of Gomes, B.; et al. (2003) compared to the free Pd(II) and their ligands including, the generally antibiotic compounds, there are pepstain A using pepsin assay and E-64 using papain assay. Moreover, the inhibition model of a great inhibitor was calculated by the Michaelis-Menten equation.

Results and Discussion

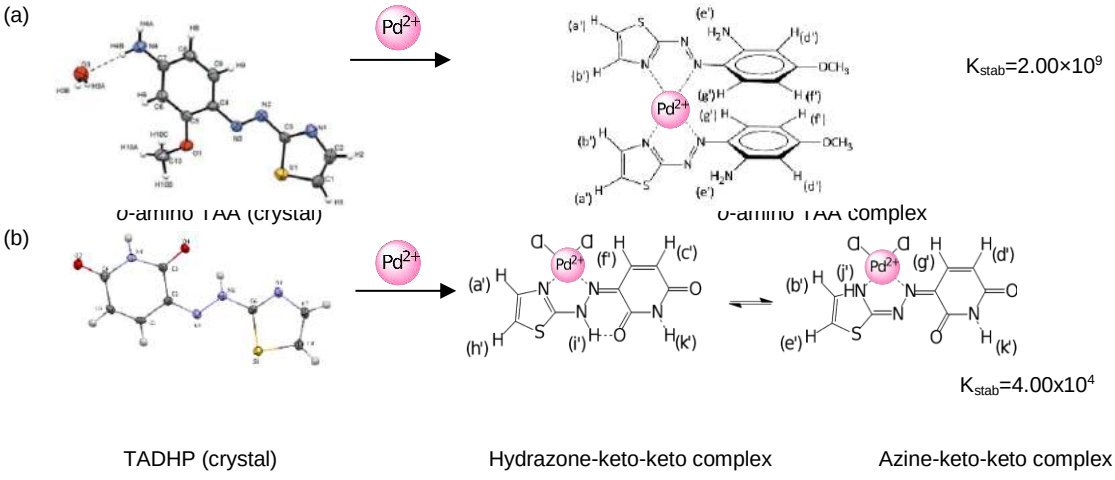

Figure 2 The complexation of *o*-amino TAA (a) and TADHP (b) with Pd(II) and the stability constant of each complexes at pH 4

The NMR spectrum of Pd(II) complex with TADHP and o-amino TAA in DMSO-d_6 exhibited different chemical shift ($^{TM}_{H}$) values from that of the free ligands, especially protons adjacent to nitrogen atoms on the azo bond and thiazole ring. The molecular structures of two complexes were proposed in **Figure 2**. In the pepsin assay, the Pd(II) complex with TADHP provided the IC_{50} of 12.09 $\pm$ 0.03 which is closed to pepstatin A as shown in **Table 1**.

Table 1 The IC_{50} and R-square (R^2) values of the samples in pepsin assay

Inhibitors	IC_{50} (ʃM)	Inhibitors	IC_{50} (ʃM)
Pd(II)	15.47 ± 0.02	TADHP-Pd(II) complex	12.09 ± 0.03
TADHP	29.83 ± 0.02	*o*-amino TAA-Pd(II) complex	14.97 ± 0.01
o-amino TAA	25.01 ± 0.04	Pepstatin A	10.99 ± 0.03

Conclusion

TADHP and *o*-amino TAA were synthesized by coupling reaction. The azine form of TADHP is obviously stable in acidic pH more than the hydrazone form of TADHP. The stoichiometric of Pd (II) complexes with TADHP and *o*-amino TAA was found that the ratio of 1:1 and 1:2, respectively and *o*-amino TAA complex provides the stronger coordination with Pd(II). However, the Pd(II) complex with TADHP could inhibit pepsin which is the highest efficiency but its configuration structure is not selective with the active site of papain enzyme.

Acknowledgement

The authors are greatly appreciated in the Department of Chemistry, Faculty of Science, Kasetsart University to support and facilitate our research. Moreover, we are grateful to PERCH-CIC and SAST scholarship for funding source.

References

Levine, W.G., 1991. Metabolism of Azo Dyes: Implication for Detoxication and Activation. *Drug Metabolism Reviews*. 23(3-4), 253-309.

Gomes, R.A.d.S.; et al, 2003. A Fluorometric Method for the Determination of Pepsin Activity. *Analytical Biochemistry*. 316(1), 11-14.

Piyasaengthong, A., N. Boonyalai, S. Suramitr and A. Songsasen. 2015. Synthesis, Characterization, and Pepsin Inhibition Study of Au(III)–3-(2′-Thiazolylazo)-2,6-Diaminopyridine Complex*. Inorganic Chemistry Communications*. 59(88-90).

DETERMINATION OF PALMITIC ACID USING ELECTRODE MODIFIED WITH REDUCED GRAPHENE OXIDE/GOLD NANOPARTICLES COMPOSITE

Chin Boon Ching[1], Jaafar Abdullah[1]*, Nor Azah Yusof[1]

[1]Department of Chemistry, Faculty of Science, Universiti Putra Malaysia, 43400 UPM Serdang, Selangor, Malaysia.

*Corresponding author: jafar@upm.edu.my

Abstract
Malaysia is one of the largest producers of palm oil in the world. The quality of palm oil is very important to be examined and one of the quality indices is free fatty acid (FFA) content. Thus, in this study, an electrochemical technique for the determination of FFA as an alternative to conventional method (titration) has been explored. The electrochemical method was developed based on electrochemically reduced graphene oxide/gold nanoparticles composite deposited onto screen printed carbon electrode (SPCE) via drop casting technique. The modified electrode was characterized by physical and electrochemical methods, respectively. The voltammetric behaviour of 2-methyl-1,4-naphthaquinone in the presence of palmitic acid at the modified electrode was investigated in an acetonitrile/water (3:1) mixture containing 2.5 M LiClO4. The proposed method was based on the voltammetric reduction of 2-methyl-1,4-naphthaquinone which is proportional to the concentration of palmitic acid. The exploration of the new developed system is expected to achieve high sensitivity and excellent selectivity towards determination of FFA content in palm oil.

Keywords: Electrochemistry, Graphene Oxide, Gold Nanoparticles, Free Fatty Acid

Introduction
Free fatty acid (FFA) is one of the most frequently determined quality indices during production, storage and marketing of palm oil products and the oil price is dictated by FFA content. Traditionally, FFA levels in palm oil are determined using manual titration method but this method is attended with problems such as requirement for high amount of solvent and the presence of carotene causes difficulties to determine the end point of the titration. To avoid the problems above, we proposed investigation of electrochemical behaviour and analytical potential of screen printed carbon electrode (SPCE) modified with reduced graphene oxide/gold nanoparticles composite for the determination of FFA content in palm oil. Graphene oxide (GO) have been utilized for electrode modification, attribute to its high electrical conductivity, biocompatibility and versatile surface modification. Gold nanoparticles (AuNPs) have found many applications in sensors due to their excellent characteristics such as high catalytic activity, huge surface area and small dimensional size. Voltammetric method is used for determining acid values based on the reduction peak of 2-methyl-1,4-naphthoquinone (VK_3), which appear due to the presence of acid. Thus, the objectives of this study were: (i) to prepare and characterize SPCE modified with reduced graphene oxide/gold nanoparticles composite and (ii) to evaluate the analytical performance of modified SPCE for the determination of palmitic acid content in palm oil.

Methodology
Preparation of reduced graphene oxide/gold nanoparticles-modified SPCE, characterization and optimization of modified SPCE, performance study of modified SPCE towards palmitic acid detection and applicability study of modified SPCE with real sample analysis were carried out.

Results and Discussion

Electrochemical Characterization of Modified SPCE

Cyclic voltammogram in Fig.1 depicted redox current of rGO/AuNPs > rGO > AuNPs > bare > GO-modified SPCE. Highly conductive AuNPs on the rGO sheets behaved as an electron transfer channel, which further improve the conductivity of rGO film. rGO-modified SPCE increases in the peak current compared to bare SPCE as a results of its excellent conductivity and large surface area. GO-modified SPCE has the lowest peak current because GO acts as an insulating layer, as a result of plenty of polar and negatively charged functional groups, making interfacial charge transfer difficult .

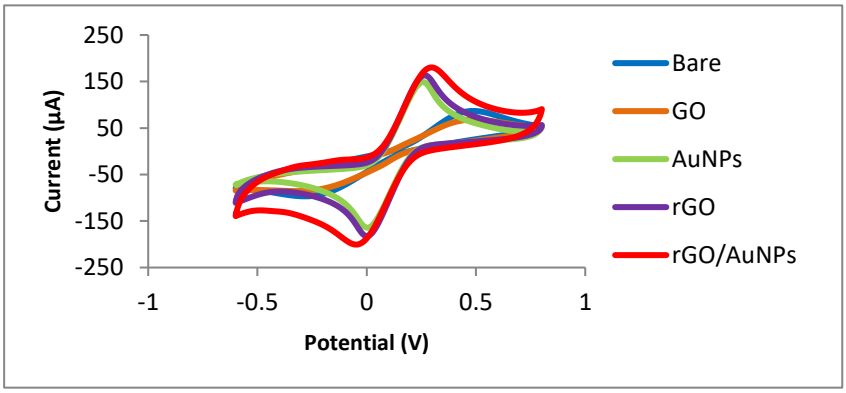

Fig.1 Cyclic voltammogram of bare SPCE, GO, AuNPs, rGO and rGO/AuNPs-modified SPCE in 0.1M KCl solution containing 5.0mM $[Fe(CN)_6]^{3-/4-}$ solution. The scan rate was 100mV/s.

The working solution was prepared by dissolving VK_3 and $LiClO_4$ in acetronitrile/water mixed solvent. The optimum VK_3 concentration and $LiClO_4$ concentration are 3mM and 2.5M, respectively. The best ratios of acetonitrile to water was 1:3. For the detection using linear sweep voltammetry (LSV), the current response is proportional to the concentration of palmitic acid. The linear calibration curve of palmitic acid has been obtained with sensitivity of 163.22µA/mM and correlation coefficient of R^2 = 0.9883, respectively.

Conclusion

In summary, an electrochemical sensor based on SPCE modified with reduced graphene oxide/gold nanoparticles was successfully designed for the detection of palmitic acid content. The analytical performance of modified SPCE for determination of palmitic acid concentration was successfully evaluated.

Acknowledgement

The authors would like to thank the Ministry of Higher Education, Institute of Advanced Technology, Universiti Putra Malaysia and Department of Chemistry, Faculty of Science, University Putra Malaysia for all facilities and funds provided (GP-IPS/2018/9652900).

References

1. Kim, J., Chung, T. D., & Kim, H. (2001). Determination of biologically active acids based on the electrochemical reduction of quinone in acetonitrile+ water mixed solvent. *Journal of Electroanalytical Chemistry*, *499*(1), 78-84.

2. Kotani, A., & Kusu, F. (2002). HPLC with electrochemical detection for determining the distribution of free fatty acids in skin surface lipids from the human face and scalp. *Archives of dermatological research*, *294*(4), 172-177.

AN ELECTROCHEMICAL BIOSENSOR FOR THE DETECTION OF PORCINE DNA BASED ON SiNWs/PtNPs-MODIFIED SPCE

N. Kusnin[1], N. A. Yusof,[1,2*], J. Abdullah[2], S. Sabri[3], S. Mustafa[3,4]

[1]Institute of Advanced Technology, Universiti Putra Malaysia, 43400 UPM Serdang, Selangor, Malaysia
[2]Department of Chemistry, Faculty of Science, Universiti Putra Malaysia, 43400 UPM Serdang, Selangor, Malaysia
[3]Department of Microbiology, Faculty of Biotechnology and Biomolecular Sciences, Universiti Putra Malaysia, 43400 UPM Serdang, Selangor, Malaysia
[4]Halal Product research Institute, Universiti Putra Malaysia, 43400 UPM, Serdang, Selangor, Malaysia

*Corresponding author: azahy@upm.edu.my

Abstract
A rapid and sensitive electrochemical biosensor was developed based on the fabrication of the silicon nanowires/platinum nanoparticles (SiNWs/PtNPs) nanocomposite onto screen-printed carbon electrode (SPCE) for detection of porcine oligonucleotides. The chemical bonding and morphology of SiNWs/PtNPs-modified SPCE were studied by fourier-transform infrared spectroscopy (FTIR) and field enhance scanning electron microscopy-energy dispersive X-ray spectroscopy (FESEM-EDX), respectively. From both studies, it clearly showed that SiNWs/PtNPS was successfully coated onto SPCE through drop cast technique. Cyclic voltammetry (CV) was used to study the electrochemical properties of the modified electrode. The effective surface area for SiNWs/PtNPs-modified SPCE was enhanced when compared with bare SPCE. Differential pulse voltammetry (DPV) was used to monitored hybridization events between immobilized DNA probe and complementary sequences of porcine oligonucleotides with ferrocenylnaphthalene diimide (FND) as redox indicator. The results demonstrated that the oxidation peak current of ferrocene was significantly increased after DNA hybridization process. The developed electrochemical biosensor is sensitive, low sample volume, rapid, and disposable, which is suitable for porcine DNA detection in food products.

Keywords: Electrochemical biosensor; screen-printed carbon electrode (SPCE); silicon nanowires/platinum nanoparticles; porcine DNA; ferrocenylnaphthalene diimide.

Introduction
Halal food is sensitive and serious matter to Muslim. Authentication and verification for halal has become one of the major challenges in analysis of processed food. There have been some issues associated with the adulteration of food products in Malaysia. Among the issues were lard adulteration in bread and the use of pig intestine casings in sausage (Aida et al., 2005). These are some examples of how important it is to develop a reliable technique to ensure the halal status of the food products which is crucial for Muslims and halal authentication. In most countries, food manufactures choose to use porcine derivatives because they are cheap and readily available (Erwanto, 2018). There are very limited analytical method available for halal food verification. Rapid and reliable method are urgently needed for detection of non-halal origin in food products. Electrochemical biosensor application may overcome the limitation of the existing porcine DNA detection, which allows the continuous monitoring, rapid response, cost effective method, high sensitivity and selectivity and easy operation with minimum sample preparation.

Methodology

The carbon working electrode of SPCE was treated in NaOH to form hydroxyl group. Then the suspension of silicon nanowires (SiNWs) in APTES was dropped cast on working surface and incubated for 2 hours at room temperature, rinse with ethyl-ethanol and baked at 70°C for 30 min. The modified electrode was drop-casted with 5 mM ethanolic 3,3-dithiodipropionic acid (DTDPA) and incubated for 1 hour at room temperature. The SiNWs-electrode then was drop-casted with PtNPs suspension, rinse with deionized water to remove the excess of PtNPs and dried with N_2 gas. The thiolated DNA probe (ssDNA) was immobilized on the surface of SiNWs/PtNPs-SPCE surface through Pt-S bond. It will be performed by drop cast thiolated DNA probe on the modified SPCE surface and incubate for 24 hours at 4°C. The hybridization process was conducted by incubating ssDNA-PtNPs/SiNWs-SPCE with complementary DNA target for several hours at 40°C. For electrochemical measurement, the SiNWs/PtNPs-modified SPCE (with and without complementary DNA) were immersed into buffer containing ferrocenylnaphthalene diimide (FND) without applying any potential for 30 min at room temperature, followed by washing it with Tris-HCl buffer to remove any excess unbounded FND. Finally, the modified SPCE was measured using differential pulse voltammetry for electrochemical detection of target DNA.

Results and Discussion

Several factors were successfully optimized to enhance the sensitivity of the screen-printed carbon electrode including volume of SiNWs, concentration of dithiodipropionic acid (DTDPA), volume and size of PtNPs, DNA probe concentration and DNA probe immobilization time. The modified SPCE exhibited well defined redox due to oxidation and reduction process of $[Fe(CN)_6]^{3-/4-}$ and produced higher peak currents compared with bare SPCE. By using Randles-Servcik equation, surface area of SiNWs/PtNPs-modified SPCE provide 16.8 folds greater than bare SPCE. The enhancement of electrochemical signal of the ferrocene oxidation peak was successfully monitored by some experimental conditions such as pH, ionic strength, buffer composition, hybridization temperature and also hybridization time. The obtained results demonstrate that FND intercalator bind specifically to the dsDNA. Finally, the sensitivity of fabricated biosensor was evaluated by the hybridization of probe DNA with different concentrations of complementary DNA.

Conclusion

In this work, we managed to develop a simple and rapid electrochemical biosensor technique based on SiNWs/PtNPs-modified SPCE. The optimized biosensor showed a great potential for porcine DNA detection in food samples

Acknowledgement: The authors would like to thank the Universiti Putra Malaysia for their financial support [Project Number = GP-IPS/2017/9540500].

References

1. Aida, A.A., Che Man, Y.B., Wong, C.M.V.L., Raha, A.R. and Son, R. (2005). Analysis of raw meats and fats of pigs using polymerase chain reaction for halal authentication. *Meat Science*. 69, 47-52.
2. Erwanto, Y. (2018). Molecular based method using PCR technology on porcine derivative detection for halal authentication, IntechOpen Limited, United Kingdom.
3. Yogeswaran, U. and Chen, S.M. (2008). A review on the electrochemical sensors and biosensors composed of nanowires as sensing material. *Sensors*. 8, 290-313.

A STUDY ON THE SPATIAL VARIABILITY IN SURFACE WATER QUALITY OF LAKES AND EX-MINING PONDS IN MALACCA, MALAYSIA: THE GEOCHEMICAL INFLUENCE

I.B. Koki[1,2]*, K.H. Low[1], S.M. Zain[1], H. Juahir[3], A.S. Bayero[2], A. Azid[4], M.A. Zali[5]

[1]Department of Chemistry, Faculty of Science, University Malaya, Kuala Lumpur 50603, Malaysia
[2]Department of Chemistry, Yusuf Maitama Sule University Kano, PMB 3220 Kano Nigeria
[3]East Coast Environmental Research Institute (ESERI), University Sultan Zainal Abidin, Kuala Terengganu, Malaysia
[4]Faculty of Bioresources and Food Industry, Universiti Sultan Zainal Abidin, Besut Campus, 22200 Besut, Terengganu, Malaysia
[5]Environmental Health Division, Department of Chemistry Malaysia, Jalan Sultan, 46661 Petaling Jaya, Selangor, Malaysia

*Corresponding author: isakoki@yahoo.com

Abstract
A surface water quality assessment was carried out to explore the spatial variations between lakes and ex-mining ponds in Malacca with the aid of chemometrics tools. The physico-chemical variables include pH, dissolved oxygen, total dissolved solids, electrical conductivity, biological oxygen demand, total suspended solids, and ammoniacal nitrogen were measured in situ; while the elemental concentrations were determined by inductively coupled plasma-mass spectrophotometry. The chemometric analysis suggested that variability in the water quality depends mainly on the nature of the ponds/lakes and the dissolution of rocks; and part of the variation was originated from their current uses. Despite the inherent variability characteristics between both water sources, the corresponding metal index revealed no significant As threat. Thus, these surface water sources could be considered as the potential reservoirs for potable supply after conventional treatment.

Keywords: Chemometrics, Drinking water, Geochemistry, Metal, Pattern recognition

Introduction
The quality of water is a major factor of consideration for maintaining a healthy ecosystem due to the reported effects of water pollutants to humans, animals and plants (Al-Ansari et al. 2018). Seasonal water shortages were experienced in Malacca, and this causes limited water availability, potential issues of water quality, and therefore the urgent need arises to search for other supporting sources. Malacca experienced the worst water crisis in 1991 due to a very low level of water from its major reservoirs; the Durian Tunggal Lake (LDT) and Jus Dam (JD). These water sources are not enough to cater for the three districts of Jasin, Alor Gajah, and Malacca Tengah, thus larger portion of the daily water supply in Malacca is imported from Muar River of Johor (MWA 2008). Furthermore, the authorities in Malacca have made an effort to identify additional potable water sources to complement the needs of the public (Azzlan et al. 2016). In this study, chemometric techniques were applied to evaluate the water quality dataset collected from selected ex-mining ponds and lakes in Malacca, in addition to conventional metal index approach. The multivariate models aim to unveil the underlying variations in the metal concentrations and physico-chemical parameters with respect to the geological influences and to characterize the water samples from both sources.

Methodology

By using Wildco water sampler, nine sub-samples were collected per site from a depth of 25 cm. The samples drawn were immediately preserved with addition of concentrated HNO_3 (Suprapur®, Merck) to pH < 2 and conserved at 4°C. The physico-chemical parameters were determined in the field. The preserved water samples were analysed using an Agilent 7500ce inductively coupled plasma-mass spectrometer (ICP-MS). The water quality dataset was preprocessed with Microsoft® Excel 2010. Pattern recognition techniques were applied using SAS® JMP Pro 12.

Results and Discussion

The physical-chemical measurements of the water catchments (Table 1) were found to be within the Malaysia's Interim National Water Quality Standards (DOE 2012). The pH of all the sampling sites were ranging between 6.5 and 8.5, except LR (10.3 ± 0.1) which is located in Negeri Sembilan state near Malacca with a more basic rock basement. Similarly, TR that surrounded by much greeny vegetation has recorded the highest DO of about 9.16 mg/L whereas less than 5 mg/L (the recommended level) were observed in both LT and LBK. The low dissolved oxygen levels might be associated with low water level at LT where imbalance between oxygen supply from the surface waters and removal of oxygen from bottom water; as well as the organic matter corresponding to residential discharges into LBK. The water quality status of the ex-mining ponds and lakes with respect to metals are also listed in Table 1 which revealed notable variations.

Table 1. Physico-chemical characteristics of water samples from lakes and ex-mining ponds

TYPE	**EX-MINING**				**LAKE**			
SITE	**LBC1**	**LBC2**	**LBC3**	**LR**	**JD**	**LDT**	**LT**	**LBK**
DO	5.1 ± 0.2	6.1 ± 0.1	5.0 ± 0.2	9.2 ± 0.3	4.9 ± 0.1	6.1 ± 0.5	4.6 ± 0.3	3.7 ± 0.1
BOD	0.90 ± 0.01	1.15 ± 0.02	1.16 ± 0.02	1.96 ± 0.01	1.25 ± 0.03	1.09 ± 0.01	2.12 ± 0.01	1.50 ± 0.01
pH	7.2 ± 0.1	7.3 ± 0.1	7.0 ± 0.1	10.3 ± 0.1	8 ± 1	7.2 ± 0.1	7.1 ± 0.1	6.9 ± 0.1
TDS	47.5 ± 0.1	59.0 ± 0.3	55.9 ± 0.1	77.0 ± 0.9	44.9 ± 0.1	61 ± 1	26.7 ± 0.1	48.0 ± 0.3
AN	0.02 ± 0.01	0.07 ± 0.01	0.07 ± 0.01	0.22 ± 0.02	0.28 ± 0.04	0.17 ± 0.01	0.03 ± 0.01	0.09 ± 0.01
EC	82.3 ± 0.1	102.3 ± 0.1	97.5 ± 0.1	136.0 ± 0.5	77.4 ± 0.1	107.6 ± 0.1	46.0 ± 0.1	80.0 ± 0.4
As	0.19	0.13	0.14	0.05	0.01	0.03	0.21	0.09
Mn	0.23	0.51	1.12*	1.32*	1.28*	0.20	1.07*	1.70*
Fe	0.01	0.07	0.31	0.34	0.19	0.11	1.44*	0.86
MI	0.43	0.71	1.57*	1.71*	1.49*	0.33	2.71*	2.65*

Electrical conductivity in µs/cm, pH (No unit), other physico-chemical parameters in mg/L
Concentration of TSS < 5 mg/L considered as limit of detection.

Conclusion

This work revealed the spatial variations in quality parameters between lakes and ex-mining ponds in Malacca. The results demonstrated that the water quality of surface water could not be judged based solely on the historical identity of the sites because the impacts of geochemistry and current land-use are more crucial. The outcomes of multivariate analyses suggested the major variations in water quality are mainly originated from the dissolution of underlying rocks and current anthropogenic inputs such as agricultural and recreational activities instead of ex-mining. Since a relatively low contribution of As, the overall metal index suggested that those sources could be considered as the potential reservoirs for potable supply after conventional treatment processes.

Acknowledgement

The authors acknowledge the financial support of University of Malaya [PG147- 2014B].

References

1. Al-Ansari, N., Adamo, N., Sissakian, V., Knutsson S., Laue, J., 2018. Water Resources of the Tigris River Catchment: Water Resources of the Tigris River Catchment. *J. Earth Sci. Geotech. Eng.* 8, 21-42.
2. Azzlan, A. F., Cheong, C. B., Lau, K. L., 2016. Sustainable water management for water supply efficiency: A case study at Syarikat Air Melaka Berhad. *J. Tech. Manag. Bus.* 3, 01-21.
3. DOE. 2012. Department of Environment Malaysia: Environmental Quality Act report, Ministry of Science, Technology and the Environment, Putrajaya, Malaysia.
4. MWA. 2008. Malaysian Water Association.

SIZE-CONTROLLED SYNTHESIS OF CARBON DOTS COMBINED WITH $Ni(OH)_2$ FOR SUPERCAPACITOR APPLICATION

A. Tibodee[1], T. Thaweechai[2], W. Sirisaksoontorn[1*]

[1]Department of Chemistry and Centre of Excellence for Innovation in Chemistry, Faculty of Science, Kasetsart University, Chatuchak, Bangkok 10900 Thailand
[2]Knowledge of the Land for Sustainable Development, School of Integrated Science, Kasetsart University, Chatuchak, Bangkok 10900 Thailand

*Corresponding author: fsciwks@ku.ac.th

Abstract
The composites of $Ni(OH)_2$/CDs were prepared via a hydrothermal method. The as-prepared products were thoroughly analyzed through physical and electrochemical characterizations. The electrostatic forces between CDs and $Ni(OH)_2$ help facilitate the self-assembly of $Ni(OH)_2$/CD composites. The $Ni(OH)_2$/CD composite with a smaller size of CD provided the better electrochemical performance compared to $Ni(OH)_2$ and $Ni(OH)_2$/CD with a larger size of CD. The $Ni(OH)_2$/CD20 exhibits high specific supercapacitance of 1487 F g^{-1} at a current density of 2 A g^{-1} in 2 M KOH electrolyte.

Keywords: Carbon dots, $Ni(OH)_2$ nanoflower, Supercapacitor

Introduction
Carbon dots (CDs), as a zero-dimensional (0D) carbon nanomaterial, consist of nanometer-scaled graphene particles. CDs have tremendous interest owing to their electronic properties, quantum confinement and edge effects. CDs have emerged as promising materials for supercapacitors, batteries, optoelectronics and biomedical field. $Ni(OH)_2$ is one of the most promising electrode materials for supercapacitor applications due to its low cost, well-defined electrochemical redox behavior, and high theoretical specific capacitance. Nevertheless, its electrochemical performance is limited by low electrical conductivity, low rate capability and poor cycling stability. From the previous work, $Ni(OH)_2$ combined with several types of carbonaceous materials has been reported (Wang et al. 2016). To date, although several $Ni(OH)_2$/carbon-based composites were studied with the enhanced electrochemical performance, few attempts have been made to use CDs with the variation in the particle sizes for the assembly of $Ni(OH)_2$ composites. Herein, $Ni(OH)_2$/CD composites were prepared by using a hydrothermal method and their electrochemical properties were systematically investigated. CDs with the variation of particle sizes were synthesized by a pyrolysis approach.

Methodology
0.2488 g of $Ni(CH_3COO)_2{\cdot}4H_2O$ and 0.24 g of urea were dissolved in aqueous solution and mixed with 0.030 g of CDs prepared by controlling the carbonization with different reaction time. The samples were denoted as $Ni(OH)_2$/CDX; where x represents reaction time used to synthesize CDs. Then, the solution was continuously stirred to form a homogeneous solution. After that, the mixture was transferred into a Teflon-lined stainless steel autoclave and maintained at 150°C for 6 h. The autoclave was cooled to room temperature. The precipitates were collected and washed with distilled water and ethanol for several times. The final product was dried in a vacuum oven at 60°C. The $Ni(OH)_2$ was synthesized by following a similar procedure except no addition of CDs in the mixture. The electrochemical performance of all samples was evaluated by using a conventional three-electrode system.

Results and Discussion

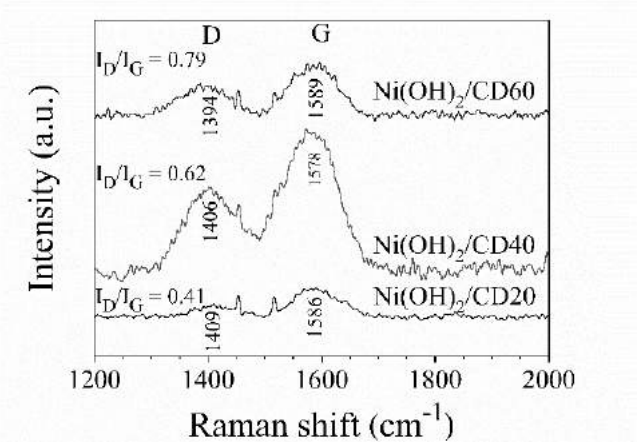

Figure 1 Raman spectra of $Ni(OH)_2$/CD20, $Ni(OH)_2$/CD40 and $Ni(OH)_2$/CD60.

In Figure 1, Raman spectra of $Ni(OH)_2$/CD20, $Ni(OH)_2$/CD40 and $Ni(OH)_2$/CD60 show two broad peaks assigned to D-band and G-band, respectively. The integrated intensity ratio of the D and G bands (I_D/I_G) of $Ni(OH)_2$/CD20 composite was found to be 0.41. The I_D/I_G ratio gets increased to 0.62 and 0.79 for $Ni(OH)_2$/CD40 and $Ni(OH)_2$/CD60, respectively. The increase in I_D/I_G is due to the presence of lattice distortion (sp^3/sp^2 ratio) and surface functionalities of oxygen functional groups. These results suggest that the degree of structural disorder relies on reaction time of CD carbonization.

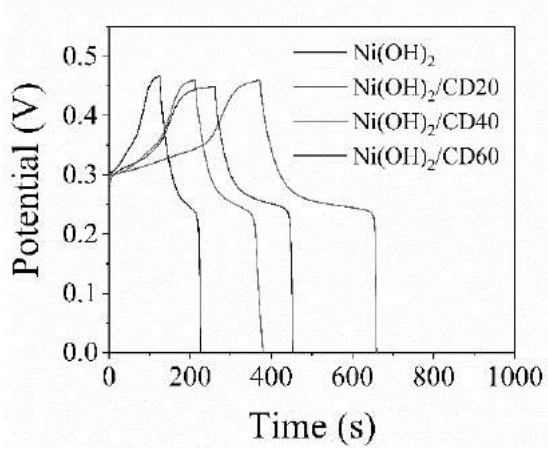

Figure 2 Galvanostatic charge-discharge curves of $Ni(OH)_2$, $Ni(OH)_2$/CD20, $Ni(OH)_2$/CD40 and $Ni(OH)_2$/CD60 composites at 2 A g^{-1}.

Figure 2 presents the charge-discharge curves for the $Ni(OH)_2$, $Ni(OH)_2$/CD20, $Ni(OH)_2$/CD40, and $Ni(OH)_2$/CD60. The discharge time observed in $Ni(OH)_2$/CD20, $Ni(OH)_2$/CD40 and $Ni(OH)_2$/CD60 composites is longer than that of $Ni(OH)_2$, suggesting the a higher specific capacitance of 1487 F g^{-1} for $Ni(OH)_2$/CD20, 1044 F g^{-1} for $Ni(OH)_2$/CD40, and 818 F g^{-1} for $Ni(OH)_2$/CD60 at 2 A g^{-1} (versus 512 F g^{-1} for $Ni(OH)_2$). Moreover, $Ni(OH)_2$/CD60 with a larger CD size provides lower specific capacitance compared to $Ni(OH)_2$/CD40 and $Ni(OH)_2$/CD20 that contain smaller average CD size. This

might be due to the absence of long-range ordering of $Ni(OH)_2$ and more structural disorder of a larger CD size, leading to the lower conductivity.

Conclusion

In conclusion, we successfully synthesized $Ni(OH)_2$/CD composites via a hydrothermal method. The $Ni(OH)_2$/CD composite with a small particle size of CD exhibits the greater specific capacitance of 1487 F g^{-1} at a current density of 2 A g^{-1}.

Acknowledgement

This research was financially supported by the Graduate School and Kasetsart University Research and Development Institute (KURDI) for financial support.

Reference

Wang, R., Jayakumar, A., Xu, C., Lee, J.M., 2016. $Ni(OH)_2$ nanoflowers/graphene hydrogels: A new assembly for supercapacitors. *ACS Sustainable Chem. Eng*. 4, 3736-3742.

NOVEL CORE-EXPANDED PERYLENE DIIMIDE DYE: SYNTHESIS, CHARACTERIZATION AND OPTICAL PROPERTIES

Adamu A. Usman D. Basma B. I. A and Huriye I.

Department of Chemistry, Faculty of Science, Eastern Mediterranean University
Gazimağusa, North Cyprus.

*Corresponding author: bbg2015@yahoo.com

ABSTRACT

Perylene molecules bearing two aryloxy substituents on bay position (1,7 positions) and two receptor units at the imide positions are most useful fluorescent building blocks for the realization of a broad variety of self-assembly architectures. High absorption of perylene diimides (PDIs) in the visible region offers many advantages for photonic applications, optimum electron transport properties, flexible synthetic potentials to adjust energy levels, solubility, stacking properties, excellent thermal and photo-stability.

In this study, a novel perylene diimide with tyramine substitution at the bay (1,7-position) and imide position was designed and synthesized successfully. The synthesized product was characterized by FTIR, UV-vis, emission, TGA, DSC techniques and elemental analysis. The photophysical and thermal properties of Ty-B-PDI reveal that it as a good candidate for photovoltaic applications.

Keywords: Perylene diimides, Tyramine, electron transport, Self-assembly.

Introduction

Perylene dyes and pigments have emerged as an important class of Rylene dyes with diverse scientific research field, starting from organic electronics [1], to solar cell research [2]. The great performance pigments called Perylene dyes, was formed from N,N-disubstituted Perylene diimides (PDIs) or Perylene-3,4,9,10-tetracarboxylic dianhydride (PDA) [3].The planar π-system of (PDA) have a rigid structure that has inherently low solubility, due to its strong π-π interaction, [4].

However poor solubility in perylene promotes difficulty during purification, synthesis, and Spectroscopy analysis, and also decreases Φ_f by the feasible aggregation from solution. Notably, the basic interest is to get readily synthesized perylene dyes together with great fluorescent quantum yields. Usually, the broad Absorption in the visible region couple with high fluorescence quantum yield, excellent photochemical stability along with various fascinating chemical and physical properties of the Perylene diimide played an essential role in an industrial pigment [5].

Certainly, one of the practical techniques used to generate soluble PDI is the halogenation of bay substituents, this idea results in the distortion on planarity of its structure that is π-π self-aggregation [6]. However, it is clear that bay functionalization ways are important for controlling the physical and chemical structures of PDI dyes. Recently, much attention have been focus on 1,7-dibromoperylene tetra carboxylic diimide intermediate, as the best method for the preparation of bay functionalized PDI because of its easy swap of bromo substituent on the bay region with different nucleophiles. This novel strategy report the synthesis of new class of PDI derivative, Ty-B-PDI, with excellent optical and thermal properties that will emerge as a good candidate for photovoltaic applications.

Methodology

A novel class of perylene derivative Ty-B-PDI was synthesized according to the published method [7]. with slight modificaiton via two steps, Bay and imide substitutions. The brominated perylene tetracarboxylic dianhydride was directly converted to an intermediate product via condensation with 4-(2-aminoethyl) phenol at 150 °C for 24 hrs. The reaction was further continuous for 4 hrs at 120 ^{0}C, for 3 hrs at 150 ^{0}C, for 2hrs at 180 ^{0}C and for 1 hr at 200 ^{0}C under argon atmosphere.

Results and Discussion

The improved solubility of PDI derivatives have originated from the bulky substituent on core area and imide position of perylene chromophore. However, the presence of tyramine also known as 4-(2-aminoethyl) phenol on the synthesized product have shown a good solubility in dipolar aprotic solvents and also little or partially soluble in polar protic solvents as in (Table 1.1). The partial solubility of the product in polar protic solvents could be due to the presence of hydrogen bonding.

Table1.1:The solubility properties of Ty-B-PD1 in different solvents

Solvents	Solubility	Color
DMF	(+ +)	Red
NMP	(+ +)	Red
DMSO	(– +)	Red
m-CRESOL	(– +)	Red
TFA	(– +)*	Pale red
ACETONE	(– +)*	Pale orange
DCM	(– –)	Colorless
TCE	(– –)	Colorless
CCl_4	(– –)	Colorless

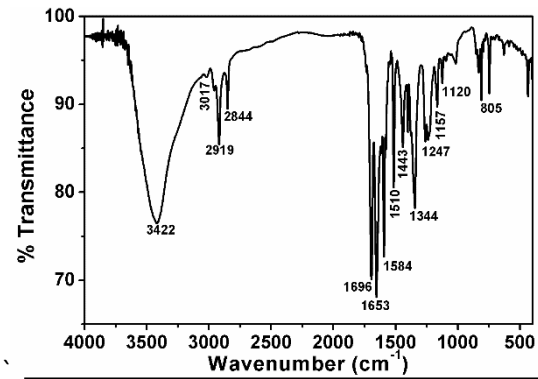

Fig.1.1 FTIR spectrum of Ty-B-PDI

The IR Spectrum of Ty-B-PDI in Fig. 1.1 , has shown the characteristic bands at 3422cm^{-1} (O-H and N-H stretch); 3017 cm^{-1} (Ar C-H stretch); 2919cm^{-1} and 2844 cm^{-1} (aliphatic C-H stretch); 1696 cm^{-1} and 1653cm^{-1} (imide C=O); 1584cm^{-1} and 1510cm^{-1} (C=C stretch); 1344cm^{-1} (C-N stretch); 1157cm^{-1} (C-O stretch) and 805cm^{-1} (C-H bend), confirmed the structure of Ty-B-PDI.

Following the IR spectrum of Br-PDA the characteristic bands of the anhydride C=O stretch (1762 cm^{-1}) had vanished and were substituted by imide C=O stretch (1696 and 1653 cm^{-1}). Similarly, the characteristic band of the C–O–C stretching (1024 cm^{-1}) had disappeared and was replaced by C–N stretch (1344cm^{-1}).

The absorption spectra of the compound in various solvent were presented in fig. 1.2A. indicate the absorption spectrum of Ty-B-PDI in dipolar aprotic solvent DMF with the characteristic bands at 525, 490 and 460 nm, respectively. The UV spectrum of Ty-B-PDI in NMP shows three characteristic peaks at 527, 490 and 460 nm with a shoulder peak at 430 nm after microfiltration. The UV spectrum of Ty-B-PDI in TFA shows the traditional characteristic absorption bands at 535, 497, and 462 nm, with a shoulder peak of 426nm respectively. .

The emission spectra of all Ty-B-PDI were taken at λ_{exc}= 485 nm excitation wavelength as presented in Fig.1.2B. The characteristics emission bands of Ty-B-PDI in different solvents are observed at 541 and 547 nm for DMF, 545 and 578 nm for NMP and 554 nm, 589 nm for TFA. The red shift in polar aprotic indicate the better solvation of the excited state than the polar ground state of Ty-B-PDI. Fluorescence quantum yields (Φ_f) of the compound are measured in different solvents and were presented in Table 4.2. Essentially, the Ty-B-PDI has displayed low fluorescence quantum yield (Φ_f) in NMP.
Thermal properties of Ty-B-PDI were investigated by DSC (differential scanning calorimetry) at 10 k mn^{-1} and TGA (thermogravimetry) at 5 k mn^{-1}. Ty-B-PDI compound did not show any glass transition temperature in DSC run. The TGA curve displayed high starting decomposition temperature $T_{d,}$ which proved thermal stability property of the compound.

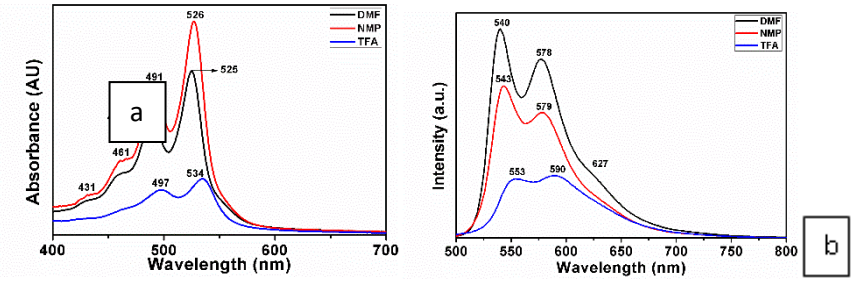

Figure1.2:(a)Absorption spectra of Ty-B-PDI in DMF, NMP and TFA (b) Emission spectra of Ty-B-PDI in DMF, NMP and TFA

The compound was also stable at 450 ^{0}C. Ty-B-PDI experienced a rapid weight loss of 10 % occurred at 450 ^{0}C and 530 ^{0}C. When Ty-B-PDI compound was heated up to 800 ^{0}C, 98 % of initial weight were lost and 2 % char yield was observed.

CONCLUSION

Perylene dyes have been favorably synthesized from reactants involving 1,7-dibromoperylene-3,4,9,10-tetracaboxylic dianhydride (Br-PDA) and 4-(2-aminoethyl)phenol. The structure and the properties of the Ty-B-PDI compound have been well investigated and characterized by FTIR, UV-vis, DSC, TGA, and elemental analysis.
The compound showed a good solubility in polar aprotic solvent and partial solubility in polar protic solvents. However, the compound was not soluble in non –polar solvents. Ty-B-PDI achieved high thermal stability at >450 ^{0}C where it is possible to use it in some devices as temperature and heat resistant compound.
The compound recorded high absorption ability in DMF and NMP; hence the high absorptivity of a chromophore is an attractive property toward photovoltaic materials.

The emission spectra of the core substituted Perylene diimide in various solvents before and after microfiltration were also reported. All the emission spectra show two emission peaks of 0 and 0 transitions of perylene chromophore which where mirror images of Absorption spectra. Fluorescence quantum yield value of Ty-B-PDI is low in NMP and DMF. On balance, the analysis results obtained from the research could bring about further development in photovoltaic applications.

References

[1] Haung, C., Barlow, S., & Marder, S. R. (2011) Perylene-3,4,9,10-tetracarboxylic acid diimides synthesis, physical properties, and use in Organic Electronics. *Journal of Organic Chemistry*, 76, 2386-2407.

[2] Li, C., & Wonneberger, H. (2012). Perylene imides for Organic Photovoltaics Yesterday, Today, and Tomorrow. *Advanced Materials*, 24, 613-636.

[3] Greene, M., Faulkner, E. B., Schwartz, R., & Eds. J. (2009). Wiley-VCH: Weinheim. *High Performance Pigments.* John Wiley & Sons.

[4] Faulted, E. B. (2009). Wiley-VCH Weinhein. *High Performance Pigments.*

[5] Lv, A., Puniredd, S. R., Zhang, J., Li, Z., Zhu, H., Jiang, W., Dong, H., He, Y., jiang, L., & Li, Y. (2012). High mobility, air Stable, Organic Single Crystal Transistors of an n-type diperylene bisimide. *Advance material,* 24, 2626-2630.

[6] Wurhner, F. (2006). bay-substituted perylene bisimides Twisted fluorophores for supramolecular chemistry. *Pure Applied Chemistry*, 78, 2341- 2349.

[7] Würthner, F., Stepanenko, V., Chen, Z. J., Saha-Moller, C. R., Kocher, N., & Stake, D. J. (2004). Preparation and characterization of regioisiomerically pure 1,7-disubstituted Perylene bisimide dyes*. Journal of Organic Chemistry*, 69, 7933-7936.

ELUCIDATING THE METABOLITE PROFILE OF *Isochrysis galbana*

Intan Safinar Ismail [1,2]*, M. Safwan Ahamad Bustamam[1], Khozirah Shaari [1,2], Chong Chou Min [1]

[1]Institute of Bioscience, Universiti Putra Malaysia, [2]Department of Chemistry, Faculty of Science, Universiti Putra Malaysia, Selangor

*Corresponding author: safinar@upm.edu.my

Abstract
The present study was designed with the aim to profile the metabolites of an indigenous algae species, *Isochrysis galbana* (IG). The comprehensive identification of IG in different polarity of solvents extraction was established using proton Nuclear Magnetic Resonance (^{1}HNMR) spectroscopy and Liquid Chromatography-Mass spectrometry (LC-MS). The Principal Component Analysis (PCA) of IG extracts in different solvents of aqueous (Aq), 50% ethanol (AqE), absolute ethanol (EtOH), ethyl acetate (EtOAc) and hexane (Hex), indicated that EtOAc and hexane gave a more comprehensive range of metabolites and in higher concentrations of the major components. There were 22 metabolites including carotenoids, polyunsaturated fatty acids, and amino acids tentatively identified by ^{1}HNMR. Eighteen metabolites were successfully annotated by LC-MS in which some of these metabolites namely palmitic acid, oleic acid, *α*-linolenic acid, DHA, DPA, fucoxanthin, astaxanthin and chlorophyll were similar to those identified in NMR.

Keywords: *Isochrysis galbana*, NMR, LCMS, profiling

Introduction
Isochrysis galbana (IG) is a golden-brown flagellate marine microalga (Grima et al., 1994) which is rich in polyunsaturated fatty acids (PUFA) such as docosahexaenoic acid (DHA) and eicosapentaenoic acid (EPA) (Cho et al., 1999). Due to its nutritional value, it is proposed as live feed for aquaculture health (Meireles et al., 2003) and as supplement for human health benefits. Previously, some works have been done on the profiling of IG focusing on carotenoids (Ahmed et al., 2014), lipids and fatty acids (Batista et al., 2013), and recently Aguilera-Sáez et al. (2019) has profiled much on amino acids, lipids and sterols using ^{1}HNMR-based metabolomics. However, to our best knowledge, there is no reported study on the holistic metabolite of IG in different polarity of solvent extracts profiled by ^{1}HNMR in complementary with LC-MS analysis. Both of these analytical platforms were adopted in this study to cover as much metabolite identification as possible.

Methodology

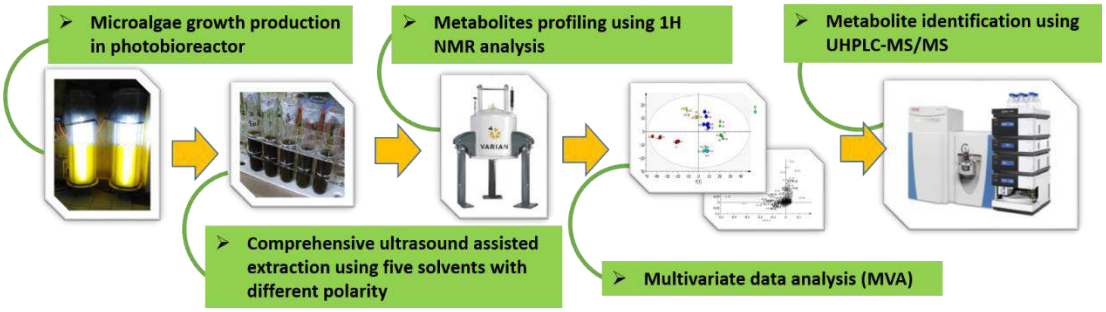

Results and Discussion

A total of 22 tentative metabolites from different chemical classes were successfully identified based on their chemical shifts assignment, corresponding multiplicities and further confirmation with 2D-HMBC data. Amino acids were identified in the upfield region of the spectrum with some were reportedly found in microalgae *Pleurochrysis carterae* under the same phylum Haptophyta (Chengxu et al., 2016). Two saturated fatty acids and 6 unsaturated fatty acids including PUFAs presented in all solvent extracts except for aqueous. Several assigned fatty acids were in agreement with FAME profile of IG ethanol extracts determined by GCMS analysis (Maadane et al., 2015). In the middle region between 3.5 and 5.5 ppm, some carbohydrates were discovered even though the assignment of the metabolites was challenging due to the congestion of signals. The spectral downfield region from 6.0 ppm indicated the presence of carotenoids and chlorophylls which mainly observed in hexane and ethyl acetate extracts. Principal Component Analysis (PCA) was used to identify and compare the metabolites in the different solvent extracts of IG whereby Aq, AqE, and EtOH extracts were discriminated from Hex and EtOAc by principal component (PC) 1. The discrimination suggests the different metabolites content between these two big groups. The metabolites prominent in Hex and EtOAc extracts are carotenoids and fatty acids, meanwhile some primary metabolites and amino acids are higher in AqE, EtOH and Aq extracts. The identification of these discriminants was supported by UHPLC-MS/MS with proposed fragmentation patterns.

Conclusion

The extraction of IG in 5 different solvents polarity has successfully led to the identification of metabolites from different classes of compounds. The results of PCA, HCA and statistical analyses unambiguously established ethyl acetate as the best solvent for extraction of IG due to its larger number and higher concentration of compounds obtained. The identification of the important metabolites in ethyl acetate extract was further confirmed by UHPLC-MS/MS analysis whereby 8 secondary metabolites namely palmitic acid, oleic acid, α-linolenic acid, DHA, DPA, fucoxanthin, astaxanthin, and chlorophyll were identified in both instrumental platforms.

Acknowledgement

This study was financially supported by Japan Science and Technology Agency (JST)/Japan International Cooperation Agency (JICA) in partnership with Ministry of Higher Education Malaysia (MOHE) through joint research program Science and Technology Research Partnership for Sustainable Development (SATREPS).

References

1. Ahmed, F., Fanning, K., Netzel, M., Turner, W., Li, Y., & Schenk, P. M. (2014). Profiling of carotenoids and antioxidant capacity of microalgae from subtropical coastal and brackish waters. *Food Chemistry*, *165*, 300–306.
2. Aguilera-Sáez, L. M., Abreu, A. C., Camacho-Rodríguez, J., González-López, C. V., Del Carmen Cerón-García, M., & Fernández, I. (2019). NMR Metabolomics as an Effective Tool to Unravel the Effect of Light Intensity and Temperature on the Composition of the Marine Microalgae Isochrysis galbana. *Journal of Agricultural and Food Chemistry*, *67*(14), 3879–3889.
3. Batista, A. P., Gouveia, L., Bandarra, N. M., Franco, J. M., & Raymundo, A. (2013). Comparison of microalgal biomass pro files as novel functional ingredient for food products. *Algal Research*, *2*(2), 164–173.

4. Chengxu, Z., Jie, L., Yangfang, Y., Xiaojun, Y., Baoning, L., & Xin, W. (2016). The metabolite profi ling of coastal coccolithophorid species Pleurochrysis carterae (Haptophyta). *Chinese Journal of Oceanology and Limnology*, *34*(4), 749–756
5. Cho, J., HJ, J., HJ, L., JNC, W., & Yk, H. (1999). Growth activation of the microalga Isochrysis galbana by the aqueous extract of the seaweed Monostroma nitidum. Journal of Applied Phycology, 10, 561–567.
6. Grima, E. M., Perez, J. A. U., Camacho, F. G., Fernbndez, F. G. A., Alonso, D. L., & Castillo, C. I. S. (1994). Preservation of the marine microalga ,Isochrysis galbana : influence on the fatty acid profile. 123, 377–385.
7. Maadane, A., Merghoub, N., Ainane, T., El Arroussi, H., Benhima, R., Amzazi, S., Wahby, I. (2015). Antioxidant activity of some Moroccan marine microalgae: Pufa profiles, carotenoids and phenolic content. *Journal of Biotechnology*, *215*, 13–19
8. Meireles, L.A., Guedes, A.C., Malcata, F. X. (2003). Lipid class composition of the microalga Pavlova lutheri: eicosapentaenoic and docosahexaenoic acids. Journal of Agricultural and Food Chemistry 51 (8), 2237–2241, 51(10), 2237–2241.

MECHANOCHEMICAL SYNTHESIS, CHARACTERIZATION AND ANTIPATHOGENIC STUDY OF 4,4′-BIPYRIDINE LEAD (II) COMPLEXES

H. Usman[1], S. A Garba[2]* and S. G. Yammama[1]

[1]Department of Chemistry, Isa Kaita College of Education, PMB 5007, Dutsin-ma Katsina State
[2]Chemistry Department, Sule Lamido University. Kafin Hausa
Jigawa State. Nigeria

*Correspondence author: saghadejia@gmail.com

Abstract
The polymeric complexes of some M^{2+} transition metals with 4,4′-bipyridinium chloride were synthesized by mechanochemical synthetic method. The M^{2+} salts and 4,4′-bipyridinium chloride were pounded using a pestle and mortar. The complexes obtained were characterized by decomposition temperature determination, conductivity measurement and solubility test, elemental analysis and infrared spectral studies. The molar conductivity value ranges from 49.7-56.0 $\Omega^{-1}cm^2\ mol^{-1}$, indicating non-electrolytic nature of the complexes. The decomposition temperature of the complexes ranges from 186–192^oC which shows that the complexes are very stable. The elemental analytical data and infrared values indicated that the complexation has taken place. The complexes were effective against some selected bacteria and fungi (*escherichia coli*, *pseudomonas aeruginosa*, *streptococcus pneumonae*, *staphylococcus aureus*, *klebsiella specie* and *penicillium specie*, *meterhizium specie*, *aspergilus species*) at 1000µg/disk highest concentration, toxicity test on complexes should be performed.

Keywords: 4,4'-bipyridinium chloride, M^{2+} Salt, Molar Conductivity, Polymeric complexes,

Introduction
Mechanosynthesis, i.e. the use of mechanical energy to cause chemical reactions between solids, can be a way to address the problem (Do, 2016; Howard et al., 2014). This type of protocol can be a valid instrument for preparing ligands and for synthesizing the respective metal complexes (Ferguson et al., 2014; Adams et al., 2017). The apparent benefits of using such a strategy are the comparatively big amount of starting materials that can be used, the shorter response times, and the decrease of side reactions (Howard et al., 2014; Jame et al., 2012). Dehydrochlorination of crystalline metal chloride salts of pyridinium derivatives by mechanochemical means such as grinding with bases such as KOH or K_2CO_3 has been used to produce metal-pyridine complexes in the solid state. The reactions proceed at room temperature with and without the use of bulk solvent (Adams *et al.*, 2007). Recently a range of room temperature, solid-state methods for the preparation of crystalline metal complexes [4,4'-H_2bipy][MCl_4] and [MCl_2(4,4'-bipy)] (M = Co, Zn or Pt) in which the transformations between phases are achieved by mechanochemical and solid-gas reactions without the use of solvents (Adams *et al.*, 2007).

Methodology
Preparation of the Ligand:
4.0g of 4,4'-bipy was placed in a 50ml beaker, the beaker and its contents were inserted in a 500ml beaker containing 100ml concentrated hydrochloric acid in an upright position, the 500ml beaker was then covered and allowed the spurt HCl gas to enter the 50ml beaker directly. This set-up was allowed to stand for 6hrs to yield [(4,4′-H_2bipy)]Cl_2. This product was confirmed by Infrared spectrum and Elemental analytical data (Kurawa and Yammama, 2014)

Synthesis of [{$PbCl_2$(4,4′-bipy)}$_n$]

0.229g (1mole) of [4,4′-H_2Bipy]Cl_2 and 0.379 mg (1mole) of [$Pb(CH_3COO)_2$].3H_2O were ground in an agate mortar for minutes, the mixture turned milky and released of strong odour of acetic acid was observed. The complex was then dried in vacuo (Kurawa and Yammama, 2014).

Synthesis of [{Pb(4,4′-bipy)}$_n$]

0.04g (0.1mole) of [{$PbCl_2$(4,4′-bipy)}$_n$] and 0.014g (0.1mole) of K_2CO_3 were ground together in an agate mortar for minutes, the milky mixture turned tan powder. Excess water was then removed *in vacuo* (Kurawa and Yammama, 2014).

Results and Discussion

The complexes obtained were characterized by decomposition temperature determination, conductivity measurement and solubility test, elemental analysis and infrared spectral studies.

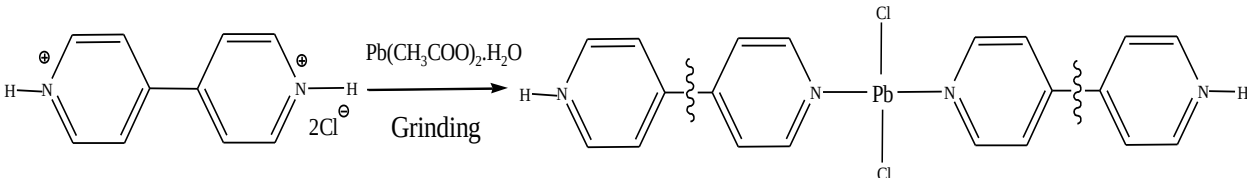

Equation 1: Formation of [{$PbCl_2$(4,4′-bipy)}$_n$]

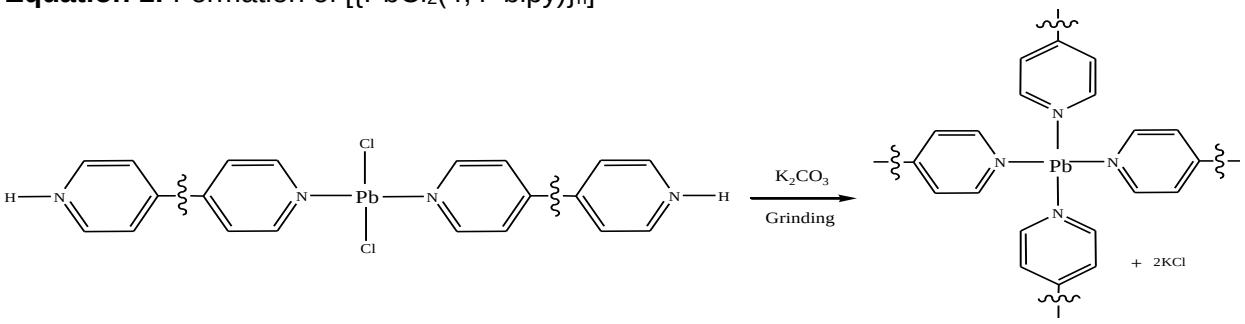

Equation 2: Formation of [Pb(4,4′-bipy)$_n$]

Table 1: Anti-Bacterial Activity Inhibition Zones

Complexes	Concentrations (µg/disk)	*E. coli* (mm)	*Ps*. (mm)	*Strep*. (mm)	*Staph*. (mm)	*Kleb*. (mm)
[{$PbCl_2$(4,4′-bipy)}$_n$]	50	6	6	6	6	6
	500	6	6	6	6	6
	1000	14	14	6	13	18
[Pb(4,4′-bipy)$_n$]	50	6	6	6	13	6
	500	13	6	14	18	6
	1000	18	6	17	21	6
CONTROL (Gentemecyn)	10	45	31	38	37	46

Table 2: Anti-fungal Activity Inhibition Zones

Complexes	Concentrations (µg/disk)	*Pen* (mm)	*Met* (mm)	*Asp* (mm)
	50	6	6	6
	500	6	6	6
[{$PbCl_2$(4,4′-bipy)}n]	1000	6	6	6
	50	6	6	6
	500	6	6	6
[Pb(4,4′-bipy)n]	1000	6	6	6
CONTROL (Apron plus)	10	38	28	20

References

1. Adams C. J., Kurawa M. A. and Orpen G. A (2010): Coordination Chemistry in the Solid State: Synthesis and Interconversion of Pyrazolium Salts Complexes and Pyrazolate MOFs. *Dalton Trans*, 39. 6974-6984.
2. Kurawa M. A. (2008): Solid State Synthesis of Metal Salts and Coordination Compounds. PhD. Thesis. School of Chemistry, University of Bristol. Pp 006.

WELDING POWER EFFECT IN LASER WELDING OF CARBON STEEL

M. K. Umar[1*], H. Lijia[2]

[1]Department of Chemistry, Bauchi State University, Gadau, Nigeria,
[2]School of Materials Science and Engineering, Liaoning University of Technology, China.

*Corresponding author: mkalfuldi@yahoo.com

Abstract
The present study is concerned with the effects of welding power in laser welding of carbon steel using IPG YLS-3000W Fiber Laser with Robot. The effects of welding power (1500W-2500W) on weld width, penetration depth, microstructure, and microhardness were investigated. After laser welding of the sample, the welded sample was cut for grinding and scanning. The grinding was done using 180#, 240#, 320#, 400#, 500# and 600# grits of sandpaper. Al_2O_3 polishing solution was used to polish the sample, 4% nitric acid solution was used in etching the sample, and then finally dried. The microstructure of the welded sample was observed under metallographic microscope. The results showed that both weld bead width and penetration depth increase with increase in laser power.

Keywords: Microstructure, Power, Speed, Welding

Introduction
Laser welding provides important benefits over the conventional welding processes. The advantages of laser welding e.g. deep and narrow welds with high speed and low heat input are accompanied by some disadvantages including the necessary precise preparation of the edges of the parts to be joined and the precise clamping of the work pieces. Due to the medium-high carbon content of carbon Steel, it can be welded by the conventional welding processes with some precautions.

Methodology
The laser welding machine used for this experiment is IPG YLS-3000W Fiber Laser with Robot. At an incident laser power density of 3.06x104W/cm^2, welding speed of 0.01m/s, laser powers were set for 1500W, 1750W, 2000W, 2220W and 2500W, and argon used as the shielding gas. The experimental procedure was done as described by Benyounis et.al 2005, Jassim et.a 2004l, and Young-Tae et.al. 2014.

Results and Discussion

Table 1. The Weld Width and Depth under Different Power

Power (W)	Width W (mm)	Depth H (mm)	Depth-Width Ratio (D/W)
1500	2.00	2.76	1.38
1750	2.70	2.86	1.10
2000	3.10	3.70	1.19
2250	3.22	4.82	1.49
2500	3.48	4.92	1.41

Table 1 shows the weld width and depth under different welding power. At welding power of 2250W, the weld depth-width ratio reaches a maximum of 1.49, when the welding power

is 2500W, the weld penetration increases because the welding power is too large and caused weld defects, called burn through, which causes deeper penetration of the weld. Figure 2 shows the weld microstructure for laser powers 1500W, 1750W, 2000W, 2250W and 2500W. It can be observed that the microstructure has many small grains, with the increase in laser power, the lath ferrite increases and martensite decreases and becomes rough.

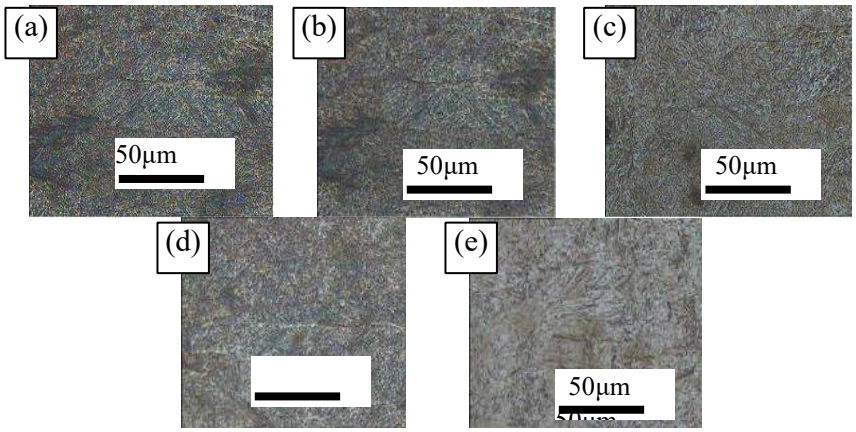

(a) P=1500W (b) P=1750W (c) P=2000W(d) P=2250W(e) P=2500W

Figure 2. Weld Microstructure under Different Laser Power

Conclusion

Based on the conducted research to obtain a better understanding of the effects of laser power on the weld seam, microstructure and microhardness profile the following conclusions were drawn:

1. Increase in laser power, increases the weld bead width and penetration depth.
2. As observed from the weld microstructure, with the increase in laser power, the lath ferrite increases and martensite decreases and becomes rough.

Acknowledgement

The authors are grateful to Liaoning University of Technology for the provision of laboratory facilities, and the support from The Innovation Talents Program of University of Liaoning Province(LR2016072) and Liaoning Research Foundation (20170540432).

References

B.S.Yilbas, A.F.M Arif and Abdul Aleem, 2010. Laser Welding Of Low Carbon Steel And Thermal Stress Analysis. Optics And Laser Technology. 42, 760-765.

Baiju Sasidharan, Dr.K.P.Narayanan, and Aneesh K.N, 2013. A Comparative Study Of Tensile And Microstructural Characteristics Of Friction Welded Joints And Conventionally Welded Joints Of Aluminium Alloy 6061. International Journal of Innovative Research in Science, Engineering and Technology. 2, 557-564.

H. W. Ebert and F. J. Winsor, 1980. Carbon Steel Submerged Arc WeldsTensile Strength vs. Corrosion Resistance. Welding Research Supplement. 193-198.

Jassim M. Salman and Khalid Mutashar Abed, 2014. Laser Welding for Dissimilar Metals Stainless Steel AISI 304H to Low Carbon Steel DIN St33, by Nd: YAG Laser. International Journal of Current Engineering and Technology. 4(5), 3489-3497.

Young-Tae Yoo et al., 2004. Welding characteristics of S45C medium carbon steel in laser welding processing using a high power CW Nd:YAG laser. Journal of Materials Science 39(19), 6117-6119.

K. Y. Benyounis, A. G. Olabi and M. S. J. Hashmi, 2005. Optimising the laser-welded butt-joints of medium carbon steel using RSM. Journal of Materials Processing Technology. 164, 986-989.

MORPHOLOGY AND ELECTROCHEMICAL CAPACITANCE OF TITANIA NANOTUBES GROWN BY VARIATION OF ANODIZATION VOLTAGE AND TIME FROM GLYCEROL BATH

M. M. Muzakir [1,3], Z. Zainal [1,2] *, H. N. Lim [1,2] and A. H. Abdullah [1,2]

[1]Department of Chemistry, Faculty of Science, Universiti Putra Malaysia, 43400 Serdang, Selangor, Malaysia.
[2]Materials Synthesis and Characterization Laboratory, Institute of Advanced Technology, Universiti Putra Malaysia, 43400 Serdang, Selangor, Malaysia
[3]Department of Chemistry, Faculty of Science, Gombe State University, PMB 127, Gombe, Nigeria.

Corresponding author: zulkar@upm.edu.my

Abstract
We report the synthesis of self-organised titania nanotubes by simple, facile and single step potentiostatic anodization in glycerol containing NH_4F (0.5 wt.%) and 25 v/v % water content. Effect of variation of anodization voltage and time on the morphology and capacitive performance of the synthesised samples were investigated. FESEM and XRD were used to study the morphology and crystallinity of the synthesised samples. It was found that the tube diameter and tubes separation are greatly influenced by the voltage and the tube lengths are affected by the anodization time. Capacitive behaviour of the samples was evaluated using cyclic voltammetry (CV) and galvanostatic charge discharge (GCD). Sample synthesised at voltage of 30 V and anodization time of 60 min have 86 nm, 1.4 µm tube diameter and length respectively and showed high specific capacitance of 330 µF cm^{-2} at current density of 20 µAcm^{-2}.

Keywords: Anodization, titania nanotubes, glycerol, electrochemical capacitance.

Introduction
Among the various methods reported for the synthesis of titania nanotubes, the electrochemical anodization method has been the most promising method as its offers suitably back-connected nanotubes on the titanium foil substrate which can be used directly as a binder-free supercapacitor electrode (Samsudin et al., 2018).

Considerable studies have been conducted to investigate the morphology of TNTs under different anodizing conditions such as anodizing potential (Mehedi et al., 2017), time (Regonini & Clemens, 2015) and temperature (Kapusta-Kołodziej et al., 2017, 2014), but very few studies have evaluated the electrochemical capacitance of TNTs with respect to the morphology of TNTs under varying anodization voltage and time. For example, Endut et al., 2013 have obtained an increase in specific capacitance of sample prepared in ethylene glycol from 18.3 µFcm^{-2} for 10s anodization to 49.9 µFcm^{-2} after 30 min anodization time.

In view of the above, we report the effect of anodization voltage and time in the synthesis of TNTs in glycerol containing 0.5 wt % NH_4F and 25 v/v % water on the morphology and electrochemical capacitance.

Methodology
Preparation of titanium foil and the anodization was conducted similar to the report by Samsudin et al., 2018. Glycerol containing NH_4F (0.5 wt.%) and 25 v/v % water was used as electrolyte. The morphological and crystalline structure of the samples were examined by FESEM and XRD. The electrochemical capacitance of the samples was evaluated by cyclic voltammetry (CV) and galvanostatic charge-discharge (GCD) in a three-electrode

cell containing 1 M aqueous KCl as electrolyte, Pt wire as a counter electrode and Ag/AgCl as a reference electrode.

Results and Discussion

The tube diameter doubled from 60 to 129 nm as the voltage was increased from 10 to 40 V. At the voltage of 50 V nanotube layers collapsed and a sponge-like structures were formed, this is due to the strong fluoride ions attack on the surface of the nanotubes. On the other hand, the specific capacitance (SC) increased almost four times from 90 μFcm^{-2} to 330 μFcm^{-2} as the voltage was increased from 10 to 30 V. Meanwhile the tube length increased from 0.7 µm to 1.7 µm as anodization time was increased from 30 to 120 min with no significant increase in SC after 90 min.

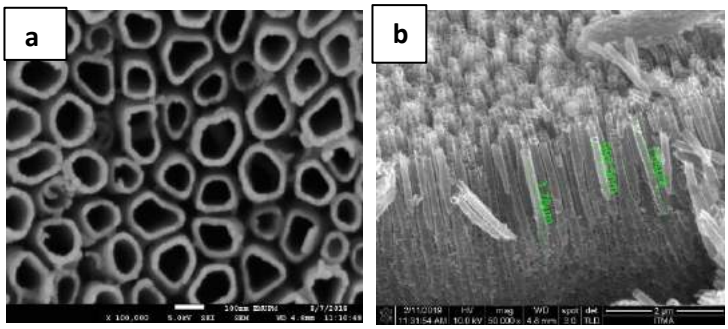

Figure 1: FESEM images of TNTs synthesised at 30 V (a) top view and (b) side view

Conclusion

Anodization voltage and time have great influence on the morphology of TNTs. The tube diameter, length and separation between the tubes affects the electrochemical capacitance of the TNTs.

Acknowledgement

We appreciate the Ministry of Education Malaysia for the grant FRGS 01-01-17-1912FR and thank Gombe State University and Tertiary Education Trust Fund (TETFUND) for sponsorship for M.M. Muzakir.

References

Endut, Z., Hamdi, M., & Basirun, W. J. (2013). An investigation on formation and electrochemical capacitance of anodized titania nanotubes. *Applied Surface Science*, *280*, 962–966.

Kapusta-Kołodziej, J., Syrek, K., Pawlik, A., Jarosz, M., Tynkevych, O., & Sulka, G. D. (2017). Effects of anodizing potential and temperature on the growth of anodic TiO 2 and its photoelectrochemical properties. *Applied Surface Science*, *396*, 1119–1129.

Kapusta-Kołodziej, J., Tynkevych, O., Pawlik, A., Jarosz, M., Mech, J., & Sulka, G. D. (2014). Electrochemical growth of porous titanium dioxide in a glycerol-based electrolyte at different temperatures. *Electrochimica Acta*, *144*, 127–135.

Mehedi, I. M., Hossain, M. F., Takahashi, T., & Islam, M. S. (2017). Nano-structural variation of highly aligned anodic Titania nanotube arrays for gas phase photocatalytic application. *Journal of Photochemistry and Photobiology A: Chemistry*, *335*, 200–210.

Regonini, D., & Clemens, F. J. (2015). Anodized TiO2 nanotubes: Effect of anodizing time on film length, morphology and photoelectrochemical properties. *Materials Letters*, *142*, 97–101.

Samsudin, N. A., Zainal, Z., Lim, H. N., Sulaiman, Y., Chang, S. K., Lim, Y. C., & Mohd Amin, W. N. (2018). Enhancement of Capacitive Performance in Titania Nanotubes Modified by an Electrochemical Reduction Method. *Journal of Nanomaterials*, *2018*.

ELECTRODEPOSITION OF Cr-Al_2O_3 NANOCOMPOSITE COATINGS AT VARIOUS DEPOSITION TIME FROM TRIVALENT CHROMIUM BATH

E. Tey[1], K. P. Lim[2], I. Ismail[1], Z. Zainal[1, 3]*

[1]*Material Synthesis and Characterization Laboratory, Institute of Advanced Technology, Universiti Putra Malaysia, 43400 Serdang, Selangor, Malaysia.*
[2]*Department of Physics, Faculty of Science, Universiti Putra Malaysia, 43400 Serdang, Selangor, Malaysia.*
[3]*Department of Chemistry, Faculty of Science, Universiti Putra Malaysia, 43400 Serdang, Selangor, Malaysia.*

*Corresponding author: zulkar@upm.edu.my

Abstract
In the present work, Cr-Al_2O_3 nanocomposite coatings were electrodeposited onto copper substrate using a modified trivalent chromium electroplating bath with the addition of 80 nm Al_2O_3 powder. The effects of deposition time on Al_2O_3 particles embedment and agglomeration were studied. The Cr-Al_2O_3 nanocomposite samples were subjected to different tests to characterize their surface morphology, crystalline structure and mechanical properties. The crystalline structure, composition and surface morphology of the deposits were studied by X-ray diffraction (XRD), energy-dispersive X-ray spectroscopy (EDX) and field emission scanning electron microscopy (FESEM). The corrosion resistance test was carried out by electrochemical polarization method. The microhardness was studied via Vickers Microhardness Test. The variation in the microhardness as a main crucial to achieve enhancement of Al_2O_3 incorporations with Cr matrix. From the EDX analysis, the deposition of Cr-Al_2O_3 nanocomposite for 60 minutes showed the highest weight percentage (wt%) of alumina. However, the longer electrodeposition time caused the increases of agglomerated alumina particles sizes. The microhardness results indicated the coating hardness deposited at 60 minutes is higher than that of 10 minutes and 30 minutes. Furthermore, the corrosion current density (icorr) of Cr- Al_2O_3 coating showed the highest value among the others. This result indicated that the corrosion resistance performance of Cr- Al_2O_3 coating decreases with increasing Al_2O_3 particles content.

Keywords: Trivalent Chromium Bath, Electrodeposition, Nanocomposite, Aluminium Oxide, Chromium

Introduction
Chromium coating has been widely used for decorative and functional finished due to their extraordinary properties such as good wear and corrosion resistance, high hardness and low coefficient. Trivalent chromium electrodeposition as an environment friendly and less toxic choices to alternate the conventional highly toxic and carcinogen hexavalent chromium electrodeposition have been studied [1-4]. In order to develop an alternative coating which can meet the performance of hard chrome plating, chromium matrix composite coatings have been fabricated to improve the physical and chemical properties. In the present work, the effect of various electrodeposition time on the Cr-Al_2O_3 nanocomposite coatings on structure, surface morphology, particle agglomeration, hardness and corrosion resistance have been investigated.

Methodology
The trivalent chromium electroplating bath was prepared as reported by V.S. Protsenko [4]. The electrolyte pH was adjusted to pH 1.5 by adding H_2SO_4 or NaOH solutions. Al_2O_3

powder with an average size of 80 nm was added into the bath as received. A mixed metal oxides (MMOs: iridium oxide and tantalum oxide) coated titanium plate was used as an anode in this experiment. A copper disk (substrate) was embedded in a polytetrafluoroethylene (PTFE) sample holder with a working surface area 1 cm^2 was used as a cathode. The electrodeposition was carried out at a current density of 20 A/dm^2 for 1 hour at 35℃. During the co-deposition process, the bath was mechanically stirred with a magnetic stirrer at 200 rpm to ensure the nanoparticles remain suspended in the bath. After electroplating, the sample was rinsed with deionized water and dried before analysis.

Results and Discussion

Figure 1 shows a nodular structure with uniform and compact growth grains of chromium matrix with incorporated Al_2O_3 nanoparticles. The white spots and dust-like particles were identified as agglomerated Al_2O_3 particles by Energy dispersive X-ray (EDX) elemental mapping analysis. FESEM images (Fig. 1 (a) to (c)) show the increase of Cr grain sizes as the electrodeposition time was varied from 10 mins to 60 mins. Meanwhile, the agglomeration of incorporated Al_2O_3 particles sizes also increase with increasing deposition time.

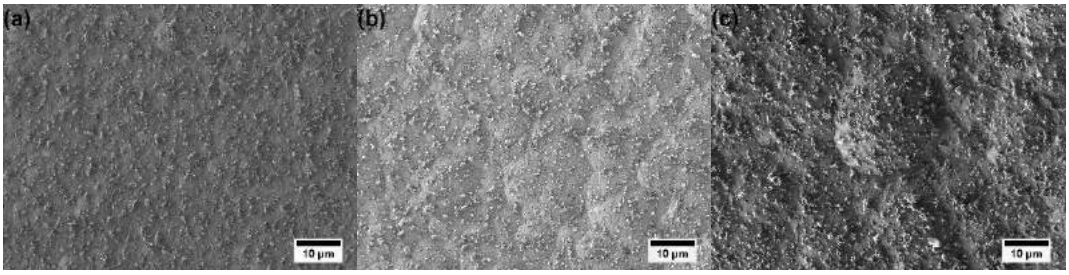

Figure 1: FESEM images of Cr-Al_2O_3 nanocomposite coatings electrodeposited from various deposition time: (a) 10 mins, (b) 30 mins and (c) 60 mins.

The coating hardness of 60 minutes deposition was higher than that of 10 minutes and 30 minutes. The longer the time, the thicker the coating, and the larger amount of Al_2O_3 particles can be incorporated into Cr matrix. The corrosion resistance performance of Cr-Al_2O_3 coating decreases with increasing Al_2O_3 content.

Conclusion

In summary, the grain sizes, the Al_2O_3 content and the agglomeration of Al_2O_3 particles sizes increase with deposition time increases. The Cr-Al_2O_3 nanocomposite coating deposited for 60 mins showed the highest hardness value which was related to the coating thickness and the Al_2O_3 content. While Cr-Al_2O_3 deposited for 60 mins has the lowest corrosion resistance.

Acknowledgement

Support for this work from the Institute of Advanced Technology (ITMA) and Faculty of Science, Universiti Putra Malaysia is gratefully acknowledged. Putra grant (UPM/700-2/1/GPB/2017) received to partially support this project is highly appreciated.

References

[1] Protsenko, V., Gordiienko, V., Butyrina, T., Vasileva, E., & Danilov, F. (2014). Hard chromium electrodeposition from a trivalent chromium bath containing water-soluble polymer. *Turkish Journal of Chemistry*, *38*(1), 50-55.

[2] Hong, G., Siow, K. S., Zhiqiang, G., & Hsieh, A. K. (2001). Hard chromium plating from trivalent chromium solution. *Plating and surface finishing*, *88*(3), 69-75.

[3] Danilov, F. I., Protsenko, V. S., Gordiienko, V. O., Kwon, S. C., Lee, J. Y., & Kim, M. (2011). Nanocrystalline hard chromium electrodeposition from trivalent chromium bath containing carbamide and formic acid: structure, composition, electrochemical corrosion behavior, hardness and wear characteristics of deposits. *Applied Surface Science*, *257*(18), 8048-8053.

[4] Protsenko, V. S., Gordiienko, V. O., & Danilov, F. I. (2012). Unusual" chemical" mechanism of carbon co-deposition in Cr-C alloy electrodeposition process from trivalent chromium bath. *Electrochemistry communications*, *17*, 85-87.

SYNTHESIS AND ELECTROCHEMICAL CAPACITANCE OF SELF-ASSEMBLED MESOPOROUS CARBON (SAMPC)

M.A.M. Sarif[1,3], Z. Zainal[1,2*], M.Z. Hussein[1], M.H. Wahid[2], Asla, A.AL-Zahrani[2,4] and L. Mohd Fudzi[2]

[1]Materials Synthesis and Characterization Laboratory, Institute of Advanced Technology, Universiti Putra Malaysia, 43400 UPM Serdang, Selangor, Malaysia
[2]Department of Chemistry, Faculty of Science, Universiti Putra Malaysia, 43400 UPM Serdang, Selangor, Malaysia
[3]Forest Product Division, Forest Research Institute Malaysia, 52109 Kepong, Selangor, Malaysia
[4]Imam Abdulrahman bin Fiasal University, Eastern Region, Dammam, Saudi Arabia.

*Corresponding author's email: zulkar@upm.edu.my

Abstract
Mesoporous carbon (MPC) has become increasing popular in electronic application such as supercapacitor due to its nanoporous nature, large accessible area and structure stability. In this work, self-assembled mesoporous carbon (SAMPC) was synthesized through self-polymerization of resorcinol (R) and formaldehyde (F) as a carbon precursor and spontaneous triblock copolymer Pluoronic F127 (F127) micelles which act as structure directing agent for the pore structure geometry tuning while preparing the MPC film. The resultant SAMPC possess a typical BET surface area of 773 m^2/g, pore size of 5.7 nm, and pore volume of 0.83 cm^3/g. It was carbonized to obtain the final product of SAMPC film. The carbonized SAMPC film show excellent electrochemical property for supercapacitor application and the specific capacitance 15.23 $mFcm^{-1}$ at 5 mV s^{-1} scan rate was obtained using electrolyte of 1.0 M potassium chloride neutral aqueous solution. These results suggest that the SAMPC film-coated titanium foil is a promising candidate for high performance electrodes for electric double layer capacitors (EDLC).

Keywords: self-assembled mesoporous carbon, polymerization, carbonization, supercapacitor, electrochemical characterization

Introduction
The flexible, lightweight, eco-friendly and high-performance power storage/conversion systems of supercapacitor are one of the most potential applications that are more essential for mobile and wearable electronic devices consumers. It is therefore essential for supercapacitor implementation to develop an eco-friendly, easy and cost-effective electrode material with excellent conductivity, elevated specific surface area and helpful porous composition. Today, extremely nanostructured mesoporous carbon (MPC) materials with customized and interconnected porous structures have attracted significant attention due to their distinctive chemical and mechanical stability, electronic and thermal conductivity, facilitated mass transportation and superior electrical characteristics [1-3]. In this paper, we report a straightforward, reproducible, environmentally friendly and cost-effective approach for the manufacturing of the MPC thin film for the freestanding and non-adhesive flexible electrode components.

Methodology
Resorcinol (R) was dissolved in ethanol solution, and then triblock copolymer 'Pluronic F127' (F127) was added and stirred for 60 min. After that, formaldehyde (37 wt%) (F) was added to the above solution and the solution was stirred for 10 min. Finally, hydrochloric acid (HCl) was added as a catalyst to the solution [3]. After stirring at various stirring time, the resultant solution was deposited dropwise onto a Ti substrate, and then the substrate

was spun up to 1000 rpm for 60 s. The deposited sample was heated at 90 °C for 5 h. Then, the resultant sample was carbonized under a nitrogen atmosphere at different temperature for 3 h at a heating rate of 2.3 °C min^{-1}. The electrochemical properties will be investigated in a three-electrode cell containing 1.0 M potassium chloride (KCl) (neutral) as the electrolyte with Platinum plate and Ag/AgCl/saturated KCL serve as the counter and reference electrodes respectively.

Results and Discussion

These samples exhibited increment of capacitance value as the stirring time increased but then decreased when stirred at longer duration as can be seen in Figure 1. It shows nearly rectangular shapes at various stirring time at lowest 5 mV s^{-1} of scan rate in the potential range of 0.8 to -0.2 V, indicating the ideal double-layer behaviour of supercapacitor after carbonization. This result suggests that stirring time also plays an important role for formation of carbon particles and clearly indicate that the electrochemical performance of carbon film materials was successfully obtained in this study.

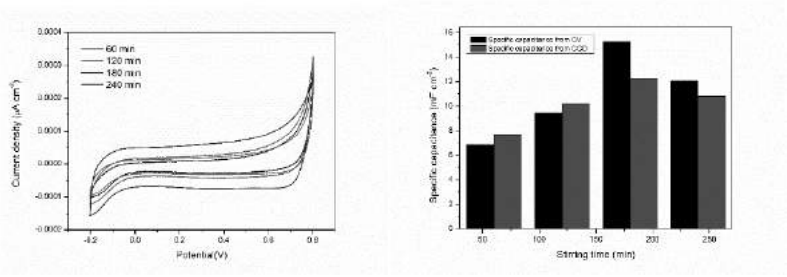

(a) (b)

Figure 1 Cyclic voltammograms (CV) of the SAMPC film (a) and specific capacitance obtained from CV and GCD analysis (b) at different stirring time

Conclusion

In summary, SAMPC films with homogeneous, continuous, and crack-free have been successfully synthesized. After stirred at 180 min and carbonization at 700°C for 3 h, SAMPC film show excellent electrochemical property for supercapacitor application and the specific capacitance up to 15.23 $mFcm^{-1}$ respectively at 5 mV s^{-1} the lowest scan rate which are comparable or even better performance compared to the reported literature [1-3]. It proved that the pore structure and existence of mesopores seem to contribute to the reduction of the diffusion resistance of ions in the electrode.

Acknowledgement

This work was supported by the Research Management Center (RMC), Universiti Putra Malaysia (UPM), under Grant no.GP/IPS/2017/9548000 and JPA scholarship for Doctoral Program for MSMA is gratefully acknowledged.

References

1. Lu, X., Dou, H., Zhang, X. 2016. Mesoporous carbon nanospheres inserting into graphene sheets for flexible supercapacitor film electrode. *Materials Letters.* 178, 304–307.
2. Chou, T.C., Huang, C.H., Doong, R.A. 2014. Fabrication of hierarchically ordered porous carbons using sugarcane bagasse as the scaffold for supercapacitor applications. *Synthetic Metals*. 194, 29–37.

3. Mitome, T., Uchida, Y., Egashira, Y., Nishiyama, N. 2014. Synthesis of ordered mesoporous carbon films with a 3D pore structure and the electrochemical performance of electrochemical double layer capacitors. *Colloids and Surfaces A: Physicochem. Eng. Aspects.* 449, 51–56.

EFFECT OF ELECTRODEPOSITION TIME ON ZnSe/ZnO NANORODS FOR PHOTOELECTROCHEMICAL CELL

L. Mohd Fudzi[1], Z. Zainal[1,2]*, H. N. Lim[1,2], S. Shafie[2,3], M.A.M. Sarif[2,4], A. AL-Zahrani[1,5] and S. K. Chang[1,2]

[1]Department of Chemistry, Faculty of Science, Universiti Putra Malaysia, 43400 UPM Serdang, Selangor, Malaysia.
[2]Materials Synthesis and Characterization Laboratory, Institute of Advanced Technology, Universiti Putra Malaysia, 43400 UPM Serdang, Selangor, Malaysia.
[3]Department of Electronic Engineering, Universiti Putra Malaysia, Serdang 43400, Malaysia.
[4]Forest Product Division, Forest Research Institute Malaysia, 52109 Kepong, Selangor, Malaysia.
[5]Imam Abdulrahman bin Faisal University, Eastern Region, Dammam, Saudi Arabia.

*Corresponding author: zulkar@upm.edu.my

Abstract
Endless effort have been put out by researchers to enhance photocatalytic performance of nanostructured zinc oxide (ZnO). One of the most notable trend is by depositing another layer of material, forming binary semiconductor heterostructure. In this work, an additional layer of zinc selenide (ZnSe) was electrodeposited on ZnO to form ZnSe/ZnO from 1 minute to 30 minutes. Based on X-ray diffractometry, the crystallite size of ZnSe increased from 22.8nm to 24.4nm with the electrodeposition time. FESEM images showed that more ZnSe particles was coated and piled up at the bottom of the nanorods after 30 minutes of deposition which caused blocking to light penetration. Such a phenomenon is in agreement with the results from photocurrent measurement, where sample deposited for shorter duration had greater photocurrent generated than sample deposited for 30 minutes.

Keywords: electrodeposition, ZnSe/ZnO, nanorods, photoelectrochemical cell

Introduction
Numerous techniques on depositing ZnSe have been discovered, from metal organic chemical vapour deposition [1] to sputtering [2]. However, electrodeposition technique stands out among other readily available techniques due to its simplicity, inexpensive and enables control of film properties such as composition, morphology and film thickness by adjusting the deposition parameters [3]. In this study, ZnSe was electrodeposited on ZnO nanorods which was prepared via dip coating and simple hydrothermal growth technique [4]. Deposition duration was varied by 1, 5, 15 and 30 minutes. The electrodeposited ZnSe/ZnO was expected to enhance the photocatalytic performance of the nanostructure due to the change in morphological and optical characteristics.

Methodology
A mixture of zinc acetate dihydrate and diethanolamine in ethanol was heated and stirred to form sol-gel precursor to synthesize ZnO seed layer by using dip coating method. Sonicated ITO glasses were dip coated for 40s followed by annealing at 350^{o}C for 1h. Calcined ZnO seed layer was then undergone hydrothermal growth process for 4h at 120^{o}C. ZnO nanorods synthesized were used in three-electrode system as the working electrode. Platinum wire and Ag/AgCl electrode were employed as the counter and reference electrodes respectively. A mixture of 0.01M zinc acetate and selenium dioxide was used as electrodeposition bath. The electrodeposition was carried out at -0.7V at the duration of 1, 5, 15 and 30 minutes. Photoelectrochemical measurement was carried out by using similar setup as electrodeposition with polysulfide solution as the electrolyte and halogen lamp as the light source.

Results and Discussion

FESEM image (Fig. 1) of sample electrodeposited for 1 minute shows ZnSe particles were partially covering nanorod wall, having an average particle size of 32.51nm. Meanwhile according to results in Table 1, band gap energy measured showed an increment trend as time increased from 1 minute to 30 minutes. For photoelectrochemical measurements, 1 minute deposition showed the highest current density while 30 minutes showed the lowest.

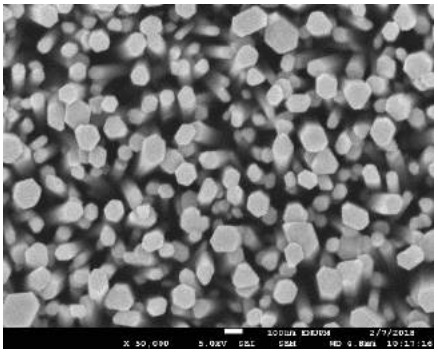

Fig.1 FESEM image of ZnSe/ZnO electrodeposited for 1 minute at magnification of x50,000.

Time (min)	Band gap (eV)	Current density ($mAcm^{-2}$)
1	2.91	0.2736
5	2.98	0.1908
15	2.97	0.2621
30	3.09	0.2148

Table 1 Band gap energy and current density of ZnSe/ZnO/ITO prepared at different deposition duration.

Conclusion

ZnSe/ZnO electrodeposited with a short duration showed better photoelectrochemical performance with 40.7% enhancement for 1 minute electrodeposition compared to ZnO/ITO sample. ZnSe were partially covered the wall of nanorods, and the amount of particles coated increases with time. Band gap energy was lower for shorter duration.

Acknowledgement

This work is supported by the Ministry of Higher Education of Malaysia through FRGS grant (01-01-17-1912FR) and providing a MyBrain SC Scholarship to Laimy Mohd Fudzi.

References

1. Wu, Z., Zhang, Y., Zheng, J., Lin, X., Chen, X., Huang, B., Wang, H., Huang, K., Li, S. and Kang, J., 2011. An all-inorganic type-II heterojunction array with nearly full solar spectral response based on ZnO/ZnSe core/shell nanowires. Journal of Materials Chemistry, 21(16), pp.6020-6026.
2. Vivet, N., Morales, M., Levalois, M., Charvet, S. and Jomard, F., 2010. Optimization of the structural, microstructural and optical properties of nanostructured Cr {sup 2+}: ZnSe films deposited by magnetron co-sputtering for mid-infrared applications.
3. Riveros, G., Gomez, H., Henriquez, R., Schrebler, R., Marotti, R.E. and Dalchiele, E.A., 2001. Electrodeposition and characterization of ZnSe semiconductor thin films. Solar energy materials and solar cells, 70(3), pp.255-268.
4. Mohd Fudzi, L., Zainal, Z., Lim, H., Chang, S.K. and Holi, A., 2018. Effect of Temperature and Growth Time on Vertically Aligned ZnO Nanorods by Simplified Hydrothermal Technique for Photoelectrochemical Cells. Materials, 11(5), p.704.

ORAL PRESENTATION

PHYSICS

STRUCTURAL PROPERTIES OF Nd-Ca-Mn-O SYNTHESISED BY SOL-GEL ROUTE

A.N. Ishak, K.P. Lim*, L.N. Lau, M.M. Awang Kechik, S.K. Chen and S.A. Halim

Superconductor and Thin Film Laboratory, Department of Physics, Faculty of Science, Universiti Putra Malaysia, 43400 UPM Serdang, Selangor Darul Ehsan, Malaysia.

*Corresponding author: limkp@upm.edu.my

Abstract
Mixed-valent manganites perovskites have caught the eye of the researches over the past few years due to their captivating properties such as colossal magnetoresistance (CMR) effect and potential industrial application as magnetic field sensing element. In this study, $Nd_{0.67}Ca_{0.33}MnO_3$ (NCMO) compounds have been synthesised by sol-gel method and were characterized by using X-ray diffraction (XRD) to study the structural properties of the compounds. Based on the XRD results, all samples showed single phase formation with orthorhombic crystal structure. The crystallite size of the samples increases as the sintering temperature increases because higher temperature promotes crystallite growth.

Keywords: Manganites, NCMO, CMR materials, Sol-gel method

Introduction
In 1950, Jonker and van Santen have discovered the colossal magnetoresistance (CMR) in perovskite manganites which then has attracted many researches due to its potential industrial application as magnetid field sensing element. From previous study, it was proven that by using sol-gel method, the grain growth will be restricted sun-micron region due to lower sintering temperature and it shown broader metal-insulator transition (T_{MI}) as compared to solid state reaction method (Reshi & Shelke, 2014). On the other hand, the crystallite size that are in nanometer range are found to be decreased as sintering temperature decreased and this promote higher magnetoresistance (MR) value (Venkataiah et al., 2003). However, there is only a few study on the neodymium calcium manganite (NCMO) and thus this research is to investage and study about the crystal structural properties of the NCMO system using sol-gel route by varying the sintering temperature.

Methodology
$Nd_{0.67}Ca_{0.33}MnO_3$ (NCMO) sample was prepared by sol-gel method. A stoichiometric amount of the precursors $La(NO_3)_3.6H_2O$, $Ca(NO_3)_3.4H_2O$ and $Mn(NO_3)_2.4H_2O$ were mixed together and dissolved in distilled water. The nitrate solution was mixed with citric acid (CA) and ethylene glycol (EG) and then the solution was heated up to 110°C to remove the moisture before calcined at 500°C. Finally, the after calcined powder was sintered at various temperatures starting at 550°C, 600°C, 700°C, 800°C, 900°C and 1000°C. The samples were then characterized by an X-ray diffractometer (XRD; Philips PW 3040/60 X'Pert PRO) to study about the structural properties and phase formation of the samples.

Results and Discussion
All synthesized NCMO samples were fully crystalline in single phase without any detectable impurities and exhibited orthorhombic crystal structure based on the XRD pattern in Fig.1 (a). As the sintering temperature increased, the intensity of the X-ray peaks also increased. This indicated that sintering temperature promoted NCMO crystal phase formation and/or grain growth. Fig.1 (b) shown the crystallite size as a function of sintering

temperature. The average calculated crystallite size for all samples are ~23.1 nm, ~25.7 nm, ~27.9 nm, ~33.3 nm, ~51.5 nm and ~93.1 nm for sintering temperature 550 ˚C, 600 ˚C, 700 ˚C, 800 ˚C, 900 ˚C and 1000 ˚C respectively. As the sintering temperature increased, the crystallite growth increased due to congregation of the grains (Lim et al., 2018). The crystallite increased exponentially to the sintering temperature.

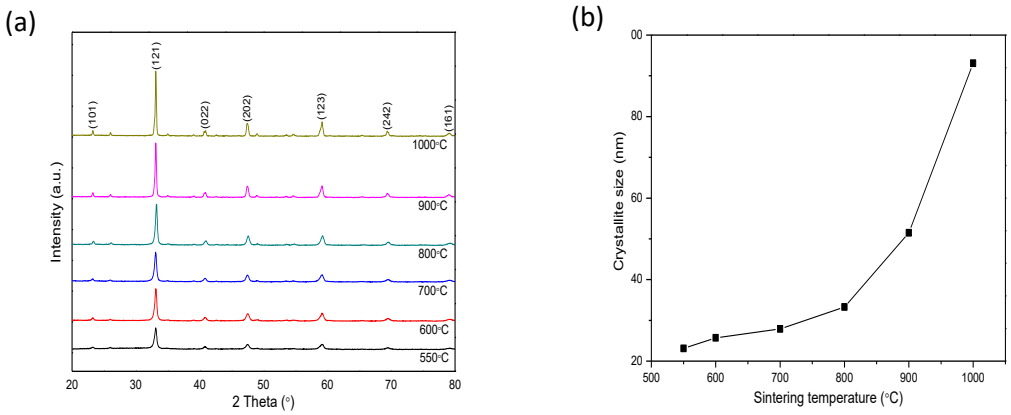

Fig. 1: (a) structural properties and (b) crystallite size of NCMO at various sintering temperatures (550˚C, 600˚C, 700˚C, 800˚C, 900˚C and 1000˚C)

Conclusion

Single crystalline phase of $Nd_{0.67}Ca_{0.33}MnO_3$ compound had been sucessfully synthesized using sol-gel method. All sample exhibited orthorhombic crystal structure having Pnma space group (62). Rietveld's refinement results showed that the crystallite size has a strong dependence on sintering temperature as it will increased when the sintering temperature increased. The crystallite size growth exponentially with the sintering temperature.

Acknowledgement

This research is funded and supported by Universiti Putra Malaysia (UPM) research grants, GP/2017/9567400 and GP-IPS/2018/9663900.

References

Lim, K. P., Halim, S. A., Chen, S. K., Awang Kechik, M. M., Ng, S. W., & Wan Jusoh, W. N. W. (2018). Grain Size Effect on Electrical and Magnetotransport Properties of Grain Size Effect on Electrical and Magnetotransport, 0–8.

Reshi, H. A., & Shelke, V. (2014). Grain Size Induced Metal-insulator Transition in La0.7Sr0.3MnO3 Compounds, *5*(4), 12–14.

Venkataiah, G., Lakshmi, Y. K., & Reddy, P. V. (2003). Influence of Sintering Temperature on Magnetotransport Behavior of Some Nanocrystalline Manganites.

STRUCTURAL, MICROSTRUCTURAL AND MAGNETIC PROPERTIES IN BULK AND NANO-SIZED Nd-Sr-Mn-O MANGANITES

L.N. Lau[1], K.P. Lim[1]*, A.N. Ishak[1], M.M. Awang Kechik[1], S.K. Chen[1], N.B. Ibrahim[2] and S.A. Halim[1]

[1]Superconductor and Thin Film Laboratory, Department of Physics, Faculty of Science, Universiti Putra Malaysia, 43400 UPM Serdang, Selangor Darul Ehsan, Malaysia.
[2]School of Applied Physics, Faculty of Science and Technology, Universiti Kebangsaan Malaysia, 43600 UKM Bangi, Selangor Darul Ehsan, Malaysia.

*Corresponding author: limkp@upm.edu.my

Abstract
Colossal magnetoresistive (CMR) manganites have attracted scientific interest and studied extensively as it also accompanied with several other intriguing phenomena. The Nd-Sr-Mn-O (NSMO) compounds were prepared by solid-state reaction and sol-gel method in order to obtain the bulk and nano-sized manganites. The size reduction could influence the structural, microstructural and magnetic properties of NSMO. Structural analysis revealed that the both samples exhibit in orthorhombic crystal structure and a strong orientation towards (121). The peak broadening can be observed in nano-sized NSMO indicates the smaller crystallite size as compared to bulk. The irregular shape of grains have been formed in NSMO compounds from the observation of field emission scanning electron microscope (FESEM). The average grain size for bulk and nano-sized NSMO are ~ 31 nm and ~ 0.94 μm respectively. The AC susceptibility results showed that Curie temperature (T_C) decreases as the grain size decreases. This behaviour can be attributed to the loss of long-range ferromagnetic ordering in nano-sized grain. The structural, microstructural and magnetic properties in bulk and nano-sized NSMO have been investigated successfully in this work.

Keywords: NSMO, CMR materials, Sol-gel method, Solid-state reaction

Introduction
Mixed-valence manganites have attracted scientific interest for its remarkable colossal magnetoresistance (CMR) phenomenon and it also accompanied by several intriguing phenomena such as metal-insulator transition and ferromagnetic-paramagnetic transition. From literature review, lots of studies have been carried out on these manganite compounds but limited study had been reported on the neodymium strontium manganite (NSMO). Comparative study of structural, microstructural and magnetic of bulk and nano-sized NSMO in this study will increase our understandings on this material. The size reduction of NSMO can be done by synthesis routes and it will influence the physical properties of materials (Arun et al., 2016).

Methodology
NSMO was synthesized by solid-state reaction and sol-gel method. For solid-state reaction method, Nd_2O_3, $SrCO_3$ and $MnCO_3$ were used as the starting materials. The starting powders were well mixed by ball-milling and then calcined at 900 °C. The calcined powder was pressed into pellet and sintered at 1100 °C. For sol-gel route, the stoichiometric amount of precursors $Nd(NO_3)_3.6H_2O$, N_2O_6Sr and $Mn(NO_3)_2.4H_2O$ were dissolved in distilled water. The solution was mixed with citric acid (CA) and ethylene glycol (EG) then heated up to 110 °C to remove the moisture and calcined at 500 °C. Later, the powder was pressed into pellet and sintered at 800 °C to form the NSMO phase. The samples were

studied by X-ray diffractometer (XRD; Philips PW 3040/60 X'Pert PRO), field emission scanning electron microscope (FESEM; JEOL JSM-7600F) and AC susceptometer (ACS; CryoBIND T).

Results and Discussion

Figure 1 (a) shows that the XRD patterns of bulk and nano-sized NSMO are fully crystalline in single phase. Both samples exhibit in orthorhombic crystal structure and the peak broadening can be observed in nano-sized NSMO indicates the smaller crystallite size as compared to bulk. From microstructural analysis, the average grain size for bulk and nano-sized NSMO are ~ 31 nm and ~ 0.94 µm respectively. The AC susceptibility results showed that Curie temperature (T_C) decreases as the grain size decreases. This behaviour can be attributed to the loss of long-range ferromagnetic ordering and magnetic disordered layer for nano-sized grain (Ng et al., 2018).

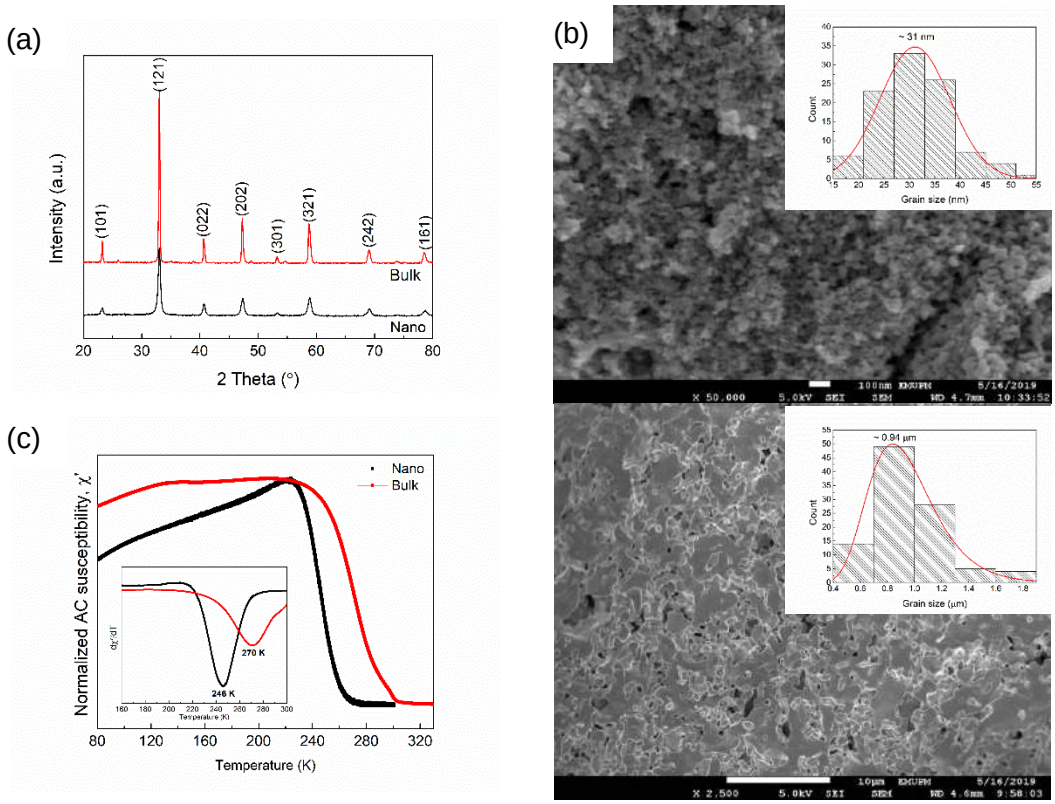

Fig. 1 The (a) structural, (b) microstructural and (c) magnetic properties of bulk and nano-sized NSMO manganite compounds.

Conclusion

The experimental results in this work revealed that the grain size reduction influences severely on the structural, microstructural and magnetic properties of NSMO.

Acknowledgement

This research is funded and supported by Universiti Putra Malaysia (UPM) research grants, GP/2017/9567400 and GP-IPS/2018/9663900.

References

Arun, B., Suneesh, M. V., & Vasundhara, M. (2016). Comparative Study of Magnetic Ordering and Electrical Transport in Bulk and Nano-Grained $Nd_{0.67}Sr_{0.33}MnO_3$ Manganites. *Journal of Magnetism and Magnetic Materials, 418*, 265-272.

Ng, S., Lim, K., Halim, S., & Jumiah, H. (2018). Grain size effect on the electrical and magneto-transport properties of nanosized $Pr_{0.67}Sr_{0.33}MnO_3$. *Results in Physics, 9*, 1192-1200.

SYNTHESIS AND CHARACTERISATION OF $La_{0.67}Ca_{0.33}MnO_3/Al_2O_3$ NANOCOMPOSITES

K.P. Lim*, L.N. Lau, A.N. Ishak, M.M. Awang Kechik, S.K. Chen, S.A. Halim and L.M. Ngai

Superconductor and Thin Film Laboratory, Department of Physics, Faculty of Science, Universiti Putra Malaysia, 43400 UPM Serdang, Selangor Darul Ehsan, Malaysia.

*Corresponding author: limkp@upm.edu.my

Abstract
Noticeable attention has been paid to the perovskite manganites due to their colossal magnetoresistance (CMR) effect and technological application in magnetic field sensing devices. Low-field magnetoresistance (LFMR) is needed by most of the high efficiency magnetic devices. Previous research showed that the enhanced LFMR can be achieved by introducing a secondary insulating phase which acts as the artificial barrier layer. In this research, the (1-x) $La_{0.67}Ca_{0.33}MnO_3$ (LCMO): x Al_2O_3 (x = 0.00, 0.05, 0.10, 0.15 and 0.20) composites have been prepared by sol-gel method. Their structural, magnetic and magnetotransport properties were systematically investigated. The X-ray diffraction (XRD) analysis indicates that Al_2O_3 and LCMO coexisted in the composites. The pure LCMO is in paramagnetic state at room temperature as its Curie temperature is 250K. Results of Hall measurement system show that the resistivity of the pure LCMO decreases as magnetic field increases. This is due to the localized spin of t_{2g} in 3d orbital aligned parallel to each other which makes the electron transfer more easily. At low temperature, the LFMR that related to the spin-polarized tunneling at the grain boundaries has been observed. The LFMR shows a higher value as the temperature drops.

Keywords: LCMO, CMR materials, Sol-gel method, LFMR

Introduction
$La_{1-x}Ca_xMnO_3$ is known to exhibit metal-insulator (M-I) transition and colossal magnetoresistance (CMR) in the vicinity of the Curie temperature (T_C). The coupled dynamics of charge and spin can be explained by double-exchange (DE) interaction between pairs of Mn^{3+} and Mn^{4+} ions through an oxygen atom (Zener, 1951). However, CMR phenomenon cannot be explained alone by the DE mechanism. Some other interactions should also be considered such as Jahn-Teller (JT) polaron and phase separation. Most of the magnetic applications require magnetoresistance at low magnetic field (LFMR) while intrinsic CMR only happens at high magnetic fields and limited in narrow temperature range (Wang et al., 2010). Therefore, the addition of oxide as an artificial grain boundary is important in enhancing the LFMR effect as demonstrated by the previous works (Navin & Kurchania, 2018; Thanh et al., 2011). In current work, Al_2O_3 has been chosen as the secondary phase in manganite composite as the paramagnetic Al_2O_3 is an electrical insulator material exhibits with high thermal conductivity.

Methodology
$La_{0.67}Ca_{0.33}MnO_3$ (LCMO) was synthesized by sol-gel method and added with nano-sized aluminium oxide, (1-x) LCMO: x Al_2O_3 where x = 0.00, 0.05, 0.10, 0.15 and 0.20. The stoichiometric amount of the precursors $La(NO_3)_3.6H_2O$, $Ca(NO_3)_3.4H_2O$ and $Mn(NO_3)_2.4H_2O$ were dissolved in distilled water. The solution was mixed with citric acid (CA) and ethylene glycol (EG) then heated up to 110 °C to remove the moisture and calcined at 500 °C. Later, the powder was pre-sintered at 800 °C to facilitate the formation of LCMO phase. Finally, the LCMO powder was added with Al_2O_3 (MTI Corp, 99.99 %)

nanopowder (30 nm) and sintered at 600 °C. The samples were studied by an X-ray diffractometer (XRD; Philips PW 3040/60 X'Pert PRO), a vibrating sample magnetometer (VSM; Lakeshore 7407) and a Hall effect measurement system (HMS; Lakeshore 7604).

Results and Discussion

XRD patterns show that all samples are fully crystalline in single phase where there is no extra peak as shown in fig. 1(a). The lattice parameter of composites exhibits almost same values as compared with the pure LCMO. Besides that, the bond angle and bond distance also remain unchanged. Hence, we can deduce that the Al_2O_3 only segregated at the grain boundaries or the surface of LCMO grains where there is no reaction between Al_2O_3 and LCMO. From the M-H graph as illustrated in fig. 1(b), LCMO and its composites behave as paramagnetic state in room temperature as the T_C of LCMO is reported as ~250 K (Thanh et al., 2011). The localized spin aligned parallel to each other when there is an applied magnetic field. This will lead to less electron scattering and gives rise to %MR. LFMR is more pronounced in low temperature by showing a higher value as the temperature drops.

Fig. 1 The (a) structural and (b) magnetic properties of (1-x) LCMO: x Al_2O_3, x = 0.00, 0.05, 0.10, 0.15 and 0.20 at room temperature

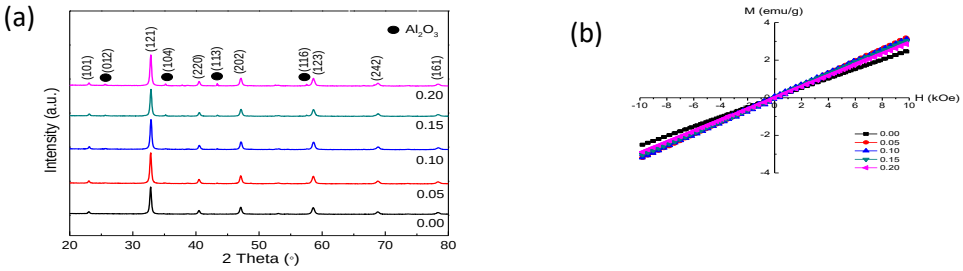

Conclusion

The influence of Al_2O_3 addition on structural, magnetic and magnetotransport properties of sol-gel grown $La_{0.67}Ca_{0.33}MnO_3$ nanocomposites has been successfully investigated. XRD analysis indicates that there is no reaction between LCMO and Al_2O_3. Results of Hall measurement system show that the resistivity of the pure LCMO decreases as magnetic field increases.

Acknowledgement

This research is funded and supported by Universiti Putra Malaysia (UPM) research grants, GP/2017/9567400 and GP-IPS/2018/9663900.

References

Navin, K., & Kurchania, R. (2018). Structural, magnetic and transport properties of the $La_{0.7}Sr_{0.3}MnO_3$-ZnO nanocomposites. *Journal of Magnetism and Magnetic Materials, 448*, 228-235.

Thanh, T. D., Phong, P. T., Dai, N. V., Manh, D. H., Khiem, N. V., Hong, L. V., & Phuc, N. X. (2011). Magneto-transport and magnetic properties of (1–x)$La_{0.7}Ca_{0.3}MnO_3$+xAl_2O_3 composites. *Journal of Magnetism and Magnetic Materials, 323*(1), 179-184.

Wang, T., Chen, X., Wang, F., & Shi, W. (2010). Low-field magnetoresistance in $La_{0.7}Sr_{0.3}MnO_3/CuCrO_2$ composites. *Physica B: Condensed Matter, 405*(15), 3088-3091.

Zener, C. (1951). Interaction between the d-shells in the transition metals. II. Ferromagnetic compounds of manganese with perovskite structure. *Physical Review, 82*(3), 403.

IMPROVED ELECTROMAGNETIC INTERFERENCE SHIELDING EFFECTIVENESS OF OPEFB/PLA POLYMER FIBER COMPOSITE WITH ACTIVATED CARBON FILLER FOR MICROWAVE APPLICATION

Ismail Ibrahin Lakin[1], Zulkifly Abas[1]*, Rabaah Syahidah Azis[1]
, Nor Azowa Ibrahim[2], Zulkarnain Zainal[2]

[1]Department of Physics, Faculty of Science, University Putra Malaysia, 43400 UPM, Serdang, Selangor, Malaysia
[2]Department of Chemistry, Faculty of Science, University Putra Malaysia, 43400 UPM, Serdang, Selangor, Malaysia

*****Corresponding author: za@upm.edu.my

Abstract
Oil palm empty fruit bunch (OPEFB) fiber and Polylactic acid (PLA) based composites have been synthesized by incorporation of up to 22 wt% activated carbon (AC) derived from OPEFB fiber in OPEFB/PLA matrix to investigate microwave dielectric properties along with electromagnetic interference (EMI) shielding performance. The composites were characterized by X-ray diffraction (XRD), Fourier transforms infrared (FTIR), Field emission scanning Microscopy (FESEM), coaxial probe and microstrip line techniques. The dielectric measurements carried out at X band frequency revealed that 22 wt% AC concentration composite display higher dielectric constant and loss factor values (3.96 and 0.52) respectively compared to OPEFB/PLA (2.99 and 0.34). The result further indicates that the porous structure and permittivity value contribute towards good EMI shielding effectiveness value of -23.33 dB, suggesting this novel composite as a promising candidate for microwave absorption and electromagnetic interference applications.

Keywords: Polymer, fiber, Activated carbon, permittivity, EMI shielding effectiveness

Introduction
Electromagnetic interference (EMI) shielding is an unwanted electromagnetic (EM) induction triggered by extensive use of alternating current/voltage which tries to produce corresponding induced signals (current/voltage) in the nearby electronic circuitry, thereby degrading the device performance (Saini et al., 2012). Therefore, systematic measures are essential to prevent/attenuate EMI so as to ensure uninterrupted performance of the devices (Rodriguez et al., 1997). This paper is aimed at enhancing the dielectric properties (dielectric constant and loss factor) of a composite with different ratio of environmentally friendly PLA, OPEFB and AC derived from OPEFB for electromagnetic interference shielding in the microwave frequency band using an open-ended coaxial probe (OEC) and microstrip line technique respectively. The OPEFB/PLA/AC composite can be used in the fabrication of microstrip antenna and transmission line components which can be found in mobile communication, aerospace and defence industry.

Methodology
The OPEFB fibres were soaked in distilled water for 24 h to remove the wax layer of the fibers. The fibers were rinsed with acetone and dried in an oven at 80 ºC for 6 h to reduce the moisture. The dried fibres were crushed into powder using crusher machine (Mainland Hunan, China), which were then sieved through a laboratory test sieve (Endecotts, London, England) to 100 µm. Part of the processed 100 µm OPEFB was used as the raw material

for the synthesis of activated carbon. The synthesis was carried out using a single step direct activation. The OPEFB, PLA and the AC were compounded by the melt-blending technique using brabender internal mixer at 160 ºC with 50 rpm of rotor speed for 15 min. First, the PLA pellets were put into the mixing chamber for 2 min to melt. Then, the OPEFB and the AC were added, blending was continued for another 13 min, followed by compression molding to produce rectangular substrates with dimensions of (6 × 3.5 × 0.8) cm^3 using a hot press (Yangzhou Hi-tech, Jiangsu, China). The compression molding was performed using the hydraulic hot press at 120 ºC molding temperature, 150 kg/cm^2 pressure, for 10 min. then cooled at 30 ºC for 10 min. The samples were characterized using XRD, FTIR, and FE-SEM.

Results and Discussion

Figure 1 shows the XRD patterns of PLA, OPEFB, AC and OPEFB/PLA/AC composites. The peak characteristic of PLA is located at 2θ value of ≈ 18º. The PLA did not show any characteristic peak, indicating that PLA has an amorphous structure (Kristiani et al., 2015). Table 1 shows the summary of the dielectric constant and loss factor for OPEFB, PLA, OPEFB/PLA and OPEFB/PLA/AC composites.

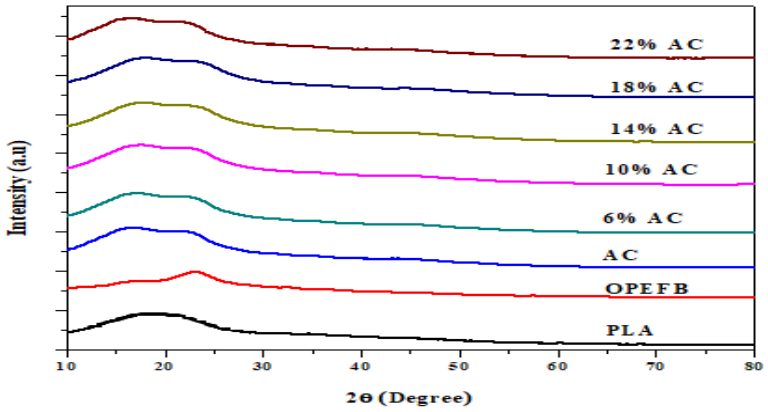

Figure 1. XRD pattern of OPEFB, PLA, AC and OPEFB/PLA/AC composites with different concentration of AC.

Table 1. Dielectric constant and loss factor values for AC, OPEFB, PLA and OPEFB-PLA-AC composites

Content	Dielectric const. (ε')	Loss factor (ε'')
OPEFB	3.5973	0.6391
PLA	2.6950	0.0657
AC	4.6836	0.6477
OPEFB/PLA	2.9857	0.3406
OPEFB/PLA 6% AC	3.1649	0.4079
OPEFB/PLA 10% AC	3.2897	0.4412
OPEFB/PLA 14% AC	3.4761	0.4738
OPEFB/PLA 18% AC	3.7687	0.4984
OPEFB/PLA 22% AC	3.9634	0.5255

Conclusion

OPEFB/PLA and OPEFB/PLA/AC composites containing different % of AC have been successfully prepared using melt-blend technique. The dielectric measurement showed that OPEFB/PLA composite displays low ε' and ε'' values (2.99 and 0.34) that increases with addition of AC and reaches 3.96 and 0.52 respectively for 22% AC containing composite, which also shows EMI shielding effectiveness value of -23.33 dB.

Acknowledgement

This work was supported by Universiti Putra Malaysia Grants (UPM/700-1/2/GPPI/2017/954160), Impact Putra Grants (GP-IPS/2017/9580600) and the ministry of Education Malaysia (Fundamental Research Grants Scheme (FGRS) (No. 5524942)

References

Kristiani, A., Effendi, N., Aristiawan, Y., Aulia, F., & Sudiyani, Y. (2015). Effect of combining chemical and irradiation pretreatment process to characteristic of oil palm's empty fruit bunches as raw material for second generation bioethanol. *Energy Procedia, 68*, 195-204.

Rodriguez, J., Grande, H. J., & Otero, T. F. (1997). Handbook of organic conductive molecules and polymers. John Wiley & Sons Ltd: New York, 2.

Saini, P., & Arora, M. (2012). Microwave absorption and EMI shielding behavior of nanocomposites based on intrinsically conducting polymers, graphene and carbon nanotubes. New Polymers for Special Applications, 3, 73-112.

EFFECT OF SINTERING ENVIRONMENT ON THE SYNTHESIS OF CARBON NANOTUBE-ZINC SILICATE COMPOSITE

Chan Kar Fei[1*], Siti Maryam Jameelah binti Masanuri[1], Mohd Hafiz Mohd Zaid[1] and Yazid Yaakob[1]

[1]*Department of Physics, Faculty of Science, Universiti Putra Malaysia, 43400 UPM Serdang, Selangor, Malaysia.*

*Corresponding author: kfeichan08@gmail.com

Abstract
In this work, synthesis of multi walled carbon nanotube - zinc silicate composite (CNTs/Zn_2SiO_4) has been done by powder processing technique and heat treatment. Carbon nanotube tailoring in ceramics matrix system and preserving nanotube from decomposing in high temperature heat treatment has been studied. Heat treatment has been conducted in two gaseous environments: open air and inert gas. X-ray diffraction was applied to examine the phase formation of the composite while UV-Vis was used to determine absorbance properties as a function of wavelength. In UV-Vis spectrum, 2wt% CNT mixed with Zinc Silicate sintered in inert gas environment shows great absorbance in the range of visible light to infrared region (400-800nm).

Keywords: Carbon nanotube tailoring, ceramics matrix system, surface morphology, optical band gap, inert gas annealing

Introduction
Carbon allotrope can be categorized by its carbon atom arrangement and shape. Single layer of carbon hexagonal arrangement structure developed a graphene layer. Graphene layer transform into different form of carbon allotropes via various mechanism. Different allotrope formed with different mechanism:1) fullerene (0D, wrapping mechanism), 2) carbon nanotube (1D, rolling mechanism) and graphite (2-dimension, stacking mechanism).
In year 1991, Iijima and researchers first discovered tubular structure of carbon in his research on fullerene formation. For the next two decades, researchers around the globe reported its unique properties. Carbon nanotubes (CNTs) possessed unique properties of thermal, mechanical and thermal properties. Due to the properties, CNTs act as an enhancement material in various application.
CNT reinforcement in glass-ceramics matrix had been widely reported. However, there is two issue in this reinforcement: a) CNT dispersion in matrix system and b) preserve CNT in heat treatment process. In this work, CNT-zinc silicate was prepared via powder processing method. The heat treatment (600°C) was conducted separately in open air furnace and inert gas condition.

Methodology
Pristine carbon nanotubes (P-CNTs) and zinc silicate powder (Zn_2SiO_4, produced by melt and quench method from Soda lime waste glass (SLS)) were used in this work. P-CNTs was mixed with Zn_2SiO_4 with varying weight percentage as per Zn_2SiO_4, x = 0.8, 1.0 and 2.0wt%.
A load of 5 tonnes was applied onto 1g of mixed powder for 10 minutes in order to form a pellet with 12.7 mm in diameter and 2 mm in thickness. Pellet sample was sintered in electric furnace in open air environment and inert gas (argon gas, Ar) environment respectively. The annealing temperature and period were set as 800°C and 2 hours. In

Argon gas environment, the gas flow was set as 100 cc/min. Inert gas was selected as the heating environment due to the melting point of CNTs is around 3000°C in inert gas while low melting point in oxidizing environment (in the range of 600-700°C). Mixed powder sintered in inert gas environment and open-air environment were labelled as Ar W-PC and O2 W-PC respectively.
Surface morphology of sample was observed under field emission scanning electron microscopy (FESEM). Ultraviolet-visible spectroscopy (UV-Vis) was applied to quantitatively measure the adsorption spectrum of the sample at different wavelength. Photoluminescence (PL) analysis was utilized to measure the intensity of emitted light from sample under optical excitation.

Results and Discussions

From the XRD spectrum, sintered sample from both environments had shown the formation of α-willemite and akermanite as the impurities. Akermanite was formed due to the magnesium ion (Mg^{2+}) and calcium ion (Ca^{2+}) found in the SLS glass. At 26° (2 theta position), graphite peak was found as result of CNT successfully dispersed in the glass ceramics composite.
From absorbance to wavelength spectrum, the spectrum showed the material capable to absorb electromagnetic (EM) radiation from visible-infrared radiation (400-800nm). The highest absorbance properties (absorbance≈0.8) possessed by 2wt% P-CNTs mixed composite.

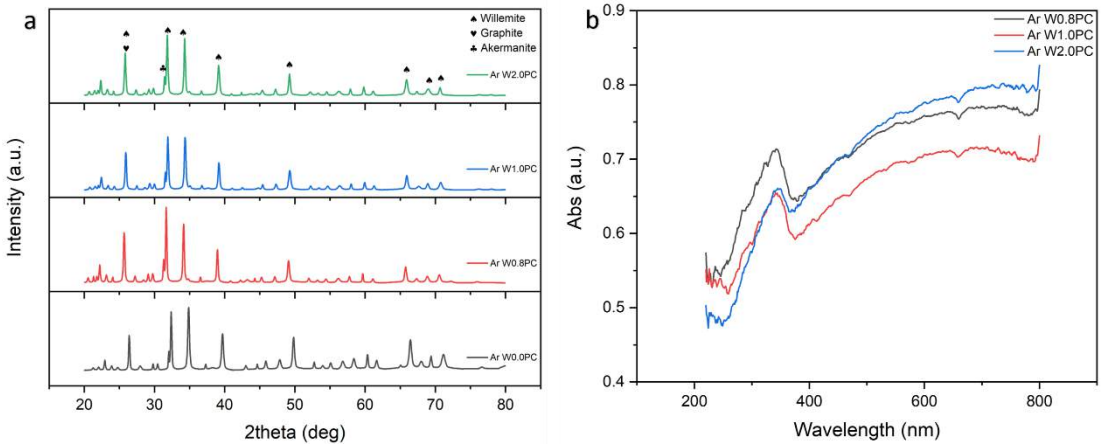

Figure 1 Spectroscopy result from Ar W-PC a) XRD and b) UV-Vis.

Conclusions

In this study, CNTs- zinc silicate glass composite in inert gas and open-air environment was successfully synthesised. CNTs was not decomposed during inert gas sintering environment. Willemite with 2wt% of P-CNTs addition shows a great result in visible light absorbance. This composite potentially acts as radiation shielding material.

Acknowledgement

This work is supported by the Malaysian Ministry of Education under FRGS, Project No: 5540132.

References

[1] A. Nieto, A. Bisht, D. Lahiri, C. Zhang, and A. Agarwal, “Graphene reinforced metal and ceramic matrix composites: a review,” *Int. Mater. Rev.*, vol. 62, no. 5, pp. 241–302, 2017.
[2] G. D. Zhan, J. D. Kuntz, J. Wan, and A. K. Mukherjee, “Single-wall carbon

nanotubes as attractive toughening agents in alumina-based nanocomposites," *Nat. Mater.*, vol. 2, no. 1, pp. 38–42, 2003.

[3] D. Cai and L. Liu, "The screening effects of carbon nanotube arrays and its field emission optimum density," *AIP Adv.*, vol. 3, no. 12, pp. 0–9, 2013.

[4] C. Balázsi, K. Sedláčková, and Z. Czigány, "Structural characterization of Si3N4-carbon nanotube interfaces by transmission electron microscopy," *Compos. Sci. Technol.*, vol. 68, no. 6, pp. 1596–1599, 2008.

MAGNETIC PHASE TRANSITION OF ZnO AND Fe DOPED ZnO NANOPARTICLES SYNTHESIZED BY MICROWAVE ASSISTED SYNTHETIC METHOD

S. S. Abdullahi[a,b,d], J. Y.C. Liew[b,d], G.S.M Galadanci[c] N.M. Saiden[b,*,d]

[a]*Physics Department, Federal University Dutse, P.M.B. 7156, Dutse, Jigawa State Nigeria*
[b]*Physics Department, Faculty of Science, Universiti Putra Malaysia, 43400 UPM Serdang, Selangor Malaysia.*
[c]*Physics Department Bayero University, Kano Nigeria. P.M.B.3011, Kano Nigeria*
[d]*Institute of Advanced Technology, Universiti Putra Malaysia, 43400 UPM Serdang, Selangor, Malaysia.*

*Corresponding author: sabiusaid1@yahoo.com, nlaily@upm.edu.my

Abstract
Significant research interest has been devoted to dilute magnetic semiconductor due to their promising potentials for spintronic applications. Tremendous attention was given *ZnO* because of its ferromagnetic behavior at room temperature when doped with transition metals. The paper present a synthesis and characterization of $Fe_xZn_{1-x}O$ nanoparticles via microwave assisted method calcined at 600℃. The structural, optical and magnetic properties of these nanoparticles were studied using X-ray diffraction (XRD), Field Emission Scanning Electron Microscopy (FESEM), UV-Visible and Photoluminescence Spectroscopy and Vibrating Sample Magnetometer (VSM) respectively. Single phase Wurtzite hexagonal crystal structure with no agglomerated nanoparticles is observed. The optical property show a blue shift in the band gap of the nanoparticles with three emission observed from the PL. The magnetic measurement reveals a magnetic phase transition from diamagnetic to ferromagnetic behavior as a result of the Fe dopant, the magnetic saturation increases with an increase in the Fe concentration. The material will be good for spintronic applications.

Keywords: ZnO, Fe doped ZnO, structural, optical, magnetic properties.

Introduction
ZnO is a semiconducting material with a wide band gap of 3.37*eV* and large exciting binding energy of 60*meV*, its low cost, nontoxicity, good chemical and thermal stability, and also its magnetic as well as optical property when doped with transition metals like Fe, Co, Ni, Mn makes it to be a potential candidate for spintronic applications [1][2].
Specifically, Fe is selected as a dopant because of being one of the best magnetic activator that has good magnetic, and magneto transport, its ability to tune the optical properties of ZnO material, moreover its ionic radius is highly comparable to that of Zn ion [3].
Zn ions and transition Fe irons are strongly bonded ionically between the metallic ions and the amide group in a polymeric chain. PVP acts as a stabilizer for dissolved metallic salts through steric and electrostatic stabilization of the amide groups of the pyrolidine rings and the methylene groups. PVP decompose to some extent, thereby producing shorter polymer chains that are capped when they are adsorbed onto the surfaces of metallic ions that is well dispersed in the cavities and networks created as a result of the shorter polymer chains [4].

Methodology
ZnO and Fe doped ZnO nanoparticle were synthesized by microwave assisted synthesis method using an appropriate molar ratio of Zinc nitrate hexahydrate ($Zn(NO_3)_2.6H_2O$) as Zinc precursor and ($Fe(NO_3)_3.9H_2O$) as Fe precursor, all the chemicals used are analytical grade. 1g Poly-vinylpyrrolidone PVP (MW= 40,000) as capping agent, was completely dissolved in 20ml of distilled water using a magnetic stirer for 30minutes, an appropriate

molar ratio of $Zn(NO_3)_2.6H_2O$) and ($Fe(NO_3)_3.9H_2O$) was added, the mixture was stirred for 1hour until all the solute dissolved completely. NaOH was used drop wise to control the PH value to 12. The solution was taken to microwave oven for 5 minutes at 380W. The solution was allowed to cool at room temperature after which it has been centrifuged and washed many times with distilled water using 3000rpm for 5 minutes followed by drying in an oven for 24 hour at 60℃. The solid phase was finally grounded to form a nano powder. The powder was calcined in an atmosphere at 600℃ for 2 hours at the rate of 3.1℃/min.

Results and Discussion

Table 1 shows the crystal size, bandgap, coercivity and magnetic saturation of the ZnO and Fe doped ZnO nanoparticles calcined at 600℃.

Table 1: crystal size, bandgap, coercivity and magnetic saturation

Sample	Particle size (nm)	Band gap (eV)	Coercivity (G)	Saturation Magnetisation (emu/g)
ZnO	37	3.25		
$Fe_{0.05}Zn_{0.95}O$	37	3.25	11.07	0.3249
$Fe_{0.1}Zn_{0.9}O$	43	3.23	8.32	0.5803
$Fe_{0.15}Zn_{0.85}O$	32	3.19	3.49	2.3941

Conclusion

Single phase Wurtzite hexagonal crystal structure with no agglomerated nanoparticles is observed. The optical property show a blue shift in the band gap of the nanoparticles with three emission observed from the PL. The magnetic measurement reveals a magnetic phase transition from diamagnetic to ferromagnetic behavior as a result of the Fe dopant, the magnetic saturation increases with an increase in the Fe concentration while its coercivity decreases.

Acknowledgment

The author want to acknowledged the Federal Republic of Nigeria for the complete sponsor of the Research.

References

[1] R. Elilarassi and G. Chandrasekaran, “Structural, optical and magnetic characterization of Cu-doped ZnO nanoparticles synthesized using solid state reaction method,” *J. Mater. Sci. Mater. Electron.*, vol. 21, no. 11, pp. 1168–1173, 2010.

[2] J. M. Zhang, D. Gao, and K. W. Xu, “The structural, electronic and magnetic properties of the 3d TM (V, Cr, Mn, Fe, Co, Ni and Cu) doped ZnO nanotubes: A first-principles study,” *Sci. China Physics, Mech. Astron.*, vol. 55, no. 3, pp. 428–435, 2012.

[3] M. Asemi, B. Mortezapour, and M. Ghanaatshoar, “Structural, Optical, and Magnetic Properties of Hydrothermally Grown Fe-Doped ZnO Nanorod Arrays on Glass Substrate,” *J. Supercond. Nov. Magn.*, vol. 32, no. 2, pp. 269–275, 2019.

[4] A. H. Naseri, M. G, Saion, E. B., Shaari, “Role of PVP on the Phase Composition and Morphology of Manganese Ferrite Nanoparticles Prepared by Thermal Treatment Method,” *Int. Nano Lett.*, vol. 3, pp. 1–19, 2013.

HYDROTHERMAL SYNTHESIS OF VO_2 (M) AND ITS THERMOCHROMIC PROPERTIES

H. M. Barra[1,4], S. K. Chen[1,3*], N. Tamchek[1], Z. A. Talib[1], K. B. Tan[2], O. J. Lee[5]

[1]Department of Physics, Faculty of Science, Universiti Putra Malaysia, 43400 UPM Serdang, Selangor, Malaysia.
[2]Department of Chemistry, Faculty of Science, Universiti Putra Malaysia, 43400 UPM Serdang, Selangor, Malaysia.
[3]Institute of Advanced Technology, Universiti Putra Malaysia, 43400 UPM Serdang, Selangor, Malaysia.
[4]Department of Physics, Mindanao State University-Main Campus, Marawi City, 9700, Philippines
[5]School of Fundamental Science, Universiti Malaysia Terengganu, 21300 Kuala Terengganu, Terengganu, Malaysia.

*Corresponding author: chensk@upm.edu.my

Abstract
In this work, vanadium dioxide, VO_2 (M) was synthesized by annealing hydrothermally-prepared VO_2 (B) at different temperatures and times. Conversion of the metastable VO_2 (B) to the thermochromic VO_2 polymorph was studied using thermogravimetric analyzer (TGA) under N_2 atmosphere. Phase formation and grain morphology of the samples were studied using X-ray diffraction (XRD) and field-emission scanning electron microscopy (FESEM), respectively. XRD patterns of all the annealed samples exhibited the presence of monoclinic VO_2 (M). FESEM images of the samples showed the formation of nanorods and nanospheres, particularly those heated at high temperatures (650 and 700 °C). Meanwhile, differential scanning calorimetry (DSC) was used to measure the phase transition temperature (T_c), hysteresis, and enthalpy of the prepared VO_2. Based on the results, all samples displayed a transition temperature, $T_c \sim 66$ °C. However, the hysteresis is high for the samples annealed at lower temperatures (550 and 600 °C) while the enthalpy is very low for samples heated at lower annealing time (1.5 and 1 h). These findings showed that crystallinity and nanostructure formation affected the thermochromic properties of the samples.

Keywords: Annealing, hydrothermal synthesis, thermochromic, vanadium dioxide.

Introduction
Thermochromic materials exhibit a phase transition from metal to semiconductor at a certain critical temperature, T_c [1]. Vanadium oxide (VO_2) is one of such materials which have been studied intensively due to the fact that its critical temperature is close to room temperature. The phase transition of VO_2 occurs at $T_c \sim 66$ °C. Recently, it has been found that the experimental conditions can affect the morphology and crystallinity of VO_2 [2]. Moreover, the morphology and structure of VO_2 were shown to directly influence its thermochromic and functional properties [3]. Accordingly, we are motivated to study the evolution of VO_2 (M/R) synthesized via hydrothermal method. The effects of annealing condition such as annealing temperature and time on the structure, morphology and thermochromic properties of VO_2 are reported.

Methodology
Sample preparation was carried out using hydrothermal method. Appropriate amounts of V_2O_5 and $H_2C_2O_4$ were dissolved in deionized water. The mixture was later transferred into a Teflon-lined steel autoclave and heated inside an electric oven at 180 °C for 72 h. Then, the resulting precipitate was collected and washed with water and ethanol before drying at 60 °C. Finally, the obtained powder was annealed in the temperature range of 550 - 700 °C

for 1 – 2 hours. The samples were characterized using X-ray diffraction (XRD), field-emission scanning electron microscopy (FESEM), differential scanning calorimetry (DSC) and thermal gravimetric analysis (TGA).

Results and Discussion

TGA analysis showed the evolution of VO_2 (B) to VO_2 (R) at around 320 °C. Based on the XRD patterns, all the annealed samples showed monoclinic VO_2 (M) phase. The sample annealed at 700 °C exhibited further reduction of oxidation state as evidenced in the presence of V_2O_3. DSC measurements showed that all samples have $T_c \sim 66$ °C. The sample annealed at 550 °C displayed the highest hysteresis at 10.66. Meanwhile, the enthalpy of the samples significantly decreased at lower annealing time. These low hysteresis and enthalpy may be due to poor crystallinity and the presence of impurities. The sample annealed at 650 °C for 2 h showed better crystallinity giving rise to better thermochromic properties.

Conclusion

This work shows that enhanced crystallinity via control of annealing condition is crucial for achieving better thermochromic properties of VO_2.

Acknowledgement

We would like to thank the Ministry of Education Malaysia for their financial support under the Fundamental Research Grant Scheme (Project Code: 01-01-18-2006FR).

References

1. Mott N. F., *Metal-Insulator Transitions, 2nd Ed.*, Taylor & Francis Ltd., London, 1990.
2. Alie D., Gedvilas L., Wang Z., Tenent R., Engtrakul C., Yan Y., Shaheen S. E., Dillon A. C. and Ban C., *J. Solid State Chem.,* 212 (2014), 237-241.
3. Chen R., Miao L., Liu C., Zhou J., Cheng H., Asaka T., Iwamoto Y. and Tanemura S., *Sci. Rep.,* 5 (2015), 14087.

EFFECT OF CARBON NANOFIBERS AND CARBON NANOTUBES ADDITION ON THE SUPERCONDUCTING PROPERTIES OF BULK $YBa_2Cu_3O_{7-\delta}$ SUPERCONDUCTOR

N. A. Khalid[1], M. M. Awang Kechik[1]*

[1]*Department of Physics, Faculty of Science, Universiti Putra Malaysia, 43400 UPM Serdang, Selangor, Malaysia.*

*Corresponding author: mmak@upm.edu.my

Abstract
An ultrafine $YBa_2Cu_3O_{7-\delta}$ precursor was prepared by co-precipitation (COP) process. Small amounts (0, 0.2, 0.4 and 0.6 wt. %) of carbon nanofibers (CNFs) and carbon nanotubes (CNTs) were added into Y-123 superconductors. The effects of CNFs and CNTs addition on the critical temperature (T_c) and phase formation were studied. Introduction of CNFs and CNTs have significantly enhanced transport critical current density (J_c). CNFs addition with x = 0.4 wt. % showed the optimal amount as it exhibited the highest T_c and J_c of 88.0 K and 830 A/cm^2 respectively. CNTs addition showed T_c and J_c value of 80.0 K and 477 A/cm^2 for x = 0.2 wt. % which gave the optimal amount for its content in Y-123 superconductor. Most of the samples showed a dominant Y-123 phase of an orthorhombic structure with minor phase of $BaCO_3$ and Y-124. The CNFs-added samples showed a higher J_c compared to the CNTs- added materials.

Keywords: Carbon nanofibers, Carbon nanotubes, Critical current density, Critical temperature, $YBa_2Cu_3O_{7-\delta}$,

Introduction
The observation of superconductivity in the high temperature superconductor (HTS) compound Y-Ba-Cu-O system was discovered in 1986 and this compound has been extensively studied until now. YBCO or named as Y-123 with chemical formula of $YBa_2Cu_3O_{7-\delta}$ was the first ever material with T_c above the boiling point of liquid nitrogen (77 K). The high transition temperature (T_c) can be translated into a lower operation and maintenance cost and thus a wider range of applications [1]. Y-123 superconductor gave huge impacts to the market penetration for power applications [2-4] due to its high T_c.

Over the years, many researches have been carried out to study the superconducting properties of high temperature superconductor [5, 6]. High T_c and J_c value play important roles in the practical application of YBCO. However, there is insufficient and low J_c in YBCO due to weak link effects and weak pinning capability. This work proposes to prepare a good quality of pure YBCO-123 via co-precipitation method. Nanoparticles of CNFs and CNTs are also introduced as the addition to YBCO which can be act as artificial pinning centers. The effects of nano-phase particles from carbon sources into superconductor matrix, is study through the determination of their superconducting properties and the determination of the phase formation of Y-123.
Many successful groups claim that the improvement of J_c in HTS can be achieved by introduction of nanoparticles addition that acts as artificial pinning centers [7]. The effective artificial pinning centers will further enhance a strong Jc at higher fields and higher temperature, which can be obtained when the flux lines are pinned and automatically, their movement will be prevented [8]. In this study, carbon precursor's sources like CNFs and CNTs are particularly interesting due to their nanometer diameter (≈39 – 50 nm and ≈2 nm) respectively, that can serve as the effective pinning centers.

Co-precipitation technique is one of the most widely used methods to produce various kinds of nanoparticles in current industry [9]. It is a method to synthesis ultrafine YBCO powder from saturated solutions of metal acetates and isopropanol solution of oxalic acid. The substance is carried out down through precipitation under the conditions employed. The method involves the separation of a solid containing various ionic species chemically bound to one another from a liquid or a solution [10].

Methodology

Metal acetate (Yttrium, Barium and Copper) and oxalic acid (high purity powders ≥ 99.9 % supplied by Alfa Aesar) are weighed in the appropriate molar ratios with the required stoichiometric ratios of Y^{3+}, Ba^{2+} and Cu^{3+} (1: 2: 3, respectively). The cations are mixed in solution, and then added to 0.5 M oxalic acid dissolved in 2-propanol and distilled water until become precipitated as a mixed oxalate system. Blue precipitated slurry is obtained. The powder then, calcined for 36 hours at the temperature of 900°C. The obtained precursor calcined powders was reground and mixed with several weighed percentages of CNFs and CNTs with x= 0, 0.2, 0.4 and 0.6 wt. %) and pressed into pellets. The pellets then were sintered at 920°C for 45 hours in air. The electrical resistance measurements were carried out by standard four-probe technique, in a closed cycle helium cryostat at temperature between 25 and 300 K. Silver paint was used as contact points between four tiny wires on the sample. Transition temperature (T_c) is the temperature at which the resistance displays a sudden drop. In this measurement, the value of onset critical temperature ($T_{c\text{-onset}}$) and offset critical temperature ($T_{c\text{-offset}}$) were recorded for pure and the added samples. The transport critical current density (J_c) of all the samples was measured by four-probe technique, similar instrument used to determine T_c. The pellets were cut into a rectangular bar shape before being placed onto the sample holder. The transport measurements were carried out at low temperature of 30 K in self-fields which are zero magnetic fields. J_c is the maximum current that can flow through a cross-sectional area, which can be calculated using equation $J_c = I_c/A$, where I_c is the critical current value and A is the cross-sectional area of the bar-shaped samples. I_c can be determined from V-I plotted graph where it is indicated when the voltage started to reach zero. The samples' structure and phase identification were identified by X-ray diffraction (XRD) powder method using a Philips 1710 diffractometer with Cu Kα radiation source. Co-precipitation was chosen as the preparation to synthesis both series of samples which is believed to produce and obtain powders of higher purity and homogeneity.

Results and Discussion

Table 1: $T_{c\text{-onset}}$, $T_{c\text{-offset}}$, ΔT_c, J_c at 30 K, lattice parameters a, b, c and volume fraction of Y-123 for $YBa_2Cu_3O_{7-\delta}$ with addition of carbon nanofibers (CNFs)

Y-CNFs								
x (wt. %)	$T_{c\text{-onset}}$ (K)	$T_{c\text{-offset}}$ (K)	ΔT_c (K)	J_c at 30 K (A/cm^2)	a (Å)	b (Å)	c (Å)	Volume fraction of Y-123 (%)
0	91	86	5	11	3.827	3.886	11.68	96.2
0.2	86	62	24	534	3.827	3.885	11.68	97.6
0.4	88	66	22	830	3.831	3.886	11.68	96.3
0.6	82	50	32	823	3.831	3.888	11.68	94.5

Table 2: $T_{c\text{-onset}}$, $T_{c\text{-offset}}$, ΔT_c, J_c at 30 K, lattice parameters *a*, *b*, *c* and volume fraction of Y-123 for $YBa_2Cu_3O_{7-\delta}$ with addition of carbon nanotubes (CNTs)

Y-CNTs								
x(wt. %)	$T_{c\text{-onset}}$ (K)	$T_{c\text{-offset}}$ (K)	ΔT_c (K)	J_c at 30 K (A/cm^2)	a (Å)	b (Å)	c (Å)	Volume fraction of Y-123 (%)
0	91	86	5	11	3.827	3.886	11.68	96.2
0.2	80	40	40	477	3.834	3.886	11.68	83.0
0.4	76	32	44	263	3.832	3.886	11.67	78.7
0.6	74	24	50	407	3.835	3.888	11.68	75.9

Conclusion

In conclusion, the effect of CNFs and CNTs addition on $YBa_2Cu_3O_{7-\delta}$ bulk superconductors has been analysed and discussed. The addition of CNFs and CNTs in Y-123 system improved the transport critical current density as compared to the pure sample. This study showed that both CNFs and CNTs are found to function as effective flux pinning centers that assist the improvement of J_c in Y-123 host system. However, the CNFs addition is better than CNTs addition for improving the J_c at the highest value up to 830 A/cm^2.

Acknowledgement

This project is funded by the Ministry of Higher Education, Malaysia (MOHE) under the Exploratory Research Grant Scheme ERGS (5527174) and UPM. Grant is gratefully acknowledged.

References

1. Abd-Shukor, R., 2004. Introduction to Superconductivity in Metals, Alloys & Cuprates, Penerbit Universiti Pendidikan Sultan Idris, Tanjung Malim.
2. Khalid, N.A., Awang Kechik, M. M., Baharuddin, N. A., Chen, S. K., Baqiah, H., Mohd Yusuf, N. N., Shaari A. H., Hashim, A., Talib, Z. A., 2018. Impact of carbon nanotubes addition on transport and superconducting properties of $YBa_2Cu_3O_{7-\delta}$ ceramics. Ceramics International. 44(8), 9568-9573.
3. Hawsey, R.A. and D.K. Christen, 2006. Progress in research, development, and pre-commercial deployment of second generation HTS wires in the USA. Physica C: Superconductivity and its Applications. 445–448, 488-495.
4. Dadras, S., 2009. Increase of critical current density with doping carbon nano-tubes in $YBa_2Cu_3O_{7-\delta}$. Physica C: Superconductivity. 469(1), 55-59.
5. Blundell, S., 2009. Superconductivity A Very Short Introduction, Oxford University Press, New York.
6. Frank J. Owens and Charles P. Poole, J., 2002. The New Superconductors, Kluwer Academic, New York, Boston, Dordecht, London, Moscow.
7. Mawassi R., S.M., M. Roumié, R. Awad, M. Korek, I. Hassan, 2014. Improvement of superconducting parameters of $Bi_{1.8}Pb_{0.4}Sr_2Ca_2Cu_3O_{10+\delta}$ added with nano-Ag. Journal of Superconductivity and Novel Magnetism. 27(5), 1131-1142.
8. Kechik, M.M.A., 2010. Improvement of Critical Current Density in $YBa_2Cu_3O_{7-\delta}$ Films with Nano-Inclusions, in School of Metallurgy and Materials, University of Birmingham, Birmingham, 219.
9. Mody, V.V., Siwale, R., Singh, A., & Mody, H. R., 2010. Introduction to metallic nanoparticles. Journal of Pharmacy and Bioallied Sciences. 2(4), 282.
10. Schildermans, I., M.V.B., E. Knaepen, J. Yperman, J. Mullens, L. C. Van Poucke, 1997. Synthesis of the high temperature superconductor $YBa_2Cu_3O_{7-\delta}$ by the hydroxide co-precipitation method. Physica C: Superconductivity. 278, 55-61.

THICKNESS EFFECT ON MORPHOLOGICAL STUDIES FOR SnSe THIN FILM PREPARED VIA THERMAL EVAPORATION TECHNIQUE

J.Y.C. Liew[1,2,*], Z.A. Talib[1], Z. Zainal[2,3], M.A. Kamarudin[1], N. Osman[1], H.K. Lee[1], Y.J. Low[1]

[1]Department of Physics, Faculty of Science, Universiti Putra Malaysia, 43400 UPM Serdang, Selangor Darul Ehsan, Malaysia.
[2]Materials Synthesis and Characterization Laboratory, Institute of Advanced Technology, Universiti Putra Malaysia, 43400 UPM Serdang, Selangor, Malaysia
[3]Department of Chemistry, Faculty of Science, Universiti Putra Malaysia, 43400 UPM Serdang, Selangor Darul Ehsan, Malaysia.

*Corresponding author: josephine@upm.edu.my

Abstract
Tin Selenide is an important IV-VI semiconductor compound which attracted tremendous attention due to it's semiconducting nature and great potential applications. Tin Selenide thin film with 5 different thickness (162.4 nm, 312.2 nm, 475.3 nm, 643.0 nm and 790.0 nm) have been successfully deposited on glass substrate via thermal evaporation technique. The formation of the SnSe thin film has been characterized through X-ray Diffraction (XRD) Technique. The impact of thickness on the morphology of the SnSe film have been studied in detail through the ellipsometer, stylus profiler and atomic force microscopy technique.

Keywords: thickness, morphology, AFM, surface roughness, grain size

Introduction
Metal chalcogenide have attracted considerable research interest due to their outstanding semiconducting and optical properties (Cheng et al., 2017). Tin Selenide (SnSe) binary chalcogenide compounds have been explored due to their promising applications in memory switching, photoelectrical cells, holographic recording system, thermoelectric cooling, optoelectronic devices, radiation detector, solar cells and etc (Ariswan et al., 2017; Narro-Ríos et al., 2018; Shi et al., 2018; Soonmin and Anand, 2015; Urmila et al., 2016). In addition, this materials are nontoxic and consist of economical earth-abundant elements, which are significantly valuable in use for sustainable electronic and photonic system (Shi et al., 2018). Different technique of SnSe thin film preparation have been described in literature, such as atomic layer deposition, chemical bath deposition, vacuum evaporation, chemical vapor deposition, spray pyrolysis, electrodeposition, flash evaporation etc (Afrin et al., 2018; Biçer and Şişman, 2011; Fadavieslam and Bagheri-Mohagheghi, 2013; Hema Chandra et al., 2007; Indirajith et al., 2011; Sabli et al., 2014; Solanki et al., 2017; Zainal et al., 2004). Since the quality of the SnSe thin film are sensitive to the method of preparation, therefore thermal evaporation technique have been chosen in order to produce homogeneous surface and high quality film. The present paper reports the preparation and morphological study of the SnSe thin film in various thickness obtained through thermal evaporation technique.

Methodology
SnSe thin films were physically deposited on microscope glass substrate using the thermal evaporation technique (Auto 306 Edwards). Thermal evaporation is one of the simple physical vapour deposition process which involves resistive heating in vacuum of source material to be evaporated. The pressure during the deposition process was maintained at $(2.0 – 5.0) \times 10^{-5}$ torr as the pressure rose slightly during the actual evaporation. A single layer of SnSe films in various thicknesses have been deposited by varying the weight of

the synthesized SnSe powder. A small quantity such as 0.05, 0.10, 0.15, 0.20 and 0.25 g of source material is loaded into a clean molybdenum boat for evaporation to prepare a series of films with different thicknesses. The XRD patterns of the film were acquired using PANalytical X'pert PRO PW3040 X-ray diffractometer using Cu Kα (λ_w = 1.5418 Å) radiation. The surface morphology and roughness of the thin films were characterized using an atomic force microscopy (AFM) technique (Quesant Q-Scope 250) operated in air at ambient conditions (300 K). High precision ellipsometer system (ELX-02C) using a monochromatic light source (HeNe laser) with single wavelength 632.8 nm was used to determine the thickness and refractive index of the film.

Results and Discussion

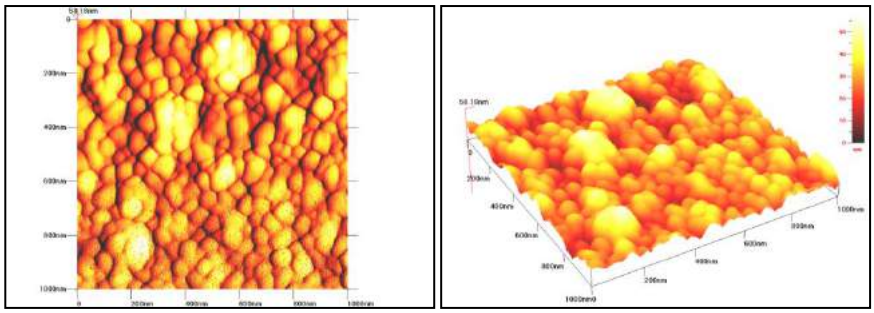

Figure 1: 2D and 3D AFM images for SnSe film with thickness 162.4 nm

Figure 1 show the 2D and 3D AFM images from the surfaces of SnSe thin films with thickness of 162.4 nm. All SnSe films formed by single layer deposition are polycrystalline in nature and composed of a large number of spherical or elliptical grain uniformly distributed throughout the surface. The shape of the films changes from a spherical or elliptical grain to a pentahetron-like structures as the thickness of the film increased. It is also observed that as the thickness of the SnSe film increases, most of the grains grow uniformly on nucleation site produced coalescence of grains distributed all over the surface.

Conclusion

SnSe thin films have been successfully fabricated using the synthesized powder via thermal evaporation technique. The AFM topography revealed that all films fabricated were uniformly distributed with well defined spherical and elliptical grains. It was observed that the average grain size of all SnSe films increase as the thickness of the film increased. The results obtained indicate that the morphological of the SnSe thin films can be influenced by the process conditions and methods during deposition.

Acknowledgement

This work was supported by Ministry of Education and Department of Physics, Faculty of Science, Universiti Putra Malaysia under FRGS (5540133) and Geran Putra (9618700).

References

Afrin, S., Kuperman, N., Solanki, R., 2018. Atomic layer Deposition of 2-dimensional, Semiconducting SnSe Thin Films, 2018 IEEE 13th Nanotechnology Materials and Devices Conference (NMDC). pp. 1-4.

Ariswan, Sutrisno, H., Prasetyawati, R., 2017. Crystal Structure, Optical, and Electrical Properties of SnSe and SnS Semiconductor Thin Films Prepared by Vacuum Evaporation Techniques for Solar Cell Applications. IOP Conference Series: Materials Science and Engineering 202, 012042.

Biçer, M., Şişman, İ., 2011. Electrodeposition and growth mechanism of SnSe thin films. Applied Surface Science 257(7), 2944-2949.

Cheng, L., Li, D., Dong, X., Ma, Q., Yu, W., Wang, X., Yu, H., Wang, J., Liu, G., 2017. Synthesis, Characterization and Photocatalytic Performance of SnS Nanofibers and SnSe Nanofibers Derived from the Electrospinning-made SnO2 Nanofibers Materials Research 20(6), 1748-1755.

Fadavieslam, M.R., Bagheri-Mohagheghi, M.M., 2013. Spray pyrolysis of tin selenide thin-film semiconductors: the effect of selenium concentration on the properties of the thin films. Journal of Semiconductors 34(8), 082001.

Hema Chandra, G., Naveen Kumar, J., Madhusudhana Rao, N., Uthanna, S., 2007. Preparation and characterization of flash evaporated tin selenide thin films. J. Cryst. Growth 306(1), 68-74.

Indirajith, R., Rajalakshmi, M., Gopalakrishnan, R., Ramamurthi, K., 2011. Effects of Annealing on Thermally Evaporated SnSe Thin Films. Ferroelectrics 413(1), 108-114.

Narro-Ríos, J.S., Martínez-Escobar, D., Sánchez-Juárez, A., 2018. Tin Selenide Thin Films Deposited by Ultrasonic Spray Pyrolysis for Photovoltaic Applications, 2018 15th International Conference on Electrical Engineering, Computing Science and Automatic Control (CCE). pp. 1-5.

Sabli, N., Talib, Z.A., Bin, C.C., Yunus, W.M.M., Zainal, Z., Hilal, H.S., Chyi, J.L.Y., Fujii, M., 2014. Deposition and Characterization of SnSe and $CuInSe_2$ Thin Films by Thermal Evaporation Technique from Synthesized SnSe and $CuInSe_2$ Sources. Sains Malaysiana 43(7), 1061–1067.

Shi, W., Gao, M., Wei, J., Gao, J., Fan, C., Ashalley, E., Li, H., Wang, Z., 2018. Tin Selenide (SnSe): Growth, Properties, and Applications. Advanced Science 5(4), 1700602.

Solanki, V.R., Parmar, R.J., Pathak, R.J., Parmar, M.D., 2017. Structural and optical properties of tin selenide thin films prepared by chemical bath deposition method. AIP Conference Proceedings 1837(1), 040019.

Soonmin, H., Anand, T.J.S., 2015. A Review of Chalcogenide Thin Films for Solar Cell Applications. Indian Journal of Science and Technology 8(12), 67499.

Urmila, K.S., Namitha, T.A., Rajani, J., Philip, R.R., Pradeep, B., 2016. Optoelectronic properties and Seebeck coefficient in SnSe thin films. Journal of Semiconductors 37(9), 093002.

Zainal, Z., Saravanan, N., Anuar, K., Hussein, M.Z., Yunus, W.M.M., 2004. Chemical bath deposition of tin selenide thin films. Materials Science and Engineering: B 107(2), 181-185.

SILICA ENCAPSULATION OF PbS QUANTUM DOTS VIA AQUEOUS SYNTHESIS

Hani Syazlin Rosli[1], Josephine Liew Ying Chyi[1], Haslina Ahmad[2], Mazliana Ahmad Kamarudin[1*]

[1]Department of Physics, Faculty of Science, Universiti Putra Malaysia, 43400 UPM Serdang, Selangor, Malaysia.
[2]Department of Chemistry, Faculty of Science, Universiti Putra Malaysia, 43400 UPM Serdang, Selangor, Malaysia.

*Corresponding author: mazliana_ak@upm.edu.my

Abstract
In bio-imaging applications, it is vital for a fluorescent probe to have unique optical properties such as narrow emission bands. Quantum dots (QDs) possess the ability that allow it to be an excellent fluorescent probe. Wet chemical synthesis was used to synthesize PbS QDs whereas silica-capped PbS QDs ($PbS@SiO_2$) was done via a modified Stober method. PbS and $PbS@SiO_2$ QDs were characterized using Fourier-transform infrared (FT-IR) spectroscopy and photoluminescence (PL) spectroscopy to determine their structural and optical properties. The emission spectra shows a blue shift with higher intensity for $PbS@SiO_2$ compared to bare PbS QDs. The performances of colloidal $PbS@SiO_2$ QDs show a promising bio-imaging applications.

Keywords: PbS quantum dots, silica encapsulation, Stober method.

Introduction
The tunability of the emitted wavelength of the QDs makes the QDs desirable for optical purposes such as bio-imaging. However, the surface defects on the QDs may quench the PL intensity and quantum yield. Attempts to overcome this problem include coating the QDs with semiconductors or silica (Postnova *et al.*, 2018). In this study, PbS QDs are synthesized via wet chemical synthesis method whereas Stober method is used for the silanization process. PL and FT-IR were used to characterize the sample emission and to confirm the formation of silica on the surface of the QDs.

Methodology
PbS QDs were synthesized by preparing Pb^{2+} and S^{2-} precursors in the mol ratio of 1:0.3. Under N_2 flow, Pb^{2+}, thioglycerol (TGL), and dithioglycerol (DTG) were stirred homogenously and the pH was adjusted to 10. S^{2-} precursor was added into the solution and the solution was left to stir for 30 minutes. To coat the QDs with silica, a portion of the freshly prepared QDs was diluted with deionized water and Pb^{2+} precursor, TGL, and DTG were added. Then, different volumes of tetraethyl orthosilicate (TEOS) were added slowly into the mixture and stirred for 4 hours.

Results and Discussion

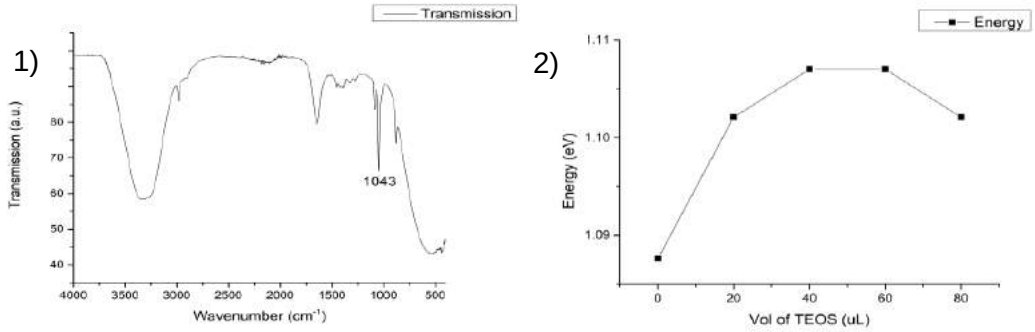

Figure 1: FT-IR spectra of $PbS@SiO_2$
Figure 2: Graph of volume of TEOS versus PL peak energy of $PbS@SiO_2$ QDs

From Figure 1, FT-IR spectra shows a peak in the range of 1000-1100 cm^{-1} which corresponds to the Si-OH and Si-O-Si groups of the silica shell (Ghiyasi *et al.*, 2018). The PL peak energy (Figure 2) of the PbS QDs increased with increasing volume of TEOS, which could be due to the corrosion during the silica deposition process (He *et al.*, 2007).

Conclusion

The PL peak energy of the QDs were increased when PbS QDs are coated with silica. The encapsulation of SiO_2 on PbS QDs also helps in preventing photodegradation, which affects the stability and the intensity of the QDs. Furthermore, the coating also have a potential to prevent Pb^{2+} from leeching into the environment, thus reducing the toxicity of the QDs.

Acknowledgement

The authors would like to thank the Ministry of Higher Education, Malaysia for supporting this research through Putra Grant (VOT: 9567500, 9664000) and FRGS (VOT: 5540137).

References

[1] Ghiyasi, S. *et al*. (2018). Progress in Organic Coatings, 120, 100-109.
[2] He, R., You, X., Shao, J., Gao, F., Pan, B., & Cui, D. (2007). Nanotechnology, 18(31), 315601.
[3] Postnova, I., Voznesenskiy, S., Sergeev, A., Galkina, A., Kulchin, Y., & Shchipunov, Y. (2018). Colloids and Surfaces A: Physicochemical and Engineering Aspects, 536, 3-9.

SYNTHESIS AND CHARACTERIZATION OF PbS QDs CAPPING WITH MnTe SHELL

Nur Diyana Halim[1], Josephine Liew Ying Chi[1], Mazliana Ahmad Kamarudin[1]*

[1]*Department of Physics, Faculty of Science, Universiti Putra Malaysia, 43400 UPM Serdang, Selangor, Malaysia.*
*Corresponding author: mazliana_ak@upm.edu.my

Abstract
PbS quantum dots (QDs) capped with MnTe shell were synthesized in aqueous phase in room temperature. The synthesized of PbS/MnTe core/shell QDs with various shell thickness were characterized by using High Resolution Transmission Electron Microscopy (HRTEM) and Photoluminescence Spectroscopy (PL) to observe their size dependent structural and optical properties. The prepared QDs were systematically investigated and different monolayer of MnTe shell significantly affected the photoluminescence emission. The emission spectra of PbS/MnTe core/shell QDs was blue-shifted compared to bare PbS QDs probably due to the shrinkage of PbS core or strong quantum confinement effect.

Keywords: PbS, PbS/MnTe quantum dots, core/shell

Introduction
Quantum dots (QDs) have been attracting interest due to their great size dependent structural and optical properties. Since that, QDs has been becoming more advantageous in biological applications but required QDs to stable in aqueous solution instead in organic solution which has been costly, time-consuming and hazardous experimental (Dai et al., 2012). Although, due to the surface defects of the QDs, the photoluminescence quantum yields and fluorescence stability may be reduced. However, capping the QDs with shell layer may overcome these problems.

In this paper, PbS/MnTe core/shell QDs with different monolayer of shell capped with thioglycerol (TGL) and dithioglyrcerol (DTG) have been prepared in aqueous media and the structural and optical properties of the QDs were characterized via PL and HRTEM.

Methodology
PbS QDs are were synthesized in aqueous phase followed to procedure as reported (Zaini et al., 2019). Precisely, $Pb(CH_3COO)_2$ (0.190 g), TGL (26 uL) and DTG (10 uL) were dissolved in deionized water and well-mixed under vigorous stirring with nitrogen (N_2) gas. Then, the pH of solution was tuned to 10-11 by added triethylamine. Then, S^{2-} precursor was prepared by dissolved $Na_2S.9H_2O$ (0.120 g) to deionized water. After the preparation of the Pb^{2+} precursor, S^{2-} solution was added and stirred for at least 30 min to form PbS QDs solution. Meanwhile, precursor of MnTe shell was prepared by dissolved (0.060 g) of $Mn(CH_3CO_2)_2{\cdot}4H_2O$, tellurium powder (0.032 g) and $NaBH_4$ (0.05g) in deionized water. After that, the precursor shell of MnTe was added with different volume into the PbS solution to form PbS/MnTe core/shell QDs with different thickness.

Results and Discussion
Figure 1 shows the HRTEM image of PbS QDs. An average diameter of PbS QDs size is 5±1 nm which is smaller compared to the exciton Bohr radius of PbS (~18nm). This lead to the strong confinement effect (Gao et al., 2011).

From the PL, PbS QDs emitted at 1.064 eV. The PL peak is shifted to shorter wavelength (blue-shifted) with increasing MnTe shell thickness as plotted in Figure 2. This indicates the significantly quantum confinement effect which is the shell layer will keep electron and hole confined in the core (Dai et al., 2012).

1)

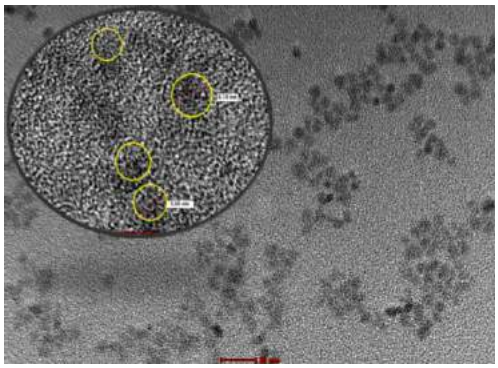

2)

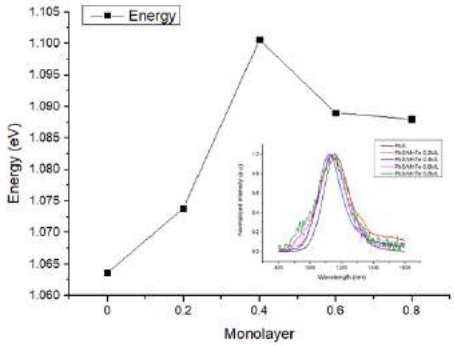

Figure 1): HRTEM of PbS QDs

Figure 2): PL spectra for PbS QDs and PbS/MnTe QDs with different monolayer of shell.

Conclusion

A high energy of PbS QDs capped with MnTe shell with different monolayer were successfully synthesized using aqueous method. The blue-shifted of PbS/MnTe core/shell QDs compared to the bare PbS QDs was attributed to quantum confinement effect. The synthesized QDs was very useful to the biological application due their unique structural and optical properties in near-infrared (NIR) region.

Acknowledgement

The authors would like to thank the Ministry of Higher Education, Malaysia for supporting this research through Putra Grant (VOT: 9567500, 9664000) and FRGS (VOT: 5540137).

References

1. Dai, Meng-Qiao, et al. Journal of Materials Chemistry, vol 22, no.32, 2012, p1636.

2. Cao, Thanh Ha, et al. Journal of Non-Crystalline Solids, vol. 431, 2016, pp. 76–78., doi: 10.1016/j.jnoncrysol.2015.05.006.

3. Gao, F. 2011. Appl Phys Lett 98(193105): 3-6.

4. Zaini, Muhammad Safwan, et al. Sains Malaysiana, vol. 48, no. 6, 2019, pp. 1281–1288.

THE DEGRADATION PHENOMENA OF SLS GLASS DOPED ZnO BASED VARISTOR CERAMICS

Nur Quratul Aini Ismail, Nor Kamilah Sa'at*, Mohd Hafiz Mohd Zaid, Nor Hasanah Isa

Department of Physics, Faculty of Science, University Putra Malaysia, 43400 UPM Serdang, Selangor, Malaysia

*Corresponding author: kamilah@upm.edu.my

Abstract
The investigation of degradation phenomena is an important subject for prolonging their lives. The vulnerability of varistor ceramics to electrical degradation during operation not only affects their nonlinear properties but also leads to shortening of device's lifetime by increasing the risk of failures. In this study, we investigate the degradation process of ZnO_{1-x}-SLS_x-$CoO_{2.0}$ varistor ceramics where x= 0.5, 1.0, 1.5, and 2.0 mol % by using conventional solid state method at sintering temperature of 1100 ˚C for 2 hour. The stability of their nonlinear properties under prolonged application of DC electric field in different concentration of SLS glass was investigated. Degradation process was accelerated by applying direct current (DC) 85 % of electric field for 12 hours at temperature of 85 ˚C. A concentration of 2 mol % SLS glass doped ZnO varistor shows the best degradation properties as its nonlinear coefficient has reduced by 3.56 % reduction, the breakdown field has reduced by 3.85 %, and the leakage current density (J_L) increased by 2.40 % in comparison to its initial value.

Keywords: zinc oxide, SLS glass, varistor, nonlinear coefficient, degradation

Introduction
The development of varistor has challenges to reduce their long term degradation. The degradation usually focused on the steady increase in the leakage current (Clarke, 1999). Previous research report focus on the conventional high voltage Bi_2O_3 varistor ceramics, very little attention has been paid on the degradation phenomena in low-voltage ceramics. In 1980, the degradation phenomena study by Eda et al. (Eda, 1980) and reviewed by Philipp and Levinson in 1983 (Philipp & Levinson, 1983). The aim of this research to investigate the degradation phenomena varied in concentration of SLS glass doped ZnO based varistor ceramics by conventional solid state method.

Methodology

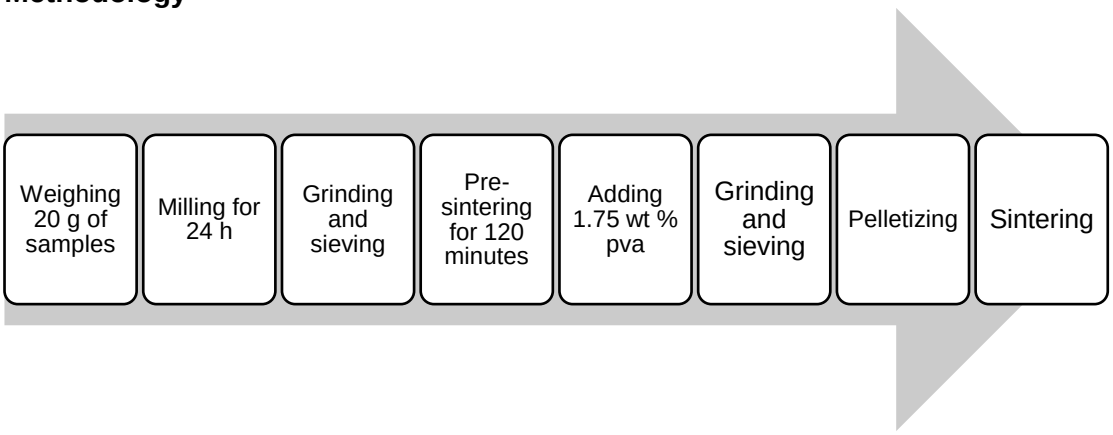

Figure 1: Flowchart of the samples preparation

Results and Discussion

The electrical properties of ZnO_{1-x}-SLS_x-CoO_2 based varistor ceramics before degradation were simplified in the Table 1.

Table 1: The electrical properties before degradation process

Nonlinear coefficient (α)	Breakdown voltage (E_b)	Leakage current (J_L)
5.52	120.39	5.40
5.73	101.57	5.13
6.42	185.74	5.14
6.97	261.14	4.87

Application of stress conditions of 0.85 E_b / 85 ˚C/ 12 hours affected the nonlinear characteristics of ZnO_{1-x}-SLS_x-CoO_2 ceramics. Table 2 indicates the variation of electrical properties of ZnO_{1-x}-SLS_x-CoO_2 ceramics after electrical degradation.

Table 2: Variation in electrical properties due to electrical degradation

Samples (mol%)	Stress condition	$\%\Delta\alpha$	$\%\Delta E_b$	$\%\Delta J_L$
0.5	0.85 E_b / 85 ˚C / 12 hours	-10.52	-4.176	-3.26
1.0	0.85 E_b / 85 ˚C / 12 hours	-22.55	-107.62	+15.63
1.5	0.85 E_b / 85 ˚C / 12 hours	-23.16	-122.69	+11.45
2.0	0.85 E_b / 85 ˚C / 12 hours	-3.56	-3.85	+2.4

The degradation process refers to the steady increase in the leakage current when a varistor constant dc applied. The sign of the degradation included negative (-) decrease while positive (+) increase.

Conclusion

Electrical stability of ZnO_{1-x}-SLS_x-CoO_2 varistor ceramics by conventional solid state method was evaluated. These ceramics exhibited susceptibility to prolonged DC electrical field application. The 2 mol % SLS glass has the %∆Eb -3.85 % after the electrical degradation and also increasing in leakage current +2.4. The value shows below the 10% limit of the allowable variation in Eb for commercial varistor materials.

Acknowledgement

The authors are grateful to the University Putra Malaysia for supporting the work under grant no. GP-IPS/2018/9664200.

References

1. D.R. Clarke, Varistors Cermics, 502 (1999) 485–502.
2. K. Eda, A. Iga, and M. Matsuoka, “Degradation Mecha- nism of Non-ohmic Zinc Oxide Ceramics,”J. Appl. Pbys., Vol. 51, pp. 2678-2684, 1980.
3. H.R. Philipp and L.M. Levinson, “Degradation Phenomena in Zinc Oxide Varistors: A Review,” Advances in Electronic Ceramics, Vol. 7, edited by M. F. Yan and A. H. Heuer, American Ceramic Society, pp. 1-21, 1983.

SYNTHESIS OF ZnO-ZrO_2 BINARY OXIDE NANOPARTICLES BY THERMAL TREATMENT PROCESS

I.M Hamidu [1,2], H.M. Kamari [1*], N. M. Al-Hada [1], C.K. Tim [1.]

[1]*Department of Physics, Faculty of Science, University Putra Malaysia, Serdang 43400, Selangor, Malaysia.*
[2]*Department of Science Laboratory Technology, Federal Polytechnic Mubi, Adamawa State, Nigeria.*

*Corresponding author: hmk6360@gmail.com

Abstract

In this study, the product of ZnO-ZrO_2 binary oxide nanoparticles has been prepared using thermal treatment route. A unique product nanosized is obtained through thermal calcination which contain organic and inorganic materials and different from the bulk. Zinc and Zirconia nitrates were used to prepare $(ZnO)_{0.8}$ $(ZrO_2)_{0.2}$ nanoparticles. Thus, binary oxide $(ZnO)_X$ $(ZrO_2)_{1-X}$ nanoparticles at constant polyvinylpyrrolidone of 4 g, calcined at various temperature was prepared using thermal treatment route. The following characterization of the samples were performed thus; Thermogravimetric analysis was done to determine the thermal behaviour of the precursor and show the required temperature for calcination to occur. The X – Ray diffraction pattern analysis demonstrated that nanoparticles obtained after calcination, indicated a hexagonal crystalline pattern of ZnO and a tetragonal crystalline pattern of ZrO_2 NPs respectively. Transmission electron microscopy (TEM) results indicated an increase in average particle size due to increment in calcination temperature. Furthermore, Photoluminescence (PL) spectra showed an increase in intensity of PL with increase in particle size. The desired structural and optical properties of binary oxide (ZnO) and (ZrO_2) nanoparticles made it a promising material for many applications.

Keywords: binary oxide, nanoparticles, calcination, thermal treatment process

Introduction

Nowadays, nanocrystalline metal oxides have attracted extensive interest owing to their nanoparticle size which is different from their bulk sizes. This encourages researchers from various fields and areas to explore these features ((Kamari et al., 2017) and potential applications ((Varughese et al, 2014; Zhang et al., 2017). The study was conducted to synthesize ZnO and ZrO_2 nanoparticles (NPs). It was found that a hexagonal crystalline ZnO and tetragonal ZrO2 NPs were produced. Hexagonal and tetragonal (ZnO, ZrO_2) nanoparticles are group II-VI composites semiconductors. Thus, the unique properties of ZnO and ZrO_2 nanomaterials obtained in a determined distinctive manner and dimensions of nanoscale size particle can benefit many applications and researches in future.

Methodology

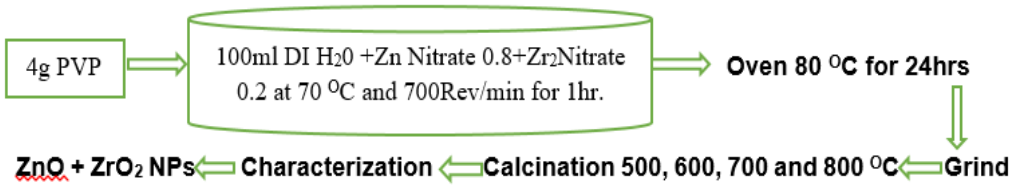

Results and discussion

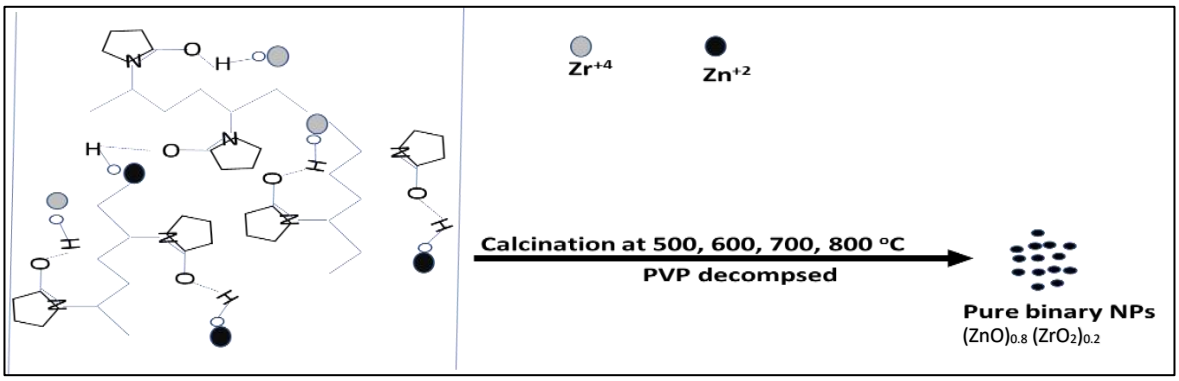

Figure 1. Schematic illustration of mechanism of interaction between metallic ions and polymer (PVP).

As the calcination temperature increase the crystallinity of the metal oxide increase ((Al-Hada et al., 2014). That's why calcination is performed at various temperatures which is in agreement with the XRD result. The crystalline size calculated using Scherrer's equation $D = \frac{0.9\lambda}{\beta Cos\theta}$; Thus, 500, 600, 700, and 800 ^{O}C are 19.8, 23.4, 42.9 and 51.2 nm respectively.

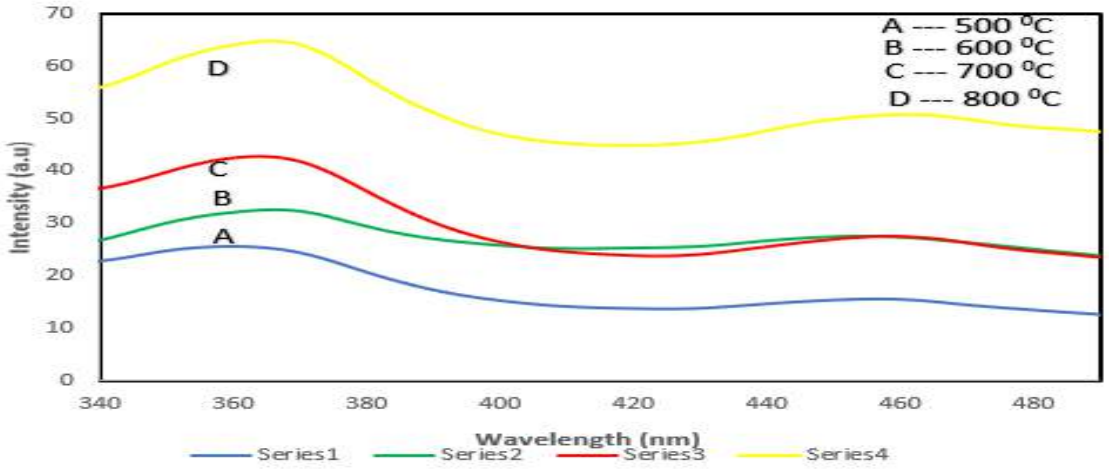

Figure 2. PL spectra of $(ZnO)_{0.8}$ $(ZrO2)_{0.2}$ nanoparticles calcined at various temperatures (a) 500 (b) 600 (c) 700 and (d) 800 ^{O}C respectively.

Conclusion

The metal oxide (hexagonal and tetragonal) $(ZnO)_{0.8}$ $(ZrO_2)_{0.2}$ have been effectively synthesized by thermal treatment process. The outcome showed crystalline nanoparticle increment with an increase in calcination temperature from 19.8 -51.2nm were confirmed from XRD using Scherrer's equation.

Acknowledgement

The authors would like to thank the Faculty of Science, Universiti Putra Malaysia and Geran Putra Berimpak (9597200).

References

Al-Hada, N. M., Saion, E. B., Shaari, A. H., Kamarudin, M. A., Flaifel, M. H., Ahmad, S. H., & Gene, S. A. (2014). A facile thermal-treatment route to synthesize ZnO nanosheets and effect of calcination temperature. *PloS One*, *9*(8), e103134.

Kamari, H., Al-Hada, N., Saion, E., Shaari, A., Talib, Z., Flaifel, M., & Ahmed, A. (2017). Calcined Solution-Based PVP Influence on ZnO Semiconductor Nanoparticle Properties. *Crystals*, *7*(2), 2. https://doi.org/10.3390/cryst7020002

Varughese, G., K.T, U., & A.S, K. (2014). Characterisation and band gap energy of wurtzite ZnO nanocrystallites. *May-Juni 2014*, *3*(3), 133–136.

Zhang, Q. P., Xu, X. N., Liu, Y. T., Xu, M., Deng, S. H., Chen, Y., Xiong, G. (2017). A feasible strategy to balance the crystallinity and specific surface area of metal oxide nanocrystals. *Scientific Reports*, *7*, 1–12. https://doi.org/10.1038/srep46424

STRUCTURAL AND OPTICAL PROPERTIES OF GLASSES BASED ON Li_2O-B_2O_3 GLASS WITH Al_2O_3 AS A MODIFIER AND DOPED Dy_2O_3 SYSTEM

O.B Aljewaw[1], M.K.A Karim[1*], M.H.M Zaid[1], H.M Kamari[1], N.M Noor[2]

[1]Department of Physics, Faculty of Science, Universiti Putra Malaysia, 43400 UPM Serdang, Selangor, Malaysia.
[2]Department of Imaging, Faculty of Medicine, Universiti Putra Malaysia, 43400 UPM Serdang, Selangor, Malaysia.

*Corresponding author: khalis.karim@gmail.com

Abstract
A 23Li_2O-72B_2O_3 (mol%) glass system with Al_2O_3 (5mol %) as modifiers were synthesised and co-doped with different concentrations (0.3 and 0.5 mol %) rear earth of Dy_2O_3. Several series of glasses prepared by the melt-quenching technique. the UV-Vis absorption and the luminescence spectra in this study are found similar to those obtained in the previous research elsewhere. The absorption spectra of Dy^{3+} doped Li_2O-Al_2O_3-B_2O_3 glass corresponds with several bands, the values of optical direct and indirect energy bandgap decrease from 2.76→1.2 eV and 4.02→3.76 eV respectively with an increasing concentration of doped. This research promotes the hypothesis that dopant ions produce new traps and electron sources in the prepared samples which may suit for industrial applications such as dosimetry.

Keywords: Lithium-aluminium-borate glasses; Dy^{+3} ions, UV-Visible absorption, Energy bandgap

Introduction
Optical properties of rare-earth (RE) ions in glass greatly influence by the chemical structure and nature of the glass matrix [1]. Adding alkaline oxides can enhance the borate glass characteristics and even have certain circumstances appears during preparation. Lithium is a major alkali cation, and Al2O3 is a significant modification [2], [3]. The addition of (Al_2O_3) ions to the glass scheme contributes modification in its structural and optical properties [2]. Furthermore, trivalent lanthanide ions are common ions that demonstrate the magnetic, optical and catalytic characteristics of *4f* electrons in lanthanide compounds that have been a long time driving fundamental and applied research because the ions have interesting spectroscopic characteristics. These properties have been widely utilised on laser, radiation dosimeters and other state-of-the-art technologies. Hence, the main aims of this study are to evaluate the refractive index, structural and the optical band gap of various composition of lithium-aluminium borate glass which co-doped with $Dy3^+$.

Methodology
Glass preparation
The series of glasses were prepared by using the melt-quenching technique as given in Table 1. The present composition was prepared based on the proportion suggested: 23 Li_2O–(72-x) B_2O_3– 5Al_2O_3 with x-mol% of Dy^{3+} where x=0.3 and 0.5 .

Materials Characterization
The amorphous phase of the samples was determined by x-ray diffraction (XRD). The UV - Vis - NIR spectroscopy was used to measure the visible and near-ultraviolet region of the samples.

Results and Discussion

Fig. 1 demonstrate the typical X-ray diffraction (XRD) pattern of all different glass concentration glass samples.

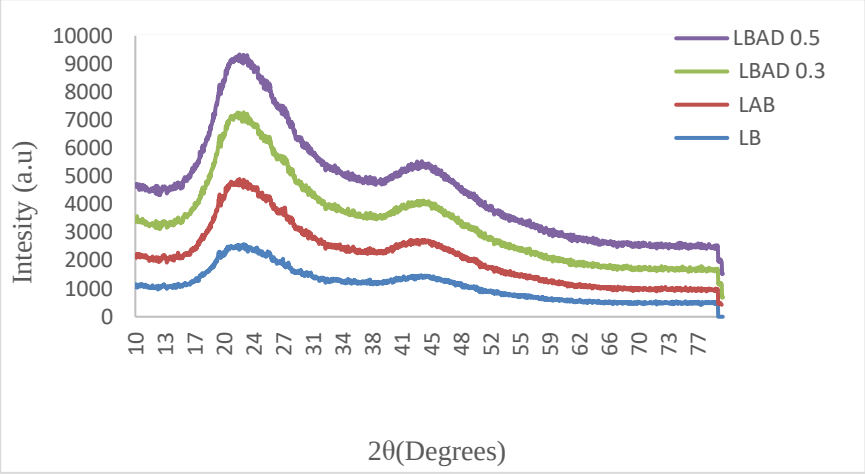

Fig. 1. XRD pattern for Li_2O –B_2O_3 with 5% Al_2O_3 as modifier and different concentrates doped Dy^{3+} ion.

Some of important physical properties that were used to characterize the glass samples are shown in Table 1. The density of the glass is increased, and molar volume is decrease with the increasing of Dy2O3 contents into the glass network.

Table 1 Compositions and some physical properties of prepared glass samples

Sample code	*S1(LB)*	*S2(LB: A)*	*S3(LAB: Dy)*	*S4(LAB: Dy)*
Al_2O_3,%*	-	5	-	-
Dy_2O_3,%*	-	-	0.3	0.5
Density, ρ (g/cm^3)	2.076	2.0825	2.146	2.1673
Molar volume (cm^3/mol)	29.13173	29.81735	29.44149	29.35466
Direct optical band gap (eV)	2.76	1.54	1.45	1.2
Indirect optical band gap (eV)	4.02	3.86	3.81	3.76

* Weight percentage used.

The straight replacement of B_2O_3 by the dopants causes change in boron to oxygen ratio and converts trigonal BO_3 to tetrahedral BO_4 units [3]. The values of optical direct and indirect energy band gap decrease from 2.76→1.2 eV and 4.02→3.76 eV respectively with an increase concentration of doped. This promotes the hypothesis that fresh traps and electron sources are produced by dopant ions in the prepared network [4].

Conclusion

Stable binary glasses using Li_2O-B_2O_3 as network former and Al_2O_3 as network modifier with different concentrate doped Dy^{3+} synthesized by using melt-quenching technique. There was significant modification observed in the optical, structural and physical characteristics of the prepared glass scheme due to various properties in its structure.

References

[1] S. Damodaraiah, V. R. Prasad, S. Babu, and Y. C. Ratnakaram, “Structural and luminescence properties of Dy 3 þ doped bismuth phosphate glasses for greenish yellow light applications,” *Opt. Mater. (Amst).*, vol. 67, pp. 14–24, 2017.

[2] D. T. Dongare & A. B. Lad and Impact Factor, “Electrical Conductivity and Dielectric Relaxation of Lithium Alumino Borate Glasses,” *Int. J. Metall. Mater. Sci. Eng.*, vol. 5, no. 1, pp. 1–8, 2015.

[3] P. P. Pawar, S. R. Munishwar, S. Gautam, and R. S. Gedam, “Physical , thermal , structural and optical properties of Dy3 + doped lithium alumino-borate glasses for bright W-LED Physical , thermal , structural and optical properties of Dy 3 þ doped lithium alumino-borate glasses for bright W-LED,” *J. Lumin.*, vol. 183, no. February 2018, pp. 79–88, 2017.

[4] R. S. E. S. Dawaud, S. Hashim, Y. S. M. Alajerami, M. H. A. Mhareb, and N. Tamchek, “Optical and structural properties of lithium sodium borate glasses doped Dy3+ions,” *J. Mol. Struct.*, vol. 1075, pp. 113–117, 2014.

INFLUENCE OF SILVER OXIDE ON STRUCTURAL AND OPTICAL PROPERTIES OF ZINC TELLURITE GLASS SYSTEM DOPED WITH Sm^{3+} IONS

R. A. Tafida [1,2], M. K. Halimah [1*], F.D. Muhammad [1], K.T. Chan [1].

[1]*Glass and Dielectric Lab, Physics Department, Faculty of Science, Universiti Putra Malaysia.*
[2]*Nigerian Defence Academy, Afaka, PMB 2109, Kaduna, Nigeria.*

*Corresponding author: hmk6360@gmail.com

Abstract
Zinc tellurite glass system co-doped with samarium and silver oxide with composition of $[\{(TeO_2)_{0.7}\ (ZnO)_{0.3}\}_{0.99}\ (Sm_2O_3)_{0.01}]_{1-y}\ (Ag_2O)_y$, y = 0.005. 0.01, 0.015, 0.02 and 0.025 molar fraction are fabricated using melt quenching technique. Structural changes were measured using x-ray diffraction (XRD) and Fourier transform infrared (FTIR). Optical absorption studies were performed via ultra violet visible (UV-Vis) spectrometry. Density was measured using Archimedes' principle while molar volume was calculated. Optical properties such as optical band gap (E_{opt}), Urbach energy (ΔE), molar refraction (R_M), metallization criterion (M), electronic polarizability of the oxide ion (α_o^-) and refractive index (n) have been determined from optical absorption data and were found to be dependent on the glass composition. Optical band gap (E_{opt}) increases from 2.9691 to 3.1054 eV and the Urbach energy, refractive index and polarizability decrease with an increase of Ag_2O content. The XRD and FTIR studies are also carried out to reveal the structural properties.

Keywords: Tellurite glasses, Band gap energy, Samarium oxide, Urbach energy, Silver oxide

Introduction
Tellurite glasses are known for a variety of technological applications due to their important physical properties [1]. In this research, tellurite was selected to be one of the glass former because of its low melting point, good chemical durability, high thermal stability as well as significant rare earth ion solubility [2]. Since tellurite oxide is a conditional glass former the combination of zinc oxide should help in improving the glass forming ability[3]. The addition of silver oxide will leads to the enhancement in the optical properties of the glass network. This work is aim at synthesizing zinc tellurite glass co-doped with samarium and silver oxide and also to study the structural and optical properties of the fabricated glasses.

Methodology
Zinc tellurite glass co-doped with samarium and silver oxide is fabricated with chemical composition of $[\{(TeO_2)_{0.7}\ (ZnO)_{0.3}\}_{0.99}\ (Sm_2O_3)_{0.01}]_{1-y}\ (Ag_2O)_y$, with y = 0.005, 0.01, 0.015, 0.02 and 0.025 molar fraction. The chemical powders (99.99%, Alfa Aesar) of tellurium oxide (TeO_2), zinc oxide (ZnO), samarium oxide (Sm_2O_3) and silver oxide (Ag_2O), are measured for glass fabrication process. The chemical powders are stirred for about 30 minutes. Preheating and melting process was observed at 400°C and 900° C respectively. The molten liquid was poured rapidly into the preheated mould and immediately transferred to annealing process in the first furnace at 400° C for 1 hour 30 minutes. The glasses were polished with sand papers of various grade for other characterization.

Results and Discussion
Density is used in measuring the compactness in the structure of glasses [5]. Archimedes principles is used to obtain the density of each sample. The result show steady increasing trend while the molar volume exhibited a decreasing trend respectively. The increase in

density is due to the replacement of lower molecular weight of TeO_2 by a higher molecular weight of Ag_2O in the glass network while the decreasing molar volume reflect the decrease in free volume of the glass system[6].

Table 1: Density and molar volume of $[\{(TeO_2)_{0.7}(ZnO)_{0.3}\}_{0.99}(Sm_2O_3)_{0.01}]_{1-y}(Ag_2O)_y$ glass system

Molar fraction	Density (g/cm^3)	Molar volume (cm^3/mol)
0.005	5.1999	26.6788
0.01	5.2307	26.6111
0.015	5.2692	26.5053
0.02	5.3158	26.3609
0.025	5.3747	26.1590

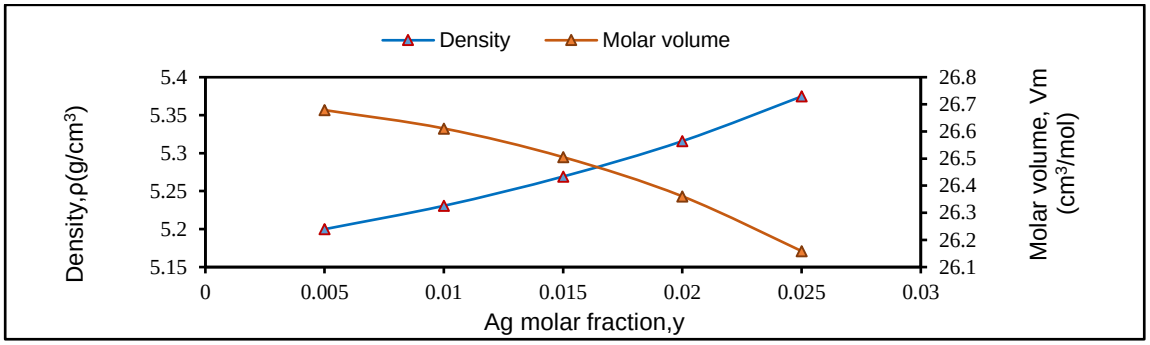

Figure 1: Density and molar volume of $[\{(TeO_2)_{0.7}(ZnO)_{0.3}\}_{0.99}(Sm_2O_3)_{0.01}]_{1-y}(Ag_2O)_y$ glass system

The XRD shows absence of crystalline peaks in the spectra and is amorphous in nature[7]. The IR studies showed that the present glass system consist of five structural units[8]. The Urbach energy and refractive index decrease with increase in dopant. The decrease in Urbach energy indicate the decrease in more defects in the glass system [9].

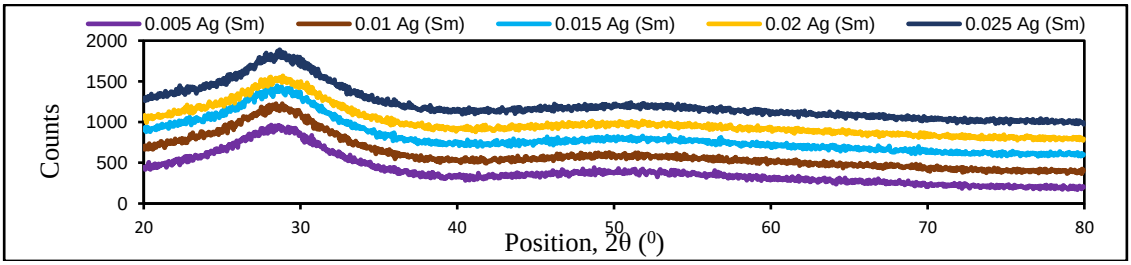

Figure 2: XRD pattern of prepared glass sample with different concentration of dopant.

Conclusion

The structural properties is revealed by FTIR and XRD of the glass material, refractive index as well as the glass Urbach energy is obtained using band gap energy. The refractive index increases while the Urbach energy decreases which is attributed to the creation of more non-bridging oxygen in the glass matrix. The optical properties such as optical band gap, Urbach energy, molar refraction, metallization criterion, electronic polarizability of the oxide ion and refractive index have been determined from optical absorption data and were found to be dependent on the glass composition.

Acknowledgement
The research was reinforced by the Malaysian Ministry of Higher Education and University Putra Malaysia (UPM), Malaysia using Geran Putra Berimpak (vot no. 9597200).

References

[1] G. Upender, C. Sameera, and V. C. Mouli, “Role of WO 3 on DC conductivity and some optical properties of TeO 2 based glasses,” *Mater. Res. Bull.*, vol. 47, no. 11, pp. 3764–3769, 2012.

[2] F. M. Fudzi, H. M. Kamari, F. D. Muhammad, A. A. Latif, and Z. Ismail, “Structural and Optical Properties of Zinc Borotellurite Glass Co-Doped with Lanthanum and Silver Oxide,” pp. 18–23, 2018.

[3] M. K. Halimah, W. M. Daud, H. A. A. Sidek, A. W. Zaidan, and A. S. Zainal, “Optical properties of ternary tellurite glasses,” *Mater. Sci. Pol.*, vol. 28, no. 1, pp. 173–180, 2010.

[4] M. F. Faznny, M. . K. Halimah, and M. N. Azlan, “Effect of Lantahnum Oxide on Optical Properties of Zinc Borotellurite Glass System,” *Optoelectron. Biomed. Mater.*, vol. 8, no. 2, pp. 49–59, 2016.

[5] H. . A. . A. . Sidek, S. . Rosmawati, Z. . A. . Talib, M. . K. . Halimah, and W. M. . Daud, “Synthesis and Optical Properties of ZnO-TeO 2 Glass System,” *Am. J. Appl. Sci.*, vol. 6, no. 8, pp. 1489–1494, 2009.

[6] N. M. Yusoff and M. R. Sahar, “Effect of silver nanoparticles incorporated with samarium-doped magnesium tellurite glasses,” *Phys. B Phys. Condens. Matter*, vol. 456, pp. 191–196, 2015.

[7] M. N. Azlan, M. K. Halimah, S. Z. Shafinas, and W. M. Daud, “Polarizability and Optical Basicity of Er 3+ Ions Doped Tellurite Based Glasses,” *Chalcogenide Lett.*, vol. 11, no. 7, pp. 319–335, 2014.

[8] A. Usman, M. K. Halimah, A. A. Latif, F. D. Muhammad, and A. I. Abubakar, “Influence of Ho3 +ions on structural and optical properties of zinc borotellurite glass system,” *J. Non. Cryst. Solids*, vol. 483, no. October 2017, pp. 18–25, 2018.

[9] P. G. Pavani, K. Sadhana, and V. . C. Mouli, “Optical , physical and structural studies of boro-zinc tellurite glasses,” *Phys. B Phys. Condens. Matter*, vol. 406, no. 6–7, pp. 1242–1247, 2011.

SOLITON MODE-LOCKING IN C-BAND REGION ENABLED BY ZnO NANOPARTICLES COATED ON STRETCHED FIBER

F. D. Muhammad[1]*, S. A. S. Husin[1], C. A. C. Abdullah[1], M. A. Mahdi[2]

[1]Department of Physics, Faculty of Science, Universiti Putra Malaysia, 43400 UPM Serdang, Selangor, Malaysia.
[2]Wireless and Photonic Network Research Centre, Faculty of Engineering, Universiti Putra Malaysia, 43400 UPM Serdang, Selangor, Malaysia

*Corresponding author: farahdiana@upm.edu.my

Abstract
We demonstrate a passively mode-locked erbium-doped fiber laser (EDFL) based on zinc-oxide/polydimethylsiloxane (ZnO/PDMS) saturable absorber (SA) that evanescently interacts with light on a tapered fiber. The ZnO/PDMS composite is coated around the whole surface of the tapered fiber to guarantee the maximum efficiency of the SA device. We achieve this by embedding a tapered fiber in ZnO/PDMS polymer-composite solution and spreading the solution evenly throughout the tapered region for whole surface deposition. The measured insertion loss, modulation depth and saturation intensity of the SA device are 0.87 dB, 6.4% and 4.15 $MWcm^{-2}$ respectively. Subsequently, we propose and demonstrate the use of the fabricated ZnO/PDMS-clad tapered fiber as an SA to generate mode-locked pulses in an EDFL cavity based on evanescent field interaction. The proposed laser is able to generate soliton mode-locking operation at a threshold power of 33.07 mW, with a 3 dB spectral bandwidth of 5.02 nm and a central wavelength of 1558 nm. The generated output pulse yields a repetition rate and pulse width of 9.77 MHz and 1.03 ps respectively.

Keywords: Soliton, mode-locked, C-band, fiber laser, saturable absorber

Introduction
Mode locked fiber lasers are of great interest to researchers due to their ability to generate ultrashort pulses which can find potential applications in various fields, including spectroscopy, basic scientific research, material processing, metrology, telecommunications and biomedical research [1-3]. Recently, zinc-oxide (ZnO) has emerged as a strong candidate to be employed as the saturable absorber due to its superior properties such as large carrier density excitation [4] and high third-nonlinear coefficient [5], making it highly attractive for optical applications. In this paper, we demonstrate the fabrication of ZnO/PDMS polymer-composite wrapped around the whole surface of the tapered fiber to guarantee the maximum efficiency of the nonlinear effect of the ZnO. The ZnO/PDMS-clad tapered fiber is then employed as an SA to realize mode-locked pulse operation in an EDFL based on evanescent field interaction scheme. The measured modulation depth of the SA is 6.4 %, with an insertion loss of 0.87 dB. The proposed laser is able to generate soliton mode-locking operation at a threshold power of 33.07 mW. The generated output pulse yields a repetition rate and pulse width of 9.77 MHz and 1.03 ps respectively. These results indicate that the proposed ZnO/PDMS-clad tapered fiber could be useful as a simple and low-cost SA device for ultrafast laser applications.

Methodology

An EDFL cavity is constructed by employing a section of 5 m EDF, which is pumped by a 980 nm Laser Diode (LD) through a 980 nm port of a fused 980/1550 nm wavelength division multiplexer (WDM). A 80:20 coupler is used for tapping out a 20% portion of the signal for analysis. The remaining signal in the 80% port of the coupler will propagate through the fabricated ZnO/PDMS-clad microfiber which acts as the mode locking element in the laser cavity. A polarization controller (PC) is placed after the SA assembly to adjust the birefringence effect in the laser cavity. The output signal from the PC signal is finally channelled back to the 1550 nm port of the WDM, thus completing the laser resonator. An optical spectrum analyser, oscilloscope, radio frequency spectrum analyser and auto-correlator are used for the analysis of the output pulse performance.

Results and Discussion

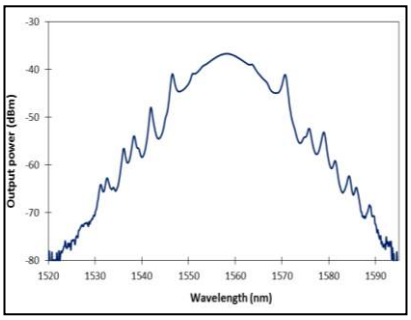

Figure 1: Soliton mode-locked output spectrum from OSA (3 dB bandwidth: 5 nm)

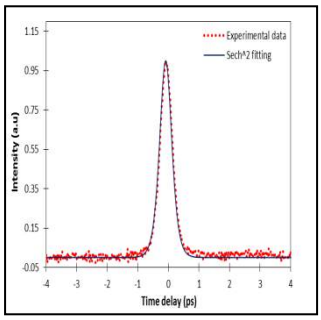

Figure 2: Autocorrelation trace form auto-correlator (Pulse width: 1 ps)

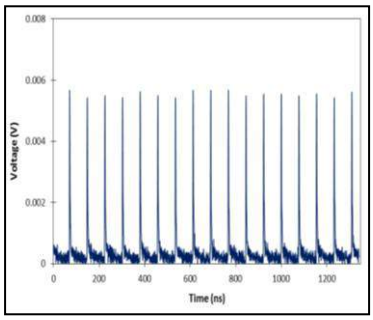

Figure 3: Output pulse train from oscilloscope (Repetition rate: 9.8 MHz)

Conclusion

A passively mode-locked EDFL based on ZnO/PDMS coated on the tapered fiber as the SA has been demonstrated. The proposed SA is able to generate mode-locked pulses in an EDFL cavity based on evanescent field interaction at a threshold power of 33.07 mW, with a 3 dB spectral bandwidth of 5.02 nm and a central wavelength of 1558 nm. The modulation depth and saturation intensity of the fabricated SA device are measured to be 6.4 % and 4.15 $MWcm^{-2}$ respectively. The generated output pulse yields a repetition rate and pulse width of 9.77 MHz and 1.03 ps respectively.

Acknowledgement

We would like to thank the Ministry of Higher Education of Malaysia (MOHE) for providing the grant of FRGS/1/2016/STG02/UPM/02/5 and Universiti Putra Malaysia for providing the grant of GP-IPM/2016/9484300.

References

1. Brida, D., Krauss, G., Sell, A., Leitenstorfer, A., 2014. Ultrabroadband Er: fibre lasers. *Laser Photonics Rev*. 8, 409–428.
2. Keller, U., 2003. Recent developments in compact ultrafast lasers. *Nature* 424, 831–838.
3. Grelu, P., Akhmediev, N., 2012. Dissipative solitons for mode-locked lasers. *Nature Photonics* 6, 84–92.

4. Ahmad, H., Lee, C. S. J., Ismail, M. A., Ali, Z. A., Reduan, S. A., Ruslan, N. E., Ismail, M. F., Harun, S. W., 2016. ZnO nanoparticles as saturable absorber in passively Q-switched fiber laser. *Optics Communications* 381, 72–76.
5. Wang, Z. L., 2014. Zinc oxide nanostructures: growth, properties and applications, *J.Phys.: Condens. Matter* 16, R829–R858.

PASSIVELY MODE-LOCKED FIBER LASER USING GALLIUM-DOPED FIBER AS A GAIN MEDIUM

A. A. Latif[1]*, N. Mohd Radzi[1], N. A. Zazali[1], N. Tamchek[1], M. K. Halimah[1] and A. H. Shaari[1]

[1]Department of Physics, Faculty of Science, Universiti Putra Malaysia, 43400 UPM Serdang, Selangor Darul Ehsan, Malaysia.

*Corresponding author: amirahlatif@upm.edu.my

Abstract
Mode locked fiber lasers are significantly being explored by researchers due to thier potential application in optical communications, optical spectroscopy, laser cutting and laser micromachining. One of the splendid thoughts is to make an adjustment on the graphene layer as a saturable absorber to ensure it functions as a light modulator. In the exploration, we have proposed and shown a passively mode-locked fiber laser utilizing a Gallium co-doped Erbium doped fiber laser as the active gain medium. Graphene fiber was utilized as a saturable absorber in a ring cavity configuration. The distinctive methodology may add to various effects on the beam quality of the pulsed beam produced. The experiment includes the addition of the graphene layer on the fiber ferrules, where the graphene layer will be illuminated by the laser light. This consequently initiates the pulse with a certain amount of modes and dependable on the properties of the laser cavity. The 3 dB spectral widths emitted by the mode-locked laser was 3 nm at 1555 nm regions. The maximum value of average output power was 27 mW with the pulse durations of 860 fs. The pulse train for the proposed Ga-EDF lengths are observed to have a repetition rate of 12.73 MHz, 12.41 MHz and 12.25 MHz for 1.0, 1.5 and 2.0 meter of the Ga-EDF used, respectively. The repetition rates obtained are well matched to the total cavity length of the laser configuration. The proposed plan was extremely straightforward, steady, high bar quality and dependable for various types of utilizations.

Keywords: Mode-Locked Fiber Laser, repetition rate and pulse width.

Introduction
Ultrafast lasers come with numerous applications, such as ultrafast probing, optical fiber communications, nonlinear microscopy, optical coherent tomography, and frequency comb generation [1,2]. The corner stone of ultrafast optics is the mode-locked laser, and development of mode-locked laser has been a huge research field in itself. Fiber laser-based mode-locking generation becomes an interest in going researching due to its strong light confinement over very long distance and the simplicity of gain generation using doped fiber amplifying medium [3-4]. A passively mode-locked erbium-doped fiber laser (MLEDFL) is able to generate pulses of light of extremely short duration on order from picosecond (ps) to femtosecond (fs) pulse duration.

Experimental setup of Mode-Locked Fiber Laser
The proposed erbium-doped fiber laser architecture was tested and investigated by using a ring cavity laser setup as illustrated in Figure 1. A 980 nm laser diode (LD), a wavelength division multiplexer, erbium doped fiber EDF, optical isolators and an optical coupler are used in the experiment, as shown in Figure 1.

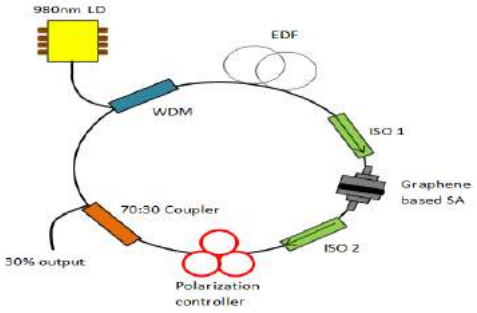

Figure 1. Experimental setup configuration

Results and Discussion

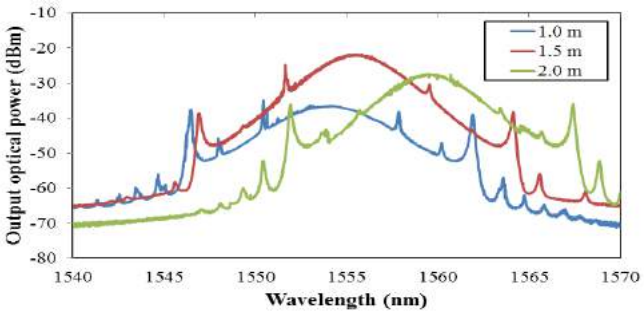

Figure 2. The output spectrum of mode-locked integrated with 1.0 m, 1.5 m and 2.0 meter length of Ga-EDF.

Conclusion

The 3 dB spectral widths emitted by the mode-locked laser was 3 nm at 1555 nm regions. The maximum value of average output power was 27 mW with the pulse durations of 860 fs. The pulse train for the proposed Ga-EDF lengths are observed to have a repetition rate of 12.73 MHz, 12.41 MHz and 12.25 MHz for 1.0, 1.5 and 2.0 meter of the Ga-EDF used, respectively. The proposed design was extremely straightforward and steady for many optical applications.

Acknowledgement

The authors would like to acknowledge the Ministry of Education Malaysia for the project fund No. FRGS/1/2018/STG02/UPM/02/1/5540123 for the financial support given.

References

1. F. Dausinger, F. Lichtner, and H. Lubatschowski, Femtosecond Technology for Technical and Medical Applications, Top. Appl. Phys., (Springer, 2004), vol. 96.
2. U. Keller, “Recent developments in compact ultrafast lasers,” Nature 424(6950), 831–838 (2003).
3. H. Xiu-Jiang, S. Zhan, L. Yong-Zhi, L. Ming-Zhong, L. Hong-Huan, W. Jian-Jun, L. Xin, Z. De-Shuang, and C. Hai-Yan, Research on highly Yb31-doped passive mode-locked fiber ring laser, Microwave Opt Technol Lett 45 (2005), 269–270.
4. F. Haxsen, A. Wienke, D. Wandt, J. Neumann, and D. Kracht, Tmdoped mode-locked fiber lasers, Opt Fiber Technol 20 (2014), 650– 656.

TRANSPORT PROPERTIES FOR RANDOM WALK ON TESSELLATED NETWROK MODEL

N. N. A. Kamal[1], K. T. Chan[1, 2*], N.M. Shah[1, 2], and H. Zainuddin[1, 2]

[1]Laboratory of Computational Sciences and Mathematical Physics, Institute for Mathematical Research (INSPEM), Universiti Putra Malaysia, Malaysia
[2]Department of Physics, Faculty of Science, Universiti Putra Malaysia, 43400 UPM Serdang, Selangor, Malaysia

*Corresponding author: chankt@upm.edu.my

Abstract
Network models are proposed and constructed to mimic the underlying features of some complex systems. Applying a dynamical process such as random walk on different network models provides a good platform to study and understand how the underlying geometrical and structural features influence various transport properties. In this study, we determine mean first passage time, random walk centrality, average trapping time as well as global mean first passage time for the dynamical process on a tessellated network model constructed using tessellation of hyperbolic plane from the modular group. We found that global mean first passage time grows exponentially when the network grows. This is mainly due to some central nodes that have high random walk centrality, which tends to attract the random walker more compared to a node with a lower value. This study plays an important role in determining the performance of the network.

Keywords: Complex networks, Mean first passage time, Random walk, Random walk centrality

Introduction
The world is abundant of complex networks in various field from biology, physics to computer science. Being able to identify unique and special features of complex networks, will be very useful in studying and understanding the complexity of the system itself. Network models are proposed and constructed to mimic the underlying features of some complex systems. Some of the important network models are Erdős–Rényi model [3], Watts–Strogatz model [6], Barabási–Albert model [1], hyperbolic network model [2] and the growing geometrical network [7]. Usually the networks are studied statically or dynamically. In this study, we apply a dynamical process such as random walk on a tessellated network model or growing geometrical network (GGN) constructed using tessellation of hyperbolic plane from the modular group [5]. This dynamical process will enable us to study and understand how the underlying geometrical and structural features influencing various transport properties such as mean first passage time (MFPT), random walk centrality (RWC), average trapping time (ATT) as well as global mean first passage time (GMFPT). Formulating the equation for MFPT using Laplace transform [4] will enable us to compute MFPT value for the network and thus computing for other transport properties as well. By studying these transport properties, we can shed some light about the structure of the network either it being a homogeneous or a heterogeneous network.

Methodology
The growing geometrical network is constructed based on using modular group, a discrete subgroup of *PSL(2,R)* tessellating the hyperbolic plane. To compute the value of MFPT, we use the following equation,

$$\langle T_{ij} \rangle = \begin{cases} \frac{2L}{K_j} \left[R_{jj}^{(0)} - R_{ij}^{(0)} \right] & \text{for} j \neq i \\ \frac{2L}{K_j} & \text{for} j = i \end{cases} \quad (1)$$

where L represents the number of edges, K is the number of degree and R is represented as

$$\tau_j = R_{jj}^{(n)} \equiv \sum_{t=0}^{\infty} \left[P_{jj}(t) - P_j^{\infty} \right] . \quad (2)$$

Results and Discussion

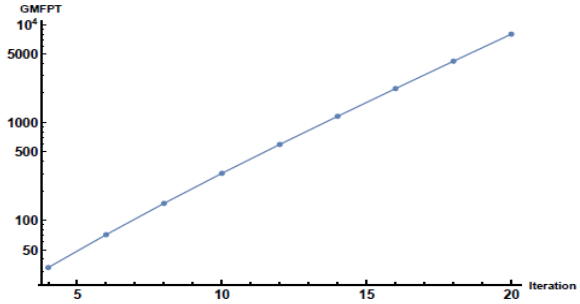

Figure 1: GMFPT against iteration.

From Figure 1, we found that GMFPT grows exponentially when the network grows.

Conclusion

From the computed MFPT, we managed to determine the random walk centrality, average trapping time and global mean first passage time. RWC and ATT have revealed that GGN of interest has heterogeneous structure due to asymmetry in dynamics. From the global perspective, the linear scaling of GMFPT indicates the structure of the networks has a scale-free property.

Acknowledgement

The authors wish to acknowledge the financial support provided through the Fundamental Research Grant Scheme (FRGS), Project No.01-01-16-1865FR by Ministry of Higher Education.

References

1. Albert, R., Jeong, H., and Barabasi, A.-L.(1999). Internet: Diameter of the world-wide web. nature, 401(6749):130.
2. Aste, T., Di Matteo, T., and Hyde, S. (2005). Complex networks on hyperbolic surfaces. Physica A: Statistical Mechanics and its Applications, 346(1-2):20-26.
3. Erdős, P.; Rényi, A. (1959). On Random Graphs. I. Publicationes Mathematicae. **6**: 290–297
4. Samsul, K. N. N. A., Chan, K. T., Mohd, S. N., and Zainuddin, H. (2018). First Passage Time Problem on Growing Geometrical Network, chapter 2, pages 16-23. UPM Press.
5. Taha, M. H. M., Chan, K. T., and Zainuddin,H. (2016). Construction of network based on modular group. Journal of Solid State Science and Technology Letters, (17):93.

6. Watts, D. J. and Strogatz, S. H. (1998). Collective dynamics of `small world networks. nature, 393(6684):440.
7. Wu, Z., Menichetti, G., Rahmede, C., and Bianconi, G. (2015). Emergent complex network geometry. Scientific reports, 5:10073.

ANALYSIS OF MULTIPLE CROSS VALIDATED MAGNETIC FIELD DATASETS FOR ON MUTIPLE DEVICES FOR INDOOR POSITIONING SYSTEM USING kNN ALGORITHM

Caceja Elyca Anak Bundak, Mohd Amiruddin Abd Rahman*, Muhammad Khalis Abdul Karim, Nurul Huda Osman

Department of Physics, Faculty of Science, Universiti Putra Malaysia, 43400 UPM Serdang, Selangor, Malaysia.

*Corresponding author: mohdamir@upm.edu.my

Abstract
Magnetic Field (MF) is a promising technology for Indoor Positioning System (IPS). To estimate location using MF, K nearest neighbour (KNN) algorithm could be applied. However, there was no detail analysis in previous study on how well kNN algorithm performs on MF dataset. Therefore, in this study, we use multiple k-fold cross validation together with multiple kNN algorithm to investigate accuracy of the positioning system. The datasets consist of 2130 samples from two mobile devices. We divide these datasets into k different k-fold (k=2, 4, 5, 8 and 10) and using multiple kNN (k=1, 2, 3, 4 and 5) for estimation. The results show that even when increase the fold, there is not much variation in positioning error. Also, the best positioning accuracy is achieved using small value of k for kNN algorithm in both devices.

Keywords: Indoor positioning; kNN; k-fold cross validation; magnetic field

Introduction
Indoor positioning system (IPS) has gained tremendous interest because it can complement GPS for indoor due to its ability to locate signal. One of the current promising technology for IPS is based on magnetic field (MF). The uniqueness signal of magnetic field stored in mobile devices can be used as fingerprints for indoor localization. This fingerprint is processed by a localization algorithm to estimate the location the user equipment (UE). The state-of-the-art algorithm is using K nearest neighbor (KNN). Previous work has use magnetic field for IPS and improve the algorithm. In [1] used two baseline KNN method which are continuous method and discrete method. The MF measure in continuous method from one point to another point lead to large errors due to estimation cannot be done in one point only. A new maximum likelihood estimation (MLE) algorithm proposed in [2] by using two separated fingerprint maps are utilize and integrated with a novel F-score-based weighting. In this study, we more focus on the dataset variation on multiple device because accuracy rate always biased towards the selected dataset. We also applied multiple K value in KNN in each of the k fold cross validation to analyses the changes in the accuracy rate.

Methodology
We apply datasets in the RFKON database [3] based on two devices namely Samsung Note 10.1 Tablet (device A) and Nexus Tablet (device B). Each measurement location is called as reference point (RP) and the measurement is taken at every grid square of 2.4m x 2.4m. There are 54 RPs and there are 40 MF signals at each RP which gives a total of 2160 samples. The datasets are divided into multiple k-fold where k=2, 4, 5, 8 and 10. We evaluate every chosen fold using multiple nearest neighbor algorithm where k=1, 2, 3, 4 and 5 to estimate the location. We apply kNN based on Euclidean distance to measure

distance between two signals of MF, $m_1 = [m_{x,1}, m_{y,1} m_{z,1}]$ and $m_2 = [m_{x,2}, m_{y,2} m_{z,2}]$ and choose the target location that minimizes the distance using:

$$d(m_1, m_2) = \sqrt{(m_{x,1} - m_{x,2})^2 + (m_{y,1} - m_{y,2})^2 + (m_{z,1} - m_{z,2})^2} \qquad (1)$$

Results and Discussion

Table 1 shows the analysis of kNN using multiple nearest neighbours and cross validation with different devices. The means error for multiple kNN in device A is increasing in each fold cross validation while for device B, the mean error decreases. For figure 1, the comparison between two devices using fix kNN and fold cross validation shows that device A is more accurate than device B. Estimation using K-fold cross validated has lower bias than the holdout method and is cheaper to implement than leave-one-out method [4]. We can observe from the table that the mean errors are stable with the changes in k-fold cross validation. This indicate that the kNN relatively insensitive to the changes in the k fold cross validated datasets.

Table 3:KNN for multiple cross validation in different devices

Device No.	*K value*	Mean Error (m) *k-fold cross validation*				
		2	4	5	8	10
Device A	1	0.1577	0.1578	0.1498	0.1588	0.1504
	2	0.1626	0.1629	0.1634	0.1616	0.1634
	3	0.1623	0.1660	0.1707	0.1728	0.1707
	4	0.1604	0.1657	0.1710	0.1706	0.1710
	5	0.1682	0.1656	0.1705	0.1715	0.1705
Device B	1	0.3259	0.3570	0.3772	0.3655	0.3772
	2	0.3041	0.3162	0.3368	0.3281	0.3368
	3	0.3030	0.3235	0.3212	0.3180	0.3212
	4	0.3078	0.3224	0.3209	0.3232	0.3209
	5	0.3000	0.3150	0.3231	0.3189	0.3231

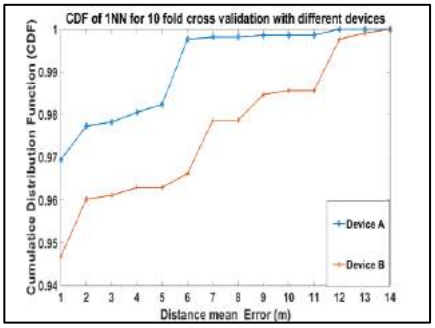

Figure 2:1NN for 2-fold cross validation in different devices.

Conclusion

We analyse the effect of K fold cross validation in selection of datasets and using kNN algorithm to evaluate the accuracy in estimation the location. From our analysis, we could obtain low positioning error using small k value of kNN algorithm. We also study that device A has more accurate in estimation location compares to device B.

Acknowledgement

We would like to thank Ministry of Education, Malaysia for supporting this work through Fundamental Research Grant Scheme (FRGS) by grant number of FRGS/1/2017/TK04/UPM/02/5.

References

[1] J. Torres-Sospedra, D. Rambla, R. Montoliu, O. Belmonte, and J. Huerta, "UJIIndoorLoc-Mag: A new database for magnetic field-based localization problems," *2015 Int. Conf. Indoor Position. Indoor Navig. IPIN 2015*, no. October, pp. 13–16, 2015.

[2] S. B. Keser, A. Yazici, and S. Gunal, "An F-Score-Weighted Indoor Positioning Algorithm Integrating WiFi and Magnetic Field Fingerprints," vol. 2018, 2018.

[3] S. B. Keser, U. Yayan, A. Yazici, and S. Gunal, "A priori verification and validation study of RFKON database," vol. 5, no. 1, pp. 20–27, 2016.

[4] J. Lu, “Classification Accuracy and Model Selection in k- Nearest Neighbors Classifiers for Data Driven Learning,” pp. 1–6.

LOW COST AND GREEN APPROACH IN THE REDUCTION OF GRAPHENE OXIDE (GO) USING PALM OIL LEAVES EXTRACT FOR POTENTIAL BIOMEDICAL AND INDUSTRIAL APPLICATIONS

Amir Faiz Muhd Shaifuddin[a], Che Azurahanim Che Abdullah[a,b*] and Raba'ah Syahidah Azis[a,b]

[a]*Department of Physics, Faculty of Science, Universiti Putra Malaysia, 43400 UPM Serdang, Selangor, Malaysia*
[b]*Material Characterization and Synthesis Lab, Institute of Advanced Technology, 43400 UPM Serdang, Selangor, Malaysia*

*Corresponding author: azurahanim@upm.edu.my

Abstract
Graphene is unique and versatile material which having worldwide reputation due to its unique properties such as very good electrical conductor, tunable band gap, and offers high mechanical strength. The process to derived graphitized carbon into graphene oxide (GO) is a big challenge and chemical method is proven as a good choice to synthesis in the big amount and shorten the time taken. However, the usage of hazardous, toxic and corrosive chemical as reducing agent such as hydrazine to form the sheet layer of graphene will limit the applications due to safety issue. As an alternative, in this research we propose the usage of palm oil leaves extract to replace the chemical use as reducing agent. The as synthesized green approach GO material were characterized using X-ray diffraction, Raman spectroscopy (XRD), Fourier transform infrared spectroscopy (FTIR), f ield emission scanning electron microscope (FESEM), and energy dispersive X-ray (ED X). The results revealed that the interspace distance between layer of carbon increase as graphite fully exfoliated and functional group inserted in between. The reduction of GO using palm oil leave extract have successfully eliminated the oxygen functional group and decrease the interspace distance between layer from the calculated value using Bragg's Law equation. The prepared GO have high potential for various potential biomedical and industrial applications such drug delivery, photocatalyst, and supercapacitor**.**

Keywords: Graphene oxide, reduced graphene oxide, green synthesis.

Introduction
It is well known the graphene oxide (GO) possess an insulator characteristic due to the presence of oxygen functional group interlamellar spaces between the graphene layer. The research reported previously claimed that the insulating GO due to presence of oxygen functional group are unstable as it was pyrolyzed at high temperature (Lv et al. 2009). Hence, a few methods of reduction of GO and chemical reduction using hydrazine, sodium borohydride, and sulphur containing compound among the most common reducing agent. However, hazardous and corrosive chemical such as hydrazine which made it as obstacle for further and bigger scale project (Liao et al. 2011). Since there have been few attempts of the reduction of GO using plant extract such as tea polyphenol, rose water, and clove extract (Liao et al. 2011; Haghighi and Tabrizi 2013; Suresh). The current project will focus on the synthesis of GO using one of the most common method which is the exfoliation and oxidation of graphite using modified Hummer's method (Paulchamy et al. 2015) and the reduction of the synthesized GO using palm oil leaves extract as reducing agent. The calculation using Bragg's Law equation shows the increase of interplanar distance with presence of oxygen functional group in GO structure. Moreover, the reduction will eliminate the oxygen functional group hence the layer of graphene will be stacked and move closer to each other. Herein, the result of X-ray diffraction (XRD), Raman spectroscopy, Fourier

transform infrared spectroscopy (Ftir), field emission scanning electron microscope (FESEM), and energy dispersive X-ray (EDX) will be discussed this paper.

Methodology

Synthesis of graphene oxide (GO)

Commercial graphite was chosen in our experiment. The graphite was exfoliated and oxidized using modified Hummer's method.

Preparation of reduced graphene oxide (rGO)

The palm oil leaves extract was prepared followed using method from Zhu et al. (2017) with minor modification. The as-prepared extract was mixed with GO powder and was refluxed in water bath for 10 hours. Ammonium hydroxide was used to maintain pH at basic range. The dried powder was then collected and washed using deionized water few times until pH level 7 achieved. The final powder was dried in an oven for 24 hours.

Results and Discussion

X-ray diffraction characterization

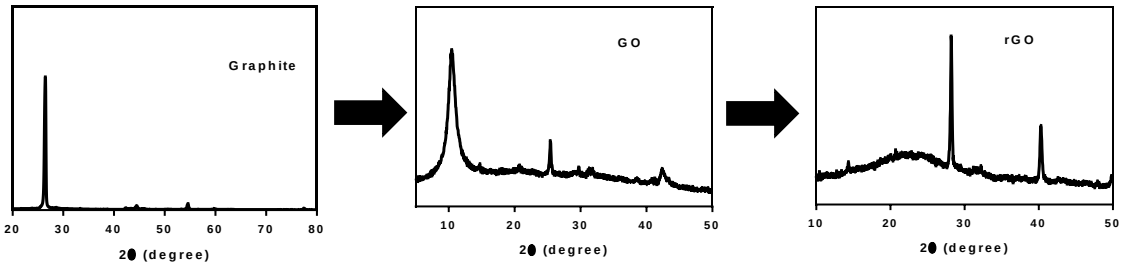

Figure 3: X-ray diffraction of changes of peak from graphite to GO and then rGO.

Table 4: distribution of 2θ of samples with calculated distance between layer using Bragg's Law

Sample	2θ (degree)	Distance between layer (nm)
Graphite	26.6°	1.72
GO	10.4°	4.27
rGO	28.2°	1.63

Conclusion

This work concluded that the exfoliation and oxidation of graphite to form GO has been successfully prepared. The reduction agent which is palm oil leaves extract have been effectively helping which resulting in the elimination of oxygen functional group and proven via the decrease in interlayer distance value. The finding suggests the restoration of structure to form a graphene layer. Reduced GO that mimic graphene layer is very useful for various application due to conductive properties of the prepared nanomaterials. The future work of current research will focus on the different degree of oxidation of GO using various methods. The degree of reduction will be exploring in the near future using green approach by using other plant extracts and their potential biomedical and industrial applications will be tested.

Acknowledgement
The authors would like to thank NANOTEDD team of Biophysics Lab and Department of Physics, Universiti Putra Malaysia for the assistance. We also thankful to Ministry of Education Malaysia via FRGS funding (FRGS 5524249) for financially support this project.

References

1. Haghighi, Behzad; Tabrizi, Mahmoud Amouzadeh (2013): Green-synthesis of reduced graphene oxide nanosheets using rose water and a survey on their characteristics and applications. In *RSC Adv.* 3 (32), p. 13365. DOI: 10.1039/c3ra40856f.
2. Liao, Ruijuan; Tang, Zhenghai; Lei, Yanda; Guo, Baochun (2011): Polyphenol-Reduced Graphene Oxide: Mechanism and Derivatization. In *J. Phys. Chem. C* 115 (42), pp. 20740–20746. DOI: 10.1021/jp2068683.
3. Lv, Wei; Tang, Dai-Ming; He, Yan-Bing; You, Cong-Hui; Shi, Zhi-Qiang; Chen, Xue-Cheng et al. (2009): Low-temperature exfoliated graphenes: vacuum-promoted exfoliation and electrochemical energy storage. In *ACS nano* 3 (11), pp. 3730–3736. DOI: 10.1021/nn900933u.
4. Paulchamy, B.; Arthi, G.; BD, Lignesh (2015): A Simple Approach to Stepwise Synthesis of Graphene Oxide Nanomaterial. In *J Nanomed Nanotechnol* 06 (01). DOI: 10.4172/2157-7439.1000253.
5. Suresh, D.: Clove extract mediated facile green reduction of graphene oxide, its dye elimination and antioxidant properties.
6. Zhu, Xin; Xu, Xiaolin; Liu, Feng; Jin, Jizhong; Liu, Lintao; Zhi, Yi et al. (2017): Green synthesis of graphene nanosheets and their in vitro cytotoxicity against human prostate cancer (DU 145) cell lines. In *Nanomaterials and Nanotechnology* 7, 184798041770279. DOI: 10.1177/1847980417702794.

ELECTRICAL CONDUCTIVITY STUDY OF SODIUM BASED CHITOSAN CONDUCTING POLYMER WITH DIFFERENT TYPES OF CONDUCTIVE FILLER

N.N. Mazu[1], M.A.H. Mohd Abdul Majid[1], N.H. Osman[1] and J.Y.C Liew[2]

[1] Applied Electromagnetic Lab I, Department of Physics, Faculty of Science, Universiti Putra Malaysia, 43400 UPM Serdang, Selangor, Malaysia.
[2]Electrical Properties Laboratory, Department of Physics, Faculty of Science, Universiti Putra Malaysia, 43400 UPM Serdang, Selangor, Malaysia.

*Corresponding author: nurulhuda@upm.edu.my

Abstract
Sodium based chitosan (CS/Na^+) conducting polymer was prepared with five different types of filler and the suitability are tested based on its electrical conductivity. The sodium based chitosan polymer was prepared by mixing the chitosan powder with sodium ion solution (Na^+) and the selected filler is added to the mixture in order to further improve the electrical properties of the composite. The filler selected for this work are Copper (II) Selenite (CuSe), Iron (III) oxide (Fe_3O_4), Reduced Graphene Oxide (rGo), Zinc Oxide (ZnO) and Fe-doped ZnO (FeZnO). The sodium based chitosan polymer with CuSe filler shows the highest electrical conductivity which is 0.52 S/cm, followed by FE_3O_4, rGo, ZnO and FeZnO.

Keywords: conducting polymer, conductivity, sodium ion, chitosan

Introduction
In the recent year, works on using polymer with conductive filler to replace pure metal have been on the rise. Chitosan (CS) polymer is a dielectric in its initial state. Having metal ions, salts and/or other conductive filler in the chitosan polymer improved the conductivity and decreased the resistivity. This changes the chitosan polymer from pure dielectric to a dielectric-conductor composite. When the conductive filler is increased to a sufficiently high content within the polymer, a conductive path is formed and makes the composite free electrons easy to travel and eventually increases the electrical conductivity to high levels (Mamunya et al., 1996). At percolation, the polymer will behave more like a metal than a dielectric.

Methodology
Sodium based chitosan polymer was prepared by direct casting technique. 0.5 g of medium molecular chitosan flakes with a deacetylation degree of 75-85% (Sigma Aldrich) were dissolved in 25 ml of 100 mg/l of Na^+ solution. 1% acetic acid was then added to the solution and stirred for 24 hours to obtain a homogeneous solution. The filler was prepared by mixing 0.1 % (w/v) of filler into water before being sonicate for 2 hours. 1 wt% of glycerol was added into the chitosan solution before mixing with filler and the solution was stirred for 24 hours. The final solution was directly cast and allowed to dry at 60 ˚C for 24 hours. 6 samples were prepared in total. One having no filler (based polymer) and each for CuSe, Fe_3O_4, rGo, ZnO and FeZnO filler.

The impedance measurements were conducted using Rohde & Schwarz HM8118 LCR meter at frequencies ranging from 20 Hz to 200 kHz at room temperature. The polymer was placed between two stainless steel electrodes of 1 cm diameter under constant pressure.

Results and Discussion

Figure 1 shows the impedance plot for all 6 samples of CS/Na^+ polymer. The impedance plot for all sample show spike behaviour without semicircle present. The absence of the semicircle suggests that the polymer is very conductive and only resistive component exists in the polymer. Using the linear fitting, the bulk resistance (R_B) value of each polymer is determined. Table 1 shows the conductivity value for all the polymer.

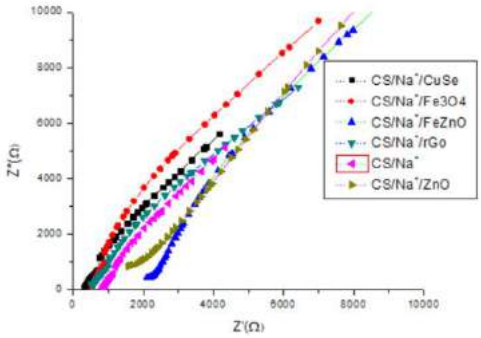

Figure 1: Impedance plot for CS/Na^+ polymer with different filler

Table 1 shows that by adding certain filler, the conductivity of the based polymer improved as compared to the sodium based chitosan polymer with only Na^+ as filler. This is due to the filler such as CuSe, Fe_3O_4 and rGo is known to have good conduction. There are however two fillers which is ZnO and FeZnO which decreased the conductivity as compared to the sodium based polymer without filler. ZnO and FeZno are a semiconductor material with lower conductivity. The conductivity of conducting polymer depends on filler type, shape, size, and filler dispersion and distribution in the polymer (D. C. Deborah, 2010).

Table 1: Thickness, bulk resistivity and conductivity for all polymer with respective filler

Polymer	Filler	Thickness (mm)	Bulk Resistance R_B (Ω)	Conductivity σ (S/cm)
CS	-	0.116	2.01×10^{6}	7.32×10^{-5}
CS	Na^+	0.174	825.21	0.268
CS/Na^+	CuSe	0.115	280	0.523
CS/Na^+	Fe_3O_4	0.189	508.64	0.473
CS/Na^+	rGo	0.100	418.99	0.304
CS/Na^+	ZnO	0.128	1028	0.159
CS/Na^+	FeZnO	0.141	1966.51	0.091

Conclusion

The conductivity study shows that adding Na^+ into the CS polymer increased the conductivity from 7.32×10^{-5} to 0.268 S/cm. It is also shown that that CuSe and Fe_3O_4 filler are the best filler to improve the conductivity in Cs/Na^+ polymer. Further investigation will be conducted to determine the right amount of filler needed to further improve the conduction of CS/Na^+ polymer.

Acknowledgement

We would like to acknowledge the Ministry of Education Malaysia under the Fundamental Research Grant (FRGS/1/2018/SRG07/UPM/02/6) for supporting this work.

References

1. D. C. Deborah (2010), Composite materials: science and applications, Engineering Materials and Processes.
2. Mamunya, E., Davidenko, V. and Lebedev, E. (1996). Effect of polymer-filler interface interactions on percolation conductivity of thermoplastics filled with carbon black. Composite Interfaces, 4(4), pp.169-176.

MANGANESE DIOXIDE NANOSTRUCTURE AS AN EFFICIENT SUPERCAPACITOR ELECTRODE MATERIAL

N. A. Zulkifli[1], K.S.Lau[2], C.H. Chia[2], Z. A. Talib[1], S. T. Tan[1*]

[1]Department of Physics, Faculty of Science, Universiti Putra Malaysia, 43400 UPM Serdang, Selangor, Malaysia.
[2]School of Applied Physics, Faculty Science and Technology, Universiti Kebangsaan Malaysia, 43600, UKM Bangi, Selangor, Malaysia.

*Corresponding author: tansintee@upm.edu.my

Abstract
Manganese oxides (MnO_2) have been considered as one of the attractive electrode material in pseudocapacitor device due to its tunable morphology from dimensionless to 3-dimension, superior conductivity and high theoretical specific capacitance. There are few methods deployed in synthesizing MnO_2 nanostructures. The hydrothermal process is the most conducted method owing to its simplicity, environmental friendly and stable process. In this work, the morphology of MnO_2 nanostructures is controlled in term reaction growth. The morphology of MnO_2 nanostructures is successfully transformed from nanoflowers to nanowires. The sheet resistance of the nanowires reduced from 3300 kΩ to 610 kΩ. The optimum nanowires based devices present a specific capacitance of 312.5 Fg^{-1}. This novel method provides an alternative approach in designing a green electrode technology.

Keywords: nanowires, nanoflower, hydrothermal, electrode, supercapacitor

Introduction
The shortcomings of the latest battery design with a comparable slow charging and, fast discharge rate as well as a rigid solid framework eventually limited the development of storage material. Therefore, it is crucial to investigate the flexible, high capacitance and power delivery energy storage device such as supercapacitor. Manganese dioxide is a common electrode material used in supercapacitor because of its high theoretical capacitance up to 1370 Fg^{-1} (Hu et al., 2011). However, it still suffered from low specific capacitance and stability due to its poor electrical conductivity and high leaching rate. In order to address these problems, many efforts have been made by controlling the physicochemical properties of MnO_2 nanostructure. There are several morphologies are successfully synthesised such as nanoneedles, nanorods, nanowires (Wang et al., 2018, Gaoa et al., 2018, Shah et al., 2018) . It is noted that the specific capacitance of the devices is associated with the electrode dimension and wettability properties (Chi et al, 2015). Therefore, in this project, a homogeneous and morphology controlled manganese dioxide nanostructures were conducted using a conventional hydrothermal method. The mutual correlation between the structural and electrical properties of MnO_2 electrode in the device performance is also elucidated in this project. It is noted that the morphology of MnO_2 is successfully transformed from there dimensional nanoflower to the one-dimensional nanowire. The optimum MnO_2 nanowires based devices recorded the specific capacitance of 312.5 Fg^{-1} at a scan rate of 0.1A/g. This project provides an alternative approach in designing a stable and flexible energy storage device.

Methodology
Manganese dioxide nanostructures were synthesized via the hydrothermal method. The precursor aqueous solution consisted of potassium permanganate ($KMnO_4$, Sigma Aldrich, 99%) and ammonia fluoride (NH_4F, Sigma Aldrich), as a reducing agent. In detail, a 0.04

M of the precursor source was dissolved in deionized water (18.2 MΩ) with the stirring rate 250 rpm for 5 minutes. After that, the mixture was transformed into autoclaves chamber and subjected to a hydrothermal growth process at 180°C for a different reaction time of 1 and 2 hours. The sediment of the MnO_2 powder was collected and used as an electrode material for supercapacitor applications. In the device fabrication, the electrode material was prepared in the form of PVDF:NMP slurry paste with the mixture ratio of (7:2:1). The paste was then coated on carbon cloth and heated at 110°C for 2 hours in the vacuum oven. The morphological properties were characterized by using field emission scanning electron microscopy (FESEM, ZEISS Merlin) that operated in an accelerating voltage of 3 KeV. The sheet resistance of the sample was measured a four-point probe set up (KeithLink Technology). The electrochemical measurement of the device was characterized using a three-electrode system (Ivium Technology) that operated in the applied bias from 0 V to 0.8 V.

Results and Discussion

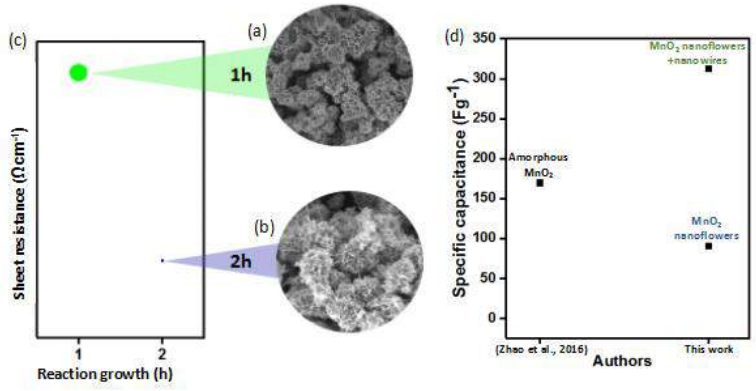

Figure 1: a) FESEM images of MnO_2 nanostructures for 1-hour reaction growth ; b) FESEM images of MnO_2 nanostructures 2 hours MnO_2 reaction growth; c) Bubble plot for the sheet resistance of MnO_2 growth in different reaction time; (d) Region plot of MnO_2 structures

Based on figure 1 (a) and (b), the morphological of manganese dioxide were characterized by FESEM analysis. It is observed that the nanostructures possess a different shape and dimension. For 1-hour reaction time, a nanoflowers was formed. In another note, a combination of nanowires and nanoflower was found in 2 hours of reaction time. This phenomenon can be explained via the oriented attachment process occurred during the crystal growth process. The sheet resistance of the sample was also measured using the Four-point probe measurement. The results are presented in the bubble plot and shown in Figure 1 (c) It is noted that the sheet resistance of the sample decreased from 3300 kΩ to 610 kΩ when the reaction time increased from 1 hour to 2 hours. This observation signified the better conductivity obtained from nanowires samples. The as-prepared sample was later subjected to the supercapacitor device analysis. It is found that the nanowire dominated sample recorded a high specific capacitance as compared to nanoflower sample which is of 312.5 Fg^{-1} and 90.9 Fg^{-1} at 0.1 Ag^{-1}.

Conclusion

The morphological MnO_2 nanostructures play a vital rule in determining the specific capacitance of energy storage devices. In this study, the MnO_2 was synthesis by the hydrothermal method in the function of reaction time. It was found that morphology of MnO_2 nanostructures changed from nanoflowers to nanowires. The sheet resistance of the

sample was reduced from 3300 kΩ to 610 kΩ when the reaction time increased from 1 hour to 2 hours. Nanowires dominated samples presents a higher specific capacitance of 312.5 Fg^{-1} at a scan rate of 0.1Ag^{-1}. These novel results provide an alternative design in future electrode technology.

Acknowledgement
This project is financial support by Universiti Putra Malaysia under research grant of GP-IPM/2019/9673800.

References

1. Chi, H. Z., Zhu, H., Gao, L. (2015). Boron-doped MnO_2/carbon fibre composite electrode for supercapacitor. *Journal of Alloys and Compounds*. 645. 199-205.
2. Gaoa, Q., Wanga, J., Kea, B., Wanga, J., & Lib, Y. (2018). Fe doped δ- MnO_2 nanoneedles as advanced supercapacitor electrodes. *Ceramics International*, 44(15), 18770-18775.
3. Hu, Z., Xiao, X., Chen, C., Li, T., Huang, L., Zhang, C., Su, J., Miao, L., Jiang, J., Zhang, Y., Zhou, J. (2015). Al-doped α-MnO_2 for high mass-loading pseudocapacitor with excellent cycling stability. *Nano Energy*.11. 226-234.
4. Shah, H. U., Wang, F., Javed, M. S., Saleem, R., Nazir, M. S., Zhan, J., Khan, Z. U. H., Farooq, M. U., Ali, S. (2018). Synthesis, characterization and electrochemical properties of α- MnO_2 nanowires as electrode material for supercapacitors. *International Journal of Electrochemical Science*. 13(7). 6426-6435.
5. Wang, F. M., Xu, G. W., & Jin, C. C. (2018). Synthesis and electrochemical performance for supercapacitors of Bi-doped *α*-MnO_2 nanorods. *Chemical Journal of Chinese Universities*, 39(3), 530-536.
6. Zhao, Y., Misch, J., Wang, C. A. (2016). Facile synthesis and characterization of MnO_2 nanomaterials as supercapacitor electrode materials. *Journal of Materials Science*: Materials in Electronics. 27(6). 5533-5542

PHOTOELECTROCHEMICAL PERFORMANCE OF γ IRRADIATED g-C_3N_4 AND g-C_3N_4@$BiVO_4$ HETEROJUNCTION FOR SOLAR WATER SPLITTING APPLICATION

Nurul Aida Mohamed[1], Mohd Asri Mat Teridi[1]*

[1] Solar Energy Research Institute (SERI), Universiti Kebangsaan Malaysia (UKM), 43600 Bangi, Selangor, Malaysia.

*Corresponding author: asri@ukm.edu.my

Abstract
The structure and morphology of g-C_3N_4@$BiVO_4$ as a heterojunction were analyzed and verified from the correlation of experimental and theoretical data. It is found that γ radiations have changed the bonding structure of g-C_3N_4, which ultimately reduces the optical band gap energy. Moreover, the performance of γ irradiated g-C_3N_4 is two-fold, compared to that of the non -irradiated one, and increases from 3.59 to 5.86 μA cm^{-2} at 1.23 V versus Ag/AgCl in 0.5 M Na_2SO_4 electrolyte solution (pH 7). Finally, it is observed that the performance of γ irradiated g-C_3N_4 in the g-C_3N_4@$BiVO_4$ heterojunction increased from 0.53 to 1.38 mA cm^{-2}, compared to that of the nonirradiated one. In summary, it has been concluded that γ irradiated g-C_3N_4 and its heterojunction can potentially be applied in PEC solar water splitting.

Keywords: *g-C3N4; energy band gap; gamma radiation; water splitting*

Introduction
The g-C_3N_4 can be synthesized through nitrogen-rich precursors such as cyanamide, dicyandiamide, melamine, thiourea, and urea. However, under visible light radiation, the g-C_3N_4 exhibits weak photocatalytic activity due to its moderate band gap (2.7 eV). γ irradiation was employed on g-C_3N_4 to improve the PEC performance, whereas BiVO4 as the heterojunction was preferred as a potential material to reinforce its performance in water splitting application. Herein, the g-C_3N_4 was irradiated with γ radiation before being deposited onto a substrate through a spin coating method. Then, in a separate experiment, $BiVO_4$ was deposited as the heterojunction through electrodeposition. To better utilize solar radiation for the improved photocatalytic activity, these two strategies, γ radiation and heterojunction, were employed.

Methodology
Materials
Urea (CH_4N_2O, ACS reagent 99.0%–100.5%), methanol (CH_3OH), R&M chemical, were purchased from Sigma Aldrich. Sodium sulphate (Na_2SO_4,>98.0%) were purchased from R&M chemicals. Bismuth (III) nitrate ($Bi(NO_3)_3{\cdot}5H_2O$, ≥98.0%) and vanadium(IV) oxide sulfate ($VOSO_4{\cdot}xH_2O$, 97%) were purchased from Sigma Aldrich. Nitric acid (HNO_3, 69%), potassium hydroxide (KOH, pellets), and sodium sulfate

Urea (3 g) was grinded and poured into a 50 mL alumina crucible with a cover (lid) and was heated in air. A temperature of 520 °C was used for 30 min for thermal polymerization from urea to g-C_3N_4. Synthesis of $BiVO_4$. The electrodes of $BiVO_4$ were prepared by an electrodeposition procedure.

Results and Discussion

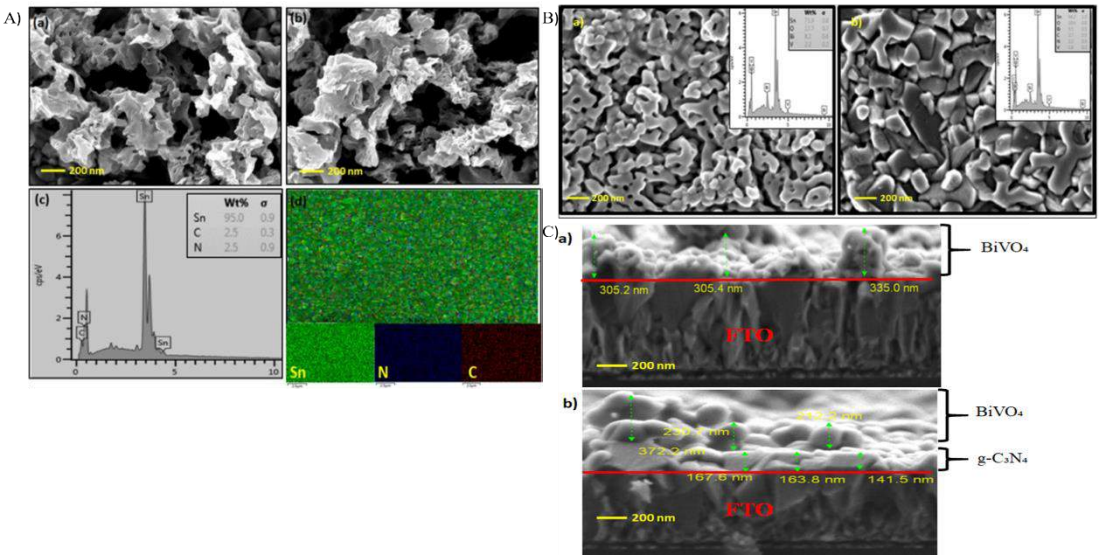

Fig. 1.(A) FESEM-EDX images of (a) g-C_3N_4 and (b) radiated g-C_3N_4 (8 Gy); (c,d) EDX and mapping of g-C_3N_4 (B) (a) BiVO4 and (b) γ radiation on g-C_3N_4@$BiVO_4$ (C) cross-sectional images of $BiVO_4$ and γ radiated g- C_3N_4@$BiVO_4$.

The surface morphologies of g-C_3N_4 and radiated g-C_3N_4 along with their corresponding $BiVO_4$ heterojunctions are determined by FESEM-EDX and mapping with 200 nm resolutions. These films consisted of mesoporous g-C_3N_4 and looked like they have a "seaweed" architecture as shown in Figure 1. It can be observed no other impurity peak was detected, except the peak of Sn (probably attributed to the FTO). The mapping results are shown in Figure 1(d) to ensure that the g-C_3N_4 is uniformly distributed on thin films. The blue and red colors are good indication for the elements of N and C, respectively.Furthermore in Figure 1 (B) it is clearly seen that the $BiVO_4$ morphology comprised a "flower"-like architecture image. Furthermore, for the γ radiated g-C_3N_4@$BiVO_4$, some of the particles seemed to agglomerate and form high rough surface. Figure 1(C) shows the cross-section of $BiVO_4$ and g-C_3N_4, treated with γ radiation and its heterojunction. The morphology of $BiVO_4$ shows different thicknesses. For the $BiVO_4$, the average thickness is in the range of 305.2−335.0 nm. The thickness doubles in the range of 405.4−584.6 nm when the heterojunction is established.

Conclusion

In summary, two different strategies have been applied (γ radiation and heterojunction) on a single photoelectrode, which has effectively increased the photoelectrochemical efficiency of solar water splitting. It is observed that the γ radiation changes the structural and chemical structures of the semiconductor, which ultimately improve the overall PEC efficiency. The band gap energy of γ irradiated g-C_3N_4 reduces from 2.82 to 2.76 eV, and the photocurrent density becomes two times that of the nonirradiated one and increases from 3.59 to 5.86 μA cm^{-2} at 1.23 V versus Ag/AgCl.

Acknowledgement

The authors would like to acknowledge financial support from National University of Malaysia through internal grants GUP-2016-089 and GUP-2018-113.

References

1. Mohamed, N.A., Safaei, J., Aznan, F.I., Mohamad Noh, M.F., Soh, M.F., Ibrahim, M.A., Ahmad Ludin, N. & Mat Teridi, M.A. 2019. Efficient photoelectrochemical performance of gamma irradiated g-C_3N_4 and its g-C_3N_4 @$BiVO_4$ heterojunction for solar water splitting. *J. Phys. Chem. C.* 123(14): 9013-9026.

Z-SCHEME WATER SPLITTING OF Se/$BiVO_4$ PHOTOANODE

S.N.F. Mohd Nasir[1]*, M. Ebadi[1], M.A. Mat Teridi[1]*

[1]*Solar Energy Research Institute, National University of Malaysia, Bangi, Selangor 43600, Malaysia*

*Corresponding author: farhanaana98@gmail.com, asri@ukm.edu.my

Abstract
A Se/$BiVO_4$ thin film photoanode for solar water splitting was fabricated via layer-by-layer deposition of Se and $BiVO_4$ using electrodeposition and aerosol-assisted chemical vapor deposition (AACVD), respectively. The addition of Se layer onto the $BiVO_4$ film was found to boost the photocurrent density by 30 % from 0.7 $mAcm^{-2}$ to 2.2 $mAcm^{-2}$ under 100 $mWcm^{-2}$. Electrochemical impedance spectroscopy (EIS) revealed favorable charge transfer characteristics of Se/$BiVO_4$ which accounts for the higher photoactivity of Se/$BiVO_4$ compared to pristine $BiVO_4$. Field emission scanning electron microscopy (FESEM) analysis showed that the Se/$BiVO_4$ thin film exhibited a porous structure of which provides good charge mobility between electrolyte/photoelectrode surface.

Keywords: Selenium, z-scheme, water splitting, photoelectrochemical, Se/$BiVO_4$.

Introduction
Since the first discovery of photoelectrochemical (PEC) water splitting of TiO_2 [1], the development of semiconducting materials as efficient photoelectrode remains a challenge. Although the band positions of TiO_2 straddle the water redox potentials, its large band gap means that it can only absorb the UV part of the solar spectrum, which only accounts for 4% of the solar irradiance. Bismuth vanadate ($BiVO_4$) with bandgap of 2.4 eV [3] is the most prevalent material for water splitting process. Hence, it implies that as much as 11 % of the solar spectrum could be absorbed compared with 4 % for TiO_2 [4]. However, the constraint of $BiVO_4$ is poor photocatalytic activity due to its more positive potential in thermodynamic level. Therefore, to improve the electron-hole separation of $BiVO_4$, coupling the $BiVO_4$ photoelectrode to form heterojunctions have been reported. In this work, we report an improvement in the PEC performance of $BiVO_4$ through combining with n-type selenium to build Z-scheme band alignment. Selenium has attractive features such as a small band gap (1.7 eV), low surface-states densities, a large carrier lifetime [5] and a high conductivity ($1x10^{-3}$ Sm^{-1}) [6]. For these reasons, Se has been extensively studied as a photoabsorber in thin film devices such as solar cells, photocatalysts, xerography and rectifiers. Since there is very limited information on Se-based PEC water splitting, this work is a step forward to provide a new way for replacing a conventional visible-light photoabsorber, that is Si.

Methodology
Conductive fluorine-doped tin oxide (FTO TEC 18 Ω/cm^2, Pilkington) coated glass were used as substrates. A potentiostat/galvanostat modulab solartron analytical was used for electrodeposition. A layer of Se was deposited galvanostatically at -20 mA *vs.* SCE for 80-100s in a solution containing 50 mM Na_2SeO_3 with an FTO working electrode, SCE reference electrode, and platinum counter electrode. Then, $BiVO_4$ thin film was loaded on Se layer by AACVD according to our previously reported work [3].

Results and Discussion
The photoelectrochemical performance of Se/$BiVO_4$ are presented in Fig. 1a. All samples of Se, $BiVO_4$, and Se/$BiVO_4$ represent anodic photocurrent patterns under illumination

which indicate that these electrodes have n-type semiconductor behaviour. The photocurrent density of Se/$BiVO_4$ was increased up to 2.2 $mAcm^{-2}$ at 1.3 V *vs*. SCE which was much better than that pristine Se and $BiVO_4$. It is found that the charge transfers resistance of the semiconductor is in the order of: $BiVO_4$ > Se/$BiVO_4$ (Fig. 1b). In addition, the porous structure (Fig. 1c) improves the electrode/electrolyte interfacial area as more photogenerated charges have to travel through a less bulk material which then reduces the charge recombination during the photo-oxidation reactions. The Se/$BiVO_4$ forms a direct Z-scheme-like heterojunction (Fig. 1d), where the enhanced photocurrent activities are because of the Se layer. Due to more negative potential of the conduction band of Se, photo-electrons at the conduction band of $BiVO_4$ recombined with the holes at the valence band of Se. Z-scheme-like heterojunction served as a centre of charge recombination between holes in the valence band of Se and electrons from the conduction band of $BiVO_4$. As a result, this facilitates the accumulation of photo-generated electrons in Se to the external circuit and generates high photocurrent.

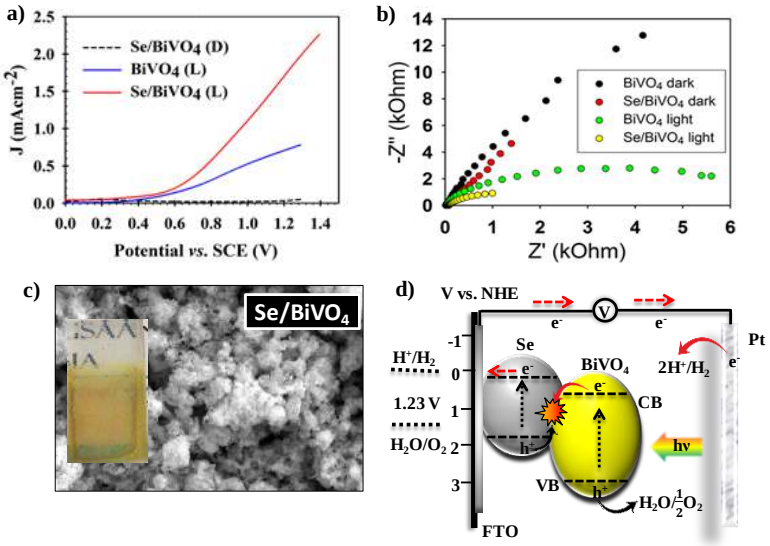

Figure 1. (a) Photocurrent density of $BiVO_4$ and Se/$BiVO_4$, (b) EIS of $BiVO_4$ and Se/$BiVO_4$, (c) FESEM of Se/$BiVO_4$ and (d) z-scheme of Se/$BiVO_4$.

Conclusion

To summarize, we have successfully fabricated a direct Z-scheme-like heterojunction of Se/$BiVO_4$. The Se layer plays important role in accumulating the electrons at the photoanode and reducing the charge transfer resistance of $BiVO_4$ to improve the PEC performance.

Acknowledgment

The authors would like to acknowledge financial support through internal grant MI-2019-004 from Universiti Kebangsaan Malaysia (UKM).

References

1. Fujishima, A. & K. Honda, K., 1972, *Nature*, 238, 37–8.
2. Tokunaga, S., Kato, H., Kudo, A., 2001. *Chem. Mater*. 13, 4624.
3. Mohd-Nasir, S.N.F., Mat-Teridi, M.A., Ebadi, M. Sagu, J.S., Sulaiman, M.Y., Ludin, N.A., Ibrahim, M.A., 2015. *Phys. Status Solidi A*, 212, 2910-2914.
4. Abdi, F.F., van de Krol, R., 2012. *J. Phys. Chem. C*, 116, 9398.

5. Ito, H., Oka, M., Ogino, T., Takeda, A., Mizushima, Y., 1982. *Jpn. J. Appl. Phys.* 21, 77.
6. Luo, C., Xu, Y.H., Zhu, Y.J., Liu, Y.H., Zheng, S.Y., Liu, Y., Langrock, A., Wang, C.S., 2013. *ACS Nano,* 7, 8003-8010.

ESTIMATION OF MEAN ANNUAL EFFECTIVE DOSE FROM MEASURED RADON CONCENTRATION IN GROUNDWATER IN AZARE, NIGERIA

Auwalu Baballe [1,a *], Bello.Y. Idi[2,b]

[1]*Physics Department, Bauchi State University Gadau - 65 Itas/Gadau – Bauchi Nigeria*
[2]*Federal University Dutse – Jigawa Nigeria*

*Corresponding author: [a]baballe@yahoo.com, [b]belyus2000@gmail.com.

Abstract
Radon monitoring has been increasingly conducted worldwide because it poses significant health hazard to human being. The study aims to determine radón concentration in water and to assess the corresponding radiológical health implication in the study area. Twenty samples of wáter were analyzed using RAD7, electronic radon detector with specialaccessory. The measured radón concentration in water samples range from 1.8 ± 0.2Bql^{-1} to 17.2 ± 1.3Bql^{-1} with mean value of 7.1 ± 1.8 Bql^{-1}. The results are used for the estimation of annual effective dose exposure to individual and was found to be 19.65 μSvy^{-1}, which is lower than the recommended safe limit of 0.1 mSvy^{-1} adopted from WHO (2004) and EU council (1998). The level of radon activity concentration in the study area is still within the normal range, thus should not pose any significant health risk to the population.

Keywords: Radon, RAD7 detector, Health hazard, Annual effective dose

Introduction
Radon is naturally occurring radionuclide noble gas, which is not perceivable to our sense. It's an alpha emitter that produced by the decay of immediate parent nuclide ^{226}Ra which a half- life of 1600 years, which is a member of the ^{238}U decay series [1]. Radon poses a significant health risk to populace, because it contributed to high percentage to the public exposure to ionizing radiation [2]. There two diseases that might cause when radon is exposed to human body, which are lung cancer from inhalation of radon daughters, and stomach cancer as a result of drinking water [3]. When radon inhaled it will either cause mutation (DNA damage) or tumour (cell multiplication) [4]. It will be of paramount importance to conduct a research in Gadau district in order to identify areas that are at risk, so that the government can take measures to mitigate the effect, which will eventually reduce the significant health hazard to the inhabitants. It is observed that the level of radon activity concentration in the study area is still within the normal range, thus should not pose any significant health risk to the population.

Experimental
Twenty samples of water were from collected from underground water. The samples were taken to the laboratory for preparation and analysis. Radon concentrations in water samples were measured using a RAD-H_2O technique. RADH_2O technique consists of RAD7 coupling with a closed-loop aeration system that extracted radon from water [12]. In this system, the radon extracts continuously from the water until a state of equilibrium is reached. The system takes 5 minutes to reach the equilibrium state, at this stage the RAD7 stops extracting radon from water. After pumping for five minutes, the coupling process repeats for four five minutes cycles, altogether it took 30mins to complete the analysis and get accurate results [13]. The RAD7 was purged for some minute before every measurement, to free radon from previous measurement. Throughout the experiment a WAT 250 that calculates the radon concentration in 250 ml along with grab mode was adopted.

Results and Discussion

The radon concentration measured and total annual effective dose due ingestion and inhalation from 20 samples of drinking water taken from hand pumps and wells are tabulated in Table 1 below.

Table 1. Radon concentration in water in Gadau district

S/n	Sampling locations	Radon concentration in water + S.D (Bql^{-1})	Annual mean effective dose (μSvy^{-1})		
			Ingestion	Inhalation	Total
1	Tulu ward	6.47 ±1.78	1.36	16.32	17.67
2	Fada ward	7.10±1.85	1.46	17.89	19.38
3	Atarawa ward	9.90±1.80	2.08	24.95	27.02
4	Tsangaya ward	7.23±2.03	1.51	18.21	19.72
5	Walai ward	5.30±1.53	1.11	13.36	13.97
	Average	7.20±1.80	1.51	18.15	19.55

From Table 1, the measured radon concentration in water samples range from 1.8 ± 0.2Bql^{-1} to 17.2 ± 1.3Bql^{-1} with mean value of 7.2 ± 1.8 Bql^{-1}. Radon concentration in all water samples is found within the safe limit of 11 Bql^{-1} recommended by USEPA (1991), with the exception of one sample in Atarawa ward with 17.2 ± 1.3Bql^{-1}. Table 2 shows the comparison of ^{222}Rn concentration in water of present study with the studies conducted in different countries. It is clearly shown that the study in Saudi Arabia is in close agreement with the present study. From the table 1, the total annual mean effective dose varies from 4.92 µSvy-1 to 46.95µSvy^{-1} with a mean value of 19.65µSvy^{-1}, which is lower than the recommended safe limit of 0.1 $mSvy^{-1}$ adopted from WHO (2004) and EU council (1998).

Countries	Radon concentration in water (Bq L^{-1})		References
	Range	Average	
Brazil	0.95-36.0	2.53	(Marques, Binesh, 2004)
Greece	0.8-24	5.4	(Nikolopoulos and Louizi, 2008)
Saudi arabia	0.57-4.67	6.90	(El-Taher, 2012)

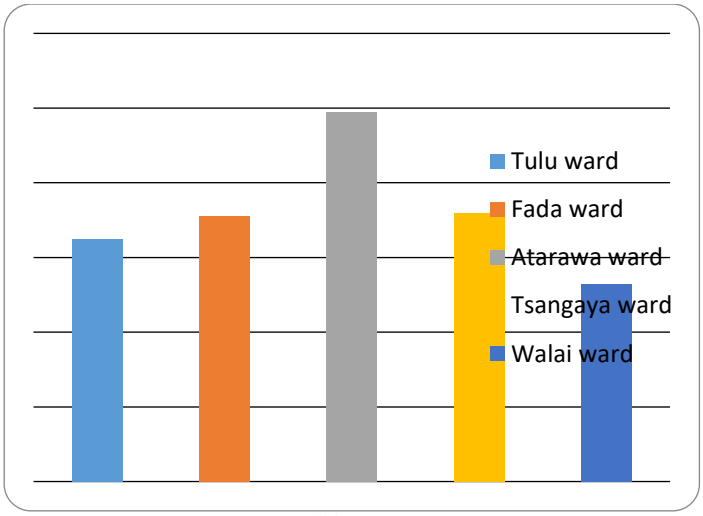

Figure 1. Mean activity concentration of ^{222}Rn in water in different ward in Gadau district

Conclusion

The measured radon concentration of all samples in Gadau district, are found within the safe limit recommeded by USEPA (1991), with exception of one simple, also the annual mean effective dose calculated is less than the recommended safe limit by WHO (2004) and EU council (1998).

Acknowledgements

The authors are highly grateful for all staffs in Physics Department, Bauchi State University for their support and advice.

Reference

1. Ali, N., Khan, E., Akhter, P., Khan, F. & Waheed, A. 2010. Estimation of mean annual effective dose through radon concentration in the water and indoor air of Islamabad and Murree. *Radiation protection dosimetry,* 141**,** 183-191.
2. Alenezy, M. D. 2014. Radon Concentrations Measurement in Aljouf, Saudi Arabia Using Active Detecting Method. *Natural Science,* 2014.
3. Mihci, M., Buyuksarac, A., Aydemir, A. & Celebi, N. 2010. Indoor and outdoor radon concentration measurements in Sivas, Turkey, in comparison with geological setting. *Journal of environmental radioactivity,* 101**,** 952-957.
4. Mittal, S., Rani, A. & Mehra, R. 2015. Estimation of radon concentration in soil and groundwater samples of Northern Rajasthan, India. *Journal of Radiation*
5. UNCEAR 2000. Effects of Ionizing Radiation, 2000 Report to the General Assembly, with Scientific Annexes. *United Nations, New York*.

ORAL PRESENTATION

MATHEMATICS

AN EVASION DIFFERENT GAME OF ONE PURSUER AND ONE EVADER WITH INTEGRAL CONSTRAINTS ON CONTROL FUNCTION

Y. Salleh[1], I. Arif Alias[2]*, G. Ibragimov[3]

[1,2,3]*Institute for Mathematical Research (INSPEM), Universiti Putra Malaysia, 43400 UPM Serdang, Selangor, Malaysia.*
[2,3]*Department of Mathematics, Universiti Putra Malaysia, 43400 UPM Serdang, Selangor, Malaysia.*

*Corresponding author: idham_aa@upm.edu.my

Abstract
We consider evasion differential game of one evader versus one pursuer in the plane. The control functions of players are subjected to coordinate-wise integral constraints. The evader maneuvers with nonnegative vertical speed in a small area of *y*-axis. We say that evasion is possible if the position of the evader does not collide with that of the pursuer at all times.

Keywords: Differential game, evasion, strategy, coordinate-wise, integral constraints

Introduction

The study of two person from different parties of differential games was initiated by Isaacs (1965). Constructing the player's optimal strategies and finding the value of the game are of specific interest in differential game. A few works are dedicated to evasion game such as Azimov (1974), Zak (1978), Chodun (1989), Kuchkarov et al. (2002), Ibragimov et al. (2012) and Alias et al. (2013).

In the present paper, we investigate an evasion differential game of one evader from one pursuer with coordinate-wise integral constraints on control functions of players. The objectives of the study to find sufficient condition of evasion and construct an explicit strategy for the evader to ensure evasion are possible from any initial position of players.

Result and Discussion

Theorem 3.1. If $\sigma_1 > \rho_1$ and $\sigma_2 > \rho_2$, then evasion is possible.

Proof. Clearly, the inequalities $\sigma_1 > \rho_1$ and $\sigma_2 > \rho_2$ imply that $\sigma^2 = \sigma_1^2 + \sigma_2^2 > \rho_1^2 + \rho_2^2 = \rho^2$. Consider two cases: $y_{20} > x_{20}$ or $y_{20} \le x_{20}$. Let a be any number satisfying $0 < a < \min\{1, |x_0 - y_0|\}$.

Case 1 : $y_{20} > x_{20}$

a) Construction of a Strategy for the Evader

$$v(t) = (0, |u_2(t)|), t \ge 0. \tag{5}$$

b) Admissibility of the Strategy

$$\int_0^\infty v_1^2(s)ds = 0 \le \sigma_1^2 \text{ and } \int_0^\infty v_2^2(s)ds = \int_0^\infty |u_2(s)|^2 ds \le \rho_2^2 \le \sigma_2^2.$$

c) Proof of Evasion is Possible

Since $y_{20} > x_{20}$, we have $y(t) \ne x(t)$ for $t \ge 0$ and hence, evasion is possible.

Case 2 : $y_{20} \le x_{20}$

a) Construction of a Strategy for the Evader

$$v(t) = (0, |u_2(t)|) \text{ if } y_2(t) \le x_2(t) \text{ and } |y(t) - x(t)| > a. \tag{6}$$

$$v(t) = \begin{cases} (0, \alpha + |u_2(t)|), & t_1 \le t \le t_1 + \alpha, \\ (0, |u_2(t)|), & t > t_1 + \alpha, \end{cases} \tag{7}$$

where α is a number that satisfies the following conditions:

$$0 < \alpha < 1,\ a\alpha < \sigma_1^2,\ a\alpha < \sigma_2^2,\ \sqrt{2\alpha} \le \sigma_1 - \rho_1, \sqrt{2\alpha} \le \sigma_2 - \rho_2. \tag{8}$$

Then we set

$$v(t) = \begin{cases} (\pm(\alpha + |u_1(t)|), \alpha + |u_2(t)|), & \tau \le t \le \tau', \\ (0, \alpha + |u_2(t)|), & \tau' < t \le \tau' + \dfrac{a}{\alpha}, \\ (0, |u_2(t)|), & t > \tau' + \dfrac{a}{\alpha}, \end{cases} \tag{9}$$

b) Admissibility of the Strategy

We now show admissibility of the strategy of the evader. By using inequality in (8), we proof all the strategies are admissible.

c) Proof of Evasion is Possible

We calculate the estimation distances of players by time interval using strategies (7) and (9). In particular, at time $t = \tau'$, $|y(\tau') - x(\tau')| > \dfrac{4a^2\alpha}{25\sigma^2} > 0.$ Hence, $y(\tau') \ne x(\tau')$. We conclude that, $y(t) \ne x(t), t \ge 0$ and proof is completed.

Conclusion

The sufficient conditions for evasion is possible are $\sigma_1 > \rho_1$ and $\sigma_2 > \rho_2$, and with the constructed strategy, it is shown that evasion is possible from any initial position of players. This result is much better than previous paper.

Acknowledgement

This research was partially supported by the National Fundamental Research Grant Scheme (FRGS) of Malaysia, No. 01-01-16-1840FR.

References

[1] Alias, I.A., Salleh, Y., Azamov, A., 2013. Evasion Differential Game of Two Evaders and One Pursuer with Integral Constraints. *AIP Conf. Proc.* 1557: 140-145.

[2] Azimov, A.Y., 1974. A linear differential evasion game with integral constraints on the controls. *USSR Computational Mathematics and Mathematical Physics*. 14(6): 56-65.

[3] Chodun, W., 1989. Differential games of evasion with many pursuers. *Journal of Mathematical Analysis and Applications*. 142(2), 370-389.

[4] Ibragimov, G.I., Salimi, M., Amini, M., 2012. Evasion from many pursuers in simple motion differential game with integral constraints. *European Journal of Operational*. 218(2), 505-511.

[5] Kuchkarov, A.S., Rikhsiyev, B.B., 2002. The possibility of avoiding an encounter in a linear differential game of evasion. *Journal of applied mathematics and mechanics*. *66*(2), 233-237.

[6[Isaacs, R., 1965. Differential Game. John Wiley and Sons. New York.

Zak, V.L., 1978. On a problem of evading many pursuers. *PMM*. 43(3): 456-465.

3-ALGEBRAS GENERATED BY BINARY ALGEBRAS

H. Ahmed[1]*, Sh.K. Said Husain[1,2] and W. Basri[1,2]

[1] *Department of Mathematics, Faculty of Science, Universiti Putra Malaysia, 43400 Selangor, Malaysia*
[2]*Institute for Mathematical Research (INSPEM), UPM, Selangor, Malaysia*

*Corresponding author: houida_m7@yahoo.com

Abstract
The aim of this paper we give answers to some questions one can ask: For any algebra, we can find a corresponding n-algebra, what about the reverse, is it true? If two algebras are not isomorphic what about the corresponding two 3-algebras of those two algebras, they are isomorphic or not?

Keywords: multilinear operator, n-algebras, associative, isomorphism.

Introduction

In 1960 Kurosh introduced the notion of multilinear operator algebra. It is known that such algebraic structures are interesting for their applications to problems of modern mathematical physics. In 1973, Nambu proposed an interesting generalization of classical Hamiltonian mechanics, Nambu bracket is a generalization of the classical Poisson bracket. To answer our questions we will use some result gotten early in [1].

Preliminaries

Definition. A vector space $\boldsymbol{V}$ over $\boldsymbol{F}$ equipped by a multilinear function $f: \underbrace{\boldsymbol{V}\times\boldsymbol{V}\times\ldots\times\boldsymbol{V}}_{n-times} \to \boldsymbol{V}$ is said to be a *n*-algebra.

Example 1. Let $\boldsymbol{A}=(\boldsymbol{V},\mu)$ be an algebra over a field F: Then multilinear function

$$f(\boldsymbol{x_1},\boldsymbol{x_2},\ldots,\boldsymbol{x_n}) = \underbrace{\mu(\boldsymbol{x_1},\mu(\boldsymbol{x_2},\ldots,\mu(\boldsymbol{x}_{n-1},\boldsymbol{x_n})\ldots)}_{(n-1)-times} \quad (1)$$

defines an n-algebra structure on $\boldsymbol{V}$.

Results and Discussion

For 2-dimensional 3-algebra $\boldsymbol{B}$ over $\boldsymbol{F}$ and with fixed basis $\boldsymbol{e}$. $\boldsymbol{B}$ can be represented by its matrix of structural constants (MSC) $B=\left(\gamma_{ijk}^{l}\right)\in M(2\times 2^3;\boldsymbol{F})$ where $i,j,k,l=1,2$ as follows:

$$B=\begin{pmatrix} \gamma^1_{111} & \gamma^1_{112} & \gamma^1_{121} & \gamma^1_{122} & \gamma^1_{211} & \gamma^1_{212} & \gamma^1_{221} & \gamma^1_{222} \\ \gamma^2_{111} & \gamma^2_{112} & \gamma^2_{121} & \gamma^2_{122} & \gamma^2_{211} & \gamma^2_{212} & \gamma^2_{221} & \gamma^2_{222} \end{pmatrix}$$

(for more information refer to [4]).

Example 2. In example 1 if $\boldsymbol{V}$ is two-dimensional vector space with a fixed basis $\{e_1,e_2\}$ and $(\boldsymbol{V},f)$ is 3-algebra structure on $\boldsymbol{V}$. Then f and μ can be expressed by their structure constants as follows: $f(e_i,e_j,e_k)=\gamma^1_{ijk}e_1+\gamma^2_{ijk}e_2$ and $\mu(e_r,e_s)=\eta^1_{rs}e_1+\eta^2_{rs}e_2$. Then due to (1) we get the system of equations

$$\left.\begin{aligned}\gamma^1_{ijk}&=\eta^1_{jk}\eta^1_{i1}+\eta^2_{jk}\eta^1_{i2}\\ \gamma^2_{ijk}&=\eta^1_{jk}\eta^2_{i1}+\eta^2_{jk}\eta^2_{i2}\end{aligned}\right\} \quad (4)$$

Using (4) we can find the 3-algebras corresponding to all algebras presented in [1] under this procedure (see table 1). We can see $\begin{pmatrix}1&0&0&1&0&1&-1&0\\0&-1&1&0&1&0&0&1\end{pmatrix}$ is a 3-algebra which cannot be expressed by any algebras and it is not isomorphic to any B_i where $i=1,\ldots,11$.

In another hand, $A_4\left(\frac{1}{3},-\frac{1}{3}\right)$ and $A_5\left(\frac{1}{3}\right)$ are not isomorphic algebras but from these two not isomorphic algebras we get one 3-algebra

$$B=\begin{pmatrix}\frac{1}{9} & 0 & 0 & 0 & 0 & 0 & 0 & 0\\ 0 & \frac{1}{9} & -\frac{2}{9} & 0 & \frac{2}{9} & 0 & 0 & 0\end{pmatrix}$$

3 - algebra								
$\alpha_1+\alpha_2$	$\alpha_1\alpha_4-\alpha_2^2$	$\alpha_1\alpha_2+\alpha_1+\beta_1\alpha_4$	$\alpha_2^2-\alpha_2-\alpha_1\alpha_4$	$\alpha_2^2+2\alpha_2-\alpha_1\alpha_4+\alpha_4+1$	α_4		
$\alpha_1^2+\beta_1\alpha_2+\beta_1-\alpha_1$	$\beta_1\alpha_4+\alpha_1\alpha_2$	$-\alpha_1^2-\beta_1\alpha_2+\alpha_1$	α_2	$-\alpha_1+1$	$\alpha_2^2-\alpha_1\alpha_4+\alpha_4$		

A_2	$B_2=\begin{pmatrix}\alpha_1^2 & 0 & 0 & \alpha_1 & \beta_1 & \beta_2 & 1-\alpha_1 & 0\\ \beta_1\alpha_1+\beta_1\beta_2 & \beta_2^2 & \beta_2(1-\alpha_1) & \beta_1 & \alpha_1(1-\alpha_1) & 0 & 0 & 1-\alpha_1\end{pmatrix}$
A_3	$B_3=\begin{pmatrix}\beta_1 & \beta_2 & 1 & -1 & 0 & 1 & 1 & 0\\ \beta_1\beta_2 & \beta_1+\beta_2^2 & \beta_2+\beta_1 & -\beta_2 & -\beta_1 & 1-\beta_2 & 0 & 1\end{pmatrix}$
A_4	$B_4=\begin{pmatrix}\alpha_1^2 & 0 & 0 & 0 & 0 & 0 & 0 & 0\\ 0 & \beta_6^2 & \beta_2(1-\alpha_1) & 0 & \alpha_1(1-\alpha_1) & 0 & 0 & 0\end{pmatrix}$
A_5	$B_5=\begin{pmatrix}\alpha_1^2 & 0 & 0 & 0 & 0 & 0 & 0 & 0\\ 3\alpha_1-1 & (2\alpha_1-1)^2 & (2\alpha_1-1)(1-\alpha_1) & 0 & \alpha_1(1-\alpha_1) & 0 & 0 & 0\end{pmatrix}$
A_6	$B_6=\begin{pmatrix}\alpha_1^2 & 0 & 0 & \alpha_1 & \beta_1 & 1-\alpha_1 & -\alpha_1 & 0\\ \beta_1 & (1-\alpha_1)^2 & -\alpha_1(1-\alpha_1) & \beta_1 & -\alpha_1^2 & 0 & 0 & -\alpha_1\end{pmatrix}$
A_7	$B_7=\begin{pmatrix}\beta_1 & \beta_1+1 & 0 & -1 & 0 & 1 & 1 & 0\\ \beta_1 & 1 & \beta_1 & -1 & -\beta_1 & -1 & 0 & 1\end{pmatrix}$
A_8	$B_8=\begin{pmatrix}\alpha_1^2 & 0 & 0 & 0 & \alpha_1^2 & 0 & 0 & 0\\ 0 & (1-\alpha_1)^2 & -\alpha_1(1-\alpha_1) & 0 & 0 & 0 & 0 & 0\end{pmatrix}$
A_9	$B_9=\begin{pmatrix}\frac{1}{9} & 0 & 0 & 0 & 0 & 0 & 0 & 0\\ 1 & \frac{4}{9} & -\frac{2}{9} & 0 & -\frac{2}{9} & 0 & 0 & 0\end{pmatrix}$
A_{10}	$B_{10}=\begin{pmatrix}0 & 0 & 0 & -1 & 0 & 1 & 1 & 0\\ 0 & 0 & 0 & 0 & 0 & 0 & 0 & 1\end{pmatrix}$
A_{11}	$B_{11}=\begin{pmatrix}1 & 0 & 0 & -1 & -1 & 1 & 1 & 0\\ 0 & 1 & 1 & 0 & 0 & 0 & 0 & 1\end{pmatrix}$
A_{12}	trivial

Table 1

Conclusion

Depend on the approach introducing in [5] and applying in [1] one can study the classification of n-algebras and then study some identities of n-algebras refer [2, 3, 4].

Acknowledgement

The authors acknowledge Universiti Putra Malaysia for support via grant IPS 9537100/UPM.

References

[1] H. Ahmed, U. Bekbaev, I. Rakhimov, 2017. Complete classification of two-dimensional algebras, AIP Conference Proceedings, 1830, 070016, 1-11.
[2] H. Ahmed, U. Bekbaev and I. Rakhimov, 2019.On two-dimensional power associative algebras over algebraically closed fields and R. Lobachevskii Journal of Mathematics 40:1-13.
[3] H. Ahmed, U. Bekbaev and I. Rakhimov, 2018. Classification of Two-Dimensional Jordan Algebras over R, Malaysian Journal of Mathematical Sciences 12:287-303.
[4] Ahmed H, Bekbaev U, Rakhimov I (2018) The Automorphism Groups and Derivation Algebras of Two-Dimensional Algebras. J Generalized Lie Theory Appl 12: 290, 1-9.
[5] U. Bekbaev,2015. On classification of finite dimensional algebras, arXiv: 1504.01194, 1–8.
[6] A.G. Kurosh,1969. *Multioperator rings and algebras*. Russ Math Surv, 24(1),1-13.
[7] Y. Nambu, 1973. *Generalized Hamiltonian mechanics*. Phys. Rev., D, 2405-2412.

A PURSUIT DIFFERENTIAL GAME WITH INTEGRAL CONSTRAINT DESCRIBED BY A FINITE SYSTEM OF DIFFERENTIAL EQUATION

M. Arif Syazani[1]*, I. Arif Alias[1], G. Ibragimov[1]

[1]*Department of Mathematics, Faculty of Science, Universiti Putra Malaysia, 43400 UPM Serdang, Selangor, Malaysia.*

*Corresponding author: m.arifsyazani@gmail.com

Abstract
We study a pursuit differential game between one pursuer and one evader described by a finite system of differential equation. Control functions of players are subjected to integral constraint. We say that pursuit can be completed if the pursuer coincides with the evader at a certain time. An explicit strategy for the pursuer is constructed to solve the problem and a guaranteed pursuit time is obtained.

Keywords: Differential game, pursuit, control, finite system of differential equations, integral constraint.

Introduction
The players in a differential game are either pursuer or evader. In a pursuit differential game, pursuer needs to catch the evader. The study on this field was introduced by Isaacs (1965). The study was extended to a pursuit differential game by some authors such as Pshenichii (1976), Ibragimov and Satimov (2012) and Ibragimov et al. (2012).

In this paper, we want to solve a differential game described by a finite first-order differential equation between one pursuer and one evader where the control functions of players are subjected to integral constraint. The objective is to find sufficient condition and construct a strategy for pursuer so that pursuit can be completed. A guaranteed pursuit time is also to be obtained.

Methodology
The detailed identification of the problems and literature review on pursuit differential game described a system of differential equation is studied.
The description of the system is obtained and the general solution is found. The time where the system is brought to the origin is found.

Results and Discussion

Let $z(t) = \begin{bmatrix} x(t) \\ y(t) \end{bmatrix}$, $\begin{bmatrix} \dot{x} \\ \dot{y} \end{bmatrix} = -\lambda \begin{bmatrix} x \\ y \end{bmatrix} + \begin{bmatrix} w_1 \\ w_2 \end{bmatrix}$. (1)
We have, $\dot{x} = -\lambda x + y + w_1$ and $\dot{y} = -\lambda y + w_2$.

The solution for equation (1) is

$$\begin{bmatrix} x(t) \\ y(t) \end{bmatrix} = e^{ct} \left(\begin{bmatrix} x_0 \\ y_0 \end{bmatrix} + \int_0^t e^{-sc} \begin{bmatrix} w_1(s) \\ w_2(s) \end{bmatrix} ds \right)$$

where $c = \begin{bmatrix} -\lambda & 1 \\ 0 & -\lambda \end{bmatrix}$.

We proved that $e^{ct} = e^{-\lambda t}\begin{bmatrix}1 & t\\ 0 & 1\end{bmatrix}$ and $e^{-sc} = e^{\lambda s}\begin{bmatrix}1 & -s\\ 0 & 1\end{bmatrix}$.
Thus our system becomes

$$\begin{bmatrix}x(t)\\ y(t)\end{bmatrix} = e^{-\lambda t}\begin{bmatrix}1 & t\\ 0 & 1\end{bmatrix}\left(\begin{bmatrix}x_0\\ y_0\end{bmatrix} + \int_0^t e^{\lambda s}\begin{bmatrix}1 & -s\\ 0 & 1\end{bmatrix}\begin{bmatrix}w_1(s)\\ w_2(s)\end{bmatrix} ds\right) \quad (2)$$

To bring the state of system to origin, we need to find time t such that $z(t) = 0$. Thus we have

$$0 = e^{-\lambda t}\begin{bmatrix}1 & t\\ 0 & 1\end{bmatrix}\left(\begin{bmatrix}x_0\\ y_0\end{bmatrix} + \int_0^t e^{\lambda s}\begin{bmatrix}1 & -s\\ 0 & 1\end{bmatrix}\begin{bmatrix}w_1(s)\\ w_2(s)\end{bmatrix} ds\right)$$

Since $e^{-\lambda t}\begin{bmatrix}1 & t\\ 0 & 1\end{bmatrix} \neq 0$ for $t > 0$, we just consider:

$$\begin{bmatrix}x_0\\ y_0\end{bmatrix} + \int_0^t e^{\lambda s}\begin{bmatrix}1 & -s\\ 0 & 1\end{bmatrix}\begin{bmatrix}w_1(s)\\ w_2(s)\end{bmatrix} ds = 0.$$

Conclusion

Pursuit can be completed is shown by finding a guaranteed pursuit time that bring the system to origin.

Acknowledgement

This research was partially supported by the National Fundamental Research Grant Scheme (FRGS) of Malaysia, No. 01-01-16-1840FR.

References

[1] Gafurjan Ibragimov, Nu'man Satimov, 2012. A multiplayer pursuit differential game on a closed convex set with integral constraints. Abstract and Applied Analysis, Article ID 460171: 12 pages, http://dx.doi.org/10.1155/2012/460171.

[2] Gafurjan Ibragimov, Mehdi Salimi, and Massoud Amini, 2012. Evasion from many pursuers in simple motion differential game with integral constraints. European Journal of Operational Research, 218 (2):505-511.

[3] Isaacs, R., 1965. Differential Game. John Wiley and Sons. New York.

[4] Pshenichii B.N., 1976. Simple pursuit by several objects. Cybernetics and Systems Analysis, 12(3): 484-485.

USE OF GREAT DELUGE ALGORITHM FOR ADDITION CHAIN PROBLEM OPTIMIZATION

A. M. Noma[1]*, A. Muhammed[2], M. A. Mohamed[3]

[1]Department of Mathematical Science, Faculty of Science, Bauchi State University Gadau, Main Campus, Bauchi State Nigeria.
[2]Faculty of Computer Science and Information Technology, Universiti Putra Malaysia,Serdang, 43000, Selangor, Malaysia.
[3]Faculty of Informatics and Computing, Universiti Sultan ZainalAbidin, Besut, 22200, Terengganu, Malaysia.

*corresponding author: adamnoma@yahoo.com

Abstract
In this paper, we adapt great deluge algorithm (GDA) heuristic to optimize the computational problem of addition chain (AC). Solving the problem forms the basis for optimising modular exponentiation operations in public key cryptographic (PKC) algorithms. We map the AC Problem to GDA, we analytically model the distribution of steps required for constructing optimal ACs and integrated the result into the algorithm. Using the novel algorithm, we study the ACs for various sets of integers, including the well-known $c(r)$integers, which serves as benchmark. The algorithm efficiently results in shorter ACs, thus promising better performance than reported metaheuristics with near optimal ACs and handling relatively larger integers.

Keywords: Addition chain; great deluge algorithm; heuristics; modular exponentiation; public key cryptography.

Introduction
The effectiveness of the cryptosystems is a function of the size of the exponent. Therefore, to efficiently apply PKCs without compromising their security effectiveness, the exponentiation process must be optimised. The modular exponentiation has additive properties whereby finding the shortest AC for an exponent *e* corresponds to that of the number of multiplications required in the modular exponentiation.

Finding the shortest AC is a persistent problem for over a decade (Dellac, 1894). The fundamental question of what is the least number of multiplications required to arrive at x^egiven x and e was raised by Scholz (1937), which Knuth later described as a mathematical problem for which no conjecture is safe (Knuth, 1998). The problem received ample studies (Brauer ,1939; Bos & Coster, 1990; Dominguez-Isidro et al., 2015). Heuristics have since become alternative approaches to solving the problem (Bos & Coster, 1990; Dominguez-Isidro et al., 2015). However, the approaches do not yield optimal solution, apart from consuming sizeable computing resources compared.

Definition 1: Given an integer e, the sequence $a_0 = 1, a_1 = 2, a_3, \dots, a_r = e,$ is said to be an addition chain for e if $\forall i \geq 1, a_i = a_j + a_k, i > j \geq k$. The length of the chain is r.

Note: if we replaced a_0 withx^1, $a_1$with $x^2 = x.x = x^{1+1}, \dots,$ and $a_r$with x^e, the chain corresponds to multiplicative means for evaluating x^e. The shortest r for which there exists an AC for e is denoted by $l(e)$.

After extensive studies of methods for solving the addition chain problem (ACP), we observed that investigating the distribution of star-chain determine optimality of the chain. Moreover, adopting the GDA (Duek, 1993) is appropriate to the problem.

The Great Deluge Addition Chain Algorithm (GDACA)

The Great Deluge Algorithm (GDA) is a trajectory-based metaheuristic considered suitable for combinatorial optimization problems (Duek, 1993). The algorithm is characterized by fewer control parameters. We adopted it as defined in (Duek, 1993). We tune the GDA to best suit the problem and fortify it with good cost functions and tight boundaries for the search process: this makes it more efficient while achieving an effective (near optimal) result.

Heuristic ACP algorithms generate star-chain (Burier chain (4)) with certain probability distributions among the steps. Thus, to efficiently attain optimal results, we studied the distributions, through a small set of optimal ACs. Based on that, we formulated expected individual step for optimal AC as follows:

$$small = \lceil lg(H(e)) \rceil;$$
$$double = \lfloor lg(e) \rfloor;$$
$$P(Lucas\ step) = P(star) = \left\lceil \frac{1}{2}\left({small}/{(small + doule)} \right) \right\rceil \quad (3).$$
$$P(double\ step) = 1 - 2 \times P(Lucas) \quad (4).$$

The GDACA is analysed to have both runtime and memory of $O(n)$.

Results and Discussion

To test the effectiveness of an ACP algorithm, a compiled set of small but hard-to-find integers has been made available (Knuth, 1998). A statistical test and comparison is also carry out on a given set of integers whose results are already established, as well as test on some selected integers considered difficult to obtain their chains (Dominguez-Isidro et al., 2015). We adopted similar benchmarking in appraising our GDACA. We also compared our results with some selected benchmark algorithms considered state-of-the-art. As for the test for small but hard-to-find integers, our GDACA returned all optimal results.

In the first experiment, we compute the accumulated ACs for a range of given integers. We carry out statistical test (means, median and standard deviations) on the results, The effectiveness and the consistency of the algorithm are statistically compared with optimal results,

Given a range of integers $e = [1, x]$ and their AC-length, the accumulated AC generated by the algorithm, alg, for the integer set is defined as:

$$T(x) = \sum_{e=1}^{x} l_{alg}(e) \quad (5)$$

For benchmarking, we run the experiments for e in the range$[1, 512]$, $[1, 1000], [1, 1024], [1, 2000], [1, 2048]$ and $[1, 4096]$. We compared our result with that of AIS in [8], ACEP in [6], SA algorithm in [28], PSO in [29], and GA approach in [30]. The results are presented in Table 1.

Table 1: Comparing Addition Chain Statistics for Sets of Small Integers

e ϵ	Statistics	Optimal	AIS	GA	PSO	ACEP	SA	GDACA
[1,512]	Best	4924	4924	4924	-	4924	-	4924
	Worst		4927	-	-	-	-	4925
	Median		4925	-	-	-	-	4924
	Mean		4925.03	4924.03	-	4924.10	-	4924.03
	Std. Div.		0.89	0.18		0.31	-	0.18
[1, 1000]	Best	10,808	10,813	10,809	-	10808	10,823	10,808
	Worst		10,825	-	-	-	-	10,812
	Median		10.818.50	-	-	-	10,834	10,810
	Mean		10,818.50	10,811.88	-	10,810.21	10,829.53	10,809.67
	Std. Div.		3.06	1.43	-	0.86	3.11	0.98
[1, 1024]	Best	11,115	11,120	-	11,120	11,115	-	11,115
	Worst		11132	-	11,125	-	-	11,119
	Median		11126	-	11,122	-	-	11,117
	Mean		11,126.43	-	11,122.43	11,118.03	-	11,116.67
	Std. Div.		3.01	-	1.95	1.40	-	0.98
[1, 2000]	Best	24,063	24,108	24,076	-	24,076	-	24,074
	Worst		24,133	-	-	-	-	24,088
	Median		24,120.00	-	-	-	-	24,079
	Mean		24,120.20	24,083.29	-	24.080.73	-	24,078.63
	Std. Div.		5.88	3.42	-	2.28	-	2.95
[1, 2048]	Best	24,731	24,778	24,748	-	24,745	-	24,742
	Worst		24,807	-	-	-	-	24,756
	Median		24,791.50	-	-	-	-	24,748
	Mean		24,792.20	24,753.02	-	24,750.47	-	24,747.53
	Std. Div.		6.09	2.97	-	3.06	-	2.90
[1, 4096]	Best	54,408	54,617	54,487	-	54,497	-	54,481
	Worst		54,674	-	-	-	-	54,519
	Median		54,640.00	-	-	-	-	54,496.50
	Mean		54,644.03	54,499.00	-	54,505.93	-	54,496.90
	Std. Div.		12.05	6.22	-	5.44	-	7.81

'-' entry indicates statistics not reported by the algorithm; Std. Div means standard deviation.

From Table 1, the results show that generally our GDACA either equals or surpasses all the others in terms of best, worst, median and mean case result. It outperforms AIS, PSO and SA. It competes with GA and ACEP only in terms of consistency (using standard deviation as the measure). In that respect, the result tallies with GA and performed better than ACEP in the first 1000 integers; better than GA but slightly worse than ACEP for the 1024; the best for 2000 and 2048 integers; and worst for the 4096.

The $c(r)$. In Knuth (1998), $c(r)$ is defined as the smallest integer e for which $l(e) = r$. The result in [3] has been adopted as the basis for benchmarking heuristic the AC algorithms. We compared our result with some best of the reported algorithms. Result on 32 trials is presented in Table 2 (Herein, to reduce space, we eliminated entries for which our algorithm returns all optimal for all the runs).

Table 2: Comparing Optimal Addition Chains for *c*(*r*) Returned by Various Algorithms

E	AIS	PSO	ACEP	SA	GDAAC
357,887	24	24	24	24 (1)	24 (25)
685,951	25	25	25	25 (1)	25 (32)
1,176,431	26	26	26	26 (1)	26 (20)
2,211,837	27	27	27	27 (2)	27 (11)
4,169,527	28	28	28	28 (1)	28 (15)
7,624,319	-	-	-	-	29 (9)
*7,924,319	29	29	29	30 (1)	28 (2)
14,143,037	30	30	30	30 (2)	30 (9)
25,450,463	-	-	-	-	31 (12)

46,444,543	-	-	-	-	32 (4)
89,209,343	-	-	-	-	33 (9)
155,691,199	-	-	-	-	34 (3)
298,695,487	-	-	-	-	35 (8)
550,040,063					36 (5)
994,660,991	-	-	-	-	37 (1)
1,886,023,151	-	-	-	-	38 (1)
3,502,562,143	-	-	-	-	39 (5)
*4,294,967,295	-	-	-	-	36 (17)

From the result (Table 2), our algorithm find all the *c*(*r*) in the given range of the 32 bits. It also surpasses the results from other heuristics reported. Furthermore, it evaluates the extended *c*(*r*) up to $r = 39$, with all the results tallying the ones reported by some exhaustive methods (Knuth, 1998).

The number in brackets as found in GDACA and SA columns represents the frequency of occurrences of the optimal result among 32 trials. This value indicates how consistent an algorithm is in finding the AC. For $c(3)$ to $c(21)$, our algorithm finds optimal r in all the 32 rounds as compared to SA with the frequency of as low as 1.

Addition chain for hard integers. Finally, we test integers for which optimal ACs are hard to get, as compiled in Dominguez-Isidro et al. (2015). In all the set of integers, our algorithm find the optimal ACs with length 27.

Conclusion and Future Works

Our GDACA is effectively competitive with or even better than the existing metaheuristic approaches, apart from its exclusive ability to handling relatively larger integers. It surpasses existing approaches by at least 200% in terms of reduced number of evaluations to find the given solution. It also comparatively saves at least 80% memory resources. The algorithm is able to generate an addition chain of at worst 1 more than the shortest (optimal) chain for the set of all integers in the range of 32 bits. All these are the results of the algorithm being simplistic in implementation, and proper selection of cost function and boundary values. Therefore, we hope the systematic approach we adopted in mapping the ACP to the GDA iwill serve as a guide in mapping metaheuristics to other intractable problems.

References

[1] H. Dellac, 1894. Question 49. L'Intermédiaire Math 1.20.
[2] A. Scholz, Jahresbericht. Deutschen Mathematiker-vereinigung. Auhfgabe 1937. 252.47. 41.
[3] D. E Knuth, 1998. Evaluation of Powers, in: Knuth, D. E. (ed) The Art of Computer Programming, third ed, vol. 2, pp 461 – 485, Addison-Wesley, USA.
[4] A. Brauer, 1939. On addition chains, Bulletin of the American Mathematical Society, 45, 736 – 739.
[5] J. Bos, M. Coster, 1990. Addition chain heuristics, in: proceeding of the Advances in Cryptology—CRYPTO'89, pp. 400-407, Springer, New York.
[6] S. Dominguez-Isidro, E. Mezura-Montes, N. Cruz-Cortés, F. Rodríguez-Henríquez, 2015. Evolutionary programming for the length minimization of addition chains, Engineering Applications of Artificial Intelligence, 37, 125–134.
[7] G. Duek, 1993. New optimization heuristics the great deluge algorithm and the record-to-record travel, Journal of Computational Physics, 104, 86 – 92.

[8] N. Cruz-Cortés, F. Rodríguez-Henríquez, R. Juárez-Morales, C. A. Coello-Coello, 2008. An artificial immune system heuristic for generating short addition chains, IEEE Transaction on Evolutionary Computation 12.1, 1 – 24.

[9] A. Jose-Garcia, H. Romero-Monsivais, C. G. Hernandez-Morales, A. Rodriguez-Cristerna, I. Rivera-Islas, J. Torres-Jimenez, 2011. A simulated annealing algorithm for the problem of minimal addition chains, in: EPIA 2011, LNAI 7026, pp. 311–325, Springer-Verlag.

[10] L. G. Osorio-Hernández, E. Mezura-Montes, N. Cruz-Cortés, F. Rodríguez-Henríquez, 2009. An improved genetic algorithm able to find minimal length addition chains for Small exponents, in: Proceedings of the IEEE Congress on Evolutionary Computation, pp. 1–6, IEEEPress.

EVASION DIFFERENTIAL GAME OF ONE EVADER AND SEVERAL PURSUERS WITH INTEGRAL CONSTRAINTS

Gafurjan Ibragimov[1]*, Massimiliano Ferrara[2], Marks Ruziboev[3],
And Bruno Antonio Pansera[4]

[1]Department of Mathematics and Institute for Mathematical Research, Universiti Putra Malaysia, 43400 UPM Serdang, Selangor Darul Ehsan, Malaysia.
[2]University Mediterranea of Reggio Calabria Department of Law, Economics and Human Sciences & ICRIOS - The Invernizzi Centre for Research in Innovation, Organization, Strategy and Entrepreneurship Bocconi University - Department of Management and Technology, Italy.
[3]Department of Mathematical Sciences, Loughborough University, Loughborough, Leicestershire, LE11 3TU, UK
[4]Department of Law and Economics, University Mediterranea of Reggio Calabria, Italy.

*Corresponding author: ibragimov@upm.edu.my

Introduction

In the present paper, we study a linear evasion differential game of many pursuers and one evader. The controls of players are subjected to integral constraints. We construct an explicit evasion strategy and prove a theorem about evasion.

Let $x_1, \dots, x_m$, $m \geq 1$, be the points moving in $\mathbb{R}^n$ whose dynamics are described by the equations

$$\dot{x}_i = -\lambda_i x_i + v - u_i, \quad x_i(0) = x_i^0, \quad i = 1,2, \dots, m, \tag{1}$$

where $u_1, \dots, u_m$ are the control parameters of pursuers and v is that of evader, $\lambda_i > 0$, $x_i, x_i^0, u_i, v \in \mathbb{R}^n$, $n \geq 2$, $x_i^0 \neq 0$, $i = 1, \dots, m$.

Definition 1.1 *Measurable functions $u_i(t)$ and $v(t)$, $t \geq 0$, that satisfy the following integral constraints*

$$\int_0^\infty |u_i(t)|^2 dt \leq \rho_i^2, \ i = 1, \dots m; \quad \int_0^\infty |v(t)|^2 dt \leq \sigma^2. \tag{2}$$

are called controls of the ith pursuer and evader, respectively.

Definition 1.2 *A function $(t, x_1, \dots, x_m, u_1, \dots, u_m) \mapsto V(t, x_1, \dots, x_m, u_1, \dots, u_m)$, $V: [0, \infty) \times \mathbb{R}^{2nm} \to \mathbb{R}^n$ is called strategy of evader if the following system of equations*

$$\dot{x}_i = -\lambda_i x_i + V(t, x_1, \dots, x_m, u_1, \dots, u_m), \quad x_i(0) = x_i^0, \ i = 1, \dots, m,$$

has a unique solution $(x_1(t), \dots, x_m(t))$, $t \geq 0$, for any controls $(u_1(t), \dots, u_m(t))$, of pursuers and along this solution

$$\int_0^\infty |V(t, x_1(t), \dots x_m(t), u_1(t), \dots, u_m(t))|^2 dt \leq \sigma^2.$$

Definition 1.3 *If there exists a strategy V of evader such that for any controls of pursuers $x_i(t) \neq 0$, $i = 1, \dots, m$, $t \geq 0$, then we say that evasion is possible.*

The problem is to find a condition for evasion to be possible. Thus, the evader knows the values $x_1(t), \dots, x_m(t)$, $u_1(t), \dots, u_m(t)$ of parameters $x_1, \dots, x_m$, $u_1, \dots, u_m$ at the current time t. Pursuers apply arbitrary controls $u_1(t), \dots, u_m(t)$, $t \geq 0$, and try to realize the equation $x_i(t) = 0$ at least for one $i \in \{1,2, \dots, m\}$, whereas the evader tries to maintain the inequalities $x_i(t) \neq 0$ for all $i = 1, \dots, m$ and $t \geq 0$.

The Main Result

The following is the main result of the current paper.

Theorem 2.1 *If* $\rho_1^2 + \cdots + \rho_m^2 \leq \sigma^2$*, then evasion is possible in game (1) - (2).*

It is sufficient to consider the case when $n = 2$ and $\rho^2 := \rho_1^2 + \cdots + \rho_m^2 < \sigma^2$ (see, for example, (Ibragimov et al. 2012, Gafurjan et al. 2018). We have studied a linear evasion differential game of many pursuers and one evader. We have constructed a strategy for the evader and proved possibility of evasion. The evader uses a manoeuvre on a set J_1 and one the set $[0,T]\setminus J_1$ evader uses the control $v(t) = \left(0, \alpha + \left(\sum_{j=1}^m |u_j(t)|^2\right)^{1/2}\right)$. The measure of the set J_1 can be made by choosing parameters a_1 and α as small as we wish. We have also shown that all the approach times τ_i can occur only before a specified time T_0, moreover $\tau_i' \leq T$. The total number of approach times τ_i of all pursuers doesn't exceed the number of pursuers m. For $t \geq T$, the evader uses the control $v(t) = \left(0, \left(\sum_{j=1}^m |u_j(t)|^2\right)^{1/2}\right)$ and there is no longer approach time occurs.

Acknowledgement
The present research was partially supported by Geran Putra Berimpak UPM/700-2/1/GPB/2017/9590200 of Universiti Putra Malaysia and the financial support by Decisions_LAB - Dept. of Law, Economics and Human Sciences - University Mediterranea of Reggio Calabria, Italy. This work completed during the stay of the author Ibragimov G.I. at University Mediterranea of Reggio Calabria - Dept Di.Gi.ES - as Visiting Researcher.

References

1. Ibragimov G.I., Salimi M., and Amini M., 2012. Evasion from many pursuers in simple motion dfferential game with integral constraints. European Journal of Operational Research 218(2), 505-511.
2. Gafurjan I., Massimiliano F., Atamurat K., and Bruno A. P., 2018. Simple motion evasion differential game of many pursuers and evaders with integral constraints. Dynamic Games and Applications 8, 352-378. https://doi.org/10.1007/s13235-017-0226-6.

NONSTATIONARY GENERALIZED EXTREME VALUE MODELLING ON EXTREME RAINFALL WITH CYCLIC COVARIATE

L. J. M. Jasmine[1], A. H. Syafrina[2*]

[1,2]Department of Mathematics, Faculty of Science, Universiti Putra Malaysia, 43400 UPM Serdang, Selangor, Malaysia.

*Corresponding author: syafrina@upm.edu.my

Abstract
This paper focuses on modelling extreme daily rainfall within 30 years in Klang Valley (Malaysia) using Generalized Extreme Value (GEV). Three nonstationary Generalized Extreme Value (NSGEV) models are constructed to assess the impact of cyclic covariates on the extreme daily rainfall events. The best nonstationary model is selected using Akaike Information Criterion (AIC) and Bayesian Information Criterion (BIC). Results indicate that the cyclic covariate in location and scale parameters provide better fits the extreme rainfall data.

Keywords: Cyclic covariate, Extreme rainfall, GEV distribution, Nonstationary

Introduction

Rainfall is a major component of the water cycle by depositing most of the fresh water (Radinović & Ćurić, 2009). High intensity rainfall over a short time scale can cause flash flooding whereas continuous heavy rainfall can cause river flooding. An increase in the number of extreme flood events or flash flood events has been observed over recent decades in Klang Valley (Suparta & Rahman, 2016) and the accuracy of existing flood estimation methods has likely diminished. Nonstationarity of extreme values may be detected by identifying trends in the extreme value (Coles, 2001). Therefore, this study developed nonstationary model with cyclic covariate. JPS Ampang station (Station ID: 3117070) was selected as it receives high rainfall amount during inter-monsoon season (Syafrina et al., 2018). The main objectives of this study are: to fit the GEV and NSGEV with cyclic covariate on extreme daily rainfall series and to identify the best fitted NSGEV model using AIC and BIC.

Methodology

Monthly maximum of extreme rainfall were blocked in this study. GEV distribution is parameterized with a shape parameter (ξ), location parameter (μ) and scale parameter (σ). Nonstationarity was introduced by revealing more than one parameters of the GEV distribution as function of cyclic covariate. μ and σ were described by sine and cosine functions while ξ was assumed to be a constant. The parameters were estimated using Maximum Likelihood Estimation method.

Table 5: Model performance of GEV models for JPS Ampang station

Model	Parameters of model	Remarks
GEV0	μ(constant), σ(constant), ξ(constant)	Stationary model
NSGEV1	σ(constant), ξ(constant), $\mu(t) = \beta_0 + \beta_1 \sin(2\pi t/12) + \beta_2 \cos(2\pi t/12)$	Nonstationary model with time dependent location parameter
NSGEV2	μ(constant), ξ(constant),	Nonstationary model with time dependent scale parameter

	$\sigma(t) = \beta_0 + \beta_1 \sin(2\pi t/12) + \beta_2 \cos(2\pi t/12)$	
NSGEV3	ξ(constant), $\mu(t) = \beta_0 + \beta_1 \sin(2\pi t/12) + \beta_2 \cos(2\pi t/12)$, $\sigma(t) = \beta_0 + \beta_1 \sin(2\pi t/12) + \beta_2 \cos(2\pi t/12)$	Nonstationary model with time dependent location and scale parameter

Results and Discussion

Table 6: Results of performance for GEV and NSGEV models

Model	Parameter estimation	AIC	BIC	$l(\theta)$	$D(\theta)$
GEV0	$\hat{\mu} = 42.0002$, $\hat{\sigma} = 20.690$, $\hat{\xi} = -0.047$	-3398.34	-3394.92	1705.17	-
NSGEV1	$\hat{\mu}_0 = 42.01$, $\hat{\mu}_1 = 0.71$, $\hat{\sigma} = 20.69$, $\hat{\xi} = -0.05$	-3401.92	-3389.96	1704.96	-0.416
NSGEV2	$\hat{\mu} = 41.97$, $\hat{\sigma}_0 = 20.68$, $\hat{\sigma}_1 = 0.23$, $\hat{\xi} = -0.05$	-3402.26	-3389.70	1705.13	-0.078
NSGEV3	$\hat{\mu}_0 = 45.26$, $\hat{\mu}_1 = 2.65$ $\hat{\sigma}_0 = 3.07$, $\hat{\sigma}_1 = 0.04$, $\hat{\xi} = -0.08$	-3409.17*	-3393.47*	1709.59	4.416

The result of model analysis with maximum rainfall series of Klang Valley is given in Table 2. NSGEV3 is found to be the best NSGEV model for monthly maximum rainfall whereby the trend is introduced in location and scale parameter with cyclic covariate. The likelihood ratio test is used to evaluate between the choices of model which is $D(\theta) = 2\{l(\hat{\theta}_0) - l(\hat{\theta})\}$ whereby l is the log likelihood function, based on Chi-Square distribution with critical value of a degree of freedom of 1 is 3.84 at the 0.05 significance level. The deviation value between NSGEV3 and GEV is 4.416 which is greater than the critical value (3.84). Overall, by considering the model selection criteria, NSGEV3 with the smallest AIC, BIC value and the greatest deviation value indicated that nonstationary GEV model with cyclic covariate trend in location and scale parameters provides better fit in describing extreme rainfall data.

Conclusion

This study assesses rainfall series using both stationary and nonstationary rainfall models. In view of the significant increasing trends of extreme rainfall events in Malaysia. It is important to concern the nonstationary nature of rainfall data to achieve better estimations of rainfall distribution. Although this study was conducted at only one station, the results and methodology could be further extended.

Acknowledgement

We appreciate the Drainage and Irrigation Department for providing the rainfall data. The R programming language and R package “ismev” and “extRemes” are used in this study. This research is fully funded by Geran Putra UPM Vote No: 9619400.

References

[1] Coles, G. S. (2001), An Introduction to Statistical Modelling of Extreme Values, 208 pp., Springer, New York.

[2] Radinović, D., & Ćurić, M. (2009). Deficit and surplus of precipitation as a continuous function of time. *Theoretical and Applied Climatology*, *98*(1-2), 197-200.
[3] Suparta, W., & Rahman, R. (2016). Spatial interpolation of GPS PWV and meteorological variables over the west coast of Peninsular Malaysia during 2013 Klang Valley Flash Flood. *Atmospheric Research*, *168*, 205-219.
[4] Syafrina A H, Norzaida A, Kartini A, Badron K. (2018). Analysis of rainfall indices at Jps Ampang station. *Journal of Fundamental and Applied Sciences,* 10(3S), 325-330.

IMPROVED FREQUENCY TABLE WITH APPLICATION TO TEMPERATURE DATA

M. M. Bappah[1,2]*, M. B. Adam[2], H. S. Zulkifli[2] and N. Ali[2]

[1]Mathematics and Computer Science, Federal University of Kashere, 0182 Gombe state, Nigeria.
[2]Department of Mathematics, Faculty of Science, Universiti Putra Malaysia, 43400 UPM Serdang, Selangor, Malaysia.

*Corresponding author: muhdb1@gmail.com

Abstract
When computing statistical measures from a frequency table for continuous data, a statistic value "Midpoint" is used to represents the magnitude of observations in each of the classes, which results to an error called grouping error. In this research, however, three new methods which use the mean, median, and the midrange of observations in each class are compared with the existing method. Computer simulation and real temperature data indicated that, the method which uses the mean outperformed the other methods. So also, in choosing the appropriate number of classes to be used in constructing the frequency table, among the seven rules used, the freedman and Diaconis rule is the suitable rule.

Keywords: Frequency Table, Statistical Measures, Midpoint, Number of Classes.

Introduction
The frequency table plays an important role in statistics. A well-organized frequency table makes possible a detailed analysis of the structure of the population with respect to a given feature. Apart from serving as a bridge between raw data and a histogram, frequency table facilitates the construction of a cumulative frequency curve, aid careful comparison of data sets, and it serves as at a glance reference into the distribution of data sets (Davies, 1929; Hald, 2001).
Though grouping is unavoidable, especially when the data set is large, the process can lead to a considerable amount of errors when compared to the original data (Davies, 1929). Various approaches to minimizing this error were suggested by different researchers in the literature. Ranging from the Sheppard's correction, Canning (1926), Davies (1929), Baten (1931), Jones (1941), Dwyer (1942), Pierce (1943), Hald (2001)[5] and to the most recent work by Di Nardo (2010). In minimizing the grouping error, this study considered substituting the midpoint with the mean, median, and midrange of observations in each class. Meanwhile, the appropriate rule among the seven rules used in choosing the number of classes will be recommended.

Methodology
To construct the frequency table, we need to: (1) Determine the Range (R) of the data, (2) Decide the suitable number of classes (k), (3) Determine the class width (w), w = $\frac{R}{K}$ and (4) Obtain the classes or class intervals. The number classes and class width formulas are given in Table 1.

Table 1: The Number of classes and Class Width Rules

Number of classes and Class width rules	Formula	Terms	Comments
Sturges (1926)	$k = 1 + \log_2 n$	n = is the sample size	Suitable for $n < 200$
Cohran (1954)	$k = \sqrt{\frac{n}{5}}$	n = is the sample size	Used because of its simplicity
Cencov (1962)	$k = \sqrt[3]{n}$	n = is the sample size	Used because of its simplicity

Doane (1976)	k=$1+\log_2 n+\log_2 \lambda$	n = is the sample size λ= $\sqrt{\frac{(n+1)\times(n+3)\times\sum_{i=1}^{n}(x_i-\bar{x})^2}{\sqrt{6\times(n-2)\times\sum_{i=1}^{n}(x_i-\bar{x})^2}}}$	Suitable for skewed data
Scott (1979)	$w=\frac{3.49\hat{\sigma}}{\sqrt[3]{n}}$	n = is the sample size $\hat{\sigma}$ =Sample standard deviation	Suitable for symmetric data
Freedman and Diaconis (1981)	$w=\frac{2\times(IQR)}{\sqrt[3]{n}}$	n = is the sample size *IQR*= Interquartile Range	A robust class width rule
Terrel and Scott (1985)	$k\geq\sqrt[3]{2n}$	n = is the sample size	Used because of its simplicity

Table 2: The Proposed Frequency Table

Class Number	CI		CB		Freq	Cum Freq
	lower	upper	Lower	upper	(f)	(cf)
1	l_1	u_1	$l_1-\frac{\delta}{2}$	$u_1+\frac{\delta}{2}$	f_1	f_1
2	l_2	u_2	$l_2-\frac{\delta}{2}$	$u_2+\frac{\delta}{2}$	f_2	$\sum_{i=1}^{2} f_i$
⋮	⋮	⋮	⋮	⋮	⋮	⋮
k	l_k	u_k	$l_k-\frac{\delta}{2}$	$u_k+\frac{\delta}{2}$	f_k	$\sum_{i=1}^{k} f_i$

Table 3: The Four Methods Used to Represent the Magnitude of Observations in the Classes.

Mean(M_e)	Median(M_d)	Midrange(M_r)	Existing(x^*)
M_{e_1}	M_{d_1}	$\frac{Min_1+Max_1}{2}$	$\frac{l_1+u_1}{2}$
M_{e_2}	M_{d_2}	$\frac{Min_2+Max_2}{2}$	$\frac{l_2+u_2}{2}$
⋮	⋮	⋮	⋮
M_{e_k}	M_{d_k}	$\frac{Min_k+Max_k}{2}$	$\frac{l_k+u_k}{2}$

Where k is the number of classes, f_i is the number of observations falling into class i, and M_{e_i} , M_{d_i}, M_{r_i} are repectively the mean, median and midrange of observations in class i .

The Root-Mean-Squared Error (RMSE)

In this research, the root-mean-square error (RMSE) is used to compare the four methods. Mathematically, the RMSE is given by

$$RMSE = \sqrt{\frac{1}{m}\sum_{i=1}^{m}(\hat{\vartheta}_i-\vartheta_i)^2},$$

where m is number of samples, $\hat{\vartheta}_i$ is the estimated statistic value of sample i, and ϑ_i is the actual statistic value of sample i, $i=1,2,\cdots,m$.

Results and Discussion

To compare the methods, we performed simulation studies using normal, uniform and exponential distributions and real temperature data are used. The seven existing rules, Sturges (1926), Cohran (1954), Cencov (1962), Doane (1976), Scott (1979), Freedman and Diaconis(1981), and Terrel and Scott (1985) rules, are used to determine the suitable number of classes. The results from this study shows that method 1 perform better the other methods.

Conclusion

Based on the simulation and the experimental data, we found that method 1 outperformed the other methods. In choosing a suitable number of classes, the Freedman and Diaconis rule is the most suitable rule for handling normal and skewed data. Using uniformly distributed data, the Doane's rule performed well when $n \leq 500$, whereas the Cohran's rule, is the most suitable for $n \geq 1000$. Indeed, the Cohran rule chose the suitable number of classes for the Seattle temperature data.

Acknowledgement

This research is partially funded by Universiti Putra Malaysia grant GP/2018/969400. The first author is supported by Tetfund, Federal government of Nigeria scholarship grant.

References

[1] Canning, J. B. (1926). Formation of Frequency Distributions, Journal of the American Statistical Association, 21(154), 133-188.
[2] Davies, G.R. (1929). The Analysis of Frequency Distributions. Journal of the American Statistical Association, 24(168), 349-366.
[3] Di Nardo, E. (2010). A New Approach to Sheppard's Corrections. Mathematical Methods of Statistics, 19(2), 151 - 162.
[4] Freedman, D., and Diaconis, P. (1981). On the Histogram as a Density Estimator. Probability Theory and Related Fields 57(4), 453-476.
[5] Hald, A. (2001). On the History of the Correction for Grouping 1873-1922. Scandinavian Journal of Statistics, 28(3), 417-428.
[6] Kenney, J. F. (1939). Mathematics of Statistics. Technical composition Co. Boston.
Scott, D. W. (1979). On Optimal and Data-Based Histograms. Biometrika, 66(3), 605-610.

AN INVESTIGATION OF SELF RELIANCE SKILLS EXISTING AMONG SCIENCE STUDENTS IN FEDERAL COLLEGE OF EDUCATION (TECHNICAL) UMUNZE ANAMBRA STATE NIGERIA

E. C. Umendu[1]*

[1]FCE (T) Umunze Anambra State, Nigeria

*Corresponding author: eumendu@yahoo.com

Abstract

Self reliance involves self dependent attributes rather than depend on others. Self reliance skills are those skills exhibited by both graduate and undergraduate students which enable them to be self reliant and possible gainful employment after graduation. It is putting into practice that knowledge that they acquire during school days after graduation. This is a survey study that was designed to find out the extent to which science students of NCE final year at FCE (T) Umunze possesses self reliant skills. The population for the study comprises of all NCE final year science students of FCE (T) Umunze Anambra State. Three research questions guided the study. The methodology adopted here is mean for data analysis. A five Likert questionnaire was used to collect data. Based on the data analyzed, and the findings made, the researcher recommends among other things that awareness and availability of resources for acquiring knowledge for self reliant should be provided for development of self reliant by the science students. In conclusion, this study clearly provides evidence for the urgent need to develop the entrepreneurial mindset of the students in order for self reliance to be achieved for gainful employment.

Keywords: Employment, Reliant, Dependent, Opportunity, Science.

Introduction

Self reliance in its general sense means the ability to set one's own goal and realizing them as much as positive through one's own effort (Onwuekwe, 2001). Self reliance involves self dependence rather than dependent on others. It also implies harnessing one's creative ability in order to enhance self development. It does not however end in economic gains for the development contributing to a great extent to the good of his/her society (Aminu, 2002; Okeke, 2007).

Self reliant skills are those skills needed by these graduates which will enable them put the various skills and knowledge acquired from the various fields into practice (Nwosu, 1993). These self reliant skills are considered the key that unlocks the operationality of the knowledge and skills acquired. However, these self reliant skills need to be inculcated into the student for the achievement of self reliance (Winter and Hawking, 2011).

The graduates from science should be able to produce the following items as the case may be on commercial scales for self reliance and self employment.

- Food beverages and water quality control scheme
- Instruction materials production
- Cosmetics, perfumes, detergents and soaps
- Identification and marketing of medical plants
- Animal feed production
- Plant and animal breeding

Others are pointed out by Nwagbo and Onyegebu (2009) as follows

- Agriculture (Bee keeping)

- Aquaculture
- Floriculture
- Horticulture
- Poultry farming
- Piggery faming
- Fish farming etc.

With all these opportunities abounding, it is observed that skill after graduating the students join the band of already unemployed people existing in the country thus the aim of the education for self reliance is not achieve.

In an effort to inculcate these self reliance skills in the students, "Entrepreneurship" as a course was introduced into the NCE curriculum with the view of inculcating in the students personal development skills, business development skill and entrepreneurial skill development.

Methodology

Research Design

The research design used for this research was a suney research design, as the research, tries to determine the self reliant skills existing among NCE science student of Federal College of Education (Technical), Umunze Anambra State

Area of Study

The area of the study is Federal College of Education (Technical) Umunze in Orumba South Local Government Area of Anambra State Nigeria.

Population of the Study

The population of this study comprise of all final year NCE science student of FCE (T) Umunze 207/208 session as follows:

Biology =100 students
Chemistry =30 students
Physics = 10 students
Mathematics=10 students
Integrated science student =10
Total 160 students.

This entire population was used for the study.

Sample and Sampling Techniques

The whole population then was used for the study looking at the small number of the population. Hence no sampling took place.

Instrument for Data Collection

The instrument for data collection was 26 itemed structures questionnaire designed by the researcher. It had two sections, section A contained personal data while section B had the research questions.

It is believed that NCE final year science students assessed personal development skill to a moderate extent because they believed that they don't have the confidence of doing any other thing perfect except teaching science subjects, they don't know how to get themselves employed if they failed to get paid employment and because science courses does not lead themselves to personal employment, etc.

It is also discovered that NCE final year science students possessed personal business development skills to a moderate extent because they lack the knowledge of existing opportunities where they can apply their knowledge and earn a living, they lack the

information on the different areas of science from which one can earn a living, they are discouraged studying science education especially now that there is no job.
Finally, it is accepted that NCE science final year students possessed entrepreneurial development skill to a great extent because they believed that they are able to raise funds required to start up a small scale business, they have the ability to compete with others in a business environment, they have the ability to take and bear the risk that may arise in business and so on.

Conclusion

Self reliant skills among NCE science students serve as a bedrock for preparing NCE science students graduate for self reliance entrepreneurship. In this regard, effort should be made to see that these students possess these self reliant skills to a very great extent so as to enable them become self reliant and enhance development of the nation. One of the major crises facing Nigeria today is the high rate of unemployment. This has been found to be one of the reasons for the current rate of extreme poverty and hunger in the society. The millennium development goal MDG (2006) report showed that there are over seventy (%) of unemployment and relatively unskilled people between the ages of thirteen to twenty years in Nigeria.

References

1. Aminu F.A., 2002. Development in Africa, retrieved on July 25 2019 from http://www.Ednory. Africa.
2. Nwosu J.D., 1993. Rudiments of National Development, Owerri Legacy press.
3. Okeke J.D., 2007. Enhancing Entrepreneurship. Retrieved on June 6 2019 from http//:www.career.org.edu.
4. Onwuekwe I. C., 2001. Self Reliance, problems and prospects, Retrieved on June 4, 2019 from http//:www.chmi.org.
5. Winter C. C. and Hawking, P.C., 2011. Self reliant Skills, retrieved on May 5 2019 from http//:www.careerhub.com.

CONVECTIVE HEAT TRANSFER IN FERROUID FLOW OVER AN OSCILLATING CONE IN PRESENCE MAGNETIC FIELD AND HEAT GENERATION/ABSORPTION

H. Hanif [1, 3]*, I. Khan[2], S. Shafie[3]

[1]*Department of Mathematics, SBK Women's University Pakistan.*
[2]*Faculty of Mathematics and Statistics, Ton Duc Thang University, Ho Chi Minh City, Vietnam*
[3]*Department of Mathematical Sciences, Faculty of Science, Universiti Teknologi Malaysia,Johor Bahru, Johor, Malaysia*

*Corresponding author: hanifa1984@graduate.utm.my

Abstract
The present research provides a numerical investigation of two dimensional ferrofluid flow over an oscillating cone in presence of magnetic field and heat generation/absorption with variable wall temperature. The model is developed to incorporate cylindrical-shaped of Fe_3O_4-nanoparticles in water based fluid. Simultaneous effects of pertinent parameters like volume fraction and heat generation/absorption on temperature profile are studied and illustrated graphically. Results showed that maximum values are obtained by increasing nanoparticle volume fraction in presence of magnetic field.

Keywords: Nanofluid; Magnetic field; Heat generation/absorption; Cone

Introduction
In thermal systems, the properties of convectional heat transfer fluid are neither sufficient nor effective due to their low thermal conductivity. Therefore, researchers are more interested in nanofluid compared with regular convectional fluid since they have unique properties such as thermal conductivity and viscosity. On the other hand, magnetic field effects in presence of heat generation/absorption parameters is another famous topic among researchers since magnetic field has numerous application in several fields of industry and manufacturing such as crystal growth, paper production, polymer extrusion, plastic films etc. Maleki *et al.* (2019) discussed heat and mass transfer of Pseudo-plastic nanofluid along a moving plate the presence of heat generation/absorption. They concluded that an increment in heat generation and volume fraction reduces Nusselt number. A study on natural convection Cu-water nanofluid in a rectangular cavity under the effects of magnetic field and heat generation is given in Rashad (2017). An investigation on MHD nanofluid flow over an oscillating plate inside porous medium with effects of heat generation is worked out in Sheikholislami *et al.* (2018). According to the results, the Nusselt number reduces with an increment in time for ramped plate.

The nanofluid properties vary by changing base fluid, size, shape and type of nanoparticles. Spherical nanoparticles are the most common particles by researchers while concerning the application and significance, they are limited. Owing to the fact, this study incorporates the cylindrical nanoparticles. Furthermore, effects of magnetic field and on convective heat transfer in ferrofluid flow over an oscillating cone with variable wall temperature is analysed numerically. The thermo-physical properties of base fluid water and Fe_3O_4 nanoparticles are used by Sheikholislami and Ganji (2014). The effects of φ and Q on temperature distribution profile are illustrated graphically and discussed in details.

Methodology

A convective heat transfer in water based Fe_3O_4 nanofluid over an oscillating cone with uniform velocity u_0 is *considered. The* nanofluid is assumed to be electrically conducting due to external magnetic field. A uniform magnetic field of strength of B is consider parallel to *y−axis*. *x*−axis is consider along the surface of cone in flow direction and normal to the cone is refer to *y−axis*. The 2D unsteady, unidirectional and incompressible nanofluid together with Boussinesq approximation followed by Kannan *et al.* (2019) along with non-dimensional parameters Parasad *et al.* (2007):

$$\frac{\partial}{\partial x}(ru) + \frac{\partial}{\partial y}(rv) = 0,$$

$$\phi_1\left(\frac{\partial u}{\partial t} + u\frac{\partial u}{\partial x} + v\frac{\partial u}{\partial y}\right) = \phi_2\frac{\partial^2 u}{\partial y^2} - \phi_3 Mu - \phi_4 GrT cos\phi,$$

$$\phi_5 Pr\left(\frac{\partial T}{\partial t} + u\frac{\partial T}{\partial x} + v\frac{\partial T}{\partial y}\right) = \phi_2\frac{\partial^2 T}{\partial y^2} + QT.$$

Here $\phi_1 - \phi_6$ refer to nanofluid constants (see: khan (2017). M, Gr, P r, α and Q denote the magnetic parameter, thermal Grashof number, Prandtl number, thermal diffusivity and heat generation or absorption parameter respectively. The corresponding dimensionless initial and boundary conditions are:

$$t \leq 0: u = 0, v = 0, T = 0,$$

$$t > 0: u = u_{0,}\ v = 0, T = x^n, \qquad at\ y = 0,$$

$$u = 0, T = 0, \ \ at \ \ x = 0,$$

$$u \to 0, T \to 0 \ \ as \ \ y \to \infty$$

The non-dimensional resulting system of non-linear, coupled Equations (1) to (3) together with corresponding conditions (5) is discretized by implicit finite difference method, namely, Crank Nicolson method. The step size is taken as small as $\Delta t = 0.01$ combined with the mesh size $\Delta x = 0.05$, $\Delta y = 0.05$ along x and y axis respectively.

Results and Discussion

The effects of cylindrical-shaped Fe_3O_4 nanoparticles on mixed convection heat transfer in electrically conducting ferrofluid over a vertical cone in presence of heat generation or absorption is studied.

The variation in the heat transfer due to volumetric concentration of cylindrical-shaped Fe_3O_4 nanoparticles is illustrated in Figure 1. It is evident from the figure that a significant increment is attained by suspended a very small amount of nanoparticles. The result is physically expected since suspension of nanoparticles increases the thermal conductivity of poor convectional fluid consequently increases the heat transfer rates. Figure 2 reveal the nature of heat transfer of ferrofluid under the effects of heat generation/absorption parameter. The positive values of Q represent heat generation and negative values refer to heat absorption. Physically, an increment in the temperature is obvious when heat is generated and Figure 2 shows that significant heat transfer rates

are

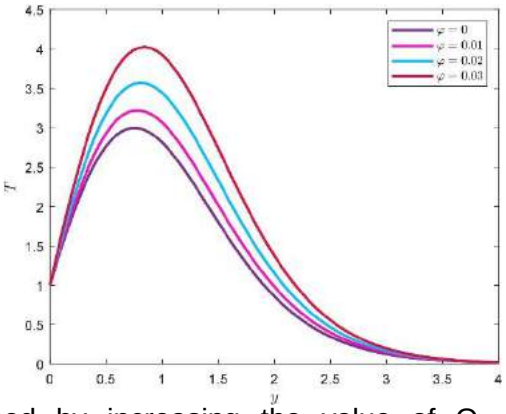

Figure 1 Effect of volume friction on temperature distribution.

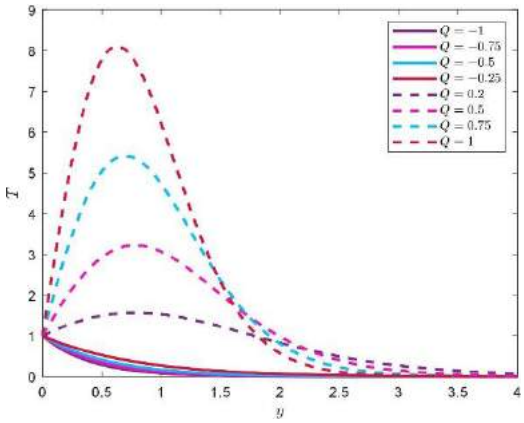

Figure 2 Effect of heat generation/absorption on temperature distribution.

attained by increasing the value of Q. On the other hand, temperature decrease with an increase in heat absorption parameter and flatten when y → 1.

Conclusion

In this study, a ferrofluid flow containing over an oscillating cone with variable wall temperature is analysed. The effects of magnetic field on heat transfer in presence of heat generation/absorption are also discussed. The effect of active parameters on temperature are exhibited graphically. The analysis showed that the temperature profile lifted up by adding nano-sized magnetite particles. It is expected in the sense that suspension of nanoparticles improves the thermal conductivity of regular base fluid (water) as a result temperature of nanofluid is higher than regular fluid. The temperature distribution attained maximum values when heat is generated in presence of magnetic field.

References

[1] Kannan, R., Pullepu, B., and Shehzad, S. A. (2019). Numerical solutions of dissipative natural convective flow from a vertical cone with heat absorption, generation, MHD and radiated surface heat ux. International Journal of Applied and Computational Mathematics, 5(1):24.

[2] Khan, I. (2017). Shape effects of MoS_2 nanoparticles on MHD slip flow of molybdenum disulphide nanofluid in a porous medium. Journal of Molecular Liquids, 233:442-451.

[3] Maleki, H., Safaei, M. R., Togun, H., and Dahari, M. (2019). Heat transfer and fluid flow of pseudo-plastic nanofluid over a moving permeable plate with viscous dissipation and heat absorption/generation. Journal of Thermal Analysis and Calorimetry, 135(3):1643-1654.

[4] Prasad, V. R., Reddy, N. B., and Muthucumaraswamy, R. (2007). Radiation and mass transfer effects on two-dimensional flow past an impulsively started infinite vertical plate. International Journal of Thermal Sciences, 46(12):1251-1258.

[5] Rashad, A., Rashidi, M., Lorenzini, G., Ahmed, S. E., and Aly, A. M. (2017). Magnetic field and internal heat generation effects on the free convection in a rectangular cavity filled with a porous medium saturated with cu-water nanofluid. International Journal of Heat and Mass Transfer, 104:878-889.

[6] Sheikholeslami, M. and Ganji, D. D. (2014). Ferrohydrodynamic and magnetohydrodynamic effects on ferrofluid ow and convective heat transfer. Energy, 75:400-410.

[7] Sheikholeslami, M., Kataria, H. R., and Mittal, A. S. (2018). Effect of thermal diffusion and heat-generation on MHD nanofluid ow past an oscillating vertical plate through porous medium. Journal of Molecular Liquids, 257:12-25.

SIMULATION OF HEALTHY AND CANCER CELLS' POPULATIONS WITH FRACTIONAL DERIVATIVE UNDER RADIOTHERAPHY

M.F. Farayola[1]*, S. Shafie[1], F.M. Siam[1]

[1]Department of Mathematical Sciences, Faculty of Science, Universiti Teknologi Malaysia, 81310 UTM Johor Bahru, Johor, Malaysia.

*Corresponding author: folarinmf@yahoo.com

Abstract
This paper presents a numerical simulation of healthy and cancer cells' population dynamics under radiotherapy. The simulation was done with the improved cancer treatment model which integrates the previous cancer treatment model with the Caputo fractional derivative. The linear-quadratic model, with repopulation terms, was coupled with the improved model to account for the population decline due to radiation. The simulation was done with 2 patients with fractionated doses of 2 Gy, 2.5 Gy, and 3 Gy. The results showed a decline in the volumes of the tumors with the corresponding percentage of damages in the populations of the healthy cells. The results of the simulations can be used to predict the best treatment plan.

Keywords: Radiotherapy, Linear-Quadratic, Cancer treatment, Fractional derivative

Introduction
The disease of cancer is a major cause of death in many parts of the world. Therefore, there are various clinical curative and palliative procedures used in treating cancer (Freedman & Belostotski, 2009; Liu & Yang, 2014). Amongst these procedures, radiotherapy is the most cost-effective (Barnett et al. 2009). However, in order to achieve a successful radiotherapy treatment, the effects of the radiation on cancer and healthy cells must be accounted for. The objective of this research is to simulate and predict the population dynamics of cancer and healthy cells during radiotherapy. The aim of radiotherapy, as well as other treatment procedures, is to eliminate the tumor cells or reduce their population while sparing the healthy cells (Jones, 1999). But during treatment, the radiation affects both cells (Rashid et al.). Therefore, it is imperative to analyze the dynamics of the population changes of both cells in order to determine the status of the treatment.

The use of mathematical models had been very significant in analyzing the interaction and population dynamics of cancer and healthy cells. These models were based on the Lotka-Volterra competitive model (Belostotski & Freedman, 2005; Caputo & Fabrizio, 2015; Freedman & Belostotski, 2009; Liu & Yang, 2014). But these models were more descriptive rather than being predictive. Therefore, the simulation in this research will be done with the improved cancer treatment model. The model will be used to predict and analyze the population changes in the tumor region during treatment. Radiotherapy operates on 4Rs; repair, repopulation, reoxygenation, and redistribution. The improved model will account for the repair and repopulation of cells during treatment. The simulation will be done with the following fractionated doses 2 Gy, 2.5 Gy, and 3 Gy on two patients with brain tumors (Nawrocki & Zubik-Kowal, 2015). The initial volumes V(1) of the tumors are 6.366 mL and 2.323 mL for the two patients respectively. The results of the simulations showed the volume decline in the tumors and the percentage declines P(D) in the populations of the healthy cells.

Methodology

The improved model used for the simulation was formulated by integrating the Caputo fractional derivative into the previous cancer treatment model. The Caputo fractional derivative takes into account the memory effect of cancer treatment (Caputo & Fabrizio, 2015). Also, the increase in populations of the cells was described by proliferation coefficients in the model. The decrease in populations of the cells was described with competition coefficients and cells' population decays. The linear-quadratic, with the repopulation terms, was coupled into the improved model to account for the cells' population decays due to doses of radiation (O'Rourke et al. 2009).

The numerical parameter used for the simulations were obtained from previous literature (Belostotski & Freedman, 2005) while the radiation parameters were obtained from reported data of treated brain cancer patients (Nawrocki & Zubik-Kowal, 2015). The reported doses were single high doses. These high doses were converted to biologically equivalent fractionated doses of 2 Gy, 2.5 Gy, and 3 Gy with an appropriate number of fractions. The simulations were done in MATLAB while the fractional differential equation code (FDE12.m) was used for the Caputo fractional derivative (Diethelm, 2003). The tumor volumes were assumed to be proportional to the populations of cancer cells while the populations of healthy cells were treated as percentages. The tumor volume decline indicates the progress of the treatment while the percentage decline of healthy cells indicates the extent of the side effects of radiotherapy.

Results and Discussion

The numerical parameters used include proliferation coefficients of 9.7041e-4 for the healthy cells and 0.3396 for the cancer cells; competition coefficients of 0.0433 for healthy cells and 0.2385 for cancer cells; carrying capacities of 1 for both cells; time for each fraction is chosen as 15 mins; half time for repair is 15 mins; initial populations of both cells are 0.5; and perturbation constant of 0.0008. The radio sensitivities include 3 Gy for the brain tissue cells as well as 1.5004e1 and 1.0463e1 for the two patients respectively (Nawrocki & Zubik-Kowal, 2015). The biologically effective doses (BED) are 90 Gy and 126 Gy. The total time for the treatment T is the number of fractions N(F) multiplied by the time for each fraction (15 mins). The initial and final percentages of the healthy cells are P(1) and P(2). The percentages of the damaged healthy cells are given by P(D). The kick-off time for the repopulation was taken to be 28 days. Table 1 shows the results of the simulations.

Table 1: Results of radiotherapy treatments on 2 patients (Pat. 1 and Pat. 2)

Radiation Parameters	2 Gy fractions		2.5 Gy fractions		3 Gy fractions	
	Pat. 1	Pat. 2	Pat. 1	Pat. 2	Pat. 1	Pat. 2
BED (Gy)	90	126	90	126	90	126
T (mins)	405	570	300	420	225	315
N(F)	27	38	20	28	15	21
V(1) mL	6.366	2.323	6.366	2.323	6.366	2.323
V(2) mL	5.969	1.037	3.670	0.618	3.067	0.476
P(1) %	100	100	100	100	100	100
P(2) %	92.90	95.79	95.14	96.92	95.55	97.05
P(D) %	7.10	4.21	4.86	3.08	4.45	2.95

Conclusion

The results showed that for Patient 1, the volumes of the tumors diminished from 6.366 mL to 5.969 mL, 3.670 mL, and 3.067 mL with 2 Gy, 2.5 Gy, and 3 Gy respectively. Also, the percentages of the damaged cells are 7.10 %, 4.86 %, and 4.45%. Similarly, for Patient 2, the volumes of the tumors diminished from 2.323 mL to 1.037 mL, 0.618 mL, and 0.476 mL with percentage healthy cells' damages of 4.21 %, 3.08 %, and 2.95 %. This shows that the best treatment was 3 Gy with an appropriate number of fractions.

Acknowledgment

The authors would like to acknowledge Ministry of Education (MOE) and Research Management Centre-UTM, Universiti Teknologi Malaysia (UTM) for the financial support through vote numbers 5F004 and 07G70, 07G72, 07G76 and 07G77 for this research.

References

[1] Barnett, G.C., West, C.M.L., Dunning, A.M., Elliott, R.M., Coles, C.E., Pharaoh, P.D.P. and Burnet, N.G., 2009. Normal tissue reactions to radiotherapy: towards tailoring treatment dose by genotype. *Nat Rev Cancer*, 9(2), pp.134-142.

[2] Belostotski, G. and Freedman, H.I., 2005. A control theory model for cancer treatment by radiotherapy. *International Journal of Pure and Applied Mathematics,* 25(4), pp.447-480.

[3] Caputo, M. and Fabrizio, M., 2015. A new definition of fractional derivative without singular kernel. *Journal of Mathematical Physics,* 2(1), pp.73-85.

[4] Diethelm, K., 2003. Efficient Solution of Multi-Term Fractional Differential Equations Using P(EC) m E Methods. *Computing,* 71(4), pp.305-319.

[5] Freedman, H.I. and Belostotski, G., 2009. Perturbed models for cancer treatment by radiotherapy. *Differ Equ Dyn Syst,* 17(1-2), pp.115-133.

[6] Jones, B., 1999. Mathematical Models of Tumour and Normal Tissue Response. *Acta Oncologica*, 38(7), pp.883-893.

[7] Liu, Z. and Yang, C., 2014. A Mathematical Model of Cancer Treatment by Radiotherapy. *Computational and Mathematical Methods in Medicine,* 2014, pp.1-12.

[8] Nawrocki, S. and Zubik-Kowal, B., 2015. Clinical study and numerical simulation of brain cancer dynamics under radiotherapy. *Communications in Nonlinear Science and Numerical Simulation,* 22(1-3), pp.564-573.

[9] O'Rourke, S.F.C., McAneney, H. and Hillen, T., 2009. Linear quadratic and tumour control probability modelling in external beam radiotherapy. *J. Math. Biol.,* 58(4-5), pp.799-817.

[10] Rashid, H., Mohd Siam, F. and Maan, N., Parameter Estimation for a Model of Ionizing Radiation Effects on Targeted Cells using Genetic Algorithm and Pattern Search Method. *mat,* 34(3), pp.1-13.

HARMONY SEARCH FOR LOCATION-INVENTORY-ROUTING PROBLEM OF REVERSE LOGISTICS SUPPLY CHAIN NETWORK DESIGN MODEL

F. Misni[2,3] , L. S. Lee[1,2]*

[1]*Laboratory of Computational Statistics and Operations Research, Institute for Mathematical Research, Universiti Putra Malaysia, 43400 UPM Serdang, Selangor, Malaysia*
[2]*Department of Mathematics, Faculty of Science, Universiti Putra Malaysia, 43400 UPM Serdang, Selangor, Malaysia*
[3]*Faculty of Industrial Sciences & Technology, Universiti Malaysia Pahang, 26300 Gambang, Kuantan, Pahang, Malaysia*

*Corresponding author: lls@upm.edu.my

Abstract
This paper study the integration of facility location, inventory management, and vehicle routing problems in a reverse logistics supply chain network design model. This model considers both demand and returned product from the customers. The main objective of the problem is to minimize the total cost of operating the facilities, cost of inventory including setup cost and holding cost, as well as the travel cost by the vehicles. The problem is solved by a proposed Harmony Search (HS) algorithm. Computational experiments on benchmark instances show that the proposed HS outperformed a standard HS for all cases.

Keywords: location-routing, production quantity, reverse logistics, harmony search.

Introduction
In a supply chain network design, the key performance of the model is the distribution network which consists of three subproblems: facility location problem, inventory control management and vehicle routing problem (Javid & Azad, 2010). As the green supply chain is gaining attention among the industries, the reverse logistics which considers the returned products from the customers are studied in the optimization of vehicle routing and inventory control. In location-inventory-routing problem (LIRP) of the reverse logistics, the aim is to determine the number and location of the open facilities, the allocation of customers to each open depot, the optimal number of production quantity for each cycle and the vehicle routing of pickup and delivery of products.

From the literature, the LIRP under e-supply chain has been solved by using Hybrid Genetic-Simulated Annealing (HGSA) algorithm and compared with the Genetic Algorithm (GA) (Li et al., 2013). They assumed the returned products are in good conditions and can be resold to the customers. Liu et al. (2015) proposed a pseudo-parallel GA integrating with SA to solve the stochastic LIRP with non-defect returns. Deng et al. (2016) solved the same problem as in Liu et al. (2015) but they considered both defect and non-defect returns with a hybrid Ant Colony Optimization. The forward and reverse logistics of LIRP is solved with a New Tabu Search (NTS) (Yuchi et al., 2016). The probability in NTS accepts the second-best solution during the search process. In this paper, the LIRP will be studied using the Economic Production Quantity model and solved by a proposed Harmony Search.

Methodology
The HS is a population-based metaheuristic algorithm that imitates the music improvisation of a group orchestra (Geem et al., 2001). In the proposed HS, a new Harmony Memory (HM_{new}) is generated at each iteration to speed up the convergence (see, Algorithm 1). To find a balance between the diversification and intensification of the method, a multi-local neighbourhood search method is implemented and the value of Harmony Memory

Considering Rate ($HMCR_{it}$) and Pitch Adjustment Rate (PAR_{it}) are changed dynamically at every iteration with the following formula:

$$HMCR_{it} = HMCR_{max} - (HMCR_{max} - HMCR_{min})\frac{it}{MaxIt}, \quad (1)$$

$$PAR_{it} = PAR_{max} - (PAR_{max} - PAR_{min})\frac{it}{MaxIt}, \quad (2)$$

where, $HMCR_{max}$ and $HMCR_{min}$ are the maximum and minimum values of the $HMCR$, respectively, PAR_{max} and PAR_{min} are the maximum and minimum values of the PAR, respectively, $MaxIt$ is the maximum iteration, and it is the current iteration.

Algorithm 1: Proposed Harmony Search

```
begin
  Define parameter value for HMCR_max, HMCR_min, PAR_max, PAR_min, harmony memory size (HMS).
  Generate initial solutions in harmony memory (HM) with a size of HMS and sort the fitness function.
  do (location-routing)
  while (the stopping criteria is not met) do
    while (number of generated solutions < size of HM_new) do
      if (rand < HMCR_it)
        Choose a solution from the HM
        if (rand < PAR_it)
          Apply multi-local search technique (swap within depot, swap between depot,
          relocation, insertion)
        end if
      else
        Generate new solution randomly within the solution space
      end if
      do (inventory production planning). Solve the LIRP
    end while
    Combine HM and HM_new and sort the fitness function
    Update the best solution vectors with the size of HMS
  end while
  Best solution = the first rank of the solution vectors in HM
end
```

Results and Discussion

The proposed HS is implemented in MATLAB software R2017b and tested with benchmark dataset of Gaskell with additional data for returned products and the production rate.

Table 1: Comparative results between standard HS and proposed HS.

	Gaskell 1	Gaskell 2	Gaskell 3	Gaskell 4	Gaskell 5
Standard HS	4392.65	2279.74	1964.70	3127.80	1013.39
Proposed HS	**4388.70**	**2258.57**	**1930.87**	**3111.09**	**986.94**

Table 1 shows that the proposed HS outperforms the standard HS for all problem instances. The modification of the HS parameters and the implementation of multi-local search techniques contribute to the success of the algorithm.

Conclusions

The integration of facility location, inventory planning, and vehicle routing is a complicated problem in the supply chain network design model. Since the problem is NP-hard, the population-based metaheuristics, i.e. HS is proposed. For a more practical application, the model considers the environmental effect which includes the returned products from the customers. The proposed HS with dynamic value of HMCR and PAR and the multi-local search techniques are successful in generating better solutions as compared to the standard HS. For future direction, the proposed HS algorithm can be compared with other

population-based metaheuristic approaches such as genetic algorithm, particle swarm optimization, and differential evolution.

Acknowledgement
This research was supported by the Geran Putra-Inisiatif Putra Siswazah (GP-IPS/2017/9579400), Universiti Putra Malaysia (UPM).

References

[1] Deng, S., Li, Y., Guo, H., and Liu, B., 2016. Solving a Closed-loop Location-Inventory-Routing Problem with Mixed Quality Defects Returns in E-commerce by Hybrid Ant Colony Optimization Algorithm. *Discrete Dynamics in Nature and Society.* Volume 2016, Article ID 6467812, 12 pages.

[2] Geem, Z.W., Kim, J.H., and Loganathan, G.V., 2001. A New Heuristic Optimization Algorithm: Harmony Search, *Simulation*. 76(2), 60-68.

[3] Javid, A.A., and Azad, N., 2010. Incorporating Location, Routing and Inventory Decisions in Supply Chain Network Design. *Transportation Research Part E: Logistics and Transportation Review*. *46*(5), 582-597.

[4] Li, Y., Guo, H., Wang, L., and Fu, J., 2013. A Hybrid Genetic-Simulated Annealing Algorithm for the Location-Inventory-Routing Problem Considering Returns under E-supply Chain Environment. *The Scientific World Journal*. Volume 2013, Article ID 125893, 10 pages.

[5] Liu, B., Chen, H., Li, Y., and Liu, X., 2015. A Pseudo-Parallel Genetic Algorithm Integrating Simulated Annealing for Stochastic Location-Inventory-Routing Problem with Consideration of Returns in E-commerce. *Discrete Dynamics in Nature and Society*. Volume 2015, Article ID 586581, 15 pages.

[6] Yuchi, Q., He, Z., Yang, Z., and Wang, N., 2016. A Location-Inventory-Routing Problem in Forward and Reverse Logistics Network Design. *Discrete Dynamics in Nature and Society*. Volume 2016, Article ID 3475369, 18 pages.

GENERATING RSA PUBLIC KEYS FOR ROGUE CERTIFICATES

A. H. A. Ghafar[1]*, M. R. K. Ariffin[1,2]

[1]*Institute for Mathematical Research, Universiti Putra Malaysia, 43400 UPM Serdang, Selangor Darul Ehsan, Malaysia*
[2]*Department of Chemistry, Faculty of Science, Universiti Putra Malaysia, 43400 UPM Serdang, Selangor Darul Ehsan, Malaysia.*

*Corresponding author: amirghafar87@gmail.com

Abstract
Digital certificate is a mechanism to deploy cryptographic solutions on IT infrastructure. An RSA digital certificate contains RSA public keys, (N, e) generated by trusted third party (TTP). In an unexpected but possible scenario, a TTP may go rogue and generate weak (N, e) that will diminish entirely the security imposed by the certificate. In thi paper, we discuss how weak keys can lead to the possible factorization of N via a generalized RSA key equation given by $eX - uY = Z$. We also show a method to factor k RSA moduli.

Keywords: RSA cryptosystem, diophantine approximations, digital certificate, LLL algorithm

Introduction

RSA cryptosystem was introduced by Rivest et al. (1978) as the first public-key encryption scheme. In the current digital world, RSA cryptosystem is mostly utilized in securing information from unauthorized access and authenticity of data transmitted. One of the platforms that deploys the RSA scheme is the digital certificate which is used by web browsers to authenticate the identity of the entities that we intend to communicate with. In generating the certificate, a trusted third party (TTP) is commonly used to form a web of trust in authorizing the certificate. However, in an unexpected but possible event, TTP may go rogue and generate weak RSA keys that are embedded in the certificate. If this occurs, the certificate cannot guarantee that the RSA private keys can be secured and possible fraudulent by an adversary is probable. In this paper, we show how these weak keys can lead to a vital factorization of RSA modulus hence expose the RSA private keys. We also study the consequences of our method if the adversary is given k set of weak RSA keys. Our method utilizes the similar methodology by Nitaj et al. (2014).

Methodology

In 1990, Wiener (1991) showed if RSA private exponent $d < \frac{1}{3}N^{1/4}$ then its corresponding RSA modulus, N can be factored. In this attack, Wiener utilizes continued fraction method to prove its feasibility. Since then, many attacks on RSA focus on RSA key equation namely $ed - k\varphi(N) = 1$ where e and d are RSA public and private exponents respectively, $\varphi(N)$ is the Euler's phi function of N and k is an integer. Another attack by Coppersmith (1996) utilizes LLL algorithm (Lenstra et al., 1983) to establish Coppersmith's method that are also extensively used to attack RSA (Boneh et al. (1998), Herrmann and May (2008)). In our method, we redefine RSA key equation by introducing a controlled parameter, u that has a relation with N as follows

$$eX - uY = Z$$

where $u = [N - 2\sqrt{N} + 1] + [N - \frac{3}{\sqrt{2}}\sqrt{N} + 1]$. Then, we utilize Lagrange's theorem on continued fraction to prove that a convergent of combination term of e, u, N can give us the suitable values of X and Y in the equation above. Using the value of Z, we obtain $\tilde{P}$ which

is an approximation of an RSA factor. By using similar methodology by Nitaj et al. (2014), we apply our method on k set of weak RSA key pairs (N_i, e_i).

Results and Discussion

We prove that given weak RSA key pair, (N, e), by computing the convergent of $\frac{e}{u} - \frac{N^{1/4}}{2u}$, we can find the values of X and Y in the redefined key equation. Thus, the value of Z can be computed. Then, we also prove that $\tilde{P} = \frac{1}{2}(S + \sqrt{S^2 - 4N})$ where $S = N - Z$. By using the value of $\tilde{P}$, we can solve for p by using results from Coppersmith (1996) by applying LLL algorithm (Lenstra et al., 1983). Using the same parameters, we successfully applied our method on k weak RSA key pairs moduli simultaneously.

Conclusion

In this paper, we have successfully showed that an RSA modulus can be factored when (N, e) satisfy our conditions. The method combines the continued fraction and Coppersmith's methods upon our defined generalized RSA key equation. The output is an approximation of p which can solve the factorization of N via the LLL algorithm. We also showed that our method works on k set of weak RSA key pairs (N_i, e_i). This result is devastating to the security of RSA cryptosystem since the weak public keys can be embedded by rogue trusted third party without being noticed by the RSA users.

References

1) Boneh, D., Durfee, G., and Frankel, Y. (1998). An attack on RSA given a small fraction of the private key bits. *In International Conference on the Theory and Application of Cryptology and Information Security*, pages 25–34. Springer.
2) Coppersmith, D. (1996). Finding a small root of a bivariate integer equation; factoring with high bits known. *In International Conference on the Theory and Applications of Cryptographic Techniques*, pages 178–189. Springer.
3) Herrmann, M. and May, A. (2008). Solving linear equations modulo divisors: On factoring given any bits. *In International Conference on the Theory and Application of Cryptology and Information Security*, pages 406–424. Springer.
4) Lenstra, A. K., Lenstra, H. W., and Lovász, L. (1982). Factoring polynomials with rational coefficients. *Mathematische Annalen*, 261(4):515–534.
5) Nitaj, A., Ariffin, M. R. K., Nassr, D. I., and Bahig, H. M. (2014). New attacks on the rsa cryptosystem. *In International Conference on Cryptology in Africa*, pages 178–198. Springer.
6) Rivest, R. L., Shamir, A., and Adleman, L. (1978). A method for obtaining digital signatures and public-key cryptosystems. *Communications of the ACM*, 21(2):120–126.
7) Wiener, M. J. (1990). Cryptanalysis of short RSA secret exponents. *IEEE Transactions on Information theory*, 36(3):553–558.

EFFICIENT ZERO-KNOWLEDGE IDENTIFICATION SCHEME IN STANDARD MODEL BASED ON BIVARIATE FUNCTION HARD PROBLEM

Boon-Chian Tea[1]*, Muhammad Rezal Kamel Ariffin[2]

[1]Institute for Mathematical Research (INSPEM), Universiti Putra Malaysia, 43400 UPM Serdang, Selangor, Malaysia
[2]Department of Mathematics, Faculty of Science, Universiti Putra Malaysia, 43400 UPM Serdang, Selangor, Malaysia.

*Corresponding author: teaboonchian@ymail.com

Abstract
A zero-knowledge identification (ID) scheme based on Diophantine Equation Hard Problem (DEHP) was proposed in 2013. The scheme was proven to be secure against impersonation under passive attack via assumption that solving DEHP is hard. However, further simulation showed that there exists non-negligible probability that the scheme can be easily impersonated without knowing the secret parameters. In this paper, an ID scheme based on Bivariate Function Hard Problem (BHFP) which is a specific problem of the DEHP is proposed. We prove by assuming that if solving the One-More BFHP is hard, then our scheme is secure against impersonation under passive, active and concurrent attacks. Also, our scheme is more efficient than some selected schemes since the operations' structure of BFHP are simple.

Keywords: Identification scheme, zero knowledge, Diophantine Equation Hard Problem, Bivariate Function Hard Problem.

Introduction
Zero-knowledge identification (ID) scheme enables a prover to identify himself to the verifier without revealing private information throughout the communication (1986). Besides confidentiality, it aims to provide authentication to protect against impersonation by adversary either passively, actively, or concurrently. Tea *et al.* (2013) proposed an ID scheme based on Diophantine Equation Hard Problem (DEHP), a problem by Ariffin *et al.* (2012). The scheme was proven to be secure against impersonation under passive attack assuming that solving DEHP is hard. However, further analysis and simulation showed that the solution to the DEHP in the form of $U = \sum_{i=1}^{2} v_i x_i$ is unique with high probability, yet with careful selection from the solutions' intervals, successful impersonation is possible without knowing the secret parameters. In this paper, we propose a new ID scheme based on the Bivariate Function Hard Problem (BFHP), a specific form of DEHP. The structure of BFHP chosen is improvised such that solving the BFHP is infeasible and the secret *preferred*-solution is unique. With additional new defined assumption of One-More BFHP, our new scheme achieved all the above-mentioned security targets while maintaining computation efficiency.

Methodology
Ariffin (2012) defined the BFHP that via careful selection and setting of the security parameters, the function $f(x, y) = A_1 x + A_2 y = K$ has a unique *preferred*-solution set (x, y) that is infeasible to be sieved through the solution set by the adversary. Having the advantage of infinitely many solutions, alongside with simple addition and multiplication operations' structure, we utilized it in designing our new ID scheme. To prove the security of our ID scheme in standard model, we defined a new One-More BFHP that binds the

adversary to solve 'one more' BFHP, and then apply the reset lemma due to Bellare and Palacio (2002) such that by resetting commitment in the simulation game, the probability of adversary winning the game (success impersonation) is negligible.

Results and Discussion

Via the assumption that solving the One-More BFHP is difficult, our proposed ID scheme is secure against impersonation under all passive, active and concurrent attacks. Moreover, our ID scheme is more efficient than the selected Fiat-Shamir (FS) (1986), Guillou-Quisquater (GQ) (1988) and Schnorr's (1989) ID schemes since our scheme features only simple addition (*Add*) and multiplication (*Mul*) operations and less modular exponentiations (*Exp*) in the protocol. The following shows the protocol of our ID scheme and computation efficiency comparison.

Key Generation:

1. Generates the secret parameters of $\{v_i\}_{i=1}^{3} \in \mathbb{Z}_{(2^{n-1},2^n-1)}$
2. Computes the parameters of $G = v_1 + v_2,\ e_1 = v_3 - v_1,\ e_2 \equiv v_1^{-1} (\mathrm{mod}\ e_1)$, and $x \equiv 1 - v_3^{-1} \pmod{G}$ with condition that $x \in \mathbb{Z}_{e_1}$, $v_1 > e_1$ or $v_1 > \frac{1}{2} v_3$. Otherwise repeat steps 1 and 2.
3. Publicizes $\{G, e_1, e_2\}$ and keeps $\{v_1, v_2, v_3, x\}$ secret.

Identification Protocol:

1. Prover P randomly selects y from $\mathbb{Z}_{(2^{n-1},2^n-1)}$, computes $Y = y + v_2$ and sends commitment Y to Verifier V.
2. Verifier V picks challenge $c \in \{0,1\}^*$ and feedback to Prover P.
3. Prover P responses Verifier V with $z \leftarrow v_3 x^c - y$.
4. Verifier V accepts if one of the conditions satisfied:
   a) If $c = 0$, then $e_1 - z - Y \equiv 0 \pmod{G}$
   b) If $c = 1$, then $e_1 - z - Y \equiv 1 \pmod{G}$.

   Otherwise reject Prover P.

Algorithm 1: The proposed Identification (ID) Scheme.

Table 1: Computation Efficiency Comparison of ID Schemes.

ID Scheme	Key Generation			Prove			Verify		
	Add	*Mul*	*Exp*	*Add*	*Mul*	*Exp*	*Add*	*Mul*	*Exp*
FS	3	4	0	2	2	0	2	1	0
GQ	0	1	1	2	1	2	0	1	2
Schnorr	0	1	1	0	1	2	0	1	2
Proposed	0	0	1	1	1	1	0	1	2

Conclusion

A new ID scheme based on BFHP is proposed. The security analysis proved that our new proposed scheme is secure in standard model against impersonation under passive, active and concurrent attacks via assumption that solving One-More BFHP is hard. Also, the computation efficiency of our ID scheme is better than the three selected schemes of FS, GQ and Schnorr's. Hence, our ID scheme is a preferable choice.

Acknowledgement

The authors would like to thank the Institute for Mathematical Research (INSPEM) and Universiti Putra Malaysia (UPM) for giving the opportunity to conduct this research.

References

1) Ariffn, M.R.K. 2012. A Proposed IND-CCA2 Scheme for Implementation on an Asymmetric Cryptosystem Based on Diophantine Equation Hard Problem. *In Proceedings of the 3rd International Conference on Cryptology and Computer Security*: 193–197.
2) Bellare, M. and Palacio, A. 2002. GQ and Schnorr Identification Schemes: Proofs of Security against Impersonation under Active and Concurrent Attacks. *Advances in Cryptology, CRYPTO'02* 2442: 162–177.
3) Fiat, A. and Shamir, A. 1986. How to Prove Yourself: Practical Solutions to Identification and Signature Problem. *Advances in Cryptology, CRYPTO'86* 263: 186–194.
4) Guillou, L. and Quisquater, J.J. 1988. A "Paradoxical" Identity-Based Signature Scheme Resulting from Zero Knowledge. *Advances in Cryptology, CRTYPTO'88* 403: 216–231.
5) Schnorr, C.P. 1989. Efficient Identification and Signature for Smart Card. *Advances in Cryptology, CRYPTO'89* 435: 239–252.
6) Tea, B.C., Ariffin, M.R.K. and Chin, J.J. 2013. An Efficient Identification Scheme in Standard Model Based on the Diophantine Equation Hard Problem. *Malaysian Journal of Mathematical Sciences* 7(S): 87–100.

AN IMPROVED ATTACK ON SOME VARIANTS OF RSA CRYPTOSYSTEM

W.N.A. Ruzai[1]*, M.R.K. Ariffin[1,2], M.A. Asbullah[1,3]

[1]*Institute for Mathematical Research, Universiti Putra Malaysia, 43400 UPM Serdang, Selangor Darul Ehsan, Malaysia.*
[2]*Department of Mathematics, Faculty of Science, Universiti Putra Malaysia, 43400, Selangor Darul Ehsan, Malaysia.*
[3]*Centre of Foundation Studies for Agriculture Science, Universiti Putra Malaysia, 43400, Selangor Darul Ehsan, Malaysia.*

*Corresponding author: wannuraqlili@gmail.com.my

Abstract
This paper proposed an improved attack upon some variants of RSA cryptosystem such as the instances of Kuwakado-Koyama-Tsuruoka cryptosytem, Castagnos cryptosystem and RSA over Gaussian integers. Remark that all these variants cryptosystems shared similarity of having its public exponent *e* and the private exponent *d* satisfying the key equation of the form $ed - k(p^2 - 1)(q^2 - 1) = 1$ where *N=pq* is an RSA modulus while $(p^2 - 1)(q^2 - 1)$ is referred as the modified Euler quotient. In this work, we introduce a strategy known as the continuous midpoint subdivision analysis which utilized the continued fractions algorithm to find the unknowns *d* and *k*.

Keywords: RSA-variants, Factoring problem, Algebraic cryptanalysis, Continued fractions method

Introduction
The RSA cryptosystem is the earliest public key cryptosystem introduced in 1978 by Rivest, Shamir and Adleman. Since then, RSA became the most widely used encryption scheme in securing our digital information. The security of RSA is based on the assumption that factoring large integers; in this case factoring the public key *N=pq* is hard. Since its introduction, the RSA cryptosystem has been generalized in various ways, in order to improve its efficiency in term of encryption and decryption time. Such cryptosystem is known as variants of RSA cryptosystem. We especially focused on variants of RSA cryptosystem with the property of having its public key *e* and private exponent *d* satisfying the key equation of the $ed - k(p^2 - 1)(q^2 - 1) = 1$ for some positive integer *k*. Recently, Bunder, Nitaj, Susilo and Tonient introduced a method to factor modulus *N* upon the previously mentioned variants of RSA cryptosystem. We recall that the attack by Bunder et al. (2016) work under certain conditions where the unknowns *d* and *k* can be discovered using the continued fractions expansion of certain related numbers. In this work, we propose a generalization of their method by introducing a strategy called the continuous midpoint subdivision analysis and we successfully extend and improve the previously mentioned attack.

Methodology
In this study, we utilized the use of continued fractions property to find the approximation of the private parameters of some variants of RSA cryptosystem by its public parameters. Back in 1990, Wiener showed that using continued fractions, one can efficiently recover the secret exponent *d* from the public key pair (*N,e*) as long as $d < \frac{1}{3}N^{0.25}$. Next after, Boneh and Durfee (2000) proposed a substantial improvement over Wiener's bound. Their attack can recover primes *p* and *q* in polynomial time if $d < N^{0.292}$. Their result is due to Coppersmith's method of finding small solutions to modular polynomial equations. In 2016,

Bunder et al. proposed an attack against RSA variants cryptosystems by utilizing the continued fractions method to find $\frac{k}{d}$ amongst the convergent of $\frac{e}{N^2+1-\frac{9}{4}N}$ wherever $d < \sqrt{\frac{2N^3-18N^2}{e}}$. Notice that, the denominator term $N^2+1-\frac{9}{4}N$ is actually the midpoint of the interval $(N^2+1-\frac{5}{2}N, N^2+1-2N)$. Note that, the modified Euler quotient lies in this interval.

Results and Discussion

In this paper, we prolonged the work by Bunder et al. (2016). In our case, one is in search for the convergent of the continued fractions expansion of $\frac{e}{\mu_{(i.j)}}$ where $\mu_{(i.j)} = N^2+1-\frac{20(2^{i-1})-1-2j}{2^{i+2}}N$ for a fixed positive integer i and some $j \in (0, 2^i-1)$. We prove that one can find the unknowns parameters *d* and *k* from the list of convergent of continued fraction expansion of $\frac{e}{\mu_{(i.j)}}$wherever $d < \sqrt{\frac{2^{i+1}N^3-(2^{2i+3}+5(2^{i+1})-2j)N^2}{e}}$. Then we provide an algorithm that leads to solve the integer factorization problem and we demonstrate the attack with numerical examples.

Conclusion

In this paper, we focused on the variants of RSA with modified Euler quotient denoted as $\varphi(N) = (p^2-1)(q^2-1)$ where the public exponent *e* and private exponent *d* satisfying the modified key equation of this form $ed - k\varphi(N) = 1$ with $N = pq$ be the RSA modulus where $q < p < 2q$. We showed that we successfully improved and extended the previously proposed method by utilizing the continued fractions algorithm to find the convergent of some related number associating with the unknowns *d* and *k*.

References

1) Boneh, D., and Durfee, G. (2000). Cryptanalysis of RSA with private key *d* less than $N^{0.292}$, *IEEE Transactions on Information Theory*, 46(4) pages 1339-1349.
2) Bunder, M.W., Nitaj, A., Susilo, W., and Tonien, J. (2016). A new attack on three variants of the RSA cryptosystem. *in: Australasian Conference on Information Security and Privacy*, pages 258-268.
3) Castagnos, G. (2007). An effcient probabilistic public key cryptosystem over quadratic field quotients. *Finite Fields and Their Applications*, 13(3):563-576.
4) Elkamchouchi, H., Elshenawy, K., and Shaban, H. (2002). Extended RSA cryptosystem and digital signature schemes in the domain of Gaussian integers. *in Proceedings of the 8th International Conference on Communication Systems*, pages 91-95.
5) Kuwakado, H., Koyama, K., and Tsuruoka, Y. (1995). A new RSA- type scheme based on singular cubic curves $y^2 = x^3 + bx^2 (mod\ n)$. *IEICE Transactions on Fundamentals*, 78(1):27-33.
6) Nitaj, A. (2013). Diophantine and Lattice Cryptanalysis of the RSA Cryptosystem. *In Articial Intelligence, Evolutionary Computing and Metaheuristics*, pages 139-168.
7) Rivest, R. L., Shamir, A., and Adleman, L. (1978). A method for Obtaining Digital Signatures and Public-Key Cryptosystems. *Communications of the ACM*, 21(2):120-126.
8) Wiener, M. J. (1990). Cryptanalysis of short RSA secret exponents. *IEEE Transactions on Information Theory*, 36(3):553-558.

CRPTANALYSIS OF RSA ON PARTIAL KEY EXPOSURE ATTACK WITH MODULUS $N = p^2q$

N. N. H. Adenan[1*] , M. R. K. Ariffin [1,2]

[1] *Institute for Mathematical Research, Universiti Putra Malaysia, 43400 UPM Serdang, Selangor Darul Ehsan, Malaysia*
[2] *Department of Chemistry, Faculty of Science, Universiti Putra Malaysia, 43400 UPM Serdang, Selangor Darul Ehsan, Malaysia.*

*Corresponding author: hanisahadenan@gmail.com

Abstract
Let $N = p^2q$ be the modulus and e be a public key such that d is the corresponding inverse modulo of e mod $\phi(N)$. In this paper, we present a partial key exposure attack on RSA whereby the prime of the modulus share their Least Significant Bits. The attack works when a certain amount of Least Significant Bits of p and q are known such that $|p - q| < 2^b u$ where b is known integer. We use extended technique of Jochemsz May to find the small roots of our integer multivariate polynomial and thus factor the modulus N.

Keywords: RSA cryptosystem, Least Significant Bits, Jochemsz May technique, multivariate polynomial.

Introduction
In 1978, Rivest, Shamir and Adleman came out with a brilliant idea by inventing the very first asymmetric cryptosystem namely RSA which is very essential in securely transmitting the digital data. The construction of RSA algorithms are key generation, encryption, and decryption. Let $N = pq$ where p and q are two distinct primes. Let e and d be the public and private key satisfying $ed - k\phi(N) = 1$. The encryption process involves $m^e \equiv c \bmod N$ while for decryption process involves $c^d \equiv m \bmod N$. m and c are the plaintext and ciphertext respectively. Since its development, researchers tried to look for the weakness of this cryptosystem. Cryptanalysis on RSA cryptosystem started by Wiener in 1990 by attacking its private key d and he showed that RSA is insecure if $d < \frac{1}{3}N^{1/4}$. Boneh and Durfee in 1999 improved Wiener's bound up to $N^{0.292}$. Their attack is based on Coppersmith's method on finding small solutions for modular polynomial equations. Thus, one needs to be careful in choosing the value of d to ensure that it does not fall into those bounds. Another attack of RSA is when some parts of information on its private key is known. This kind of attack is called partial key exposure attack. Nitaj et al. proved that the modulus $N = pq$ can be factored in polynomial time if there exist primes that share their least significant bits and two private keys d_1, d_2 share their most significant bits. We extended their research to modulus $N = p^2q$ and we showed that N can be factored when the primes p and q share their least significant bits. However in our case, we only consider the existence of one private key.

Methodology
Don Coppersmith in 1996 introduced new approach of finding small modular and integer roots of polynomial and his method has been widely applied in cryptanalysis area. Later in 2006, Jochemsz and May presented a strategy for finding small roots of polynomials either in modular or integer type. Since then, researchers often use their method to solve this type of problem since their strategy is easier to implement. In our research, we apply Jochemsz and May strategy to solve and find the roots of trivariate integer polynomial.

Results and Discussion

We prove that if the primes of the modulus $N = p^2q$ share an amount of their least significant bits such that $p - q = 2^m u$ where m is known and $2^m \approx N^\alpha$. With $e \approx N^\gamma$ and $d \approx N^\delta$, we proved that the modulus N can be factored in time polynomial if $\delta < \frac{2}{3} + \frac{3}{2}\alpha - \frac{1}{2}\gamma$. From our theorem, we showed that, the smaller the choice of public exponent e, the greater the bound of δ where N can be factored. We apply Jochemsz and May strategy and LLL algorithm to find the roots of the polynomials, which then lead to factoring modulus N.

Conclusion

Our paper showed the consequence of having primes that share a certain amount of least significant bits and some of the information leaked to the third party. The information could be used to factor modulus Nwhich then break the RSA cryptosystem. Thus, one needs to be careful in choosing the primes and ensure that the information will be kept private.

References

1) Rivest, R. L., Shamir, A., and Adleman, L. (1978). A method for obtaining digital signatures and public-key cryptosystems. *Communications of the ACM*, 21(2):120–126.
2) Wiener, M. J. (1990). Cryptanalysis of short RSA secret exponents. *IEEE Transactions on Information theory*, 36(3):553–558.
3) Boneh, D., and Durfee, (1999). Cryptanalysis of RSA private key d less than $N^{0.292}$. *Eurocrypt'99,LNCS 1592*, pages 1–11. Springer.
4) Coppersmith, D. (1996). Finding a small root of a bivariate integer equation; factoring with high bits known. *In International Conference on the Theory and Applications of Cryptographic Techniques*, pages 178–189. Springer.
5) Jochemsz, E., & May, A. (2006, December). A strategy for finding roots of multivariate polynomials with new applications in attacking RSA variants. In *International Conference on the Theory and Application of Cryptology and Information Security*(pp. 267-282). Springer, Berlin, Heidelberg.
6) Nitaj, A., Ariffin, M. R. K., Nassr, D. I., and Bahig, H. M. (2014). New attacks on the rsa cryptosystem. *In International Conference on Cryptology in Africa*, pages 178–198. Springer.

NEW VULNERABILITIES UPON POMARANCH BOOLEAN FUNCTION THROUGH FAULT INJECTION ANALYSIS (FIA)

W. Z. Omar@Othman[1,2]*, M. R. K. Ariffin[1], S. Shamsuddin[2], Z. Mahad[1], S. M. Jawi[2]

[1]Laboratory of Cryptography, Analysis and Structure, Institute for Mathematical Research, Universiti Putra Malaysia
[2]CyberSecurity Malaysia

*Corresponding author: wanzariman@cybersecurity.my

Abstract
Pomaranch stream cipher is a synchronous stream cipher submitted to eSTREAM, the ECRYPT Stream Cipher Project and was designed by Jansen et al. and publish in 2006. In this algorithm, the Boolean function given with coefficients, n is equal to five (5) and its degree, d is equal to three (3). In conducting this attack, we aim to decrease the degree of the targeted Boolean equation by find it vulnerability with constructing low degree annihilator equation(s). We adopt the Fault Injection Analysis (FIA) methodology to achieve our objectives. In this study, we found the vulnerability via annihilator(s) through FIA (inject with value of one (1)) on Boolean function of Pomaranch. With these injected Boolean functions, we proceed to utilize Hao's method to find new annihilator(s). Then we obtained new annihilator(s) on Boolean function of Pomaranch stream cipher. As a result, these newly identified annihilators successfully reduce the complexity of the published Boolean function to guess the initial secret key. It likewise gives truly necessary data on the security of these chose stream cipher concerning Fault Injection Analysis.

Keywords: Vulnerabilities, Annihilator, Boolean function, Fault Injection Analysis (FIA), Algebraic Attack

Introduction
Stream ciphers are symmetric systems, so both sender and receiver share a common secret key and both encryption and decryption depend on this key. In general, stream ciphers are much faster than public key systems that have two keys. Among all attacks upon stream cipher, the Fault Injection Analysis (FIA) is a practical method that can be used by attackers in real-world scenarios. Hoch and Shamir (2004) states that fault analysis is a very powerful cryptanalytic method upon many cryptosystems which at a glance is not vulnerable to direct attacks. In this paper, we are using FIA techniques together with Hao's method to find vulnerabilities of Pomaranch such as annihilator equation. If annihilator(s) are obtained from the specific algorithm, it can be used for an algebraic attack this algorithm.

Methodology
In 2007, Hao et al. introduced sufficient and necessary conditions of the existence of low degree multiplies for a given boolean function f is analysed and three algorithms to find annihilators, g of a boolean function f. In this research, we will used Fault Injection Analysis by inject (replace) value of one (1) to each active coefficient in each boolean function. With produced list of new injected boolean function, we used Hao's method to find the vulnerabilities upon the boolean function.

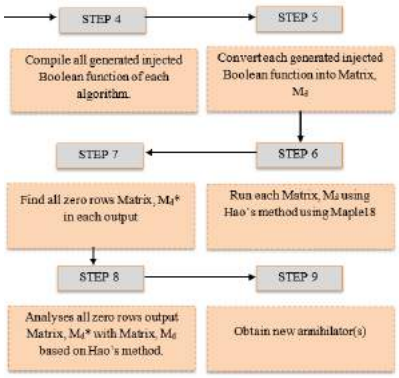

Hao's method flowchart

Results and Discussion

We prove that, using FIA and Hao's method, there is exist vulnerability on Pomaranch's boolean function. From the analysis and results we have generated fourteen injected boolean functions, we obtained two possible annihilators via coefficient x_4 and x_3x_4. We then identified that the annihilator, $g = x_1x_2 + x_1x_4 + x_2x_3 + x_3x_4$which was obtained by injecting fault value upon x_3x_4, had capacity to reduce the complexity of determining the initial key upon our injected Pomaranch boolean function. That is from complexity of $2^5 = 32$ to $2^4 = 16$.

Conclusion

This paper successfully performed Fault Injection Analysis (FIA) on Pomaranch's boolean function and reduced the complexity of this algorithm. In conclusion this identified annihilator provided much needed information on the security of Pomaranch and will be utilized to launch algebraic attacks upon Pomaranch stream cipher.

Acknowledgement

Bismilahir-Rahmanir-Rahim

To ALLAH s.w.t. the creator of all creations, all praise be to Him who is eternal and exists without place, the Most Beneficent and the Most Merciful, the Lord of the worlds. High gratitude and respect to my supervisor Associate Professor Dr Muhammad Rezal bin Dato' Kamel Ariffin for his never ending guidance and patience pushes me forward throughout this paper.

As to my lovely wife, Wan Maisarah Md Isa, my pretty daughters Wan Hannah Zahra, Wan Hawwa Zareen, my handsome son Wan Haadi Zafir and my new born princess, Wan Hajar Zafreen thank you for your never ending love and understanding of my lifelong passion – Information Security especially in cryptography.

See you all again in the next adventure!

References

1) Shannon, Claude E. « Communication theory of secrecy systems. » Bell system technical journal 28.4 : 656-715 (1949)
2) Hell, Martin, Thomas Johansson, and Willi Meier. « Grain : a stream cipher for constrained environments. » International Journal of Wireless and Mobile Computing 2.1: 86-93 (2007)

3) Barenghi, A., Breveglieri, L., Koren, I., and Naccache, D. Fault injection attacks on cryptographic devices: Theory, practice, and countermeasures. Proceedings of the IEEE, 100(11):3056–307. (2012)
4) Guilley, Sylvain, et al. "Fault injection resilience." Fault Diagnosis and Tolerance in Cryptography (FDTC), 2010 Workshop on. IEEE, (2010)
5) Courtois, Nicolas T. "Fast algebraic attacks on stream ciphers with linear feedback." Annual International Cryptology Conference. Springer, Berlin, Heidelberg, (2003)
6) Hao, C., Shimin, W., and Zepeng, Z. Several algorithms to find annihilators of boolean function. IEEE In isdpe, pages 341–343 (2007)
7) Cusick, T. W. and Stanica, P. Cryptographic Boolean functions and applications. Academic Press. (2017)
8) Katz, Jonathan, et al. Handbook of applied cryptography. CRC press, (1996)

POSTER PRESENTATION

BIOLOGY

INTERACTION BETWEEN APIGENIN AND HESPERETIN ON XANTHINE OXIDASE INHIBITION AND THEIR INHIBITORY MECHANISM

S.L. Lim, K.E. Loh*

[1]*Department of Bioscience, Faculty of Applied Sciences, Tunku Abdul Rahman University College, 53300 Setapak, Kuala Lumpur, Malaysia.*

*Corresponding author: lohke@tarc.edu.my

Abstract
Xanthine oxidase (XO) catalyses the oxidation of xanthine and hypoxanthine to uric acid. Hyperuricemia caused by the over-production or under-excretion of uric acid often associate with various diseases. The present study was carried out to investigate the XO inhibitory activity of *Chrysanthemum morifolium* ethyl acetate (EA) fraction and the interaction between apigenin and hesperetin on XO inhibition and their modes of inhibition. The EA fraction demonstrated 63.5% of XO inhibition, and the presence of apigenin and hesperetin were confirmed by using high-performance liquid chromatography. Interaction assay of apigenin and hesperetin showed additive effect on XO inhibition, and inhibition kinetics assay showed that apigenin and hesperetin inhibited XO activity reversibly in a competitive manner.

Keywords: Xanthine oxidase, apigenin, hesperetin, additive, competitive inhibition.

Introduction
Gout is defined as an inflammatory arthritis, distinguished by agonizing painful acute attacks due to monosodium urate crystal deposition in joints. Allopurinol is a clinically prescribed XO inhibitor in the treatment of gout, which serves to inhibit the terminal step in uric acid biosynthesis. However, it comes with certain disadvantages such as allergic reactions, nephropathy and hepatitis. Moreover, superoxide anion radicals produced by XO are contributing to various pathological states (Nguyen *et al.*, 2006). Thus, it is necessary for the search of alternatives that serves with reduced side effects and enhanced therapeutic activity.

According to Kong *et al*. (2000), dried chrysanthemum flowers are used as a traditional remedy for gout in China. Many studies have shown that several constituents of the flowers demonstrated anti-inflammatory activity and flavonoids have been proven for its inhibition on XO (Cos *et al*., 1998). The aim of pharmacotherapy using a merging of different drugs with similar effects is to enhance the efficiency of the treatment while reducing its toxicity. Various combinations of flavones and flavonols have been shown to exhibit synergism. Therefore, the present study is conducted to determine the interaction of apigenin and hesperetin in *C. morifolium* on XO inhibition and its inhibitory mechanism.

Methodology
XO inhibitory activity assay and kinetic analysis
The assay mixture consisted of 130 µL of 0.05M potassium phosphate buffer, 10 µL of sample and 0.1 unit/mL XO enzyme solution. After pre-incubation of the mixture at 30°C for 10 min, the reaction was initiated by the addition of 100 µl xanthine (0.15 mM) and incubated for 10 minutes at 30°C before measurement at 295 nm (Sweeney *et al*., 2001). Allopurinol was used as positive control. The mode of inhibition was determined using Lineweaver-Burk plots in the absence and presence of inhibitors with varying concentrations of substrate.
Interaction assay on XO inhibition

V_{ab} represents the relative enzymatic activity in the presence of apigenin and hesperetin. V_c represents the expected relative remnant activity of XO ($V_c = V_a \times V_b$). The values of V_{ab} - V_c below -0.10 were regarded as synergistic, and the values between −0.10 and +0.10 were considered as additive (Wang *et al.*, 2015).

Results and Discussion

The present study showed that EA fraction of *C. morifolium* demonstrated moderate XO inhibitory activity of 63.5±1.93% at 100 µg/ml. According to Kong *et al*. (2000), presence of flavonoids in flower of *C. indicum* demonstrated XO inhibitory activity. Apigenin and hesperetin were shown to be present in EA fraction at retention time of 15.99 mins and 25.68 mins, respectively, based on comparison to standard reference compounds. The interaction of apigenin and hesperetin at different concentrations demonstrated additive interaction (Table 1). Additive effect is indicated as the joint inhibitory effect of two inhibitors being equal to the sum of each inhibitor alone. Inhibition kinetics assay showed that apigenin and hesperetin inhibited XO activity reversibly in a competitive manner (Figure 1). It was suggested by Umamaheswari *et al*. (2011) that flavonoids have been reported as potential XO inhibitors due to its ability to interact with the active site of the enzyme xanthine oxidase. It is reported by Lin *et al*. (2002) that apigenin and other flavonoids are competitive inhibitors.

Table 1. Interaction effect of apigenin and hesperetin on XO inhibition.

Concentration (mol L^{-1})		Molar ratio [Apigenin] : [Hesperetin]	Value		Interaction	
Apigenin	Hesperetin		V_{ab}	V_c	V_{ab} - V_c	
3.7×10^{-4}	3.3×10^{-4}	1:1	1.013	0.988	0.025	Additive
7.4×10^{-4}	3.3×10^{-4}	2:1	0.698	0.592	0.106	Additive
3.7×10^{-4}	6.6×10^{-4}	1:2	0.693	0.55	0.143	Additive
14.8×10^{-4}	3.3×10^{-4}	4:1	0.405	0.267	0.138	Additive
3.7×10^{-4}	13.2×10^{-4}	1:4	0.457	0.32	0.137	Additive

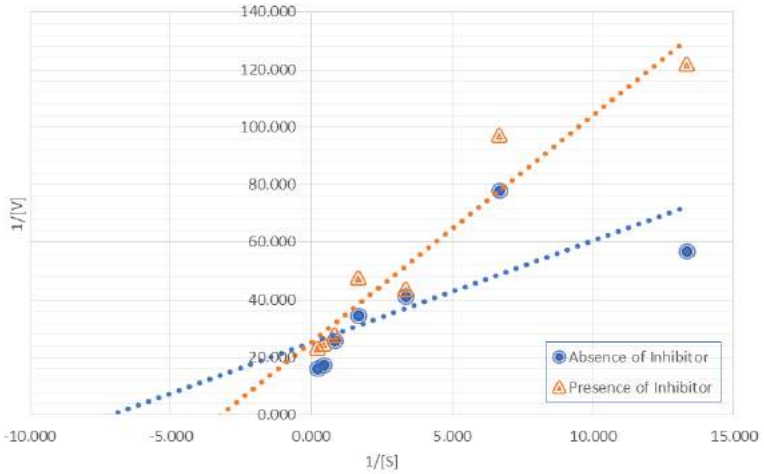

Figure 1. The Lineweaver-Burk plot for kinetic analysis of xanthine oxidase inhibition.

Conclusion

C. morifolium EA fraction was effective in XO inhibition. Apigenin and hesperetin that present in the EA fraction demonstrated additive and competitive inhibition on XO. This suggested that *C. morifolium* could potentially be used as a natural source of XO inhibitors in the treatment of hyperuricemia.

References

Cos, P, Ying, L, Calomme, M, Hu, JP, Cimanga, K, Van Poel, B, Pieters, L,Vlietinck, AJ & Vanden Berghe, D, 1998, 'Structure-activity relationship and classification of flavonoids as inhibitors of xanthine oxidase and superoxide scavengers', Journal of Natural Products, vol. 61, no. 1, pp. 71–76.

Kong, LD, Cai, Y, Huang, WW, Cheng, CH & Tan, RX, 2000, 'Inhibition of xanthine oxidase by some Chinese medicinal plants used to treat gout', Journal of Ethnopharmacology, vol. 73, pp. 199-207.

Lin, CM, Chen, CS, Chen, CT, Liang, YC & Lin, JK, 2002. 'Molecular modeling of flavonoids that inhibits xanthine oxidase', Biochemical and Biophysical Research Communications, vol. 294, no. 1, pp.167–172.

Nguyen, MTT, Awale, S, Tezuka, Y, Ueda, J, Tran, QL, & Kadota, S 2006, 'Xanthine oxidase inhibitors from the flowers of chrysanthemum sinense', Planta Medica, vol. 72, pp. 46-51.

Sweeney, AP, Wyllie, SG, Shalliker, RA & Markham, JL, 2001, 'Xanthine oxidase inhibitory activity of selected Australian native plants', Journal of Ethnopharmacology, vol. 75, no. 2-3, pp. 273–277.

Umamaheswari, M, Madeswaran, A, Asokkumar, K, Sivashanmugam, T, Subhadradevi, V & Jagannath, P, 2011, 'Discovery of potential xanthine oxidase inhibitors using in silico docking studies', Pharmaceutical Chemistry Journal, vol. 3, no. 5, pp. 240-247.

Wang, Y, Zhang, G, Pan, J & Gong, D, 2015, 'Novel Insights into the Inhibitory Mechanism of Kaempferol on Xanthine Oxidase', Journal of Agricultural and Food Chemistry, vol. 63, pp. 526-534.

PROFILING AND BIOLOGICAL STUDY OF *Xanthophyllomyces dendrorhous* EXTRACT FROM AN OVERPRODUCING MUTANT STARIN

S.Y. Khaw, A.L. Chew*

Institute For Research In Molecular Medicine (INFORMM), Universiti Sains Malaysia, 11800 Minden, Pulau Pinang

*Corresponding author: chew@usm.my

Abstract
Astaxanthin is one of the xanthophyll carotenoids that shows multiple health benefits due to its unique structure. There has been growing interest in its use as a functional food and pharmaceutical supplement because of its proven antioxidant and antitumor effects. *Xanthophyllomyces dendrorhous* is a promising producer for natural pigments as it synthesizes astaxanthin as its principal pigment. An astaxanthin-overproducing *X. dendrorhous* strain, M34, was successfully obtained in our laboratory in view of the growing consumer demand for natural pigment. In this study, the pigment in the mutant extract was profiled as astaxanthin by TLC and HPLC analysis. Total phenolic content in the yeast extract was determined to be 203.41±0.01mg GAE/g by Folin-Ciocalteu assay. Cytotoxicity analysis showed that M34 extract has no toxicity on the immortalized but non-transformed human breast epithelial cells, MCF-10A, when tested at a maximum dosage of 30ug/mL. MTT assay further determined the IC_{50} of 10.06±0.63 ug/mL and 16.81±0.19 ug/mL for wild type and mutant extracts respectively on MDA-MB-231 cells. The carotenogenic extract from M34 mutant was preliminarily shown to be promising in disease prevention and treatment based on its chemical properties and toxicity characteristics.

Keywords: Astaxanthin, *Xanthophyllomyces dendrorhous,* HPLC, total phenolic content, cytotoxicity

Introduction
Xanthophyllomyces dendrorhous is a basidiomycetous yeast that has been biotechnologically exploited due to its ability to synthesize the carotenoid astaxanthin as its primary pigment and is a suitable producer for natural pigments with enhanced yield via modern biotechnological strategies. Astaxanthin is extensively used as an integral feed supplement in aquaculture due to its colouration property since animals lack the ability to synthesize the pigment *de novo*. The United States Food and Drug Administration (FDA) has approved the use of astaxanthin in the marine and feed industry (Ambati *et al*., 2014). It has also become increasingly important in food, cosmetic and pharmaceutical sectors because of its health-promoting benefits such as antioxidant, antidiabetic and anticancer properties. Astaxanthin can be produced by chemical or biotechnological means but the synthetic one is costly and not environmental friendly. There is also increased awareness and preference for natural pigments obtained from renewable resources (Charalampia *et al*., 2017). However, the use of wild type *X. dendrorhous* in commercial scale production has not been profitable as the pigment content in wild strains is low. An astaxanthin-overproducing *X. dendrorhous* strain, M34, was successfully isolated in our laboratory in view of the growing consumer demand for natural pigments. In this study, preliminary investigations were carried out to study the properties of natural pigment and extract produced by the mutant strain to understand its potential for various applications. The pigment was extracted and analysed by TLC and HPLC for identity profiling. Folin-Ciocalteu method was used to assess the presence and level of phenolic compounds in the yeast extract. Toxicity of the extract was studied on the immortalized but non-

transformed human breast epithelial cells, MCF-10A. MTT assay was further conducted on the human breast cancer cell line (MDA-MB-231) in a dose dependent manner to establish IC_{50} of the yeast extract.

Methodology

The wild type *X. dendrorhous* (DSM 5626) and the mutant strain, M34, were grown in the yeast malt (YM) medium at 20°C with 200 rpm agitation for 96 h. The cell pellets were extracted using petroleum ether in the presence of glass beads and DMSO. Both *X. dendrorhous* yeast extracts were spotted on a TLC sheet together with astaxanthin and beta carotene standards in a solvent system acetone:n-hexane with the ratio of 3:7 (v/v). HPLC analysis was on a reversed phase ZORBAX Eclipse XDB column (150 x 4.6 mm, 5 µm) with Solvent A and Solvent B (9:1, by volume) as mobile phase with a flow rate of 1mL/min. Solvent A consisted of methanol, dichloromethane, acetonitrile and deionized (UHQ) water in the ratio of 77.5:12.5:9.5:0.5, while solvent B consisted of UHQ water only. The elution spectra were detected by using a diode array detector at the wavelength of 474 nm. Total phenolic content assay using Folin-Ciocalteu reagent was applied to assess the presence and level of phenolic compounds in the yeast extracts. Toxicity analysis was carried out on the immortalized but non-transformed human breast epithelial cells, MCF-10A. MTT assay was further conducted on the human breast cancer cell line (MDA-MB-231) in a dose dependent manner to establish IC_{50} for both yeast extracts by software SigmaPlot 12.5.

Results and Discussion

Thin layer chromatography (TLC) showed a well separation and the presence of astaxanthin. Based on comparison to astaxanthin and β-carotene standards and results reported by Nagaraj *et al*. (2012), the TLC had shown bands corresponded to free astaxanthin, astaxanthin monoester and astaxanthin diester, other than β-carotene. HPLC analysis showed that the spectrum of M34 extract was in good agreement with the authentic standards in term of elution profile and retention time. The results identified that the major carotenoid produced by M34 was astaxanthin and in high purity as there was no other carotenoid peak observed in the absorption spectrum. Folin-Ciocalteu assay showed a high level of total phenolic content of 203.41±0.01mg GAE/g in the M34 extract. Phenolic content in a compound was reported to be highly related to various bioactivities such as antioxidant, anticarcinogenic and anti-inflammatory effects (Hossain *et al*., 2017, Güner *et al*., 2019). Thus, both astaxanthin and natural phenolic compounds in the yeast extract may play important roles in disease prevention and treatment due to their bioactivities. MTT assay showed that both the extracts of wild type and mutant strains were non-toxic towards the normalized breast cancer cells, MCF-10A, as the cell viability was over 80% at 72 hours with a maximum dosage of 30 ug/mL. Meanwhile, MTT assay on MDA-MB-231 cells (triple negative human breast cancer cell line) gave IC_{50} of 10.06±0.63 ug/mL and 16.81±0.19 ug/mL for wild type and mutant extracts respectively. IC_{50}<30ug/mL indicated the high potential of a candidate compound for cancer therapy (Vijayarathna & Sasidharan, 2012).

Conclusion

The mutant yeast extract had proven to be an alternative source of natural astaxanthin based on the profile study. It was also shown as a good candidate as an anticancer agent by inhibiting the MDA-MB-231 cancer cells at a low concentration, besides its antioxidant potential indicated by the total phenolic content.

Acknowledgement
This work was funded by the Universiti Sains Malaysia Research University Grant Scheme (1001/CIPPM/8012201).

References

1. Ambati, R. R., Moi, P. S., Ravi, S., & Aswathanarayana, R. G. (2014). Astaxanthin: Sources, extraction, stability, biological activities and its commercial applications - A review. *Marine Drugs*, *12*(1), 128–152. https://doi.org/10.3390/md12010128
2. Charalampia, D., Antonios, K. E., Constantina, N., & Haralabos, C. (2017). Current trends and emerging technologies in biopigment production processes : Industrial food and health applications. *International Journal of Horticulture, Agriculture and Food Science*, *1*(2), 33–46.
3. Güner, A., Nalbantsoy, A., Sukatar, A., & Karabay Yavaşoğlu, N. Ü. (2019). Apoptosis-inducing activities of Halopteris scoparia L. Sauvageau (Brown algae) on cancer cells and its biosafety and antioxidant properties. *Cytotechnology*, *71*(3), 687–704. https://doi.org/10.1007/s10616-019-00314-5
4. Hossain, A. K. M. M., Brennan, M. A., Mason, S. L., Guo, X., Zeng, X. A., & Brennan, C. S. (2017). The Effect of Astaxanthin-Rich Microalgae "Haematococcus pluvialis" and Wholemeal Flours Incorporation in Improving the Physical and Functional Properties of Cookies. *Foods*, *6*(8), 57. https://doi.org/10.3390/foods6080057
5. Nagaraj, S., Rajaram, M. G., Arulmurugan, P., Baskaraboopathy, A., Karuppasamy, K., Jayappriyan, K. R., … Rengasamy, R. (2012). Antiproliferative potential of astaxanthin-rich alga Haematococcus pluvialis Flotow on human hepatic cancer (HepG2) cell line. *Biomedicine and Preventive Nutrition*, *2*(3), 149–153. https://doi.org/10.1016/j.bionut.2012.03.009
6. Vijayarathna, S., & Sasidharan, S. (2012). Cytotoxicity of methanol extracts of Elaeis guineensis on MCF-7 and Vero cell lines. *Asian Pacific Journal of Tropical Biomedicine*, *2*(10), 826–829. https://doi.org/10.1016/S2221-1691(12)60237-8

Utricularia SPECIES FROM WETLAND HABITATS

B. Japar Sidik [1]*, Z. Muta Harah[2] and R. Shiamala Devi[3]

[1]Department of Biology, Faculty of Science, Universiti Putra Malaysia, 43400 UPM Serdang, Selangor, Malaysia.
[2]Department of Aquaculture, Faculty of Agriculture, Universiti Putra Malaysia, 43400 UPM Serdang, Selangor, Malaysia.
[3]Department of Crop Science, Faculty of Agriculture, Science and Technology, Universiti Putra Malaysia Bintulu Campus, 97008 Bintulu, Sarawak, Malaysia.

*Corresponding author: japar@upm.edu.my

Abstract
Utricularia are insectivorous flowering plants, fairly common in Malaysia but rarely known to the people in this country. The species inhabited various habitats from dry ground, roadside with damp soil, marshes, ditches, lakes, ponds to waterways in the areas of Bintulu, Mukah, Sibu and Sarikei, Sarawak, East Malaysia. *Utricularia* species are acid-adapting plants in the environment with low water pH of ~2.82 and soil pH from 3.81 to 7.63. The terrestrial species, *Utricularia bifida, U. caerulae U. minutissima* extends their stems in the damp soils from which arise “green leaves” and slender flower stems above the ground. Aquatic species, *Utricularia aurea* and *U. gibba* float on the surface of still waters with only the flower scapes protruding above the water surface. The distinct comparative morphology on flowers, fruits, and seeds of *Utricularia* species are presented and illustrated.

Keywords: *Utricularia*, morphology, wetland, Sarawak

Introduction
Insectivorous flowering plants of Lentibulariaceae has the richest species number of about 320, comprising the genera *Pinguicula*, *Genlisea*, *Polypompholyx,* and *Utricularia*. The genera *Utricularia* or also known as the ‘bladderworts’ contributed at least 250 species (Slacks, 1979; Taylor, 1989). Ridley (1923) documented detail descriptions, the habitat characteristics and distribution localities of 15 species of *Utricularia* from Peninsular Malaysia; four are free-floating, *Utricularia flexuosa* Vahl*., U. exolata* R. Br*., U. punctata* Wall*., U. fluitans* Ridl. while the remaining 11 are terrestrial species, *U. albina* Ridl., *U. bifida* Linn., *U. griffithii* Wight*, U. involvens* Ridl*., U. minutissima* Vahl., *U. nigricaulis* Ridl*., U. ophirensis* Ridl*., U. striatula* Rees, *U. verticillata* Benj., *U. vitellina* Ridl*.* and *U. wallichiana* Wright. The *Utricularia* was little studied in Sarawak (Muta Harah et al., 2005). This present study is intended to fill in the gaps in existing and part of our research on *Utricularia* species from wetland habitats in Sarawak, East Malaysia.

Methodology
Utricularia plants were collected from various wetland habitats, e.g., ponds, ditches, streams, marshes from Bintulu, Sibu, Mukah and Sarikei Divisions in Sarawak, East Malaysia. *Utricularia* plants in the aquatic environment were collected carefully in the field. In the case of those occurring in the terrestrial habitat, plants together with their inflorescences (flowers and fruits) were lifted together with the substrate and washed in water to remove the adhering mud. The habitats associated with *Utricularia* plants within the area were recorded. A portion of the materials was preserved in a solution of 10% formalin or 50% ethanol alcohol in 5% glycerin. Some specimens were prepared for the herbarium, dried, mounted on standard herbarium sheet and labeled. The plants were examined under a Carl Zeiss and Keyence VH-S30K dissecting microscopes and

photographed. The reproductive characters observed were compared with the characters used in the taxonomy of the *Utricularia* by Taylor (1989).

Results and Discussion

Five species of insectivorous plants, *Utricularia aurea, U. gibba, U. bifida, U. caerulea*, and *U. minutissima* were recorded in habitats from dry ground, roadside with damp soil, marshes, ditches, lakes, ponds to waterways. Qualitative investigations on their ecology focused on plants' habitual behavior and some aspect of soil and water characters. *Utricularia aurea* and *U. gibba* prefer open wet and permanently submerged aquatic habitats. *Utricularia bifida*, *U. minutissima* and *U. caerulae* grow in wet or moist and even dry areas. *Utricularia* species are acid-adapting plants in environment with low water pH ~2.82 and soil pH of 3.81 to 7.63. Vegetative structures showed distinctive morphological features of the "foliar organs," bladders and stolons. All *Utricularia* plants consist of runner stolons, from each node arise various combinations of dissected or peltate or spathulate or linear "foliar organs" and unique bladder traps. Some nodes of runner stolons support a peduncle bearing inflorescences (Fig. 1). Among the *Utricularia*, plants of *U. minutissima* have stolons studded with trichomes, distinctive features not observed in the other four species. *Utricularia* species can be identified when they are producing inflorescences (flowers) as their vegetative structures, e.g., foliar organ and bladders are normally covered either by ground substrate or water. *Utricularia* species has a unique modification of corolla with three petals namely lower lip, upper lip, and spur (Fig. 2).

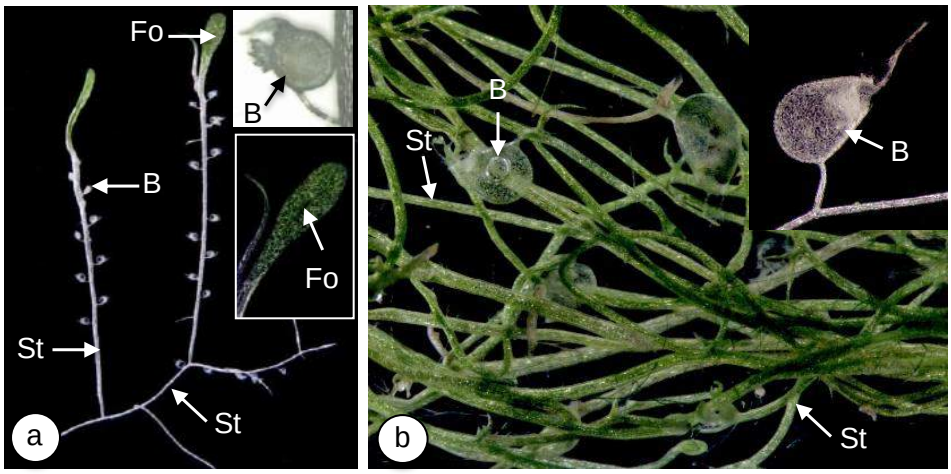

Fig. 1: An example of *Utricularia* plants (a) *U*. *minutissima*, a terrestrial bladderwort and (b) *U*. aurea, an aquatic bladderwort with runner stolon (St), foliar organ (Fo) and bladder trap (B).

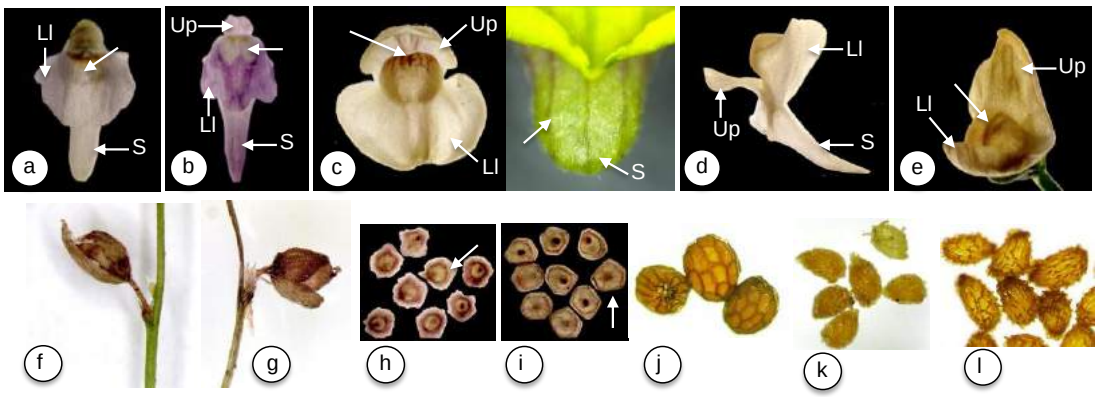

Fig. 2: Corolla of A-*U. caerulea,* B-*U. minutissima* with 2 two yellow blotches (arrow), C-*U. aurea* with red stripes on the lower lip and 3 red lines on hairy spur (arrow), D-*U. bifida*, E-*U. gibba* with red stripes on lower lip (arrow). Fruit of F-*U. minutissima,* G-*U. caerulea*, seeds of H-*U. gibba* with corky wing (arrow), G-*U. aurea* with corky wing (arrow), J-*U. minutissima*, K-*U. bifida*, L-*U. caerulea*. Ll-lower lip, Up-upper lip, S-spur.

Among the genera, *Pinguicula*, *Utricularia*, *Polypompholyx* and *Genlisea* in the Family Lentibulariaceae of carnivorous plants, *Utricularia* is the most widespread in the world and occupies the aquatic, terrestrial environment or as epiphytic herbs (Taylor, 1989). Based on old records and pioneering works of Ridley (1923) there are 15 species of *Utricularia* in Peninsular Malaysia. He classified them into 11 terrestrial species (*Utricularia albina, U. bifida*, *U. griffithii*, *U. involvens, U. minutissima, U. nigricaulis, U. ophirensis, U. striatula, U. verticillata, U. vitellina, U. wallichiana*) and 4 aquatic species (*Utricularia exoleta, U. flexuosa (*or *U. aurea), U. fluitans* and *U. punctata*). Soepadmo (1998) reported that about 14 species of bladderworts or *Utricularia* had been described. He briefly mentioned that *Utricularia* plant is rootless, body slender, fragile and branching stem bearing numerous delicate leaves. Some leaves also have small-sized hollow bladder-like traps. The descriptions of *Utricularia* is mainly for those found in Peninsular Malaysia and no mention on collections nor descriptions for *Utricularia* from Sarawak. In our inventory of aquatic plants in Bintulu, a wetland area around Bintulu Old Airport harbors among other aquatic plants, three species of *Utricularia*; *U. aurea, U*. *gibba* (*U. exoleta*) and *U. bifida* (Muta Harah et al., 2005). We anticipate that *Utricularia* species inhabit many wetland habitats that have not been explored in Sarawak.

Conclusion

Five *Utricularia* species were recorded consisting of (a) three terrestrial species; *U. bifida, U. caerulae,* and *U. minutissima* and (b) two aquatic species: *U. aurea* and *U. gibba*. The plants can be identified based on the overall morphology, and inflorescences (flowers).

Acknowledgement

This research, entitled “Biology and Diversity of Carnivorous Plants, *Utricularia* Species from Wetland Habitats” – grant number 05-10-07-381FR was funded by the Ministry of Higher Education, Malaysia.

References

1. Muta Harah, Z., Japar Sidik, B., Raesah, A., Maini, C., Suzalina, A., 2005. Aquatic Macrophytes in Natural and Man Made Water Bodies. *Bio-Science Research Bulletin* 21(1), 27-36.

2. Ridley, H.N., 1923. Flora of the Malay Peninsular Vol. II Gamopetalae. Reeve & Co., Ltd., London.
3. Slacks, A., 1979. Carnivorous Plants. Edbury Press, London.
4. Soepadmo, E., 1998. Insectivorous Flowering Plants. In The Encyclopedia of Malaysia. Volume 2. Plants. In: E. Soepadmo (ed.), p. 70-71. Editions Didier Millet, Archipelago Press. Kuala Lumpur.
5. Taylor, P., 1989. The Genus *Utricularia*. A Taxonomic Monograph. Kew Bulletin Additional Series XIV. Royal Botanic Gardens, London.

SEED GERMINATION AND SEEDLING DEVELOPMENT OF *Nelumbo nucifera* Gaertn.

Z. Muta Harah[1]*, B. Japar Sidik[2] and R. Shiamala Devi[3]

[1]*Department of Aquaculture, Faculty of Agriculture, Universiti Putra Malaysia, 43400 UPM Serdang, Selangor, Malaysia.*
[2]*Department of Biology, Faculty of Science, Universiti Putra Malaysia, 43400 UPM Serdang, Selangor, Malaysia.*
[3]*Department of Crop Science, Faculty of Agriculture, Science and Technology, Universiti Putra Malaysia Bintulu Campus, 97008 Bintulu, Sarawak, Malaysia.*
*Corresponding author: muta@upm.edu.my

Abstract
Nelumbo nucifera Gaertn. or lotus is a perennial aquatic angiosperm with economic and ornamental importance throughout the world. The plant propagates by rhizome and dispersing seeds with hard, tough seed coat in the environment and the time taken for the seed to germinate may vary from seeds to seeds. The seeds are considered impervious to water and gases and may prevent or delay germination. *Nelumbo* seeds were collected from a temporary wetland at Bintulu Old Airport, Bintulu, Sarawak and they divided into two groups. Scarification was performed on one group of seeds to investigate whether it hastens germination of the seeds. The germination stages were observed and recorded for both scarified and non-scarified seeds until they developed to the seedling stage possessing a secondary rhizome and formed juvenile plant. Germination was 100% for scarified seeds and 96% for non-scarified seeds. The germination of *Nelumbo nucifera* seeds started when the seed starts to swell, followed by seed coat splitting longitudinal and emergence of plumule, emergence of first enrolled leaf, emergence of root, second leaf, and primary rhizome. After that, the germinating seeds developed into seedlings in a series of stages from open rolled leaf blade to development of secondary rhizome and finally with seed detachment, forming juvenile plant. The range of days taken to achieve juvenile stages for scarified and non-scarified seeds was 59 to 70 days and 59 to 142 days respectively.

Keywords: *Nelumbo nucifera*, germination and development, seedling, juvenile plant

Introduction
Nelumbo nucifera Gaertn. or lotus, under the Family Nymphaeceae, is a common floating leaved aquatic plant. Worldwide there are only two species of *Nelumbo*; *Nelumbo lutea* and *Nelumbo nucifera* Gaertn. *Nelumbo nucifera*, which has pinkish-white flowers, is native to northern Australia, the Philippines, the Orient, Egypt, and the Volga River delta (Mandal *et al*., 2007). These aquatic plants are grown and consumed worldwide. Its cultivation began well before 1000 years ago, has been a prestigious crop in China for nearly 5000 years (Shen-Miller *et al*., 2002). It is widespread in India and known from Himalayan lakes at altitude up to 1400 m (Polunin and Stainton, 1984). All the vegetative and reproductive parts of the plant; leaves, rhizomes, stalk, petal, anther, pericarp, fruit receptacle, and seeds are consumed as food or medicine (Shen-Miller *et al*., 1995). Ling *et al*. (2005) reported that seeds and roots of *Nelumbo* are popular health food, and the alkaloid (Liensinine) extracted from them is effective to treat arrhythmia. Germination of any economically valued seeds assumes importance for propagation or germplasm preservation. According to Pan *et al*. (2007) it is an insect-pollinated plant which could be propagated via vegetative and sexual reproduction by rhizomes and seeds respectively. Most propagation of *N. nucifera* has been via seeds, as they could disperse to new location and be dormant until hostile environmental conditions have improved. The present study

was conducted to investigate the seed germination and compare the germination pattern of those scarified and non-scarified seeds.

Methodology

Matured seeds were collected from a temporary wetland, Bintulu Old Airport (3° 10' 34.5" N, 113° 04' 27.2" E), Sarawak. Forty-eight (48) selected mature seeds were cultured with 24 seeds undergone scarification treatment by rubbing them gently on the sandpaper until produce shiny flat surface, and another 24 seeds cultivated without any treatment. Scarified and non-scarified seeds were immersed in water at a depth of 4 cm in an aquarium tank, 42.8 x 27.6 x 32.4 cm, and exposed under natural light in laboratory. The water temperature ranged from 25ºC to 32ºC and pH 6.5-6.9. The water was changed every two days, and germination dates were recorded to calculate the percentage and rate of germination. The germination stages were observed and recorded until it reaches the seedling stage possessing a primary rhizome and forming the juvenile plant.

Results and Discussion

Seed Germination

Nelumbo nucifera seeds are round or oval with length range from 1.2 to 1.6 cm and width 0.8 to 2.0 cm (Fig. 1a). The seed coat varied in color from gray to dark brown or black, very hard and consisting of two firmly packed layers (Fig. 1b). Germination was 100% for scarified seeds and 96% for non-scarified seeds. Seeds started to germinate by the splitting of seed coat and emergent of the plumule (Fig. 1c) and occurred from 8 to 11 days after immersion in water. Non-scarified seeds showed split seed coat within 7 to 77 days. Only one seed did not germinate within the 77 days. The time of scarified seeds germinated is relatively shorter compared to non-scarified seeds. In nature, the wild plants' seeds are not germinated simultaneously, as some seeds are dormant or reserve, in case the first sprouts encounter unfavorable growing condition (Pagels, 2001). The scarification reduced the thickness of seed coat and allows water penetration and imbibition of the seeds. As such scarified seeds can overcome the dormancy and germination within 7 to 10 days. According to Shen-Miller *et al*. (1995), the rate of seed germination is variable from ~67% to 83% in old seeds and 100% in fresh seeds. The Asiatic *N. nucifera* produces very long-lived seeds; a 237-year-old *N. nucifera* seed germinated on an herbarium sheet at the flooded British Museum of Natural History after bombing in 1940 (Sculthorpe, 1967). The longevity of lotus seed is phenomenal, with the world's record for long-term seed viability reported as 1300 years for a seed from China (Mandel *et al*., 2007). The yellow lotus *Nelumbo lutea* (Willd.) Pers. also possess a hard seed coat, and requires scarification for proper germination. The hard pericarp is a very effective dormancy mechanism, and seed viability can be maintained almost indefinitely. *Nelumbo* seeds, over 500 to more than 1000 years old have been reported to germinate following acid scarification to break the dormancy (Maeda *et al*., 1996).

Germinating Seed to Seedling Development

The serial development of *N. nucifera* seeds comprised; the emergence of plumule in germinating stage followed by the development to seedling with the emergence of first enrolled leaf (Fig. 1d), simultaneous emergence of root, second leaf and primary rhizome (Fig. 1e), leaf blade open, (Fig. 1f), development of secondary rhizome (Fig. 1g) and seed detachment (Fig. 1h), which indicates the development to juvenile plant.

The range of days taken to achieve juvenile stages (when the seed detachment) for scarified and non-scarified seeds of *N. nucifera* were 59 to 70 days and 59 to 142 days

respectively. The seeds contain enough nutrients to sustain without extra nutrition until the first four leaves emerged.

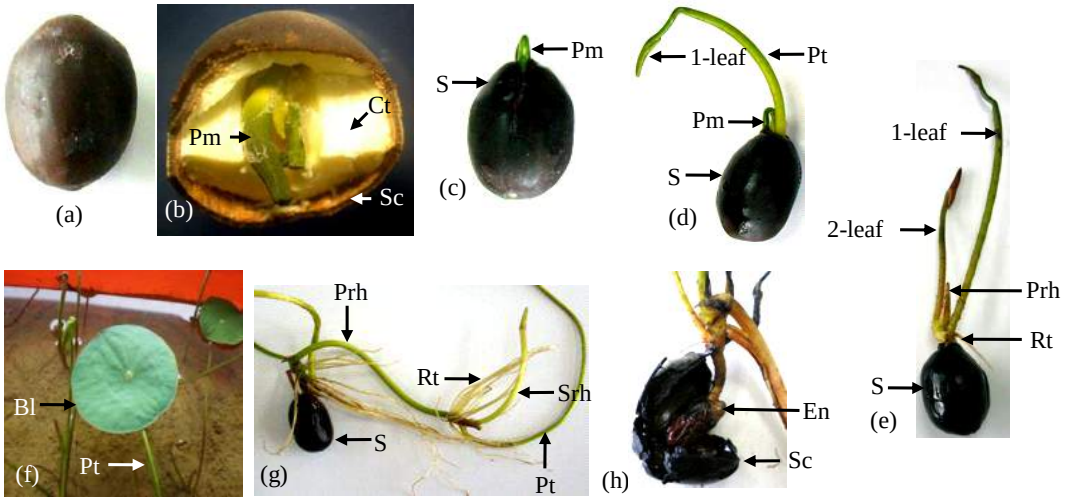

Fig. 1. Seed germination and serial developmental stages of *Nelumbo nucifera*.
(a) seed, (b) matured seed with hard seed coat, cream color cotyledon and rolled-leaf or plumule seed, (c) splitting seed coat with emergence of plumule, (d) emergence of fist rolled-leaf, (e) emergence of root, second leaf and primary rhizome, (f) rolled-leaf blade open, (g) development of secondary rhizome and (h) seed detachment. Pm-plumule, Ct-cotyledon, Sc-seed coat, S-seed, Pt-petiole, Rt-root, Prh-primary rhizome, Bl-blade, Srh-secondary rhizome, En-Endosperm.

Conclusion

The findings suggest (a) The scarification help seeds germination, (b) the attainment for the serial development of plants from germinating seeds, seedlings to juvenile plants is in a relatively shorter time.

Acknowledgement

This research is funded by the MOSTI under the ScienceFund Research Grant entitled “Ethnobotanical Study on Aquatic Macrophytes Used by Indigenous Peoples” – grant number 04-01-04-SF0864.

References

1. Ling, Z.Q., Xie, B.J., Yang, E.L., 2005. Isolation, Characterization, and Determination of Antioxidative Activity of Oligomeric Procyanidins from the Seedpod of *Nelumbo nucifera* Gaertn. *J. Agric. Food Chem*. 53, 2441-2445.
2. Maeda, Y., Minamikawa, T., Xu, B.M., 1996. Metabolic Activities in Germinated Ancient Lotus Seeds. *J. Exp. Bot*. 47(297), 577-582.
3. Mandal, R.N., Saha, G.S., Mukhopadhay, P.K., 2007. Lotus – An Aquatic Plant of Versatile Qualities. *Aquaculture Asia*, XII(1), 11-13.
4. Pagels, W. 2001. *Nelumbo* (Lotus) Germination and Seedling Growth. www.victoria-adventure.org/lotus/lotus_letters2.html
5. Pan, L., Quan, Z., Li, L.S., Liu, H., Huang, X., Ke, W., Ding, Y., 2007. Isolation and Characterization of Microsatellite Markers in the Sacred Lotus (*Nelumbo nucifera*), *Molecular Ecology Notes* 7, 1054–1056.
6. Polunin, O., Stainton, A., 1984. Flowers of the Himalaya. Oxford University Press, Delhi.

7. Sculthorpe, C.D., 1967. The Biology of Aquatic Vascular Plants. Edward Arnold Publisher, London.
8. Shen-Miller, J., 2002. Sacred Lotus, the Long-living Fruits of China Antique. Invited Review Article. Seed Science Research 12, 131–143.

SYNERGISTIC ACTION OF VARIOUS PHENOLICS IN OPIOID-MEDIATED ANTINOCICEPTIVE ACTIVITY OF *Dicranopteris linearis* LEAF'S METHANOLIC EXTRACT

M.H.M. Sani[1], S.S. Mamat[2], T. Balan[3], N.H. Marmaya[4], Z.A. Zakaria[5],

[1]Faculty of Medicine and Health Sciences, Universiti Malaysia Sabah, Kota Kinabalu, Sabah
[2]Kulliyah of Medicine and Health Sciences, Sultan Abdul Halim Mu'adzam Shah International Islamic University, Kuala Ketil, Kedah
[3]Faculty of Pharmacy and Health Sciences, Universiti Kuala Lumpur Royal College of Medicine Perak, Ipoh, Perak
[4]Faculty of Business and Management, Universiti Teknologi MARA, Bandaraya Melaka, Melaka [5]Faculty of Medicine and Health Sciences, Universiti Putra Malaysia, Serdang, Selangor

*Corresponding author: hijazsani@ums.edu.my

Abstract
Dicranopteris linearis leaf has been reported to exert antinociceptive activity. The present study elucidates the possible mechanisms of antinociception modulated by the methanol extract of *D. linearis* leaves (MEDL) using *in vivo* models of chemical- and thermal-induced nociception. The extract (25, 150, and 300 mg/kg) was administered orally to mice for 30 min prior to subjection to acetic acid-induced writhing-, hot plate- or formalin-test to establish the antinociceptive profile of MEDL. The highest dose, 300 mg/kg, was used to elucidate the possible involvement of opioid receptor in the extract's analgesic activity. The extract was also subjected to the phytochemical analyses. The results obtained confirmed that MEDL exerted significant ($p<0.05$) antinociceptive activity in those pain models, while pre-treatment with naloxone (a non-selective opioid antagonist) significantly ($p<0.05$) reversed MEDL effect on the thermal-induced nociception. Several polyphenolics and volatile antinociceptive compounds were detected in MEDL. In conclusion, MEDL exerted the opioid-mediated antinociceptive activity, thus, justify *D. linearis* as a potential source for the development of new analgesic agents.

Keywords: *Dicranopteris linearis*; family Gleicheniaceae; antinociceptive activity; opioid-dependent pathway; UHPLC

Introduction
Pain affects a substantial proportion of the population across the globe and exerts a crucial challenge in public health and clinical medicine [Manchikanti et al., 2016]. The limitations of currently available analgesics such as opioids are mostly because of their adverse effects (i.e. sedation, addiction, nausea, apnea, and constipation) while nonsteroidal anti-inflammatory drugs can produce stroke, myocardial infarction, gastrointestinal ulcers and bleeding [Del Vecchio et al., 2017]. Therefore, initiatives to find safer and potent alternatives are actively conducted and plants have been one of the potential analgesic agents.

One of the plants that have been traditionally used to heal pain-related maladies is *Dicranopteris linearis* L., a seedless vascular pteridophytes belonging to the family Gleicheniaceae [Vasuda, 1999; Chin, 1992]. Scientifically, the chloroform and aqueous extracts of *D. linearis* exert the activity in several animal models namely abdominal constriction test, hot plate test and formalin test [Zakaria et al., 2006; 2008] but no attempt was made to elucidate the antinociceptive activity of the methanol extract of D. linearis leaves (MEDL).

Methodology

Preparation of MEDL was as described in detailed by Zakaria et al. [2017]. The extract was later subjected to phytochemicals analysis by reversed phase UHPLC-ESI-HRMS in negative ion mode. Evaluation of MEDL antinociceptive potential, acetic acid-induced abdominal writhing, hot plate and formalin-induced paw licking test were used according to the detailed procedures described by Mohd Sani et al. [2012]. Rota-rod test was also conducted to eliminate the false positive interpretation of the effect seen [Ong et al., 2011]. Role of opioid receptor in the antinociceptive activity of MEDL was examined by the pre-treatment of naloxone, an opioid receptor antagonist [Mohd Sani et al., 2012].

Results and Discussion

A total of 30 metabolites identified following UHPL-ESI-HRMS and some of the important phytoconstituents identified in MEDL were gallic acid, ferulic acid, protocatechuic acid, caffeic acid, p-coumaric acid, rutin, isoquercitrin, astragalin, catechin, quercetin, apigenin, and kaempferol. MEDL at all doses (25, 150 and 300 mg/kg) demonstrated significant ($p \leq 0.001$) antinociceptive activity acetic acid-induced abdominal constriction test, with the recorded percentage of 42.30, 59.87 and 63.56%, respectively. The antinociceptive effect of 150 and 300 mg/kg MEDL was comparable to 100 mg/kg ASA. The central antinociceptive potential of MEDL was assessed against thermal-induced nociception using the hot plate test and the extract at the doses of 150 and 300 mg/kg, caused a significant change ($p \leq 0.001$) in response latency when compared to the vehicle control. However, the 150 mg/kg MEDL only prolonged the latency of nociceptive response a the interval of 60 min while the 300 mg/kg MEDL delayed the nociceptive response latency between the intervals 60 to 120 min. Morphine (MOR), as the standard pain-relieving drug, also exerted significant ($p < 0.001$) antinociceptive activity, which started at the interval of 60 min and prolonged until the end of the experiment (interval of 210 min). Pre-treatment with 5 mg/kg naloxone significantly reversed ($p < 0.001$) the antinociceptive effect of 300 mg/kg MEDL. Similarly, naloxone also significantly ($p < 0.001$) reversed the antinociceptive effect of 5 mg/kg MOR until the end of the experiment. The antinociceptive potential of MEDL against inflammatory- or non-inflammatory-mediated nociception was also evaluated using the formalin-induced paw licking test and MEDL shown to significantly ($p \leq 0.01$) reduce the amount of time taken to respond to the nociceptive stimuli in both the early and late phases of formalin-induced paw licking test.

Conclusion

In conclusion, MEDL exerts antinociceptive activity at the peripheral and central level via mechanisms of action that involved partly the modulation of opioid receptor. The antinociceptive activity of MEDL could be due to the presence of several volatile and non-volatile bioactive compounds that have previously proven to attenuate nociceptive response in rodents.

Acknowledgement

The authors thanked the Faculty of Medicine and Health Sciences, Universiti Putra Malaysia, Serdang, for providing the facilities to carry out this research.

References

Chin WY. 1992. A Guide to Medicinal Plants. Singapore: Singapore Science Centre; pp. 24.

Del Vecchio G, Spahn V, Stein C. 2017. Novel opioid analgesics and side effects. *ACS* Chem Neurosci. 8:1638-1640.

Manchikanti L, Kaye AM, Kaye AD. 2016. Current state of opioid therapy and abuse. Curr. Pain Headache Rep. 20(5): 34.
Mohd Sani MH, Zakaria ZA, Balan T, Teh LK, Salleh MZ. 2012. Antinociceptive activity of methanol extract of Muntingia calabura leaves and the mechanisms of action involved. Evid Based Complement Altern Med. 2012(1): [accessed 2018 November 12]:[10 p.].
Ong HM, Mohamad AS, Makhtar N, Khalid MH, Khalid S, Perimal EK, Mastuki SN, Zakaria ZA, Lajis N, Israf DA, Sulaiman MR. 2011. Antinociceptive activity of methanolic extract of Acmella uliginosa (Sw.) Cass. J Ethnopharmacol. 133(1):227-233.
Vasuda SM. 1999. Economic importance of pteridophytes. Indian Fern J. 16(1–2):130-152.
Zakaria ZA, Abdul Ghani ZDF, Raden Mohd Nor RNS, Hanan Gopalan HK, Sulaiman MR, Abdullah FC. 2006. Antinociceptive and anti-inflammatory activities of *Dicranopteris linearis* leaves chloroform extract in experimental animals. *Yakugaku Zasshi*. 126:1197-1203.
Zakaria ZA, Abdul Ghani ZDF, Raden Mohd. Nor RNS, Gopalan HK, Sulaiman MR, Mat Jais AM, Somchit MN, Abdul Kadir A, Ripin J. 2008. Antinociceptive, anti-inflammatory, and antipyretic properties of an aqueous extract of *Dicranopteris linearis* leaves in experimental animal models. J Nat Med. 62:179-187
Zakaria ZA, Kamisan FH, Omar MH, Mahmood ND, Othman F, Abdul Hamid SS, Abdullah MNH. 2017. Methanol extract of *Dicranopteris linearis* L. leaves impedes acetaminophen-induced liver intoxication partly by enhancing the endogenous antioxidant system. BMC Complement Altern Med. 17(1): 271-284.

APPLICATION OF METABOLOMICS IN IDENTIFYING METABOLIC SIGNATURE FOR DIAGNOSIS OF PROTEIN ENERGY WASTING IN MALAYSIAN HEMODIALYSIS PATIENTS

F.A. Pauzi[1], N.F. Zakaria[2], F. Abas[3], T. Karupaiah[4] & Z.A.M. Daud[1]

[1]Dept. of Nutrition and Dietetics, Faculty of Medicine and Health Science, Universiti Putra Malaysia
[3]Dept. of Medicine, Faculty of Medicine and Health Sciences, Universiti Putra Malaysia
[2]Dept. of Food Science, Faculty of Food Science and Technology, Universiti Putra Malaysia
[4]School of BioSciences, Taylors' University, 47500 Subang Jaya, Selangor Darul Ehsan, Malaysia.

*Corresponding author: zulfitri@upm.edu.my

Abstract
End-stage renal disease (ESRD) patients often experience a state of metabolic and nutritional derangements manifested as protein energy wasting (PEW) syndrome that is highly associated with morbidity and mortality. However, diagnosis of PEW is challenging as there is no consistent guidelines, specific biomarker or standardized scoring tools in a diverse patient-wide population. Thus, it is prudent to identify biomarkers signature of PEW by using ^{1}H-nuclear magnetic resonance (NMR) untargeted based metabolomics approach which will assist the diagnosis and treatment of PEW. In this cross-sectional study, a total of 106 subjects of ESRD patients undergoing chronic hemodialysis (HD) were stratified into PEW (n=53) and non-PEW (NPEW) (n=53) based on the established traditional criteria. Orthogonal partial least square discriminant analysis (OPLS-DA) demonstrated a significant separation between the groups and indicates that PEW syndrome induced specific metabolic pattern alteration. The metabolites that contributed to the group separation were identified and quantified using Chenomx. Further quantitative analysis showed that the level of 3-hydroxybutyrate, acetate, arabinose, maltose, ribose, sucrose and tartrate were significantly increased ($p<0.05$) in PEW subjects whilst creatinine was significantly decreased. However, analysis of covariance revealed that contribution of arabinose, maltose, ribose, sucrose and tartrate on the group discrimination might be affected by age and dialysis vintage. Pathway analysis indicated that PEW related metabolites triggered perturbation in fatty acid mechanism as well as induced gluconeogenesis, glyoxylate and dicarboxylate metabolism. This results provides primary data in understanding metabolic alteration of PEW and corresponding metabolites that potentially serve as biomarker of PEW.

Keywords: Protein Energy Wasting, hemodialysis, metabolomics, ^{1}H-NMR

Introduction
PEW syndrome that is commonly found in patients with chronic kidney disease (CKD) is characterized by multiple nutrition and catabolic alterations that caused a chronic depletion of protein stores and energy fuels in the body, manifested as low body protein and fat masses. However, traditional diagnostic criteria to identify PEW has been challenged due to lack of reliable biological validation thus signify more intensive research to identify reliable PEW biomarkers. Therefore, ^{1}H-NMR based metabolomics approach was applied as unbiased quantitative method that analyzes the changes in endogenous metabolites at a given time to facilitate the detection of plasma metabolites changes associated with PEW and explain the PEW mechanism in ESRD population.

Methodology

A total of 106 ESRD patients undergoing HD were stratified into PEW (n=53) and NPEW (n=53) based on the established traditional criteria. Fasting predialysis plasma samples with filtration were analyzed by ^{1}H-NMR and the data acquired through the combination of presaturation (PRESAT) and the Carr–Purcell–Meiboom–Gill (CPMG) pulse sequence were further processed using Chenomx NMR suite software. Multivariate data analysis (MVDA) of the processed spectra were performed using SIMCA-P software to discriminate the metabolomics profile between the two groups. Metabolites were identified using Chenomx by matching the corresponding peak with the 500MHz metabolites library. Metabolic pathway identification was performed using database from Kyoto Encyclopedia of Genes and Genomes (KEGG). One-way ANCOVA was used to determine metabolites differences between the groups, adjusted for covariates. Spearman's rank correlation coefficient was performed to evaluate the predictive effects of PEW potential biomarker in relation to traditional markers.

Results and Discussion

PEW group have significantly lower value in their anthropometric measurements and higher MIS score that indicate more severe degree of wasting condition. OPLS-DA show the difference in metabolomics profiles between PEW and NPEW groups by the principal component 1 (Figure 1) which indicates that PEW syndrome induced specific metabolic pattern alteration. A total of 32 metabolites (PEW=18; NPEW=14) were identified and quantified. Acetate, 3-hydroxybutyrate, arabinose, maltose, ribose, sucrose and tartrate were significantly increased ($p<0.05$) in PEW subjects whilst creatinine was significantly decreased (Table 1). This result is also in line with Park et al. (2013) that suggested low serum creatinine level could be considered as a proxy of PEW in this population. Pathway analysis using KEGG database indicated that PEW related metabolites triggered perturbation in fatty acid mechanism as well as induced gluconeogenesis and glyoxylate and dicarboxylate metabolism. Besides, creatinine was also showed to be significantly correlated ($p<0.01$) with the anthropometric mid-arm muscle area (r_s=0.426), lean tissue mass (r_s=0.362) and albumin (r_s=-0.315). Overall, the results indicate that patients who experienced PEW had different metabolic profiles as opposed to NPEW patients.

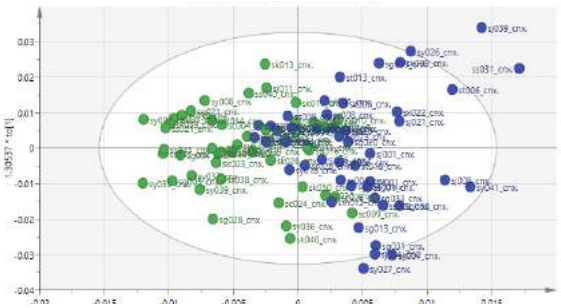

Figure 1: OPLS-DA score plot for NMR spectra acquired from plasma samples of PEW and NPEW HD patients

Table 1: Comparison on the relative concentration of discriminant metabolites between PEW and NPEW identified by ^{1}H-NMR

Metabolites	PEW	NPEW	p-value
3-Hydroxybutyrate	0.033±.037	0.018±.015	0.000
Acetate	0.188±.034	0.176±.042	0.027
Arabinose	0.191±.106	0.153±.113	0.029
Maltose	0.152±.127	0.102±.101	0.021
Ribose	0.444±.277	0.361±.260	0.041
Sucrose	0.121±.095	0.081±.082	0.008
Tartrate	0.150±.115	0.096±.127	0.018
Creatinine	0.260±.089	0.323±.074	0.000

Conclusion

Plasma metabolic profiles of subjects were altered in response to the syndrome that distinguish PEW from NPEW group which indicate that metabolomics approach can potentially be used as a non-invasive diagnostic tool for PEW syndrome.

Acknowledgement
This research was supported by the Ministry of Education Malaysia through Fundamental Research Grant Scheme (vote no.: 5524914). The authors thanks the Institute of Bioscience, UPM for the access to 1HNMR and acknowledged all the staff and HD clinics involved in this project.

References
Park, J., Mehrotra, R, Rhee, C.M. et al (2013). Serum creatinine level, a surrogate of muscle mass, predicts mortality in peritoneal dialysis patients. *Nephrol. Dial. Transplant.* 2013, *28*, 2146–2155.

POSTER PRESENTATION

CHEMISTRY

NOVEL ZEOLITIC IMIDAZOLATE FRAMEWORKS (ZIFS): SOLVOTHERMAL SYNTHESIS, CRYSTAL STRUCTURES AND THERMAL ANALYSIS

T. B. S. A. Ravoof [a,b], N. M. Nasri [a], M. I. M. Tahir [a]*

[a]Department of Chemistry, Faculty of Science, Universiti Putra Malaysia, Serdang, Selangor, Malaysia
[b]Materials Synthesis and Characterization Laboratory, Institute of Advanced Technology, Universiti Putra Malaysia, Serdang, Selangor, Malaysia

[*]Corresponding author: thahira@upm.edu.my

Abstract

Imidazole derivatives are the main building blocks for the construction of zeolitic imidazolate frameworks (ZIFs), a subclass of Metal Organic Frameworks (MOFs). Mixed-linkers ZIFs with DFT topology have been successfully synthesised using five different types of imidazolate linkers and Zinc nitrate tetrahydrate $Zn(NO_3)_2$. $4H_2O$ and the synthesised compounds were named as NZ-701, NZ-160 and NZ-150. These compounds were structurally characterised using Single-crystal X-ray diffraction (SCXRD), Powder X-ray diffraction (PXRD), Fourier transfrom infrared spectroscopy (FT-IR), Thermogravimetric analysis (TGA), elemental analysis and Nuclear magnetic resonance (NMR) and nitrogen physisorption experiments.

Keywords: Zeolitic Imidazolate Frameworks, three-dimensional network, crystal structure.

Introduction

Metal Organic Frameworks (MOFs) are a new class of porous material and have been recognized as emerging functional materials due to their high porosity, structural flexibility and tunability. MOFs are forming by self-assembly of metal-ion with multi-functional organic linkers that extends into various dimensionalities. Among the reported MOFs, Zeolitic Imidazolate Frameworks (ZIFs) are MOFs that possess the advantages of zeolites and MOFs. ZIFs are constructed from transition metals like Zn^{2+} and Co^{2+} bridged to N-donor atoms of the imidazolate linkers in a tetrahedral cluster to form a neutral larger framework. ZIFs can be tuned into specific applications which is different from traditional materials, such as zeolites and activated carbon. Mixed-linkers ZIFs have been synthesised to design hydrophobic environment in the framework using bulky imidazolate linkers that are stable as adsorbent material in gas capture applications.

Methodology

NZ-701, NZ-160 and NZ-150 were successfully synthesised using $Zn(NO_3)_2$. $4H_2O$ and respective imidazolate linkers with a solvothermal method, using mixed-solvents of dimethylformamide (DMF) and *N*-methyl-2-pyrrolidone (NMP) at 120°C for 72 hours. Solvothermal methods are set up at higher temperature with high boiling point solvents to force the formation of three dimensional frameworks. Thus, DMF and NMP were chosen to allow slow crystallization process of MOFs in high temperature and pressure. These

compounds were structurally characterised using Single-crystal X-ray diffraction (SCXRD), Powder X-ray diffraction (PXRD), Fourier transform infrared spectroscopy (FT-IR), Thermo gravimetric analysis (TGA), elemental analysis and Nuclear magnetic resonance (NMR).

Results and Discussion

Single-crystal structure analysis indicated that the Zn^{2+} centre was four-coordinated; exhibiting a tetrahedral geometry by bridging imidazolate linkers, showing that one imidazolate linker was the dominant ligand in the three crystal structures. Adjacent chains were linked through mixed ligands and coordinated to Zn^{2+} to form a three-dimensional network. No evidence was found for hydrogen bonding within the framework. The PXRD pattern of analysis of new ZIFs showed peaks below 10^{o} indicates the formation of large unit cells of the framework. Bands at 1479 cm^{-1} and 800 indicated the presence of methyl and halogen groups for NZ-160 and NZ-150. The title compounds exhibited thermal stability up to 573 K. These compounds are currently being investigated for their potential study as adsorbent material for gas capture.

	NZ-701	NZ-160	NZ-150
Empirical formula	$C_{7.25}H_{7.11}N_4Zn$	$C_8H_7N_{2.6}Cl_{0.2}Zn$	$C_6H_{7.75}N_4Zn$
Molecular weight	215.55	211.93	201.92
Crystal system	P4n2 (118)	P4n2 (118)	P4n2 (118)
Space group	Tetragonal	Tetragonal	Tetragonal
Volume	5685.13	5855.13	5901.99

Conclusions

The strategy of using mixed-linkers to make new ZIFs was successful and lead to the formation of three new ZIFs using a solvothermal method. All of the compounds crystallized in the same space group and atomic arrangement based on SCXRD data. These compounds are highly stable up to $800^{o}C$ and are currently being investigated for their potential as adsorbent material for gas capture.

References

1. Chenleng, B., Yang, Z., Zhu, Y., Xia, Y. 2014. Zeolitic Imidazolate Frameworks materials: recent progress in synthesis and applications. *J. Mater. Chem. A*. *2*(40), 16811–16831

2. Park, K.S., Ni, Z., Côté, A.P., Choi, J.Y., Huang, R., Uribe-Romo, F. J., Yaghi, O.M. 2006. Exceptional chemical and thermal stability of zeolitic imidazolate frameworks. *Proc. Natl. Acad. Sci. USA.* 103(27), 10186–91.

3. Seetharaj, R., Vandana, P.V., Arya, P., Mathew, S. 2019. Dependance of solvents, ph, molar ratio and temperature in tuning metal organic framework architecture. *Arab. J. Chem*. 12, 295-315

REMOVAL OF HEAVY METAL IONS FROM AQUEOUS SOLUTION USING MIXED MATRIX MEMBRANE ADSORPTION TECHNIQUE

Sazlinda Kamaruzaman[1*], Ku Aida Suziana Ku Jamaluddin[1], Noorfatimah Yahaya[2], Loh Saw Hong[3] and Muhammad Raznisyafiq Razak[4]

[1]Department of Chemistry, Faculty of Science, Universiti Putra Malaysia, 43400 UPM Serdang, Selangor, Malaysia.
[2]Integrative Medicine Cluster, Advanced Medical and Dental Institute, Universiti Sains Malaysia, Bertam, 13200 Kepala Batas, Penang, Malaysia.
[3]School of Marine & Environmental Sciences Universiti Malaysia Terengganu, 21030 Kuala Terengganu, Terengganu, Malaysia.
[4]Department of Environmental Sciences, Faculty of Environmental Studies, Universiti Putra Malaysia 43400 UPM Serdang, Selangor, Malaysia.

*Corresponding author: sazlinda Kamaruzaman; sazlinda@upm.edu.my

Abstract
The study of adsorption behavior of cellulose acetate/multi-walled carbon nanotube membrane towards Cu^{2+} ions from Sungai Pahang, Tasik Cheras and Air Laut Melaka was carried out Cellulose acetate/multi-walled carbon nanotube membrane was prepared by using phase inversion technique and characterized by using Fourier-Transform Infrared Spectroscopy (FTIR), Field Emission Scanning Electron Microscopy (FESEM) and Surface Area Analysis. Results proved that cellulose acetate/multi-walled carbon nanotube membrane efficiently removed 1 ppm of Cu^{2+} ion solution at pH 7 with 0.012g of membrane for 45 minutes of adsorption process (94.90% removal;1.5817 mg/g maximum adsorption capacity). Using real water samples at optimum conditions, the maximum adsorption capacity and percentage of removal for Sungai Pahang, Tasik Cheras and Air Laut Melaka are 1.4483 mg/g, 1.4885 mg/g, 1.4303 mg/g and 86.90%, 89.31%, 85.82% respectively. Desorption process was also carried out in order to investigate the possibility of Cu^{2+} ion recovery by using 1 M of hydrochloric acid with 82.78% removal and 1.2324 mg/g maximum adsorption capacity. The adsorption behavior of Cu^{2+} ions onto the CA/MWCNT membrane are well described by Freundlich isotherm while the adsorption mechanism and rate of adsorption are fitted well by pseudo-second order kinetic model.

Keywords*:* Cellulose acetate; Multi-walled carbon nanotubes; Membrane; Heavy metal; Adsorption process.

Introduction
Nowadays, water pollution has become a significant problem in the worldwide due to the growth of many large-scale industries such as mining operations, paper industries, fertilizer industries, batteries, pesticides galvanizing plants and thermoplastics [1,2]. The water resources can be polluted because the residues mostly contained hazardous pollutants such as heavy metal ions which are toxic even though at low concentration and non-biodegradable materials [1]. The World Health Organization (WHO) and the Food and Agriculture Administration (FAA) already stated that the human bodies only need 12mg/day for adult males and 10mg/day for adult females [4]. There are various types of methods in order to remove heavy metal ions from the water resources including chemical precipitation, ion exchange, reverse osmosis, electrodialysis, ultrafiltration, nanofiltration, coagulation, flocculation and floatation [5]. In this case, membrane adsorption method was selected to remove the heavy metal ions from the water system in order to increase the water quality. This method also supported by previous study because it is very efficient method, low cost, easy to handle, flexible and no production of toxic by-products [6].

Besides, cellulose acetate and multi-walled carbon nanotubes materials have been selected to be a membrane for the adsorption of heavy metal ions study. The multi-walled carbon nanotubes is chosen as additives because cellulose acetate polymer (membrane) has some disadvantages in this process such as the lack of reactive functional groups on the polymer, chemical resistance, high pressure requirement and transportation. The presence of multi-walled carbon nanotubes can give more surface area between a membrane and ions, and improve the water-transport property.

Methodology

The cellulose acetate/multi-walled carbon nanotube (CA/MWCNT) was prepared by mixing 1g cellulose acetate powder with acetone and N,N-dimethylformamide (DMF) in ratio 2:1 (15ml) while stirring by using a magnetic stirrer to avoid agglomeration. After the mixture became homogeneous, 100mg of MWCNTs was added into the mixture and mixed them well. Then, 4ml of the mixture was casting in a glass plate and left for drying at room temperature. Next, distilled water was poured into the casted membrane in order to get free standing membrane. The resulting membrane was ready to use and was stored in a dry place. Batch adsorption experiments were carried out by stirring the sample solution that contained a fixed size of adsorbent with the magnetic stirrer at various parameters. This batch process was operated at room temperature and 20ml of the sample solution was kept constant throughout the process. After the adsorption process, the sample solution was sent to the FAAS to analyze the final concentration of solution. Then, adsorption capacity, q_e (mg/g) and percentage removal of heavy metal ions (%) were calculated. For the real sample analysis, the optimum conditions for an adsorption process applied were pH 7, initial ion concentration of 1ppm, 0.0012g of CA/MWCNT with 100mg dosage (0.7%) MWCNT and 45 minutes for stirring. Then, the membrane was immersed in each water samples at the optimum condition by stirring with a magnetic stirrer to ensure the continuous of adsorption process and the final concentration was measured by using FAAS.

Results and Discussion

In this study, 0.7% of MWCNT which is added to cellulose acetate as a membrane has shown the highest percentage removal of Cu^{2+} ions through adsorption process. Adsorption behavior of CA/MWCNT membrane towards Cu^{2+} ions was successfully studied by using its own aqueous solution and real water samples from Sungai Pahang, Tasik Cheras and Air Laut Melaka which conducted at obtained optimum condition. The optimum condition was achieved at room temperature at pH 7 with 0.012g of CA/MWCNT membrane and 1 M of solution for 45 minutes adsorption process. The specific surface area of CA/MWCNT membrane is higher than CAM which is 0.379 m^2/g. The adsorption behavior of Cu^{2+} ions onto the CA/MWCNT membrane are well described by Freundlich isotherm while the adsorption mechanism and rate of adsorption are fitted well by pseudo-second order kinetic model. Recovery of Cu^{2+} ions was successfully studied by using 1M of Hydrochloric Acid solution through the desorption process at room temperature with higher desorption percentage,83%. The CA/MWCNT membrane can only be used in single removal process of Cu^{2+} ions.

Conclusion

As a conclusion, CA/MWCNT membrane is possible to be used an alternative membrane for the removal of heavy metal ions from the environmental water samples.

Acknowledgement
The authors wish to thank Universiti Putra Malaysia and Ministry of Higher Education Malaysia for facilitations and financial support through vote number 540122.

References
[1] S. A. Chaudhry, T. A. Khan, and I. Ali, “Adsorptive removal of Pb (II) and Zn (II) from water onto manganese oxide-coated sand : Isotherm , thermodynamic and kinetic studies,” Egypt. J. Basic Appl. Sci., vol. 3, no. 3, pp. 287–300, 2016.
[2] J. E. A. Chem et al., “Journal of Environmental Analytical Removal of Cu (II) and Cd (II) Ions from Environmental Water Samples by Using Cellulose Acetate Membrane,” vol. 4, no. 4, 2017.
[3] P. Kaedah et al., “Application Of Carrier Element-Free Co-Precipitation Method For Ni (II), Cu (II) and Zn (II) ions determination in water samples using chrysin,” vol. 19, no. 6, pp. 1194–1204, 2015.
[4] O. E. Abdel, N. A. Reiad, and M. M. Elshafei, “A study of the removal characteristics of heavy metals from wastewater by low-cost adsorbents,” pp. 297–303, 2011.
[5] K. C. Khulbe and T. Matsuura, “Removal of heavy metals and pollutants by membrane adsorption techniques,” Appl. Water Sci., vol. 8, no. 1, p. 19, 2018.
[6] C. F. Carolin, P. S. Kumar, A. Saravanan, G. J. Joshiba, and M. Naushad, “Journal of Environmental Chemical Engineering Efficient techniques for the removal of toxic heavy metals from aquatic environment : A review,” vol. 5, 2782–2799, 2017.

ADSORPTION OF CADMIUM IONS IN AQUEOUS SOLUTION USING OXALIC ACID MODIFIED PINEAPPLE PLANT STEM

V. Z. T. Loh, Y. P. Tan*, A. H. Abdullah

Department of Chemistry, Faculty of Science, Universiti Putra Malaysia, 43400 Serdang, Selangor Darul Ehsan, Malaysia

*Corresponding author: typ@upm.edu.my

Abstract
The release of cadmium, Cd(II) ions into water from industrial effluents and poor management of agricultural wastes lead to serious water and land pollution. Adsorption by agricultural waste is favourable in wastewater treatment due to its low cost, simple and easy operation. Pineapple plant stem (PPS) was modified with oxalic acid (OA) and proposed to be used as adsorbent in removing Cd(II) from aqueous solution. The adsorption capacity of PPS was doubled after chemically modified with OA. The batch studies of Cd(II) on OA modified PPS (OAPPS) were investigated under different parameters, namely adsorbent dosage, solution pH, contact time and initial metal ion concentration. The optimum dosage and pH for the Cd(II) adsorption by OAPPS was achieved at 2 g/L and 6, respectively. The adsorption equilibrium of Cd(II) on OAPPS was established within 30 minutes and fitted well with pseudo-second order kinetics model. The isotherm studies has shown that Langmuir isotherm was best fitted with experimental data on the removal of Cd(II) using OAPPS.

Keywords: Adsorption, Cadmium, Pineapple Plant Stem, Kinetics, Isotherm

Introduction
The industrial activities are essential to sustain human's living and heavy metal like Cd(II) are frequently used in metal refineries, batteries and textile industries. This hazardous metal ion was then released into streams through the industrial effluents and polluted large areas of water environment. Agricultural activities are as well unavoidable and its agricultural wastes were disposed through open burning which give rise to air pollution. Several agricultural biomasses were proposed and used as adsorbents in adsorption to remove metal ions from aqueous solution [1, 2]. Chemical modifications were carried out on natural adsorbents to improve its adsorptive properties [3, 4] and oxalic acid (OA) is considered as it was naturally found in most plants. Pineapple plant stem (PPS) was modified with oxalic acid (OA) and utilized as adsorbent to sequester Cd(II) from aqueous solution in this study. The adsorption performance of the adsorbent was evaluated in batch studies under different conditions. The possible adsorption mechanism was determined via isotherm and kinetics studies.

Methodology
The PPS was added to 0.5 M OA solution with the solid-to-liquid ratio of 50 g/L and the mixture was stirred for 60 minutes. Thermochemical reaction was then conducted at 120°C in oven for 90 minutes. The dried adsorbent was then washed with distilled water until neutral filtrate was obtained before drying and storage. The ready adsorbent was undergone batch studies under different parameters such as adsorbent dosage, pH, contact time and initial Cd(II) concentration.

Results and Discussion

The adsorption of Cd(II) on OAPPS was influenced by adsorbent dose, solution pH, initial Cd(II) concentration and contact time. The adsorbent dose of 0.05 g OAPPS was adequate to give optimal removal percentages of Cd(II) in 25 mL single metal ion solution. As the amount of OAPPS increased in aqueous solution, there was a greater surface area and more binding sites on OAPPS for Cd(II) ion binding, thus improved the Cd(II) uptake percentages. The OAPPS showed maximum adsorption capacity for Cd(II) at solution pH 6. The OAPPS is not suitable to work in a highly acidic solution due to the high competition between the metal ions and H^+ or H_3O^+ for active binding sites. Metal precipitates were formed at pH 7, lowered the amount of "free" Cd(II) ions for adsorption. The adsorption efficiency of OAPPS for Cd(II) was increased with increasing initial metal ion concentration due to the greater mass transfer forces. Moreover, the adsorption equilibrium was attained at 30 min regardless of the concentration of Cd(II) in aqueous solution. There was a less significant increase on the Cd(II) after 30 min as the adsorption sites on OAPPS was majorly occupied. The kinetics and isotherm studies suggested that Cd(II) are chemically bound to OAPPS on a monolayer surface.

Conclusion

The optimum Cd(II) adsorption was observed at 2 g/L dose, pH 6, 15 mg/L Cd(II) solution and 30 min. A monolayer Cd(II) adsorption occurred on OAPPS by chemical reaction was suggested from isotherm and kinetics studies.

Acknowledgement

This project was financially supported by Putra Grants Universiti Putra Malaysia.

References

1. Tasaso, P., 2014. Adsorption of copper using pomelo peel and depectinated pomelo peel. *Journal of Clean Energy Technologies*, 2 (2), 154 – 157.
2. Guiza, S., 2017. Biosorption of heavy metal from aqueous solution using cellulosic waste orange peel. *Ecological Engineering*, 99, 134 – 140.
3. Rao, R.A.K., Khan, U., 2017. Adsorption of Ni(II) on alkali treated pineapple residue (*Ananas comusus* L.): Batch and column studies. *Groundwater for Sustainable Development*, 5, 244 – 252.
4. Gondhalekar, S.C., Shukla, S.R., 2015. Biosorption of cadmium metal ions on raw and chemically modified walnut shells. *Environmental Progress and Sustainable Energy*, 34(6), 1613 – 1619.

SYNTHESIS AND CHARACTERISATION OF CHIRAL POLYANILINE FUNCTIONALIZED-GRAPHENE QUANTUM DOTS

Ruzniza Mohd Zawawi[1*], Zakira Imana Abu Mansor[1]

[1]Department of Chemistry, Faculty of Science, Universiti Putra Malaysia, 43400 UPM Serdang, Selangor, Malaysia.

*Corresponding author: ruzniza@upm.edu.my

Abstract
Graphene quantum dots-polyaniline doped with camphorsulfonic acid (GQD-PANI-CSA) composites were synthesized by electrochemical deposition processes on screen-printed carbon electrode (SPCE). The methodology for the electrode development was carefully optimized to obtain the optimal chiral detection capacity. GQD-PANI-CSA was synthesized using cyclic voltammetry at 0.3 V to 0.7 V followed by a potentiostatic of 0.55 V for 300 s. The optical properties were analyzed using ultraviolet visible (UV-Vis) spectroscopy while the surface structure was characterized using Fourier transform infrared (FTIR). The structural morphology was examined using field emission scanning electron microscopy (FESEM). The FESEM images reveals flake structure of GQD-PANI-CSA with granules. The ability of GQD to promote electron transfer on PANI doped CSA is promising as a potential fast enantio recognition of chiral compounds.

Keywords: Polyaniline, electrodeposition, graphene quantum dots.

Introduction
Conducting polymer is a fascinating material which possesses good environmental stability, ease of processing and wide range of electrical properties. The conjugated backbone structure of conducting polymer makes it unique to perform doping with dopants which subsequently making it electrically active. Among the conducting polymers, polyaniline (PANI) is the most interesting material to be experimented in this project. The material comprises of tunable properties and low synthesis of cost. It was found that PANI can possess helicity when doped with a chiral dopant (1). While recent research also shows that the helical induced PANI can perform enantioselectivity discrimination towards chiral aminohexane (2).

Graphene quantum dots (GQD) have recently gained interest for its potential in chemical sensing due to its chemical stability, low toxicity, and high electrical conductivity (3). In a vision on developing high efficacy with fast response chiral sensor, adapting GQD in helical PANI would be promising. However, preliminary studies should be handheld at first to give an overview on developing a sensitive chiral sensor.

Methodology
Graphene quantum dots (GQD) were firstly synthesized by using “bottom-up” strategy through pyrolysis of citric acid. The GQD solution prepared was firstly electrodeposited on the screen-printed carbon electrode (SPCE) and let dry at room temperature. The electrode is then electrodeposited with a cyclic scan of 0.3 V to 0.7 V in 0.14 M aniline and 0.28 M R-CSA at a scan rate of 0.05 Vs^{-1}, followed with a constant potential of 0.55 V for 300 s. The electrode then was dedoped with a constant potential of -0.35 V for 600 s in phosphate buffer solution (PBS) at pH 7. Another electrode was also be prepared using S-CSA.

Both electrodes were characterized using Fourier transform infrared (FTIR), ultraviolet-visible (UV-Vis), field emission scanning electron microscopy (FESEM).

Results and Discussion

GQD was successfully synthesized on SPCE electrochemically with cyclic potential of 0 to 1 V for 50 cycles. The IR spectroscopy of GQD shows absorbance at 1645 cm^{-1} indicating C=C vibration, which is fundamental to GQD core. The O-H stretching can be observed at 3325 cm^{-1} while C-O band can be confirmed at 1114 cm^{-1}. Lastly, the C-H bonding can be determined at 1317 cm^{-1}. As for the UV characterization of GQD, an absorption peak at 239 nm can be observed. The peak at 239 nm suggesting being caused by π to π* transition of C=C bond. In field emission scanning electron microscopy, the deposition shows irregular spherical structure with a diameter of ~47nm.

PANI-CSA-R and PANI-CSA-S were each electrodeposited on GQD-modified electrode. A wide range of cyclic voltammetry (-0.3 V to 1.1 V) was first analyzed to give preliminary view of the electrodeposition as shown in Fig. 1. In both cyclic scans show two oxidation characteristics of the PANI synthesis. These oxidation peaks would affect the oxidation state of the polymer given the polyaniline are oxidation state tunable accordingly to redox processes. The redox peak at 0.38 V in both syntheses of PANI-CSA-S and PANI-CSA-R corresponds to the oxidation-reduction process of leucoemeraldine (LE) to emeraldine (EM) transition while the redox peak at 0.75 V and 0.78 V of PANI-CSA-S and PANI-CSA-R, respectively corresponds to the oxidation-reduction peak of emeraldine (EM) to pernigraniline (PG) transition. Since emeraldine state is the only state capable to held dopant in its structure, it was determined that the polymer is best synthesized at 0.3 V to 0.7 V. The polymer was then complimented with potentiostatic at 0.55 V to prevent continuous doping-dedoping in cyclic scan which would lead to degradation of electrode.

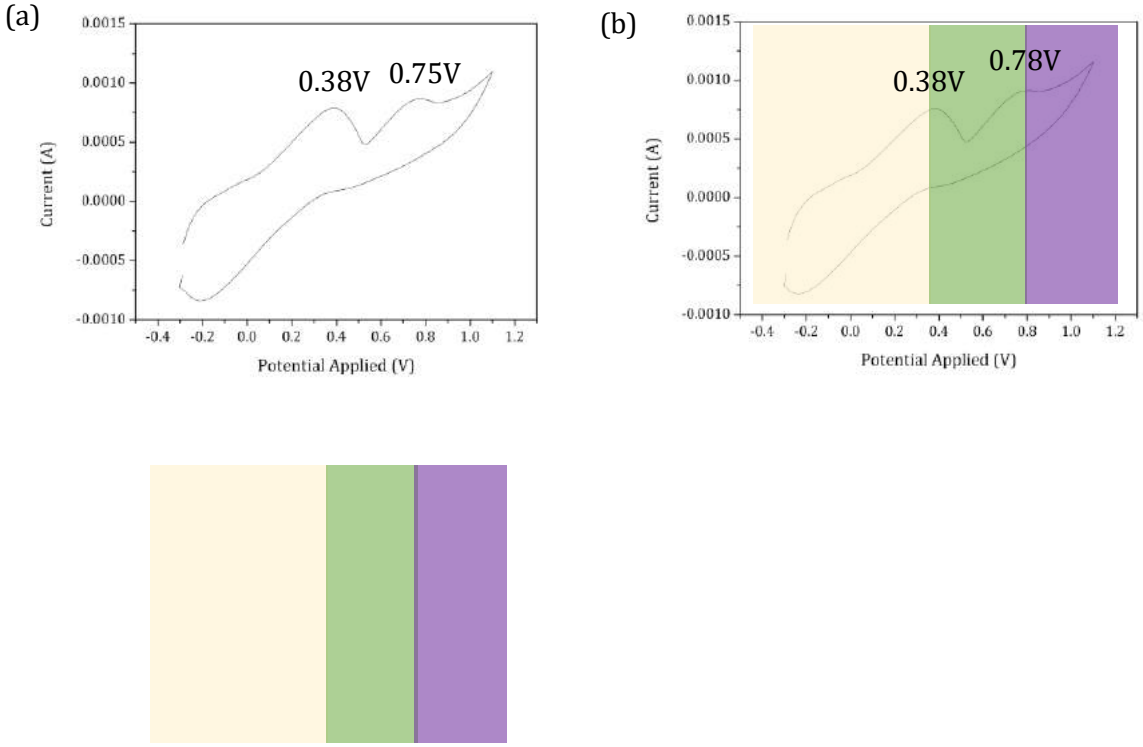

Fig.1 Cyclic voltammograms of (a) PANI-CSA-S and (b) PANI-CSA-R on GQD-modified electrodes.

Conclusion

PANI-CSA-S and PANI-CSA-R were both electrodeposited on GQD creating composite electrodes. The electrodeposition was optimized at its cyclic scan, number of growth cycle and growth time. These electrodeposited electrodes were characterized using IR, UV, and FESEM. This simple preparation electrode could be the future of a promising chiral sensor.

Acknowledgement

This work is supported by Putra Grant from Universiti Putra Malaysia.

References

1. Sudha, Kumar, D., & Iwamoto, M., Poly. J., 2013, 45, 2, pp. 160–165.
2. Zou, W., Yan, Y., Fang, J., Yang, Y., Liang, J., Deng, K., Wei, Z. J. American Chem. Society, 2014, 136,2, pp. 578–581.
3. Dong Y, Li G, Zhou N, Wang R, Chi Y, Chen G., Anal. Chem. 2012, 84, pp. 8378–8382

EFFECT OF THE HEAT TREATMENT ON THE PHOTOELECTROCHEMICAL PERFORMANCE OF BINARY HETEROSTRUCTURED PHOTOANODE AG_2S/ZNO NANORODS

A.A.AL-Zahrani [1,3], Z. Zainal [2, 3*], Z.A. Talib [4], H.N. Lim[2, 3], A. M. Holi[5]

[1]Imam Abdulrahman bin Fiasal University, eastern region, Dammam, Saudi Arabia
[2] Materials Synthesis and Characterization laboratory, Institute of Advanced Technology, Universiti Putra Malaysia,43400 UPM Serdang, Selangor, Malaysia.
[3] Department of Chemistry, Faculty of Science, Universiti Putra Malaysia,43400 UPM Serdang, Selangor, Malaysia.
[4] Department of Physics, Faculty of Science, Universiti Putra Malaysia,43400 UPM Serdang, Selangor, Malaysia.
*[5] Department of Physics, College of Education, University of Al-Qadisiyah, Al-Diwaniyah, Al-Qadisiyah58002, Iraq**

*Corresponding author: zulkar@upm.edu.my

Abstract
Successive ionic layer adsorption and reaction (SILAR) was used to fabricate a photoanode of Ag_2S nanoparticles onto the ZnO nanorods arrays for photoelectrochemical applications. A significant enhancement in the photoelectrochemical performance was observed for Ag_2S QDS/ZnO upon the heat treatment 400 ◦C which displayed a remarkable photocurrent density and photoconversion efficiency of 2.73 mA/cm^2 and 2.33% respectively by achieving ~9 times higher compared to ZnO NRAs (0.337 mA/cm^2, 0.25%). This improvement was attributed to the improved morphological structure, crystallinity and optical properties of synthesised heterostructures.

Keywords: Successive ionic layer adsorption and reaction (SILAR), heat treatment, photoconversion efficiency, Ag_2S, ZnO nanorods.

Introduction
Photoelectrochemical cells (PECs) have attracted a great interest due to their low manufacturing and enhanced photoconversion efficiency. Semiconductor-sensitized materials have been discovered to produce high efficiency photoanodes for PECs applications. ZnO is one of the most promising for these applications, due to its physical and chemical properties. However, ZnO has restriction in absorbing visible spectrum due to its wide bandgap. Moreover, a high recombination rate of photogenerated electron-hole pairs is another limitation needs to be overcome. Therefore, the reducing recombination rate by an efficient charge separation with enlargement of light absorption region are the imperative features in enhancing the photoconversion efficiency of ZnO NRAs. It was found that depositing metal chalcogenides such as Ag_2S[1], able to enhance the photoconversion efficiency of the ZnO NRAs. Ag_2S, with the narrow value of band gap, 0.9 ~ 1.1 eV, able to suppress the recombination rate of the photogenerated electron pairs in ZnO NRAs[2]. The combination of wide band gap and narrow band gap material semiconductors causes formation of heterostructured band alignment due to their different Fermi-levels positions. The current study highlights the effect of the post- heat treatment on the photoconversion efficiency on heterostructured photoanode Ag_2S/ZnO NRAs prepared via SILAR technique.

Methodology
High orientated vertically ZnO nanorods were grown on (ITO) substrate at 110◦C for 4 hours using hydrothermal method as designed in the earlier work [3]. For the deposition of

Ag_2S thin films, SILAR method was used. Briefly, 0.02 M of $AgNO_3$ aqueous solution as Ag precursor and 0.02 M of Na_2S as a sulphur precursor were used. The ZnO NRAs was immersed into the solution containing Ag, S precursor respectively for 60sec each to deposit Ag_2S. Deionized water (18.2 MΩ) was used between the immersion to eliminate the excessive loosely bonded ions. These four steps were considered as one cycle. Six SILAR cycles Ag_2S/ZnO NRAs photoanodes were synthesized and served to investigate the effect of annealing in the range between 100 ºC to 500 ºC on PEC performance.

Results and Discussion

Figure 1 (A) shows the linear sweep voltammogram of Ag_2S/ZnO NRAs as a function of annealing temperatures. The photocurrent density increased significantly after the annealing treatment, owing to the improvement of the morphological structure, crystallinity properties as well as the photo absorbance. The assembled photoanode Ag_2S/ZnO NRAs annealed at 400 ◦C showed the highest value of Jph and photoconversion efficiency (Figure 1(B)) with 2.73 mA/cm^2 and 2.33% respectively, compared to ZnO NRs (0.25%). The significant enhancement due to charge carrier transportation improvement and the decrement of the recombination rate upon the heat treatment [4].

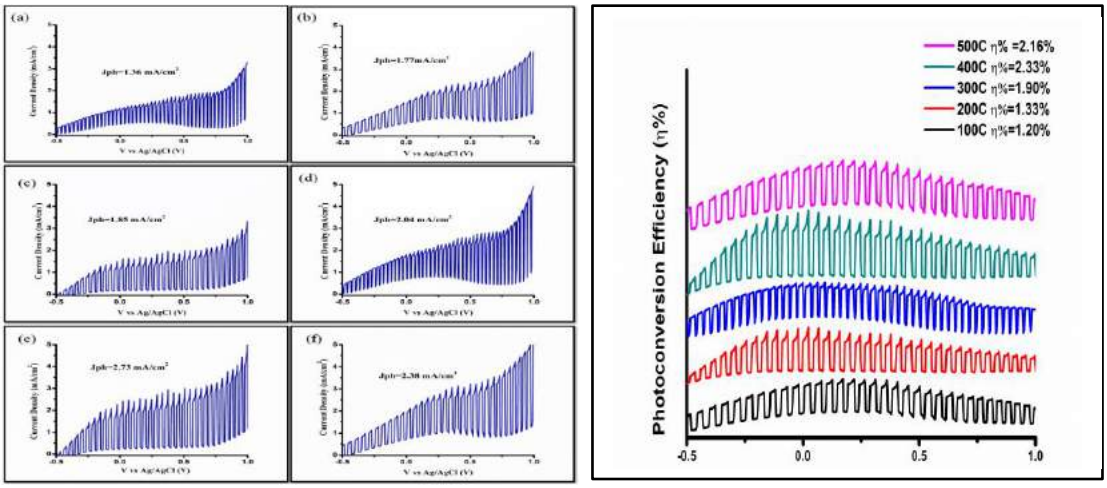

(A) **(B)**

Fig. 1. (A) Linear sweep voltammograms obtained at the scan rate of 20 mV s^{-1} at applied potentials from -1.0V to +1.0 V under illumination intensity of 100 mWcm^{-2} in 0.1M Na_2S and Na_2SO_3 electrolyte and (B) photoconversion efficiency for Ag_2S/ZnO NRAs/ITO as prepared and at different annealing temperatures.

Conclusion

Nanostructured Ag_2S/ZnO NRAs has been fabricated via SILAR method and their properties upon heat treatment at different temperatures were studied for PEC application. Significant enhancement was observed in photocurrent density of Ag_2S/ZnO NRAs annealed at 400 ◦C at the value of 2.73 mA/cm^2. The photoconversion efficiency of the particular sample was 2.33% which is almost 9 times greater compared to the pristine ZnO NRAs (0.25%).

References

[1] Xue, J., Liu, J., Mao, S., Wang, Y., Shen, W., Wang, W., Huang, L., Li, H. and Tang, J., 2018. Recent progress in synthetic methods and applications in solar cells of Ag_2S quantum dots. Materials Research Bulletin, 106, 113-123.

[2] Hu, X., Xu, W., Chen, C., Tan, F. and Zhang, W., 2017. Fabrication of Ag2S quantum dots decorated TiO2 nanorod arrays for organic/inorganic hybrid solar cells. Materials Letters, 204, 125-128.

[3] Mohd Fudzi, L., Zainal, Z., Lim, H., Chang, S.K. and Holi, A., 2018. Effect of Temperature and Growth Time on Vertically Aligned ZnO Nanorods by Simplified Hydrothermal Technique for Photoelectrochemical Cells. Materials, 11, 704.

[4] Chen, C., Li, Z., Lin, H., Wang, G., Liao, J., Li, M., Lv, S. and Li, W., 2016. Enhanced visible light photocatalytic performance of ZnO nanowires integrated with CdS and Ag_2S. Dalton transactions, 45, 3750-3758.

SYNTHESIS OF PYRAZOLE-3-TRIFLONES BY TRIFLYLDIAZOMETHANE VIA [3+2] CYCLOADDITION REACTION

Yuji Sumii[1], Pulakesh Das[1], Satoshi Gondo[1], Hiroto Uno[1], Norio Shibata[1]*

[1] *Department of Life Science and Applied Chemistry, Graduate School of Engineering, Nagoya Institute of Technology, Gokiso-cho, Showa-ku, Nagoya 466-8555, Japan.*

*Corresponding author: nozshiba@nitech.ac.jp

Abstract
Synthesis of pharmaceutically attractive pyrazole 3-triflones containing a triflyl group at the 3-position was achieved via [3+2] cycloaddition reaction of diazo-triflone (**1**) with nitroalkenes under basic conditions. Synthesis of 5-nitro-pyrazole triflones was also achieved via [3+2] cycloaddition reaction of diazo-triflone and α-bromonitrostyrene derivatives. The generation of anionic triflyl-diazomethane species followed by the [3+2] cycloaddition reaction with nitroalkenes is proposed for this transformation. Furthermore, an agrochemical attractive 5-amino-N-pyrimidinyl-pyrazole triflone was successfully prepared from 5-nitro-pyrazole triflone.

Keywords: trifluoromethanesulfonyl, pyrazole triflones, [3+2] cycloaddition, nitrostyrene

Introduction
The expedited synthesis of organofluorine compounds via novel and efficient methods is of prime importance in the fields of pharmaceuticals and agrochemicals. Trifluoro-methyl (CF_3) compounds are one of the most attractive targets in these areas of study owing to the unique proper-ties induced by the high lipophilicity and strong electron-withdrawing effect of the CF_3 group (σ_m = 0.43, σ_p = 0.54 ; π = 0.88).
Recently, trifluoromethanesulfonyl (triflyl, SO_2CF_3) have gained attention, due to the high electron-withdrawing ability and mild lipophilicity of SO_2CF_3 (σ_m = 0.79, σ_p = 0.93 ; π = 0.55) compared to CF_3. Pyrazoles are often found as an integral part of biologically active molecules, and the fluorine substitution containing pyrazoles have gathered much attention in the development of pharmaceuticals and agrochemicals. In particular, SO_2CF_3 substituted pyrazoles might be attractive drug candidates.
We recently reported a diazo-triflone (**1**) as an electrophilic trifluoromethylthiolation reagent. [1] Furthermore, we reported that **1** can be used as a building block for the synthesis of heteroaryl tryflon with or without copper catalyst. [2] As an extension of reactivity of **1**, we herein disclose the synthesis of pyrazole-3-triflones by the reaction of **1** with nitroalkenes via [3+2] cycloaddition under basic condition.

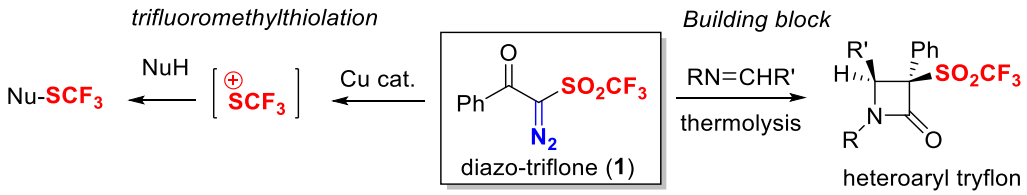

Methodology, Results and Discussion
After screening of the reaction conditions of **1** with nitroalkenes, we found that the use of 10 equiv of NaOMe in MeOH afford the desired pyrazole-3-triflon in high yield. The triflyl-diazomethane (**I**) was generated with the release of methyl benzoate (PhCO2Me) and

react with nitrostylene *via* a [3+2] cycloaddition mode to furnish the pyrazole triflen. A variety of nitroalkene derivatives (**2**) containing electron-donating, electron-withdrawing and halogenyl substituents could be applicable for this [3+2] cycloaddition to furnish the corresponding pyrazole triflones (**3**) in good to high yields. [4]

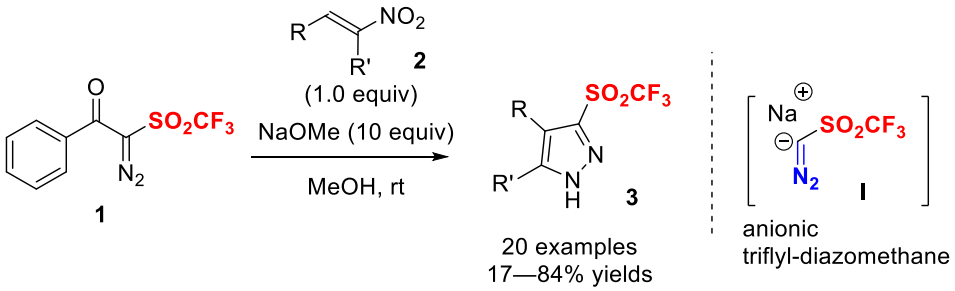

Next, α-bromonitrostyrene derivatives (**4**) were attempted this [3+2] cycloaddition. The reaction of 1 with 4 were also proceeded smoothly at lower temperature to provide the 5-nitro-pyrazole triflones (**5**) in good yield. Moreover, the agrochemically attractive 5-amino-N-pyrimidinyl-pyrazole triflone (**6**) could be obtained by 2 steps conversion from **5**. [5]

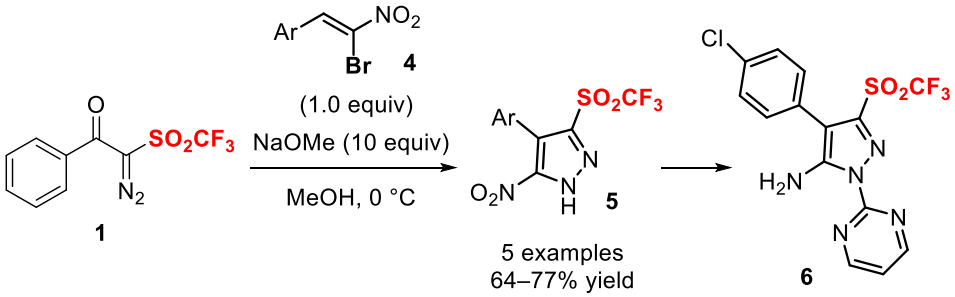

Conclusion

We disclosed the synthesis of pyrazole-3-triflones by the reaction of diazo-triflone **1** with nitroalkenes. The key for this transformation is the base-induced generation of anionic triflyl diazomethane **I** followed by the [3+2] cy-cloaddition reaction. We also succeeded in the synthesis of 5-nitro-pyrazole triflones by diazo-triflon and α-bromonitrostyrene derivatives under basic conditions. In addition, an agrochemical attractive 5-amino-N-pyrimidinyl-pyrazole triflone was obtained. These results not only indicate the efficient synthesis of pyrazole triflones, but also expand the diversity of diazo-triflone 1 for the synthesis of fluoro-functionalized compounds.

References

1. Huang, Z., Okuyama, K., Wang, C., Tokunaga, E., Li, X., Shibata, N., 2016. 2-Diazo-1-phenyl-2-((trifluoromethyl)sulfonyl)ethan-1-one: Another Utility for Electrophilic Trifluoromethylthiolation Reactions. *ChemistryOpen* 5, 188-191.
2. a) Huang, Z.; Jia, S.; Wang, C.; Tokunaga, E.; Sumii, Y.; Shibata, N., 2017. New Utility of Electrophilic Trifluoromethylthiolation Reagents for the Synthesis of a Variety of Triflones. *J. Fluorine Chem.* 198, 61-66. b) Huang, Z.; Wang, C.; Tokunaga, E.; Sumii, Y.; Shibata, N., 2015. Stereoselective Synthesis of β-Lactam-triflones under Catalyst-Free Conditions. *Org. Lett.* 17, 5610-5613.
3. Das, P.; Gondo, S.; Tokunaga, E.; Sumii, Y.; Shibata, N., 2018. Anionic Triflyldiazomethane: Generation and Its Application for Synthesis of Pyrazole-3-triflones via [3+2] Cycloaddition Reaction. *Org. Lett.* 20, 558-561.

4. Das, P.; Uno, H.; Tokunaga, E.; Sumii, Y.; Shibata, N., 2018. Synthesis of 5-nitro-pyrazole triflones via [3+2] cycloaddition reaction and its application for potential insecticide. *Fluorine notes* 116, 9-10.

DEVELOPMENT OF A NEW CLASS OF DIARYLPENTADIENONE ANALOGUES AS POTENTIAL A-GLUCOSIDASE INHIBITORS

SM. Mohd Faudzi[1,2,*], MA. Abdullah[1], ANM. Ramli[3], MFF Mohd Aluwi[3]

[1]Department of Chemistry, Faculty of Science, Universiti Putra Malaysia, 43400 UPM Serdang, Selangor, Malaysia.
[2]Laboratory of Natural Products, Institute of Bioscience, Universiti Putra Malaysia, 43400 UPM Serdang, Selangor, Malaysia.
[3]Department of Food Science, Faculty of Food Science and Technology, Universiti Putra Malaysia, 43400, Serdang, Selangor, Malaysia

*Corresponding author: sitimunirah@upm.edu.my

Abstract
Type 2 diabetes mellitus (T2DM) is a chronic disease occurred worldwide and is currently a major cause of morbidity and mortality. Several drugs such as sulfonylureas and biguanides are presently available to reduce hyperglycemia in T2DM patients, however, these medicines possess several side effects and thus searching for a new class of compounds is essential to overcome this problem. A series of aminated- and sulfonamide-containing diarylpentadienones were designed, synthesized, structurally characterized, and evaluated for their *in vitro* anti-diabetic potential on α-glucosidase enzyme. It was found that the sulfonamide-containing series were significantly inhibited the α-glucosidase, in which compound **18** demonstrated the most potent activity with IC_{50} values in the range of 4.93±0.4 μM, as compared to the standard quercetin (IC_{50} = 6.38±0.4 μM). The structure-activity relationship (SAR) studies concluded that the introduction of the trifluoromethylbenzene sulfonamide moiety is essential for the suppression of α-glucosidase. Docking simulation studies were carried out to understand the binding interactions of the most active compounds on the active site of α-glucosidase. Overall results suggest that the diarylpentadienones with sulfonamide moiety could be a new hit compound in the search of α-glucosidase inhibitors for the treatment of T2DM patients.

Keywords: sulfonamide, chalcone, α-glucosidase, T2DM

Introduction
Diabetes has become increasingly common around the world. T2DM, in particular, is caused by a metabolic disorder characterized by insulin resistance and incretins deficiency. Various therapeutic approaches have been used to alleviate diabetes, including improvement of insulin sensitivity and reduction of glucose absorption from the intestine. However, the current medications are associated with severe side effects including adverse gastrointestinal effects and abdominal discomfort (Liu *et al*, 2011). In this study we are focusing on synthesizing the potential diarylpentadienone compounds bearing the amino and sulfonamide moieties and tested them *in vitro* for anti-diabetic activities against the α-glucosidase enzyme.

Methodology
The general reaction scheme for the preparation of the targeted compound are shown in Scheme 1. The design of the compounds is based on steric and electronic properties of substituents, in which the selected functional groups were appended on *ortho*-, *meta*-, and *para*- positions of both ring A and ring B to examine their important influence towards α-glucosidase inhibitory activity.

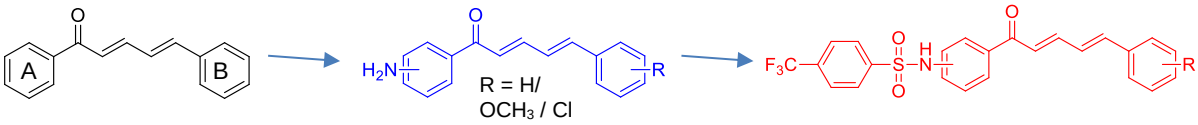

Scheme 1. General conversion of aminated-precursor to sulfonamide–diarylpentadienones

Results and Discussion

Based on the biological evaluation results, compound **18** prove to be the most active compound in the α-glucosidase inhibitory activity with IC_{50} of 4.93±0.4 µM. Further molecular docking works were conducted in understand more on the interactions of the compound with the targeted enzyme as depicted in Figure 1.

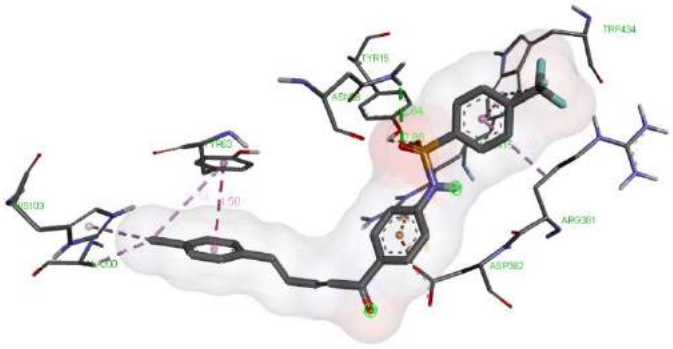

Figure 1. 3D diagram of the binding interactions of compound **18** with the active site residues of the α-glucosidase receptor

Conclusion

A series of diarylpentadienone analogues were successfully synthesized by applying Claisen-Schmidt condensation and sulfonylation reaction. The *in vitro* experimental evidence showed the potential of some sulfonamide diarylpentadienones as effective anti-diabetic hit molecules against α-glucosidase. The significance of *p*-sulfonamide diarylpentadienones with halogenated (-Cl) phenyl (Ring B) has been revealed to possess remarkable α-glucosidase inhibition activities, with compound **18** was identified as the most potent compound as α-glucosidase inhibitor.

Acknowledgement

This work was financially supported by the Universiti Putra Malaysia under the Putra Grant – Putra Young Initiative (IPM, 9480700).

References

1. Liu, M., Zhang, W., Wei, J., & Lin, X., 2011. Synthesis and α-glucosidase inhibitory mechanisms of bis (2, 3-dibromo-4, 5-dihydroxybenzyl) ether, a potential marine bromophenol α-glucosidase inhibitor. *Marine drugs*. 9, 1554-1565.

FREE-STANDING LAYER-BY-LAYER FILM FOR HIGH-PERFORMANCE SUPERCAPACITOR

Y. Sulaiman[1,2]* and S. Kulandaivalu[1]

[1]Department of Chemistry, Faculty of Science, Universiti Putra Malaysia, 43400 UPM Serdang, Selangor, Malaysia.
[2]Functional Devices Laboratory, Institute of Advanced Technology, Universiti Putra Malaysia, 43400 Serdang, Selangor, Malaysia

*Corresponding author: yusran@upm.edu.my

Abstract
Energy crisis has become a worldwide concern issue due to the rapid growth of human population together with the accelerated global economy. Therefore, effective energy storage is highly demanding. In this work, the layer-by-layer (LBL) assembly was used to fabricate the material for supercapacitor. LBL is a simple, straightforward and robust fabrication process. A free-standing LBL film nanocomposite consisting of polypyrrole/reduced graphene oxide nanocomposite (PPy/rGO) layered with multiwalled carbon nanotube/reduced graphene oxide/nanocrystalline cellulose nanocomposite (MWCNT/**r**GO/NCC) was prepared via in-situ polymerization followed by vacuum filtration and chemical reduction. The PPy/rGO|MWCNT/rGO/NCC bilayer was used as an electrode for a symmetrical supercapacitor device. The device was fabricated in a two-electrode configuration, in which a filter paper impregnated with 1 M KCl was used as a separator. The device exhibited a high specific capacitance of 882.2 F g^{-1}, remarkable cycling stability of ~90% over 10000 cycles, and high specific energy of 44.6 Wh kg^{-1} with a high specific power of 2889.9 W kg^{-1}, which outperformed many other reported polypyrrole-based materials for supercapacitors. Thus, this LBL film nanocomposite is a promising electrode for high-performance supercapacitor.

Keywords: Supercapacitor, layer-by-layer, nanocomposite

Introduction
Layer-by-layer (LBL) assembly is a simple, straightforward and robust fabrication technique. Generally, LBL assembly is a sequential process where the charged species are deposited in multiple layers. It is a convenient technique to produce multilayers by introducing diverse nanostructures, comprising nanoparticles, nanosheets and nanofibers in a thin film. Importantly, it is a well-established method to assemble advanced functionalities in multilayers with desired chemical and physical properties [1]. In this work, we attempted to fabricate economical, environmentally friendly, lightweight and freestanding LBL based active material for supercapacitor. The formation of LBL films comprising of PPy and carbon nanomaterials (MWCNT, GO, **r**GO and NCC) via chemical polymerization and vacuum filtration is reported. Our main aim in this study is to fabricate a thin layer film by combining the merits of each individual material that met the demands of today's world. In that endeavor, PPy doped GO (PPy/GO) was layered with MWCNT/GO/NCC forming a bilayer, PPy/GO**|**MWCNT/GO/NCC film. The as-formed bilayer film was further treated with hydrazine to form conductive PPy/**r**GO**|**MWCNT/**r**GO/NCC film.

Methodology
The monomer, pyrrole and ferric chloride hexahydrate were supplied by Merck and Bendosen, respectively. Py was distilled and stored at 0 ˚C prior to use. The MWCNTs

were purchased from Sigma-Aldrich and GO from Graphenea. Hydrazine monohydrate from Nacalai Tesque, Inc, was used as a reducing agent. Potassium chloride was provided by Fischer Scientific. In the typical synthesis of PPy/GO, 100 mM Py was mixed with 1 mg ml^{-1} GO aqueous dispersion. Prior to the in-situ polymerization process, the mixture was magnetically stirred at room temperature for 15 min to obtain a homogenous Py/GO solution. 100 mM $FeCl_3.6H_2O$ aqueous solution was then added dropwise into the solution mixture to initiate the polymerization. In order to prepare MWCNT/GO/NCC suspension, 25 mg of NCC powder was added into 0.5 mg ml^{-1} GO aqueous dispersion under ultra-sonication for 60 min with a concentration ratio of 1:2 (GO:NCC). The LBL nanocomposite film was prepared by filtering the obtained solutions through a cellulose nitrate membrane filter. The PPy/GO solution was drained on a membrane filter to obtain a uniform PPy/GO film by facile vacuum filtration and left dried. The second layer, MWCNT/GO/NCC was then filtered on the previous film. The obtained bilayer film was then reduced to produce a PPy/**r**GO**|**MWCNT/**r**GO/NCC film using hydrazine as reported by Mihara, et al. [2].

Results and Discussion

The electrochemical performances of the as-prepared composites were evaluated using a two-electrode symmetrical arrangement system in 1.0 M KCl aqueous electrolyte. Fig. 1a represents the comparative CV curves at a scan rate of 10 mV s^{-1}. All the curves exhibit a nearly rectangular shape explaining the exceptional ionic and electron movements within the composites [3]. Higher current response and larger closed area are noticed only in **r-**PGMGN bilayer film signifying the **r-**PGMGN has a larger electrochemical active area. The **r**-PGMGN was also further analyzed at different current densities as depicted in Fig. 1b. As the current density increases, the GCD curves transform into a symmetrical triangle due to the good reversibility and capacitive behavior of composite [4]. As shown in Fig, 1c, about 90% of capacitance retention is observed signifying the excellent cycling stability of **r**-PGMGN film over a long period charge/discharge process.

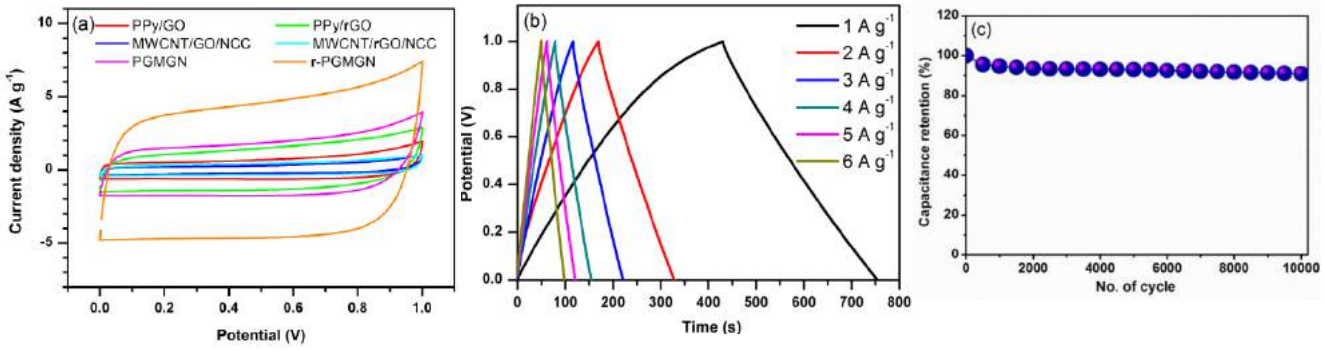

Fig. 1 (a) A comparison of CVs for different composites, (b) GCD curves and (c) stability test of **r**-PGMGN.

Conclusion

A free-standing and paper-like composite, **r**-PGMGN was fabricated using LBL assembly via simple and inexpensive techniques. The composite exhibited a high specific capacitance of 882.2 F g^{-1} with high cycling stability.

Acknowledgement

Authors would like to acknowledge the support given by the Universiti Putra Malaysia for funding this work through project no GP-IPS/2017/9580500.

References

1. K. Ariga, Y. Yamauchi, G. Rydzek, Q. Ji, Y. Yonamine, K.C.W. Wu, J.P. Hill, 2014. *Chemistry Letters.* 43, 36-68.
2. S. Mihara, T. Tsubota, N. Murakami, T. Ohno, 2012. *Journal of Nanoscience and Nanotechnology*. 12, 6930-6934.
3. S. Biswas, L.T. Drzal, 2010. *Chem. Mat.* 22, 5667-5671.
4. L. Zhang, K.N. Hui, K. San Hui, H. Lee, 2016. *J. Power Sources* 318, 76-85.

A LIPIDOMICS APPROACH TO DISTINGUISH VEGETATIVE INPUTS TO PEAT FOR PALAEOCLIMATIC RECONSTRUCTION

I.S Johari[1,2*], P.J Gates[1], I.D. Bull[1]

[1]*School of Chemistry, Cantock's Close, BS8 1TS, University of Bristol, UK.*
[2]*Chemistry Department, Faculty of Science, UPM Serdang 43400, Selangor.*

*Corresponding author: ili@upm.edu.my

Abstract
A lipidomic approach was developed to determine inputs of vegetation to peat which is useful for palaeoclimate reconstruction. The two dominant inputs studied were *Sphagnum* and sedge indicative wetter and drier climates, respectively. Commercial peats were extracted using a modified Bligh-Dyer solvent, saponified then derivatized prior to GC-qTOF-MS analysis. The results acquired from GC-qTOF-MS were processed using MassHunter Profinder and Mass Profiler Professional software. The output of PCA and HCA reveals that a lipidomic approach can distinctly differentiate between *Sphagnum* and sedge, indicates the potential of this approach as a quick screening method for determining vegetative inputs to peat for palaeoclimatic reconstructions.

Keywords: Lipidomics, palaeoclimate, PCA, HCA.

Introduction
Peatland can serve as a paleoclimate archive, arising from vegetation records preserved over long periods of time. Peat cores comprise a vegetation histories, with depth, that may be using the appropriate analytical techniques. Previously, biomarker analysis has been widely used, to determine inputs constituting peat, for palaeoclimatic reconstruction. (Zocatelli *et al*., 2014, Schellekens *et al*., 2015a). In addition, macrofossil analysis has also been used as a complementary technique (Nichols *et al*., 2006). This latter technique, works best with ombrotrophic peatlands, where the slow degradation of bryophytes (mainly *Sphagnum*) takes place, such that the plants remain only partially decayed and identifiable (Ronkainen *et al*., 2013). In contrast, sedge which dominates minerothrophic peatlands, is hardly recognized due to higher decomposition rates (Ronkainen *et al*., 2013). Moreover, the lipids biomarkers are not species-specific hence a comparison can be harder when during drier periods and/or transition phases as the vegetative input will be more complex. Lipidomics provides a more holistic analysis where whole lipid distributions are considered simultaneously in a non-targeted approach. This is followed by rigorous data processing and chemometric analyses to identify discriminator compounds in the peats studied. Such discriminant lipids can then be compared statistically between samples using principal component analysis (PCA) and hierarchical clustering (HCA) to better visualize the separation achieved.

Methodology
Commercial *Sphagnum* and sedge were purchased and oven dried at 60°C, to remove moisture, and then ground with mortar and pestle. 0.5 g samples (9 replicates each) were sonicated three times with 3 mL (3 mL × 3) of monophasic solvent of methanol:chloroform:buffered water (10:5:4, *v/v/v*) for 15 min. *n*-hexatriacontane was spiked into samples prior to extraction. After each sonication, sequential extracts were decanted into a clean vial and pooled together. Following extraction, a phase separation was conducted using chloroform and buffered water. The organic layer was transferred to

other clean vial and evaporated until dryness. Saponification was carried out using 2 mL of 5M KOH methanolic solution by heating at 120°C for one hour. The saponified samples were acidified with HCl to pH 3-4. Subsequently, the samples were extracted with chloroform (×3) and then the solvent removed under a gentle stream of nitrogen. Extracts were derivatized using *N,O*-bis(trimethylsilyl)trifluoroacetamide (BSTFA) + 1% trimethylchlorosilane (TMCS) prior to instrumental analysis. The raw GC-MS data were acquired using MassHunter Qualitative analysis software and exported to MassHunter Profinder for pre-processing then to Mass Profiler Professional software for data filtering to reduce the number of compounds to be used as final discriminators. Unpaired t-tests were performed to select the most discriminating compounds to be used for PCA and HCA.

Results and Discussions

A total of 296 compounds were aligned in all samples at the pre-processing step. Subsequently, filter by frequency, filter by coefficient variation and filter by fold change were applied to the data prior to a t-test. Eighty-seven compounds were selected as discriminant compounds and used to construct PCA and HCA for visualization. PCA reveals complete separation between *Sphagnum* and sedge along PC1, with or without the presence of quality control samples. A similar output was observed using HCA where clustering between *Sphagnum* and sedge was achieved and depicted by the dendrogram. Identification of the discriminant lipids was achieved using the IDBrowser Identification tool based on the spectral matching scores against the NIST and G1676AA Fiehn GC/MS Metabolomics libraries (Agilent). Of all compounds selected, only 24 compounds were identified, these included alcohols, hydroxy acid, triterpenoid, diterpene, obtusifoliol, alkyl resorcinol, linoleic acid, totarol and several others as their TMS derivatives.

Conclusion

A non-targeted assessment of the GC amenable lipidomes of peat samples enables discriminant lipids to be rapidly determined. PCA and HCA output distinctly shows complete separation between two vegetation types and is therefore potentially useful in distinguishing different inputs to peatlands. Known biomarkers such 5-*n*-alkylresorcinols are among the discriminant lipids identified using this technique showing that the reliability of this approach and it's potential for biomarker discovery.

References

1. Nichols, J.E., Booth, R.K., Jackson, S.T., Pendall, E.G., and Huang, Y. (2006). Palaeohydrologic reconstruction based on *n*-alkane distributions in ombrotrophic peat. *Organic Geochemistry*. 37, 1505-1513.
2. Ronkainen, T., McClymont, E. L., Väliranta, M., & Tuittila, E.-S. (2013). The *n*-alkane and sterol composition of living fen plants as a potential tool for palaeoecological studies. *Organic Geochemistry*, 59, 1–9.
3. Schellekens, J., Bindler, R., Martínez-Cortizas, A., McClymont, E.L., Abbott, G.D., Biester, H., Pontevedra-Pombal, X., and Buurman, P. (2015a). Preferential degradation of polyphenols from *Sphagnum* – 4-Isoprophenylphenol as a proxy for past hydrological conditions in *Sphagnum*-dominated peat. *Geochimica et Cosmochimica Acta* 150. 74-89.
4. Zocatelli, R., Jacob, J., Gogo, S., Le Milbeau, C., Rousseau, J., & Laggoun-Défarge, F. (2014). Spatial variability of soil lipids reflects vegetation cover in a French peatland. *Organic Geochemistry*, 76, 173–183.

FORMATION EVALUATION OF NANOZEOLITIC IMIDAZOLATE FRAMEWORK-8

Nurul Akmarina Mohd Abdul Kamal[1,2,4], Mohd Basyaruddin Abdul Rahman[1,2*,] Emilia Abdul Malek[1,2] and Sharida Fakurazi[3]

[1]Integrated Chemical BioPhysics Research, Faculty of Science,
[2]Department of Chemistry, Faculty of Science,
[3]Department of Human Anatomy, Faculty of Medicine and Health Science,
Universiti Putra Malaysia, 43400 UPM Serdang, Selangor Darul Ehsan, Malaysia
[4]Department of Pharmaceutical Technology, Faculty of Engineering Technology,
Universiti Malaysia Pahang, 26300 Kuantan, Pahang Darul Makmur, Malaysia

*Corresponding author: basya@upm.edu.my

Abstract
An evaluation of nanoZeolitic Imidazolate Framework-8 nanoparticles (nZIF-8) at a different time interval during and after the formation process is herein reported. Powder X-ray diffraction (PXRD) confirmed that the frameworks retained similar characteristics compared to their simulated counterparts. Electron microscopy (TEM) images demonstrated the transformation in particle size and shape from spherical to hexagonal with increasing reaction time. The TEM images also showed that the particle size and morphology of nZIF-8 remained unchanged in methanol suspension until 72 hours. Finally, the assessment of the decomposition of nZIF-8 revealed that the framework easily decomposed in the acidic environment compared to neutral. In conclusion, the size, stability and pH-responsive nature of nZIF-8 make it an excellent candidate for utilization as a nanocarrier for cancer therapeutics.

Keywords: anticancer, nanoparticle, morphology, size, ZIF-8

Introduction
Metal-Organic Frameworks (MOFs) are crystalline solids formed by the complexation of metal ions and organic ligands. Zeolitic imidazolate frameworks (ZIFs), a subclass of MOFs were first discovered by Yaghi's group in 2006 [1] and gaining considerable attention due to its high thermal stability and porosity. ZIF-8 exhibited sodalite (SOD) zeolite-type topology and showed significant progress for cancer nanomedicine due to its tunable size [2], morphology, stability, and pH-responsive [3]. For the anticancer study, the size and morphology of nanoparticles are crucial, depending on the route of delivery [4]. Several factors influence the size, morphology, and stability have been studied during the reaction process, including solvent [5] and metal salts [6]. There is still little attention paid to evaluate the nZIF-8 during and after the formation process. In conjunction with this, it is our interest to determine the consequence of synthesis time to the nZIF-8, followed by stability and decomposition assessment after the formation process. Here, we synthesized and evaluated the nZIF-8 stability at a different time interval at room temperature. Overall, the powder X-ray diffraction (PXRD), Fourier Transform Infra-Red-Attenuated Total Reflection (FTIR-ATR) and High-Resolution Transmission Electron Microscopy (HRTEM) demonstrated that the time manipulation regulated the different size and morphology of nZIF-8. The fact that nZIF-8 showed considerable pH-responsive characteristic and stability intrigued us in exploring its potential as a vehicle for cancer therapeutics.

Methodology

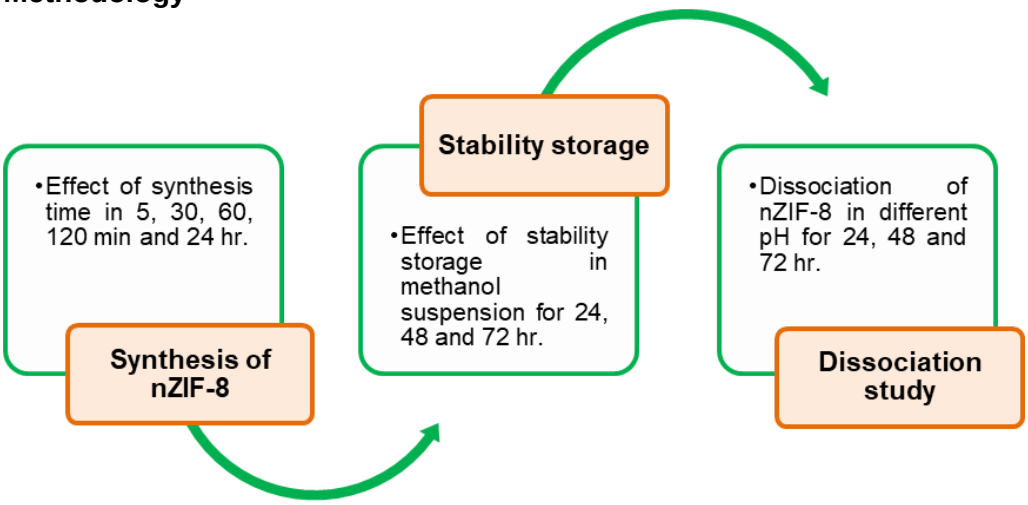

Results and Discussion

Synthesis of nZIF-8 in 5, 30, 60, 120 min, and 24 h.
PXRD of all samples indicated a similar pattern and confirmed the peak of ZIF-8 at 2θ = 7.4°, 10.4°, 12.7°, 14.7°, 16.4°, 18.0°, 22.1°, 24.5°, 26.7°, and 29.6°(Figure 1). TEM images showed the morphology of the particles transformed from spherical to hexagonal following synthesis time (Figure 2).

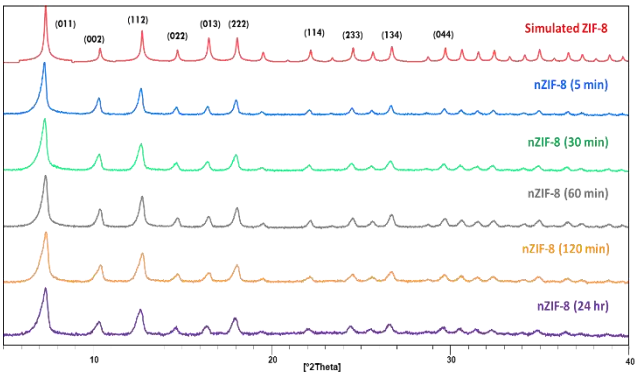

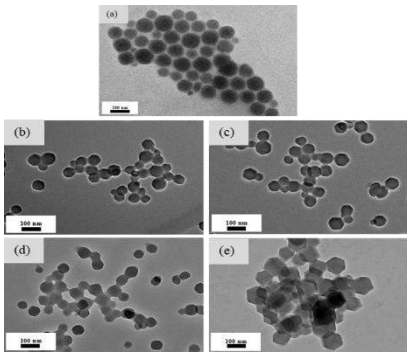

Figure 1. PXRD and Figure 2. TEM images of nZIF-8 synthesized at various times.

Stability of nZIF-8 at 24, 48 and 72 h.
The shelf-life of nZIF-8 in methanol suspension can be extended up to 72 h without changing the particles size and morphology.

Dissociation study of nZIF-8 at different pH; pH 5.5 and pH 7.4
The nZIF-8 particles in the acidic medium, decomposed into fractions less in less than 24 h compared to neutral medium suggested the pH-responsive properties could be manipulated for anticancer study.

Conclusion

We showed that synthesis time holds a crucial role to control the size and morphology of the nZIF-8 formation. The assessment on stability storage suggested that nZIF-8 can be stored in methanol at room temperature for a specified period, before starting the new experiment. Finally, we demonstrated that nZIF-8 showed different dissociation result in an acidic and neutral medium. Overall, this report envisions that the tunable, stable and pH-responsive of the nZIF-8 potentially to be a right candidate for the cancer nanomedicine study.

Acknowledgment

This work is supported by Malaysian Institute for Innovative Nanotechnology (NanoMITe) (Vote. No. 5526306), University Putra Malaysia (UPM) Grant 2017 (GP-IPB/2017) (Vote. No. 9580901), and Nurul Akmarina Mohd Abdul Kamal is financially supported by the Ministry of Education Malaysia (MoE)-University Malaysia Pahang (UMP) under SLAB program.

References

[1] J. Y. Choi *et al.*, “Exceptional chemical and thermal stability of zeolitic imidazolate frameworks,” *Proc. Natl. Acad. Sci. U.S.A,* vol. 103, pp. 10186 –10191, 2006.

[2] L. Yan *et al.*, “Size Controllable and Surface Tunable Zeolitic Imidazolate Framework-8-Poly(acrylic acid sodium salt) Nanocomposites for pH-Responsive Drug Release and Enhanced in Vivo Cancer Treatment,” *ACS Appl. Mater. Interfaces*, vol. 9, pp. 32990–33000, 2017.

[3] T. Simon-Yarza *et al.*, *4.38 "The Situation of Metal-Organic Frameworks in Biomedicine*," *Comp. Biomater*, vol. 4, pp. 719–749, 2017.

[4] C. Tamames-Tabar *et al*., "*MOFs in Pharmaceutical Technology*," *Bio-and bioins. mater*, vol. 2, pp. 83-112, 2014.

[5] E. L. Bustamante *et al*., “Influence of the solvent in the synthesis of zeolitic imidazolate framework-8 (ZIF-8) nanocrystals at room temperature,” *J. Colloid Interface Sci.*, vol. 424, pp. 37–43, 2014.

[6] J. S. Moore *et al.*, “Zeolite-like Behavior of a Coordination Network,” *J. Am. Chem. Soc.*, vol. 117, pp. 11600–11601, 1995.

SYNTHESIS OF XANTHONE BY GSS MODIFICATION METHOD

Shurutishria Ramakrishnan[1], Sakuntala Dewi Paramaswaran[1] and Nadiah Mad Nasir[1*],

[1]Department of Chemistry, Faculty of Science, Universiti Putra Malaysia, 43400 UPM Serdang, Selangor Darul Ehsan, Malaysia.

*Corresponding author: nadiahmadnasir@upm.edu.my

Abstract
Recently the group has focused on the development of xanthone based on Grover [1] and Sousa [2] (GSS) modification method. This method includes the route of benzophenone through condensation by Friedel–Crafts acylation of appropriately substituted benzoyl chloride with phenolic derivatives. Followed by the cyclization step that involves a nucleophilic substitution or a nucleophilic addition-elimination of 2,2'-dioxygenated benzophenones to produce desire xanthone. Extension of the Grover, Shah, and Shah (GSS) modification method, our group had successfully applied this method to synthesize Gentisein **(1)** and 1,3,5,6-tetrahydroxyxanthen-9-one **(2)**. From the previous reported, Gentisein **(1)** was isolated from *Gentiana lutea*, which showed bitter tonic to improve digestion.

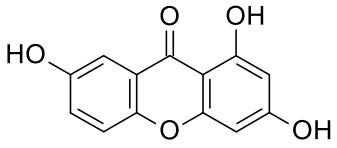

Gentisein **(1)**

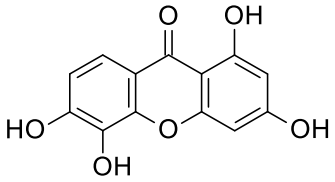

1,3,5,6-tetrahydroxyxanthen-9-one **(2)**

Keywords: Organic synthesis, Xanthone, Friedel-Crafts acylation

Introduction
Xanthones is one of the phytochemical and a group of structurally diverse natural products that exhibit significant biological and pharmacological properties, including antioxidant, anti-inflammatory, anti-bacterial, anti-fungal, and antitumor activities. Due to their vast array of biological activities, numerous research groups have pursued the synthesis of this pharmacophore for evaluation against various diseases.

One of the first methods for the synthesis of xanthones was introduced by Michael [3] and Kostanecki [4] which involved the distillation of a mixture of phenol, an *o*-hydroxybenzoic acid, and acetic anhydride. Unfortunately, this method produced a low yield with some conditions problem.

In the Grover, Shah, and Shah (GSS) reaction, better results were obtained using a mixture of phosphorus pentoxide–methanesulfonic acid (Eaton's reagent) instead of phosphorus oxychloride–zinc chloride as catalyst. This modification method providing high yields (90–95%) of the xanthone and no detectable amounts of the possible benzophenone. Therefore, our group had successfully applied this method to synthesize Gentisein **1** and 1,3,5,6-tetrahydroxyxanthen-9-one **2** (Scheme 1). From the previous reported, Gentisein **1** was isolated from *Gentiana lutea*, which showed bitter tonic to improve digestion.

Methodology

To a mixture of commercially available phloroglucinol dihydrate (0.79 mmol), and dihydroxybenzoic acid derivatives (0.79 mmol) was added slowly 1.2 mL of Eaton's reagent (P_2O_5– CH_3SO_3H). The mixture was stirred for 20 minute at 80 °C, cooled to room temperature (r.t.), and poured onto ice. After vigorous stirring at ambient temperature for 2 hour, a thin slurry formed. The solid was collected by filtration, washed with water and dried at room temperature to give **1** as a yellow solid and **2** as a pale yellow solid.

Results and Discussion

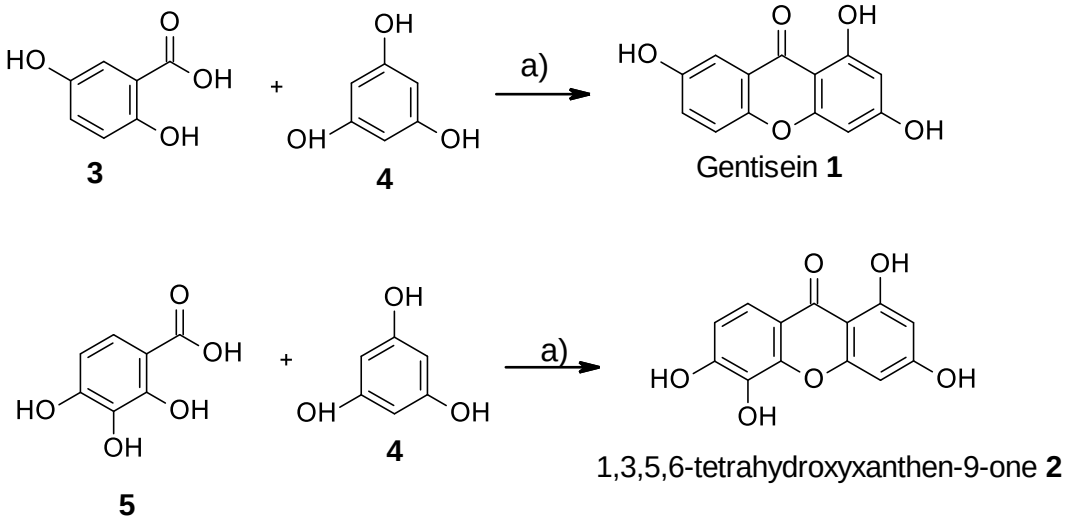

Scheme 1: a) P_2O_5_CH_3SO_3H, 80°C, 20 min, 50-60%.

Conclusion

Our main aim was to explore the flexibility and efficiency of the synthetic route by Grover, Shah, and Shah (GSS) modification method in the synthesis of xanthone.

Acknowledgement

We thank you IPM grant from Universiti Putra Malaysia for the financial support.

References

1. Grover, P.K., Shah, G.D., Shah, R.C. *J. Chem. Soc.* 1955, 3982.
2. Sousa, M. E. and Pinto, M. M. M. *Current Medicinal Chemistry.* 2005, 12*,* 2447.
3. Michael, A. *Ann. Chem. J.* 1883, *5*, 81.
4. Kostanecki. S. *Ber.* 1891, *24*, 1898.

REMOVAL OF METHYL ORANGE DYE BY CALIX[4]ARENE-MODIFIED LEAD SULPHIDE

Nor Zida Rosly[1], Mazliana Ahmad Kamarudin[2] Siti Efliza Ashari[3] and Shahrul Ainliah Alang Ahmad[1,4] *

[1]Institute of Advanced Technology (ITMA), Universiti Putra Malaysia, Serdang 43400, Selangor, Malaysia
[2]Department of Physic, Faculty of Science, Universiti Putra Malaysia, Serdang 43400, Selangor, Malaysia
[3]3Center of Foundation Studies for Agricultural Science, Serdang 43400, Selangor, Malaysia
[4]Department of Chemistry, Faculty of Science, Universiti Putra Malaysia, Serdang 43400, Selangor, Malaysia

*Corresponding author: ainliah@upm.edu.my

Abstract
This study investigated the adsorption of methyl orange (MO) dye using lead sulphide (PbS) modified with calix[4]arene as an alternative and regenerative adsorbent. The chemical and morphological features of synthesized PbS nanoparticles and calix[4]arene-modified PbS were analysed via FTIR and FESEM. The adsorption performance was estimated by the percentage removal of MO dye from the water system.

Keywords: calix[4]arene-modified PbS, adsorption, methyl orange

Introduction
In recent decades, wastewater effluent containing toxic synthetic dyes have become a critical issue due to the rapid development of industry and economy, posing a great threat to human health and safety [1]. Adsorption has been found to be an effective way for the removal of dyes because of its multiple benefits such as simplicity in design and operation, high removal efficiency and low cost [2]. Herein, the main aim of this study is to investigate an alternative nano-adsorbent, calix[4]arene-modified PbS for the removal of methyl orange (MO) wastewater.

Methodology
Modification of lead sulphide (PbS) with *p-tert*-butyl-calix[4]arene
The modification of PbS was done using 3-glycidoxypropyltrimethoxy silane (4.18 mmol), *p-tert*-butyl-calix[4]arene (3.03 mmol), 0.2 g PbS, and triethylamine (catalyst) that were stirred in dry toluene at room temperature for 6 h under nitrogen gas. The adsorbent was centrifuged and dried at 80 °C for 3 h.

Adsorption and desorption study
Adsorption experiments were done by agitating adsorbent with 10.0 mL MO dye solution of specific concentration at 150 rpm and at room temperature (27 ± 1°C). The final concentration of residual dye was determined via a UV–Vis spectrophotometer. In desorption study, different concentration of NaOH solution was used to select the best condition to elute the MO solutions.

Results and Discussion
Fourier transform infrared spectroscopy (FTIR) and field emission scanning electron microscopy (FESEM). Based on FTIR spectroscopy, the modification of calix[4]arene onto lead suphide (PbS) nanoparticles was confirmed due to the presence of band (Figure 1(c)) at 2952 cm^{-1} that correspond to the C-CH_3 stretching vibration, indicating that *p-tert*-butyl-calix[4]arene was immobilised on the surface of PbS. As can be seen in Figure 1 (d) and

(e), there are obvious morphological differences in the FESEM micrographs of unmodified PbS and the calix[4]arene-modified PbS.

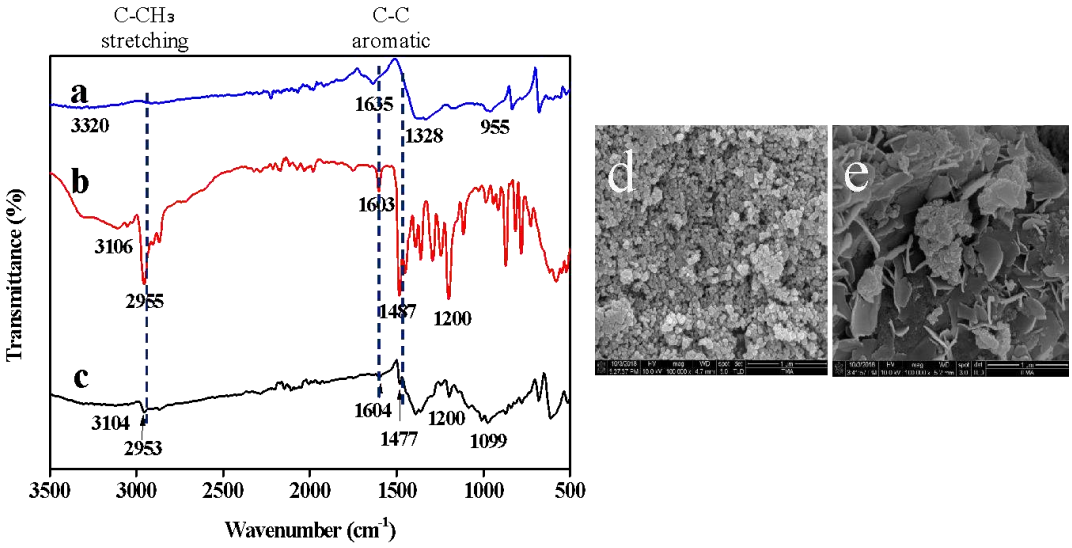

Figure 1 FTIR spectra of (a) unmodified lead sulphide (PbS) (b) *p-tert*-butyl-calix[4]arene (c) calix[4]arene-modified PbS and FESEM images of (d) unmodified PbS, and (e) calix[4]arene-modified PbS

Adsorption and desorption study

The optimised values for adsorbent dosage, contact time, and pH were found to be 89.70 mg of calix[4]arene-modified PbS, a contact time of 129.76, and pH 4. The maximum percentage adsorption of MO obtained before the desorption process was 70.26 % (control). Figure 2(a) illustrates the effects of NaOH concentration on MO desorption. The highest amount of desorption (64 %) was observed when 0.10 M NaOH was used as eluent. Figure 2(b) demonstrates the cyclic adsorption-regeneration test that shows after four cycles, the adsorbed percentage of MO decreased markedly from 70% to 50%.

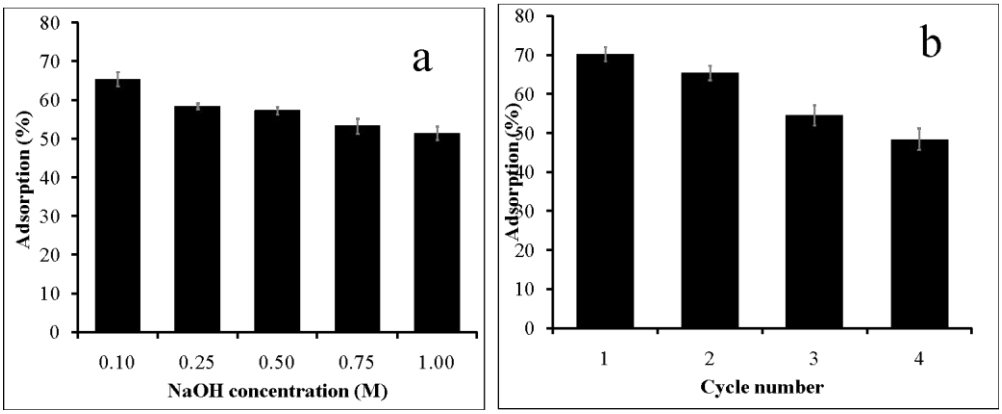

Figure 2 Adsorption of MO by calix[4]arene-modified PbS (a) under various NaOH concentrations, and (b) reusability tests.

Conclusion

This work investigated the adsorption of methyl orange (MO) by a nano-adsorbent, namely calix[4]arene-modified PbS. The optimised values for adsorbent dosage, contact time, and pH were found to be 89.70 mg of calix[4]arene-modified PbS, a contact time of 129.76, and pH 4.

Acknowledgement

The authors acknowledge the Ministry of Higher Education (Fundamental Research Grant Scheme, 5540049) and Universiti Putra Malaysia (Grant number GP-9647600) for their financial support.

References

[1] Bafana, A., Devi, S. S., & Chakrabarti, T., 2011. Azo dyes: past, present and the future. *Environmental Reviews*. 19, 350-371.

[2] Zheng, Y., Zhu, B., Chen, H., You, W., Jiang, C., & Yu, J., 2017. Hierarchical flower-like nickel (II) oxide microspheres with high adsorption capacity of Congo red in water. *Journal of colloid and interface science*. 504, 688-696.

BEHAVIOUR OF IMAZAPIC AND IMAZAPYR IN PADDY SOIL (BERIAH SOIL)

K. Mardiana-Jansar[1*], F.S.M. Bajrai[1], I. Sahid[1]

[1]Centre for Earth Sciences and Environment, Faculty of Science and Technology, Universiti Kebangsaan Malaysia, 43600 UKM Bangi, Selangor Darul Ehsan, Malaysia.

*Corresponding author: mardiana@ukm.edu.my

Abstract
Imazapic and imazapyr are herbicides that are recently widely used for weedy rice control in imidazolinone-tolerant paddy. Lacking information is available in Malaysia, concerning the fate of imazapic and imazapyr in the environment. A comprehensive study was therefore conducted to determine the adsorption, desorption, and persistence of imazapic and imazapyr in a paddy soil (Beriah soil). The adsorption and desorption of imazapic and imazapyr in the Beriah soil was studied using the batch equilibrium method. A field study was conducted to evaluate the persistence of imazapic and imazapyr, where 150 g ai ha^{-1} of these herbicides were applied to a one-hectare paddy field in Sungai Rambai, Melaka. Experimental data of the adsorption and desorption fitted well in the Freundlich adsorption isotherm. The values of K_F and K_{ads}, which is the Freundlich sorption coefficient, ranged from 1.44 to 11.45. The experimental values of $\frac{1}{n}$ fall into the range of 0 and 1; these results suggested that the initial concentrations clearly influenced the effect of imazapic and imazapyr adsorption in the soil. Slightly higher values of $\frac{1}{n}$observed in the desorption process, which indicated that these two compounds might have potential to be desorbed from the soil. The half-life of imazapic and imazapyr ($t_{\frac{1}{2}}$) deduced from the field experiments on 24.76 and 25.21 days for imazapic and imazapyr, respectively. The results showed low probability of herbicide contamination in the paddy ecosystem of Malaysia.

Keywords: Adsorption–Desorption, Persistent, Imidazolinone, Imazapic, Imazapyr

Introduction
Pesticides that are used in agriculture can enter aquatic ecosystems through agricultural water runoff from the site or through wet deposition of atmospheric leaching (Maurya & Malik 2016). The study of adsorption–desorption of pesticides in the laboratory are frequently conducted to predict pesticides mobility and determine the fate of pesticides in the soil (Bajeer et al. 2012; Katagi 2013). The adsorption of pesticides can affect the transport process, decomposition, volatilization, leaching, and bioaccumulation of pesticides and subsequently have an effect on the ultimate fate of pesticides in the soil solution (Gao et al. 2012). Soil pH may affect the adsorption process by ionizing the organic molecules and may affect the binding of the pesticides on the charged surface (Arce et al. 2011). The adsorption constant is defined as the ratio of the concentration of the pesticide adsorbed on the soil particles in the liquid phase in the soil (Bolis 2013). Imidazolinone herbicide group (imazapic and imazapyr) have higher tendencies to be found in surface and ground waters, because of its polar and ionizable members (Gianelli et al. 2014). According to Yavari et al. (2016), imazapic and imazapyr herbicides have relatively low acid dissociation constant values and high water solubility which increase their potential leaching. According to Gianelli et al. (2014), the half-life of imazapyr was negatively associated with soil pH, iron, and aluminum content and was positively related to clay content; moreover, imazapyr sorption was described by the Freundlich isotherm. Therefore, the objective of the present study is to investigate the potential risks of imazapic

and imazapyr herbicide in the environment by assessing the adsorption, desorption, and persistence in paddy soil.

Methodology

Soil samples were collected from depth in the range of 0–15 cm, air-dried in a cool roam at 16 °C, and passed through a 2-mm sieve. The soil pH, particle size distribution, cation exchange capacity, organic carbon contents, exchangeable aluminum, and electric conductivity were analysed. Adsorption experiments were conducted following the standard batch equilibration method (OECD, 2000). Stock solutions of imazapic and imazapyr were diluted with 0.01 M CaCl2 and acted as the working solutions for the experiment. The experiment was conducted in triplicate, and the control included blank samples. The original pH of the soil was maintained. The concentrations of imazapic and imazapyr were analyzed using high-performance liquid chromatography (HPLC). Desorption experiments were performed on soils used in the adsorption experiments. After the supernatant samples were removed, 25 mL of fresh 0.01 M CaCl2 solution was added into the same centrifuge bottles and shook on a horizontal shaker at 150 rpm for 24 h. Suspensions were centrifuged at 3000 rpm for 10 min; 1.5 mL of the aliquot was filtered before analysis. Determination of imazapic and imazapyr residue was carried out using the method proposed by Moser et al. (2010). HPLC 1200 (Agilent Technologies) (VWD) was used to determine the chromatogram of the compounds. HPLC was fitted with an autosampler and a 100 µL loop. The column was C8, 2.1x150 mm id, 5 µm. The absorbance wavelength was at 250 nm. The mobile phase was (A) acetonitrile: (B) formic acid 0.1% (Milli-Q pure water) in the ratio of 20:80 at the isocratic mode.

Results and Discussion

Figures 1(a) and (b) and 2 show the initial concentrations of imazapic and imazapyr adsorbed by the soil at different time intervals, respectively. For both imazapic and imazapyr compounds, a precise total equilibrium time based on the experimental data was obtained at 24 hours for the three initial concentrations of 50, 100 and 250 µg/L and 48 hours for the 500 and 750 µg/L. A very rapid adsorption process of both imazapic and imazapyr compounds occurred at the first 4 hours, thus increasing the herbicide concentration in soils. After 4 hours, minimal changes could be detected in the herbicide concentration in solution as well as indicating a slower adsorption phase. In the meantime the herbicide concentration in soils continued to increase slowly between 4-7 hours, but the chemical and physical reaction related to the adsorption continued to occur. It can be seen that the amount of adsorption increased with increment in the initial concentration of imazapic and imazapyr. The adsorption kinetics revealed two clear phases, a very rapid adsorption phase at the initial stages (within 4 hours) followed by the slow adsorption phase.

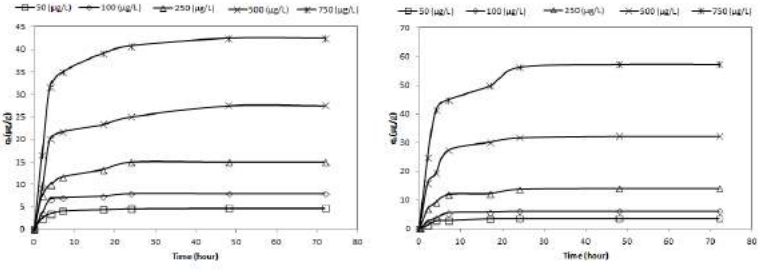

(a) (b)**Figure 1:** Effect of (a)imazapyr and (b)imazapyr adsorption in relation to concentration and time (W, 0.50 g, V, 0.50L; pH, 4.11; T, 28^{o}C)

The initial concentrations of imazapyr and imazapic desorbed from the Beriah soil at different time intervals are shown in Figures 2(a) and (b) respectively. A precise total equilibrium time based on the experimental data was obtained at 24 hours for the two initial concentrations of 50 and 100 µg/L and 48 hours for the 250, 500 and 750 µg/L. The results obtained indicated that the initial concentrations of imazapic and imazapyr desorbed from the Beriah soil decreased with increased time of shaking and became constant when it reached equilibrium.

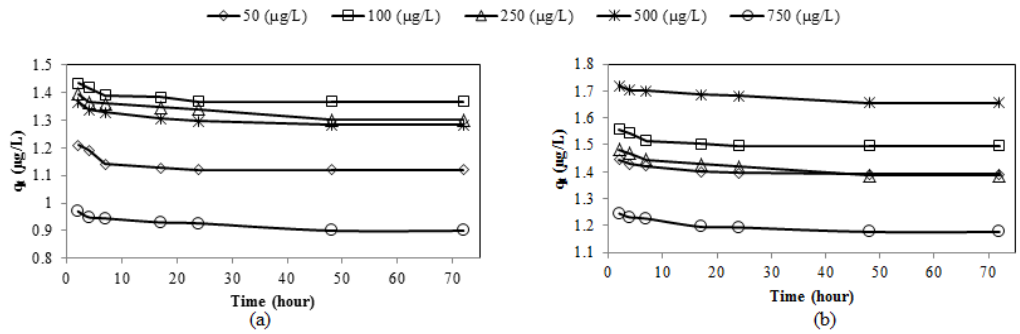

Figure 2: Effect of (a)imazapyr and (b)imazapic desorption in relation to concentration and time (W, 0.50 g, V, 0.50L; pH, 4.11; T, 28°C)

Conclusion

The higher desorption coefficient obtained for imazapyr may be attributed to its increased dissemination into the environment. Lower half-lives for both imazapic and imazapyr compared with those obtained in previous studies may be attributed to the tropical climate of Malaysia, characterized by higher soil microbial activity, as well as higher temperature and moisture levels. Further research is necessary for better understanding of the relationship between the adsorption, desorption, and persistence of imazapic and imazapyr in various soil types in Malaysia to obtain a more comprehensive picture of their behaviour under Malaysian environmental conditions.

Acknowledgement

This research was supported by research grants numbers ST 2015-011 from BASF (Malaysia) and GUP-2014-087 from Universiti Kebangsaan Malaysia.

References

[1] Bajeer, M. A., Nizamani, S. M., Sherazi, S. T. H. & Bhanger, M. I. 2012. Adsorption and Leaching Potential of Imidacloprid Pesticide through Alluvial Soil. *American Journal of analytical chemistry* 3(8): 604.

[2] Gao, J., Wang, Y., Gao, B., Wu, L., & Chen, H. (2012). *Environmental fate and transport of pesticides. Pesticides—evaluation of environmental pollution.* CRC Press Taylor and Francis Group, Boca Raton, 29-41.

[3] Gianelli, V. R., Bedmar, F. & Costa, J. L. (2014), Persistence and sorption of imazapyr in three Argentinean soils. *Environmental Toxicology and Chemistry* 33: 29–34.

[4] Katagi, T. 2013. Soil column leaching of pesticides. In *Reviews of Environmental Contamination and Toxicology* Volume 221, pp. 1-105. New York: Springer.

[5] Maurya, P.K. & Malik, D. 2016. Bioaccumulation of xenobiotics compound of pesticides in riverine system and its control technique: A critical review. *Journal of Industrial Pollution Control* 32(2): 580-594

[6] Moser, S. C. 2010. A fast and easy method for Imidazolinone residue analysis. 20th Annual Quality Assurance Conference Presentation, Dallas I, Texas. 19 October 2010.

[7] OECD. 2000. *OECD guidelines for the testing of chemicals. Adsorption/desorption using a batch equilibrium method OECD Test Guideline*. vol. 106. Paris: OECD Publications.

[8] S Yavari, A Malakahmad, NB Sapari 2016. Sorption-desorption mechanisms of imazapic and imazapyr herbicides on biochars produced from agricultural wastes. *Journal of Environmental Chemical Engineering* 4 (4), 3981-3989.

PREPARATION AND CHARACTERIZATION OF ACTIVATED CARBON NANOFIBER ADSORBENTS FROM ELECTROSPUN PAN/SAGO LIGNIN NANOFIBER FOR REMOVING Pb^{2+} IONS IN AQUEOUS SOLUTION

N.A. Nordin[1], N. Abdul Rahman[1,2]*, A.H. Abdullah[1,3]

[1]Department of Chemistry, Faculty of Science, Universiti Putra Malaysia, 43400 UPM Serdang, Selangor, Malaysia.
[2]Laboratory of Materials Processing and Technology, Institute of Advanced Technology, Universiti Putra Malaysia, 43400 UPM Serdang, Selangor, Malaysia
[3]Materials Synthesis and Characterization Laboratory, Institute of Advanced Technology, Universiti Putra Malaysia, 43400 UPM Serdang, Selangor, Malaysia.

*Corresponding author: a_norizah@upm.edu.my

Abstract
In this study, activated carbon nanofibers (A-CNFs) were fabricated from electrospun fibers comprising polyacrylonitrile (PAN) and sago lignin. Sago lignin was isolated from sago waste. The electrospun fibers were prepared using a simple electrospinning technique, followed by thermal treatment. The average diameter of nanofibers after stabilization and carbonization decreased to 371 ± 14 nm and 326 ± 26 nm, respectively. Surface modification with nitric acid was performed to create functional groups on the CNFs surface. Preliminary study showed that the percentage removal of Pb^{2+} by modified CNFs (A-CNFs) was three times higher than that of unmodified CNFs (CNFs). The adsorption data fitted the pseudo-second order kinetic model and Langmuir isotherm model with maximum adsorption capacity (q_m) of 588.24 mg/g. The experimental results indicate that the A-CNFs prepared from sago waste materials and PAN can be effectively used in removing Pb^{2+} ions in aqueous solution.

Keywords: Carbon nanofibers, sago lignin, polyacrylonitrile, electrospinning, adsorption

Introduction
Heavy metals are considered toxic to human and other biological systems, which have become an issue concerning the public health as they are non-biodegradable and persistent in nature (Jiang *et al.*, 2010). Heavy metals pollution has been a major concern in many developing countries nowadays because heavy metals cannot be destroyed or degraded. When these heavy metals exceed their acceptable level, they are harmful to human and other biological systems. Even at low concentrations, the presence of heavy metals including lead may cause diseases such as anemia, encephalopathy, hepatitis and nephritic syndrome (Zulkali *et al.*, 2006). In order to reduce human intake of heavy metals, chemical and physical treatment have been extensively studied. Water treatment by adsorption was found to be the most economical and practical treatment alternative (Ihsanullah *et al.*, 2015). Meanwhile, carbon nanofiber have been regarded as a compelling material as adsorbent owing to its chemical and thermal stability as well as large surface area (Li *et al.*, 2015). According to the study by Ishazaki (2009), 5 to 11 tons of wastes are produced every day from a single sago starch processing mill, which contain starchy lignocellulosic by-products. Sago palm is scientifically known as *Metroxylan sago*. It was originated from the species of palm in the *Metroxylan* genus. Generally, any material with carbon backbone can be used as precursors for carbon fibers. Lignin, which consists of many aromatic components, has the potential to be used as the precursor of carbon fibers production. Unlike catalytic synthesis, electrospinning method has many advantages such as simple setup, cheap, easy to control fiber diameter and less time consuming for nanofibers preparation. In this study, PAN was blended with sago lignin and electrospun

into fibers followed by stabilization and carbonization to produce CNFs. The CNF was then modified into activated CNFs (A-CNFs) after being exposed to concentrated nitric acid to enhance the ability of A-CNFs as adsorbent for removing Pb^{2+} ions in aqueous solution.

Methodology

PAN/sago lignin nanofiber was prepared by combining the solution of sago lignin and PAN in DMF. The mixture was then stirred until it became a homogenous solution. Electrospinning parameters were fixed at; the distance between the needle tip and the aluminum foil collector was 10 cm, 18 kV voltages and flow rate at 2 ml/h. After that, the electrospun nanofibers were stabilized to 250 ºC for 1 hour in air at a heating rate of 1 ºC/min. The sample was then carbonized in a tube furnace at 1,000 ºC for 1 hour under nitrogen gas with a heating rate of 10 ºC/min. A-CNFs was prepared according to Ihsanullah *et al.* (2015) with minor modifications. Activated PAN/sago lignin CNFs was denoted as A-CNFs while the unmodified PAN/sago lignin was denoted as CNFs only. The adsorption of Pb^{2+} ions by CNFs and A-CNF was studied using batch adsorption method. The experiments were conducted in 250 ml conical flask and magnetically stirred at 200 rpm under room temperature (25 ℃). After a specified time, the solution mixture was collected and analyzed for residual Pb^{2+} analysis using Inductively Coupled Plasma-Optical Emission Spectrometer (ICP-OES) (model: Perkin Elmer Optima 2100 DV).

Results and Discussion

Morphology study

Figure 1 (a)–(c) illustrates the SEM micrographs for PAN/sago lignin nanofibers after stabilization, carbonization (CNFs) and nitric acid modification (A-CNFs). The average fiber diameter of PAN/sago lignin nanofibers was reduced to 371 ± 5 nm after stabilization process and further reduced into 326 ± 5 nm after carbonization. The activation of CNF using concentrated nitric acid did not alter the fibers appearance; however, the average fiber diameter was slightly decreased to 323 ± 12 nm.

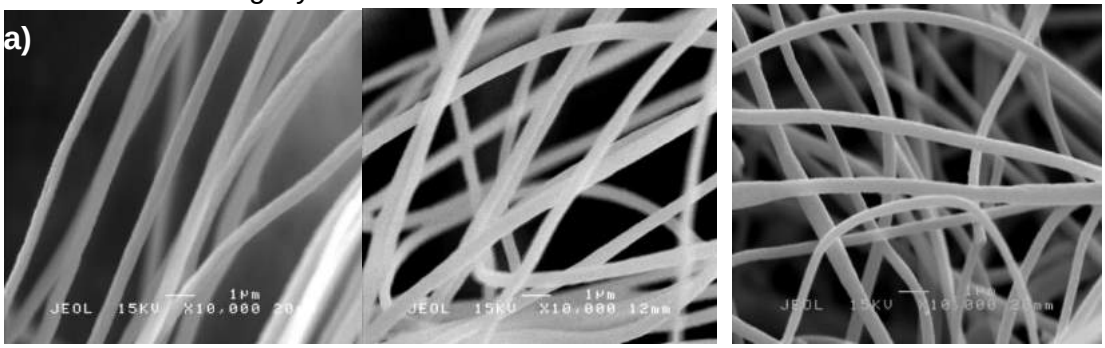

Figure 1: SEM micrographs of fiber diameter for PAN/sago lignin (a) stabilized nanofibers, (b) CNFs and (c) A-CNFs

Preliminary removal study by A-CNFs and CNFs

Figure 2 illustrates the graph of percentage removal of Pb^{2+} ions for A-CNFs and CNFs. The Pb^{2+} ions adsorption intensively occurred from 10 to 90 minutes for A-CNFs and became slower near the equilibrium. The maximum percentage removal of Pb^{2+} by A-CNFs was 63.22%. The Pb^{2+} ions adsorption by CNFs reached equilibrium faster than A-CNFs. However, the maximum percentage removal of CNFs was very low compared to A-CNFs with only 19.05% removal. A-CNFs has higher percentage of removal compared to CNFs as the A-CNFs is more hydrophilic, which improved its ability to adsorb Pb^{2+} ions in aqueous solution.

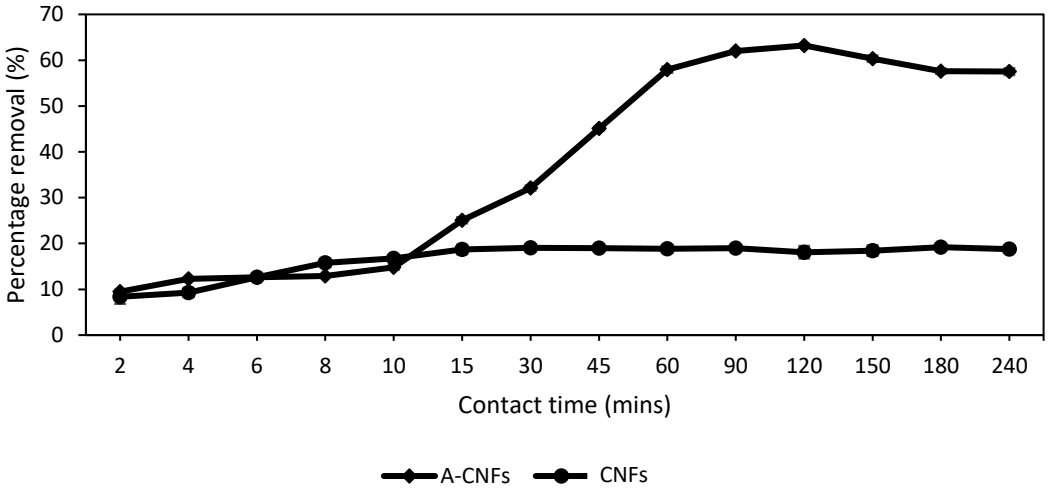

Figure 2: Percentage removal of Pb^{2+} ions for A-CNFs and CNFs. Condition: [Pb^{2+}] = 100 mg/L, dosage of adsorbent = 25 mg, pH = 5.

Kinetic study

Table 1 summarizes the calculated rate constant (k_1 and k_2) and value of R^2. By comparing the R^2, the adsorption of Pb^{2+} onto A-CNFs was fitted to pseudo-second order model. k_2 was seen initially increased because there were many available active sites A-CNF to accommodate Pb^{2+} ions. This resulted in a faster uptake rate of Pb^{2+} ions and led to the increase in rate constant. However, k_2 was decreased with further increase in initial Pb^{2+} concentration. The decrease in the k_2 was likely because most available active sites were already occupied when higher Pb^{2+} concentration was introduced, causing the uptake rate to become much slower. Based on this result, the adsorption by A-CNFs is best explained by pseudo-second order model, which can relate to chemisorption process that involves the electrons sharing between metal ions and surface of the adsorbent (Bouhamed *et al.*, 2012).

Table 1: Kinetics study of A-CNFs at different initial Pb^{2+} concentrations. Condition: contact time = 240 mins, dosage of adsorbent = 40 mg, pH = 5.

	Pseudo 1st order			**Pseudo 2nd order**		
***C_i* (mg/L)**	k_1 (min $^{-1}$)	q_e (mg/g)	R^2	k_2 (g/mg/min)	q_e (mg/g)	R^2
75	0.0258	427.3	0.8747	8.51×10^{-5}	476.19	0.9986
100	0.0178	375.67	0.9257	8.75×10^{-5}	500.00	0.9951
125	0.0256	475.61	0.9513	9.73×10^{-5}	555.56	0.9952
150	0.026	554.13	0.9502	7.30×10^{-5}	588.24	0.9811
175	0.0197	506.44	0.9425	7.10×10^{-5}	588.24	0.98

Adsorption isotherm study

Referring to Table 2, by comparing the R^2 value from both isotherms, the adsorption of Pb^{2+} ions on A-CNFs was more fitted to Langmuir adsorption isotherm with q_m = 588.24

mg/g and b_L value of 0.2537 L/mg. In Langmuir model, it was assumed that all the adsorption sites were active with energetically homogenous surface and a monolayer surface coverage formed without any interaction between adsorbate molecules (Araújo *et al.*, 2018).

Table 3: Adsorption isotherms study of A-CNFs. Condition: contact time = 240 mins, dosage of adsorbent = 40 mg, initial $[Pb^{2+}]$ = 125 mg/L, pH = 5.

	Langmuir isotherm			**Freundlich isotherm**		
Modified CNFs	q_{max} (mg/g)	b_L (L/mg)	R^2	K_F (mg/g)	$\frac{1}{n}$	R^2
	588.24	0.2537	0.999	339.94	0.1132	0.9902

Conclusion

In this study, lignin from sago waste has been successfully blended with PAN and used for fabrication of CNFs. PAN/sago lignin carbon nanofibers have been prepared via a simple and versatile technique, which was electrospinning followed by stabilization and carbonization steps. The resulting CNFs have been successfully activated using nitric acid into hydrophilic adsorbent to enhance their effectiveness in removing Pb^{2+} ions in aqueous solution. Preliminary study showed that the percentage removal of Pb^{2+} by modified CNFs (A-CNFs) was three times higher than that of unmodified CNFs. It has been determined that pseudo-second order kinetic model was well-fitted with the experimental data, which suggested that the adsorption process was dominated by chemisorption. The adsorption behavior was best described by Langmuir isotherm model in which the q_{max} was 588.24 mg/g. The experimental results indicated that the A-CNFs PAN/sago lignin can be effectively used for removing heavy metals in aqueous solution.

Acknowledgement

Authors would like to acknowledge Universiti Putra Malaysia for financial support through Research University Grant (Grant code: GP-IPS/2018/9594900). Authors would also acknowledge Graduate Research Fund (GRF) for Nurul Aida Nordin from Universiti Putra Malaysia.

References

[1] Araújo, C. S. T., Almeida, I. L. S., Rezende, H. C., Marcionilio, S. M. L. O., Léon, J. J. L. and De Matos, T. N. (2018) Elucidation of mechanism involved in adsorption of Pb(II) onto lobeira fruit (Solanum lycocarpum) using Langmuir, Freundlich and Temkin isotherms. *Microchemical Journal.* 137**.** 348-354.

[2] Bouhamed, F., Elouear, Z. and Bouzid, J. (2012) Adsorptive removal of copper(II) from aqueous solutions on activated carbon prepared from Tunisian date stones: Equilibrium, kinetics and thermodynamics. *Journal of the Taiwan Institute of Chemical Engineers.* 43**.** 741-749.

[3] Ihsanullah, Al-Khaldi, F. A., Abusharkh, B., Khaled, M., Atieh, M. A., Nasser, M. S., Laoui, T., Saleh, T. A., Agarwal, S., Tyagi, I. and Gupta, V. K. (2015) Adsorptive removal of cadmium(II) ions from liquid phase using acid modified carbon-based adsorbents. *Journal of Molecular Liquids.* 204**.** 255-263.

[4] Ishazaki, A. (2009) Sago, an attractive renewable resource which saves human's crisis of environment and energy. 3.

[5] Jiang, M.-Q., Jin, X.-Y., Lu, X.-Q. and Chen, Z.-L. (2010) Adsorption of Pb(II), Cd(II), Ni(II) and Cu(II) onto natural kaolinite clay. *Desalination.* 252**.** 33-39.
[6] Li, X., Chen, S., Fan, X., Quan, X., Tan, F., Zhang, Y. and Gao, J. (2015) Adsorption of ciprofloxacin, bisphenol and 2-chlorophenol on electrospun carbon nanofibers: In comparison with powder activated carbon. *Journal of Colloid and Interface Science.* 447**.** 120-127.
[7] Zulkali, M. M. D., Ahmad, A. L. and Norulakmal, N. H. (2006) Oryza sativa L. husk as heavy metal adsorbent: Optimization with lead as model solution. *Bioresource Technology.* 97**.** 21-25.

A NOVEL BIPHENYLDICARBOXYLIC ACID CAPPED Co-MOF FABRICATED ELECTRODE FOR SENSITIVE DETERMINATION OF RUTIN

Thushatharcchini Sivam[1], Hong Ngee Lim[1,2]*, N.S.K. Gowthaman[1]

[1]Materials Synthesis and Characterization Laboratory, Institute of Advanced Technology, Universiti Putra Malaysia, 43400 UPM Serdang, Selangor, Malaysia
[2]Department of Chemistry, Faculty of Science, Universiti Putra Malaysia, 43400 UPM Serdang, Selangor, Malaysia.

*Corresponding author: hongngee@upm.edu.my

Abstract
Rutin (RT) also known as vitamin P, is an electroactive important flavanoid in both pharmacological and cosmetic field. It is generally applied as a clinical therapeutic drug due to its functions like anti-bacterial, anti-tumor, anti-inflammatory, as well as lowering blood pressure. Therefore, it is meaningful to develop a fast, simple and reliable method to detect RT. This paper describes the synthesis of 4,4'-biphenyldicarboxylic acid capped Co-MOF (Co-BPDC MOF) and its fabrication on the electrode for the sensitive determination of RT. Initially, the Co-BPDC MOF is synthesised by solvothermal method. The XRD patterns of the synthesized Co-BPDC MOF exhibits the diffraction peaks similar to the simulated Co-BPDC MOF. The SEM images revealed that the Co-BPDC MOF possess needle-like morphology. The Co-BPDC MOF fabricated electrode is utilized for the determination of RT and it exhibits excellent electrocatalytic activity than the bare GC electrode. The sensitivity of the present sensor towards RT is found to be 573 $\mu A\ \mu M^{-1}\ cm^{-2}$. The practicability of the fabricated electrochemical sensor is testified by exploiting the sensor for the determination of RT in blood serum samples.

Keywords: Metal-organic Framework; Co-BPDC MOF; Rutin; Electrochemical Sensor.

Introduction
Rutin (RT) is one of the most commonly found flavonol glycosides that identified as vitamin P [1]. RT is generally applied as a clinical therapeutic drug due to its physiological functions including anti-bacterial, anti-tumor, anti-inflammatory, as well as lowering blood pressure. Therefore, it is meaningful to develop a fast, simple and reliable method to detect RT. The traditional methods to detect RT for instant spectrophotometry and HPLC are time-consuming analytical method and face problems like poor sensitivity [2]. Since all flavanols are electroactive compounds [3], [4], electrochemical sensing is promising for the detection of RT. In this work, a scaffold MOF was constructed using transition metal and organic ligand to function as a biosensor that can detect the presence of RT. MOF is employed as an electrode material owing to its porosity, tunability and structural diversity. The union of Co^{2+} with 4,4-biphenyldicarboxylic acid (BPDC) forge a needle-like electrocatalyst, Co-BPDC MOF. To the best of our knowledge, this is a novel report for the direct application of MOF on electrochemical sensing of RT. In this work, Co-BPDC MOF was synthesized and fabricated and a fast and highly sensitive detection of RT was achieved.

Methodology
The Co-BPDC MOF is synthesized as follows: 0.08 M of $Co(NO_3)_2$ and BPDC is dissolved in N,N-dimethyl formamide then the solution is transferred to Teflon lined container and the container is placed in autoclave reactor for 12 hours at 120° C. The formed purple colour crystalline precipitate was activated by solvent exchange process. Finally, the activated MOF is dried and denoted as Co-BPDC MOF. For fabrication, a homogenous

suspension of Co-BPDC MOF in DI water and PVDF for 30 min in a bath sonicator. Then, the well-dispersed homogenous suspension is dropped on the well-cleaned cleaned glassy carbon (GC) electrode and dried at room temperature. The as-fabricated electrode is utilized for the determination of RT.

Results and Discussion

Figure 1 (A) shows the XRD pattern of the activated Co-BPDC MOF, synthesized in this work compared with the simulated Co-BPDC MOF. The Co-BPDC MOF has a sharp main peak below 10° as the simulated Co-BPDC MOF. Furthermore, the comparison shows the synthesized Co-BPDC MOF has similar main peaks as the simulated Co-BPDC MOF. Besides, Figure 1 (B) displays the SEM images for the synthesized Co-BPDC MOF. The SEM image shows that the activated Co-BPDC MOF has needle-like morphology that arranged like a flower.

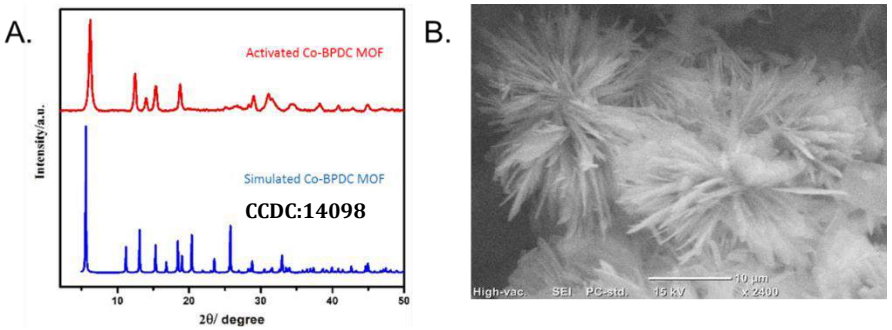

Figure 1. (A) XRD pattern and **(B)** SEM image of synthesised Co-BPDC MOF

The cyclic voltammetry response of 0.1 M phosphate buffer solution (pH 8.0) is shown in Figure 2. As can be seen, Co-BPDC MOF modified GCE detect the RT by showing an extra oxidation peak at E_{pa} = 0.25. The further addition of RT has increased the current of oxidation peak, which sums up that the particular peak is the oxidation peak of RT. Hence, the Co-BPDC MOF modified is sensitive towards detection of RT.

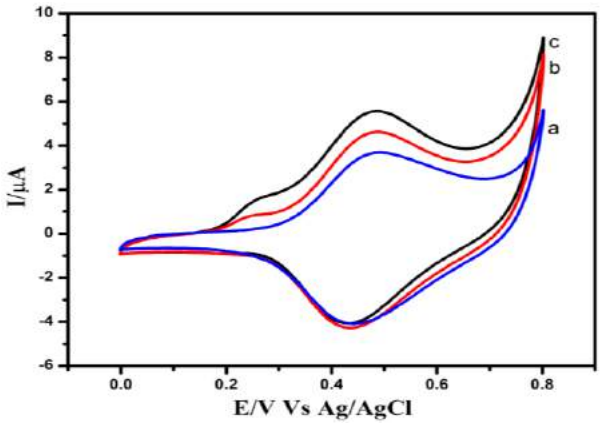

Figure 2: CV response of Co-BPDC MOF modified electrode in the (a) absence and (b) and (c) presence of (b) 0.25mM and (c) 0.5mM of RT in pH 8.

Conclusion

The synthesis of Co-BPDC and its fabrication on the electrode surface are achieved. The detection of RT using Co-BPDC MOF modified electrode is a very first attempt in the electrochemical sensing field. The sensitivity of the present sensor towards RT is found to

be 573 µA μM^{-1} cm^{-2}. The practicability is analysed in blood serum samples. This work is a new beginning for MOF on electrochemical sensing of RT.

Acknowledgement
This research was supported by FRGS MRSA (UPM/700-2/1/FRGS/MRSA/5524986) from the Ministry of Education of Malaysia.

References

1. Liu, M., Deng, J., Chen, Q., Huang, Y., Wang, L., Zhao, Y., ... & Yao, S. (2013). Biosens. Bioelectron., 41, 275-281.
2. He, Q., Wu, Y., Tian, Y., Li, G., Liu, J., Deng, P., & Chen, D. (2019). Nanomater., 9(1), 115.
3. Xing, R., Yang, H., Li, S., Yang, J., Zhao, X., Wang, Q., ... & Liu, X. (2017). J. Sold State Electrochem., 21(5), 1219-1228
4. Macikova, P., Halouzka, V., Hrbac, J., Bartak, P., & Skopalova, J. (2012). Scientific World J., 2012.

REMOVAL OF Cu(II) IONS FROM AQUEOUS SOLUTION BY CROSSLINKED CARBOXYMETHYL SAGO STARCH

N. Zainuddin*, A. A. Keirudin, N.A. Yusof

Department of Chemistry, Faculty of Science, Universiti Putra Malaysia, 43400 UPM Serdang, Selangor Darul Ehsan, Malaysia.

*Corresponding author: norhazlin@upm.edu.my

Abstract
In this study, removal of Cu(II) ion from aqueous solution using carboxymethyl sago starch/citric acid (CMSS/CA) hydrogel was investigated. CMSS/CA hydrogel composed of high porosity structure with hydrophilic character to adsorb metal ion into the polymeric network. The removal of Cu(II) ions was analysed by Inductively coupled plasma-optical emission spectrometry (ICP-OES). The effects of pH, contact time, initial concentration Cu(II) ions and temperature on the removal of Cu (II) ions were studied. From the results obtained, the removal of Cu(II) ions at pH 4 showed the optimum removal percentage with 69.02%. The influence of contact time revealed that removal percentage of Cu(II) ions considered optimum after 30 minutes with percentage of 71.04%. The highest removal percentage of Cu(II) ion was achieved as 20 ppm of initial Cu(II) ion concentration was used. However, the effect of elevating the temperature from 27°C to 55°C showed insignificant increase in removal percentage of Cu(II) ions.

Keywords: carboxymethyl, sago starch, hydrogel, removal, heavy metal

Introduction
Copper is one of the main causes to heavy metal pollution which comes from various industrial sewage. Excessive copper exposure could potentially harm to human health and environment. Several conventional methods were implemented to reduce the concentration of copper released by industrial, but these were not efficient and highly cost (Barakat, 2011; Singha and Guleria,2014). Thus, sorption process by bio-sorbent like hydrogel could enhance the binding of Cu(II) ion pollutant into the highly porosity of hydrogel (Zdanowicz et al.,2014). Carboxymethyl sago starch/citric acid (CMSS/CA) hydrogel is a polysaccharide-based hydrogel which been used as metal sorbent. The hydrogel was an excellent alternative material to remove Cu(II) ions from aqueous solution with good binding site of carboxylate towards metal cation (Aflaki Jalali et al., 2016). This study focused on removing Cu(II) ion from aqueous solution in different pH, contact time, initial concentration and temperature. The objective of the study was to optimize the removal of Cu(II) ions by CMSS/CA hydrogel from aqueous solution.

Methodology
The removal of Cu(II) ions was done by placing 0.05 g CMSS/CA hydrogel in a centrifuge tube containing 25 mL Cu(II) ion solution with a desired initial concentration and pH. The tube was agitated in water bath shaker at constant rate in room temperature for a certain period of time. The process would allow the formation of CMSS/CA-Cu complex. The filtrate was filtered to separate from the hydrogel-Cu complex and analysed by inductively coupled plasma-optical emission spectrometry (ICP-OES). The removal percentage of Cu(II) ions was calculated according to Wu et al. (2017):

$$\% \, Removal = \frac{C_o - C_e}{C_e} \times 100$$

C_o (mg/L) is the initial concentration and C_e is the final or equilibrium concentration of metal ion.

Results and Discussion

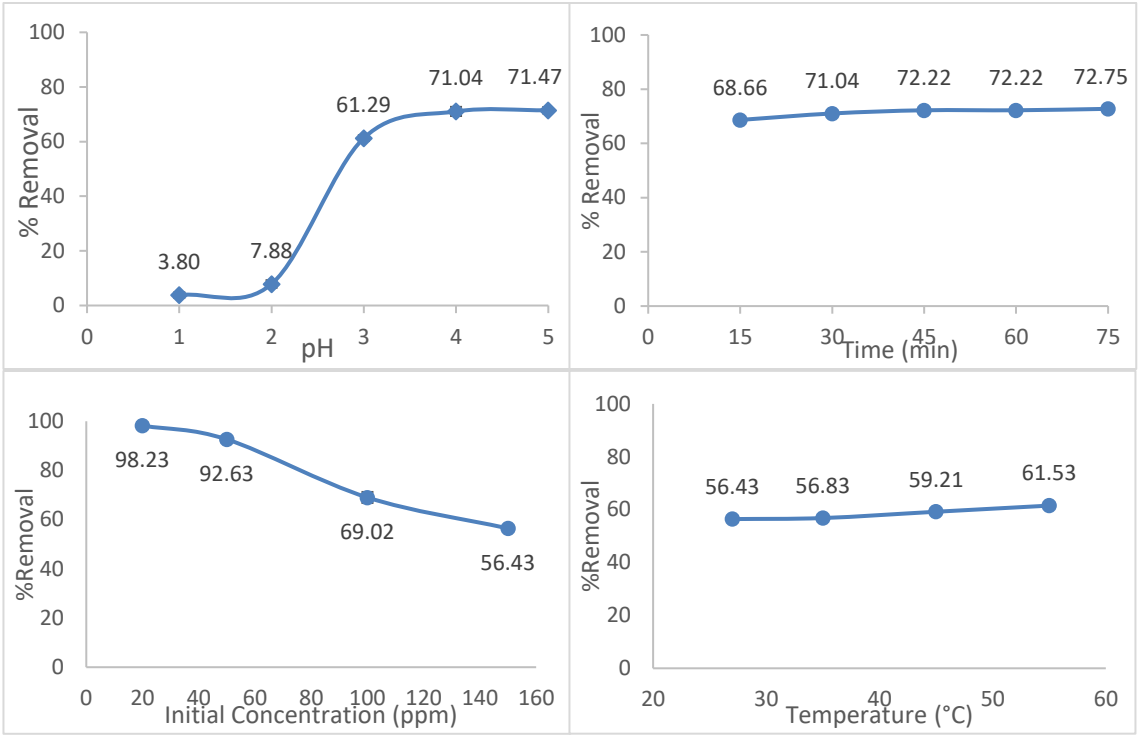

From the study, the removal of Cu(II) ions increased as the pH of Cu(II) ion solution increased from 1 to 5. At low acidity, the presence of high carboxylate ions due to deprotonation, enhance the binding with Cu(II) ions. The effect of contact time showed a steady increase in removal percentage of Cu(II) ions when the contact prolonged from 15 to 75 minutes. The increasing of initial Cu(II) ion concentration from 20 to 150 ppm resulted in the decrease of removal percentage of Cu (II) ions. This can be ascribed that Cu(II) ions become excess and unable to bind with binding sites in CMSS/CA hydrogel. By increasing the temperature up to 55°C, the removal percentage of Cu(II) ions only increased about 9.04%.

Conclusion

The CMSS/CA hydrogel showed an excellent result as metal sorbent especially in removing Cu(II) ions with highest percentage removal about 98.23%. The CMSS/CA has potential to be applied in industrial scale for sewage treatment as it provides benefit in operational cost as well as environmentally friendly. For industrial sewage, the pH of wastewater need to be adjusted to maximize the sorption of Cu(II) ions. For future work, it is recommended to study the capability of CMSS/CA hydrogel to be reused for secondary removal of Cu(II) ions.

Acknowledgement

The authors gratefully acknowledge the assistance of technical staff from Chemistry Department, Universiti Putra Malaysia. Financial support from the Graduate Research Fellowship, UPM for the sponsorship was gratefully acknowledge.

References

Aflaki Jalali, M., Dadvand Koohi, A., & Sheykhan, M. (2016). Experimental study of the removal of copper ions using hydrogels of xanthan, 2-acrylamido-2-methyl-1-propane sulfonic acid, montmorillonite: Kinetic and equilibrium study. *Carbohydrate Polymers*, *142*, 124–132.

Basri, S. N., Zainuddin, N., Hashim, K., & Yusof, N. A. (2016). Preparation and characterization of irradiated carboxymethyl sago starch-acid hydrogel and its application as metal scavenger in aqueous solution. *Carbohydrate Polymers*, *138*, 34–40.

Barakat, M. A. (2011). New trends in removing heavy metals from industrial wastewater. *Arabian Journal of Chemistry*, *4*(4), 361–377.

Singha, A. S., & Guleria, A. (2014). Chemical modification of cellulosic biopolymer and its use in removal of heavy metal ions from wastewater. *International Journal of Biological Macromolecules*, *67*, 409–417.

Wu, S. P., Dai, X. Z., Kan, J. R., Shilong, F. Di, & Zhu, M. Y. (2017). Fabrication of carboxymethyl chitosan–hemicellulose resin for adsorptive removal of heavy metals from wastewater. *Chinese Chemical Letters*, *28*(3), 625–632.

Zdanowicz, M., Spychaj, T., & Lendzion-Bieluń, Z. (2014). Crosslinked carboxymethyl starch: One step synthesis and sorption characteristics. *International Journal of Biological Macromolecules*, *71*, 87–93.

AN ALTERNATIVE WAY OF REDUCING HIGH FREE FATTY ACID (FFA) CONTENT IN CRUDE PALM OIL (CPO) USING FERUM (II) OXIDE/BIOCHAR AS AN ABSORBENT

Nor Shafizah Ishak[1], Irmawati Ramli[1*], Hishamuddin Omar[2], Muhammad Yahaya[1], Nurfaridatulakma Sulaiman[1]

[1]Department of Chemistry, Faculty of Science, Universiti Putra Malaysia, 43400 UPM Serdang, Selangor Darul Ehsan, Malaysia
[2]Department of Biology, Faculty of Science, Universiti Putra Malaysia, 43400 UPM Serdang, Selangor Darul Ehsan, Malaysia

*Corresponding author: irmawati@upm.edu.my

Abstract
In this study, a porous ferum(II) oxide doped on commercially available biochar derived from palm kernel shell was used as an absorbent to treat the free fatty acid (FFA) content in the crude palm oil (CPO) to achieve an acceptable standard quality of < 5 %. This work should be seen as a great potential for the palm oil industry. The concept is rather simple and yet cost-effective as it can be operated in a mild condition and the absorbent can be recycled and regenerated. It should not do any damage to minor compounds in CPO. The characteristic of the absorbent was evaluated and the efficiency of the absorbent in the absorption activity was examined.

Keywords: Free fatty acid, crude palm oil, absorbent

Introduction
The high FFA content in CPO becomes a nightmare to all palm oil millers. The accepted quality of CPO as set by the Palm Oil Refiners Association of Malaysia (PORAM) should contain a maximum of 5% FFA (Tan et al., 2009). The FFA content is the controlling key factor for pricing different varieties of oils and fats as the CPO determined by its FFA level. Naturally, FFA exists in CPO, however, its quantity might increase by the action of enzymes in the palm fruit and by microbial lipases. Furthermore, during storage, more FFA might be produced by the reaction of the oil with water. These phenomena would contribute to a high content of FFA in CPO which resulted in a fermented like smell hence reduced the quality of oil (Hayyan et al., 2011). The palm oil millers have to ensure the FFAs level below the offset limit which below 5 % FFAs before the CPO is transferred to the palm oil refinery. Various methods have been used for example chemical esterification in which simple alcohol is used to be esterified with the acid over acidic catalyst, molecular distillation process, and using absorbent such as rice husk and magnesium silicate. In this work ferum(II) oxide supported on biochar is proposed as absorbent for FFA reduction in CPO.

Methodology
The adsorbent was synthesised by using wetness impregnation method. It was then analysed by powder X-ray diffraction (XRD) in a scanning range $2\theta = 10^{o} – 80^{o}$. Other physical properties were obtained by Brunauer-Emmett-Teller (BET) analysis and Barrett-Joyner-Halenda (BJH). The surface morphology was by scanning electron microscopy and acidic properties was by temperature programmed desorption of ammonia (TPD-NH_3) analysis. The adsorption performance and optimization was done on a 50 ml of CPO preheated in a flask at 80 ^{o}C. The percentage of FFA reduction was measured by equation

(1). Where, the acid value was determined based on AOCS method Cd, 3d-63 (Khan et al., 2010).

$$\%FFA\ reduction = \frac{Acid\ value_{raw} - Acid\ value_{sample}}{Acid\ value_{raw}} x\ 100\ \% \quad (1)$$

Results and Discussion

XRD analysis revealed major crystalline phases of Fe_2O_3 increases as loading onto biochar was increased. The surface area decreases while the pore size increases as the Fe_2O_3 loading was increased as follows, 15 wt% > 10 wt% > 5 wt%. The pore volume is in the range of 15.4 to 19 cm^3/g. The highest amount of acid sites is given by 10wt% Fe_2O_3/biochar. While SEM images show an irregular biochar pore surface structures with Fe_2O_3 cubic structure can be observed on the biochar surface. When these samples were used for FFA reduction in a 1 L of CPO in slurry condition at 80 °C, high FFA reduction was observed as shown in Table 1. The FFA reduction of CPO was carried out at 4 different parameters which are catalyst concentration, catalyst amount, time and stirring rate.

Table 1: Design of experiment for the FFA reduction performance test.

Trial No.	Time (h)	Stirring rate (rpm)	Absorbent concentration (wt%)	Absorbent amount (wt%)	FFA conversion (%)
1.	2	500	10	1	51.54
2.	3	450	15	1	10.80
3.	1	400	5	1	53.68
4.	2	400	15	2	17.50
5.	3	500	5	2	1.77
6.	3	400	10	3	55.45
7.	1	450	10	2	1.50
8.	1	500	15	3	52.44
9.	2	450	5	3	15.40

The highest FFA reduction for 5 wt%, 10 wt% and 15 wt% absorbent is 53.68 %, 55.45 %, and 52.44 %, respectively. The absorption performance of all samples is similar which reckons the different Fe_2O_3 loadings on biochar played a small role in the FFA absorption.

Conclusion

Three loadings of Fe_2O_3 (5, 10, 15 wt%) on biochar gave similar characteristics in terms of surface area, pore size, pore diameter, and acidic active sites. The samples were able to obtain high FFA reduction in the range of 52.44 to 55.45 % at the right operating conditions and achieve the acceptance FFA level which was 5 % at a constant temperature (80 ^oC) to maintain the characteristics and quality of the CPO throughout the absorption process.

References

1. Tan, C. H., Ghazali, H. M., Kuntom, A., Tan, C. P., and Ariffin, A. A. (2009). Extraction and physicochemical properties of low free fatty acid crude palm oil. *Food Chem.* 113, 645–650.
2. Hayyan, A., Mjalli, F. S., Hashim, M. A., Hayyan, M., AlNashef, I. M., Al-Zahrani, S. M., et al. (2011). Ethanesulfonic acid-based esterification of industrial acidic crude palm oil for biodiesel production. *Bioresour. Technol.* 102, 9564–9570.
3. Khan, M. A., Yusup, S., and Ahmad, M. M. (2010). Acid esterification of a high free fatty acid crude palm oil and crude rubber seed oil blend: Optimization and parametric analysis. *Biomass and Bioenergy* 34, 1751–1756.

NANOSIZED ZnO-MONTMORILLONITE CLAY COMPOSITES FOR THE ENHANCED PHOTOCATALYTIC DEGRADATION OF RHODAMINE B

P. Pannak[1], W. Foytong[1], W. Sirisaksoontorn[2], A. Songsasen[2]*

[1]Department of Chemistry, Faculty of Science, Kasetsart University, Bangkok 10900, Thailand
[2] Department of Chemistry and center of Excellence for Innovation in Chemistry (PERCH-CIC), Faculty of Science, Kasetsart University, Chatuchak, Bangkok 10900, Thailand

*Corresponding author: fsciass@ku.ac.th

Abstract
Nanosized ZnO-montmorillonite (ZnO-MMT) composites were successfully prepared by ion exchange, followed by thermal treatment. It was found that the structure of the composite was arranged in the house-of-card structure with the homogeneous distribution of nanosized ZnO in the MMT clay sheets. Importantly, ZnO-MMT showed the small domains of crystalline ZnO with less particle aggregation. The particle size of ZnO was in the range of 1.8-3.0 nm. In addition, XAS results also suggested the existence of the short-range structural order of wurtzite ZnO. For the photocatalytic study, ZnO-MMT composite exhibited the superior photocatalytic activity for Rhodamine B (RhB) degradation with the normalized quantity (NQ) of 8.4 $mmol \cdot g^{-1}$ compared with a physical mixture of ZnO and montmorillonite (ZnO@MMT) and commercial ZnO. This photocatalytic enhancement was attributed to the strong synergistic interaction of nanosized ZnO and MMT clay sheets.

Keywords: Montmorillonite, Nanosized ZnO, Photocatalyst, Rhodamine B

Introduction
Na-montmorillonite (Na-MMT), a 2D layered silicate, can be categorized as a member of the smectite group. Owing to the presence of loosely bound and exchangeable cation in the layers, MMT clay is suitable for being used as a supporter and adsorbent for the removal of heavy metals or toxic organic dyes. However, only adsorption on the clay surface is not the most efficient approach to eradicate those toxic species. Thus, incorporation of ZnO photocatalyst into the MMT structure has come into play as a competent approach to enable the advanced oxidation process via the photoactivation inside the MMT sheets. This process relies on the production of hydroxyl radicals that initiate the decomposition of organic toxic compounds, especially organic dyes. In this work, we reported the synthesis of ZnO-MMT composites via the ion exchange reaction and heat treatment. The nanosized-ZnO in MMT was mainly characterized by XAS and TEM. Moreover, the photocatalytic study of nanosized ZnO-MMT composites was evaluated in comparison with commercial ZnO and physically mixed ZnO@MMT.

Methodology
In brief, 300 mg of pristine Na-MMT was dispersed in 30 mL of DI water with vigorous stirring for 24 h. 18.9 mg of $ZnCl_2$ (1 CEC) in 2 mL of DI water was added to the MMT suspension and the mixture was stirred for 24 h. The solid product was washed with a copious amount of DI water and dried at 60^{o}C. Then, the product was calcined at 500^{o}C for 2 h to obtain ZnO-MMT(1CEC) composite. In addition, ZnO-MMT composites prepared from different amounts of $ZnCl_2$ were also studied by varying the CEC value by factors of 5 and 10. The resulting products were denoted as ZnO-MMT(5CEC) and ZnO-MMT(10CEC). All composites were physically characterized by numerous techniques. For the photocatalytic study, 10 mg of photocatalyst was initially mixed with 100 mL of 10 ppm RhB solution. The mixture was stirred in the dark condition for 60 min. Then, the 10-W UV-

C light source was irradiated to the stirred solution. RhB solution was collected in every 30 min for 5 h. The photocatalytic activity was monitored by measuring the concentration change of RhB at the maximum wavelength of 554 nm. The normalized quantity (NQ) was calculated as follows; NQ = $N_{degraded}/N_{catalyst}$, where $N_{degraded}$ is the amount of degraded dye molecules (mmol), and $N_{catalyst}$ is the amount of ZnO (g).

Results and Discussion

The XRD patterns clearly showed the phase transformation during the synthesis of nanosized ZnO-MMT from pristine Na-MMT via the ion exchange and thermal treatment. However, crystalline wurtzite ZnO was not observed by XRD, indicating the presence of small domain or short-range ordering of crystalline phase as confirmed by XAS. The average size of ZnO in MMT sheets was about 1.8-3.0 nm as determined from TEM. The specific surface area of ZnO-MMT(1CEC) was remarkedly increased to 92.7 m^2/g, indicating more accessible porous structure.

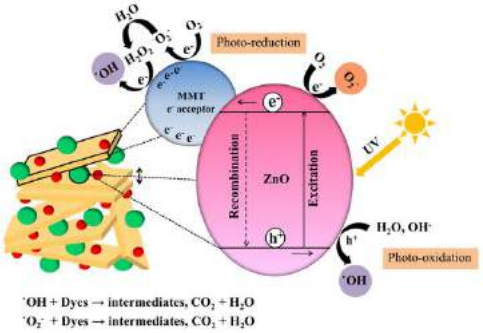

Figure 1 Proposed mechanism of ZnO-MMT for the photocatalytic study

For the photocatalytic study, nanosized ZnO-MMT composites exhibited the superior photocatalytic activity for RhB degradation under the UV light as shown in **Table 1.**

Table 1 Adsorption efficiency, photocatalytic activity and NQ of all samples

Samples	Adsorption efficiency (%)	Photocatalytic activity (%)	NQ ($mmol \cdot g^{-1}$)
ZnO-MMT(1CEC)	11.8	45.6	8.4
ZnO-MMT(5CEC)	29.9	48.3	6.9
ZnO-MMT(10CEC)	37.9	48.4	6.1
ZnO@MMT	71.3	29.4	1.8
0.1 mg ZnO	0.3	5.2	1.1

Conclusion

ZnO-MMT composites were successfully synthesized using ion exchange, followed by thermal treatment. Nanosized ZnO was grown in the MMT sheets. As proposed, ZnO-MMT adopted the house-of-card structure. Moreover, ZnO-MMT could provide the superior photocatalytic activity for RhB degradation compared to commercial ZnO and physically mixed ZnO@MMT.

Acknowledgement

This research is supported by the Department of Chemistry, Faculty of Science, Kasetsart University, and the Science Achievement Scholarship of Thailand (SAST). We gratefully

acknowledge the financial support from the Kasetsart University Research and Development Institute (KURDI) (Grant No. 33. 61).

References

Pannak, P., Songsasen, Foytong, W., Kidkhunthod, P., Sirisaksoontorn, W., 2018. Homogeneous distribution of nanosized ZnO in montmorillonite clay sheets for the photocatalytic enhancement in degradation of Rhodamine B, *Res. Chem. Intermed,* 44, 6861-6875.

CONSTRUCTION OF 3D POROUS NANOSTRUCTURED MATERIALS FROM 2D LAYERED MATERIALS

M.H. Wahid[1,2]*, N.A. Pohan[1], Z. Zainal[1,2], N.A. Ibrahim[1]

[1]Department of Chemistry, Faculty of Science, Universiti Putra Malaysia, 43400 UPM Serdang, Selangor, Malaysia.
[2]Materials Synthesis and Characterization Laboratory, Institute of Advanced Technology, Universiti Putra Malaysia, 43400 UPM Serdang, Selangor, Malaysia

*Corresponding author: mw_haniff@upm.edu.my

Abstract
3D porous graphene and boron nitride have been constructed from 2D graphene and boron nitride layers as the starting materials respectively. Both materials were oxidized using the modified Hummers' method followed by the formation of 3D nanostructures via the Pickering emulsion technique. Furthermore, by varying the preparation conditions such as sonication time, and concentration of crosslinker, nanostructures with tuneable pore characteristics were obtained.

Keywords: 2D monoatomic layered materials, 3D porous nanostructures

Introduction
Graphene and other 2D layered materials have gained considerable interest due to their unique properties namely large theoretical specific surface area, good optical properties, good mechanical properties and others which render this class of material useful for various applications. However, these layered materials tend to re-stack to each other due to the Van der Waals interaction which would then inhibit its large surface area characteristic. Thus, a mechanism has to be introduced in order to utilize the large surface area of this class of materials. A possible solution to this is by forming a stable 3D structure which would prevent from the re-stacking of the layers. At the same time, the formation of a 3D structure would also lead to development of void spaces within the isolated layers which may act as pores and by tuning the pore size, will further increase the potential applications of these materials. At present, potential applications of such materials features in drug delivery, energy storage, water treatment, gas capture and storage, catalysis and many more. Herein we adopt the formation of Pickering emulsion technique to first create the template for the porous structure. Preliminary results show that by varying the preparation conditions, different pore characteristics was obtained. The optimum preparation conditions to generate porous materials of different sizes will be identified and established.

Methodology
Graphite powder (<20 µm) and boron nitride powder (1 µm) was obtained from Sigma Aldrich. Sulphuric acid (95-98%), phosphoric acid (85%), potassium permanganate (99%), toluene (99%) and hydrogen peroxide (30 wt% in H_2O) were obtained from Chemiz (Malaysia). Hydrochloric acid (32 wt% in H_2O) was purchased from R&M Chemicals (Malaysia). All chemicals are of analytical grade and used as received without any further purification. Deionized (DI) water used for the washing was obtained from Milli-Q Plus system (Millipore). Graphene oxide and boron nitride oxide solution was prepared using the modified Hummers' method as reported by Ibrahim et al. The formation of 3D hollow structures was further configured using the method reported by Chen et al. with slight modifications.

Results and Discussion

FT-IR and Raman spectra of the samples are in good agreement with the reported results in the literature. SEM images of the graphene oxide sheets and the 3D hollow graphene are as shown in Figure 1. The 2D layered graphene oxide was successfully transformed into a three dimensional structure (Fig. 1a & b).

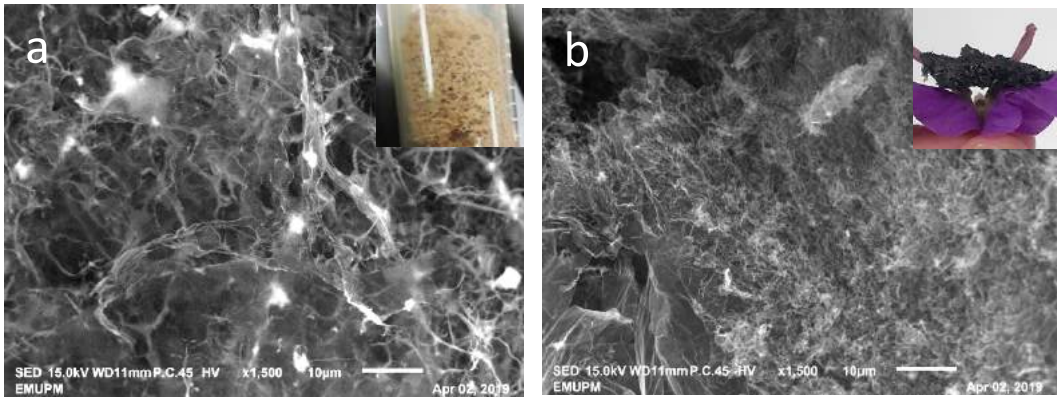

Figure 1. SEM images of porous graphene samples. (a) 3D porous graphene oxide with photograph of the sample in the inset and (b) 3D porous reduced graphene oxide with photo of the sample in the inset

Conclusion

Preparation of lightweight, 3D hollow nanostructures using the Pickering Emulsion approach was successful. The tunable pore characteristics and microscopic features of the prepared material offers high potential for wide range of applications.

Acknowledgement

We gratefully acknowledge support of this work by NanoMalaysia Bhd., Tex Cycle Sdn. Bhd. and Ministry of Education (FRGS/1/2018/STG01/UPM/02/11). (Text)

References

[1] Chen, X., Eggers, P. K., Slattery, A. D., Ogden, S. G., & Raston, C. L., 2014. Template-free assembly of three-dimensional networks of graphene hollow spheres at the water/toluene interface. *Journal of Colloid and Interface Science*, 430, 174–177.

[2] Gudarzi, M. M., & Sharif, F., 2011. Self-assembly of graphene oxide at the liquid-liquid interface: A new route to the fabrication of graphene based composites. *Soft Matter*, 7(7), 3432–3440.

[3] Ibrahim, N. A., Woei, C. B., Hussein M. Z. Patent Application No: PI 2014700668. Method of Producing a Dispersible Nano Graphene or Graphene Oxide

PROFILING THE LEAF METABOLOME OF *Christia vespertilionis*via UNTARGETED TANDEM MASS SPECTROMETRY-BASED MOLECULAR NETWORKING APPROACH

Anis Irfan Norazhar[1*], Khozirah Shaari[1], SitiMunirahMohd Faudzi[1]

[1]Laboratory of Natural Products, Institute of Bioscience, Universiti Putra Malaysia, 43400 UPM Serdang, Selangor, Malaysia.

*Corresponding Author: anisirfan1512@gmail.com

Abstract
Christia vespertilionis(L.)Bakh. f., is a non-climbing ornamental plant with a unique butterfly-shaped leaves, hence its vernacular name “red butterfly wing”or ‘pokokrerama’ in Malay. In Malaysia, the green-leafed variety gained popularity in recent years due to testimonial reports by local users and distributors for its medicinal uses, which included among others,as anticancer and antimalarial agents. Despite these popular uses, there is very limited information on the chemical constituents of the species, presenting a significant gap in the cheminformatics of the species. These gap needs to be supplemented to allow for a better understanding of the plant’s characteristics. This paper reportsthe putative chemical profile of the green-leafed *C.vespertilionis*, obtained by deploying an untargeted tandem mass spectrometry-based molecular networking approach. An offshoot of metabolomics, this approach involves generating and organizing large datasets of tandem mass spectra based on MS/MS fragmentation pattern similarity in which the output datasets were visualized as molecular networks.The multi-informative molecular map, generated for the leaf metabolome permited the identification ofa range of metabolites comprising *C*-glycosyl flavones, mono- and dihydroxy flavones, flavonol 3-*O*-glycosides, phenolic acids, chlorophyll, carotenoids, monoacylglycerols and amino acids.

Keywords: *Christia vespertilionis*, molecular network, flavonoids, *C*-glycosyl flavones

Introduction
Christia vespertilionis is a dicotyledonous flowering plant with erect, slender stems that can grow up to a height of 1 m. The species is believed to be native to Thailand, Vietnam, Cambodia, Indonesia, China and Myanmar. The common names given to the plant species alluded to the uniquely shaped terminal leaf, which look like wings of a butterfly. The plant recently became more popular for its medicinal uses rather than as a garden plant. The plant exists as two varieties viz, the red-leafed and the green-leafed variety. Similar to other species of the genus, both the green- and red-leafed variety of this pretty plant isgrown for its ornamental value. In traditional medicine, *C.vespertilionis* is reported to be used for treating tuberculosis, bronchitis, colds, muscle weakness, poor blood circulation and snake bites (Dash, 2016). In Malaysia, testimonials on the plant’s effectiveness in as a anticancer herb directed some *in-vitro* and *in-vivo* biological investigations on the green-leafed varietyin order to ascertain the properties claimed. To date, this plant species has been reported to be anti-proliferative (Hofer *et al*., 2013), anti-malarial and cytotoxic (Nguyen-Pouplin *et al*., 2007). However, a huge gap exists on the chemical characteristics of the plant. For a better understanding of the potential value of the species in terms of its medicinal uses, this gap needs to be supplemented with information. This work was undertaken with the primary objective of mapping the chemical space withinthe leaf metabolome of the plant. A comprehensive metabolite profiling of the leaf methanolic extract of green-leafed *Christia vespertilionis* was thus performed using ultra high

performance liquid chromatography coupled with tandem mass spectrometry (UHPLC-MS/MS)-based molecular networking approach.Molecular networking has recently appeared as a promising method to analyse and dereplicate complex natural products mixtures.

Methodology

Large datasets of MS/MS fragmentation spectra acquired from the single analysis of tandem mass spectrometry were processed and organized as molecular networks (MNs) using an online workflow available on Global Natural Product Social Molecular Networking (GNPS) platform. From the generated molecular networks as shown in Figure 1.1, each MS/MS spectrum of the detected molecular ions was represented as a node (blue circles), while the edges (grey lines) interconnecting the nodes indicate that they possess similar fragmentation pattern, thus, they were clustered within the same network.

Results and Discussion

The multi-informative molecular map, generated for the leaf metabolome permited the identification of a range of metabolites, comprising clusters of *C*-glycosyl flavones, mono- and dihydroxy flavones, flavonol 3-*O*-glycosides, phenolic acids, chlorophyll, carotenoids, monoacylglycerols and amino acids. Figure 1.1 shows the flavonoid cluster of the molecular map with some of the predicted structures.

Figure 1.0: green-leafed *C.vespertilionis*

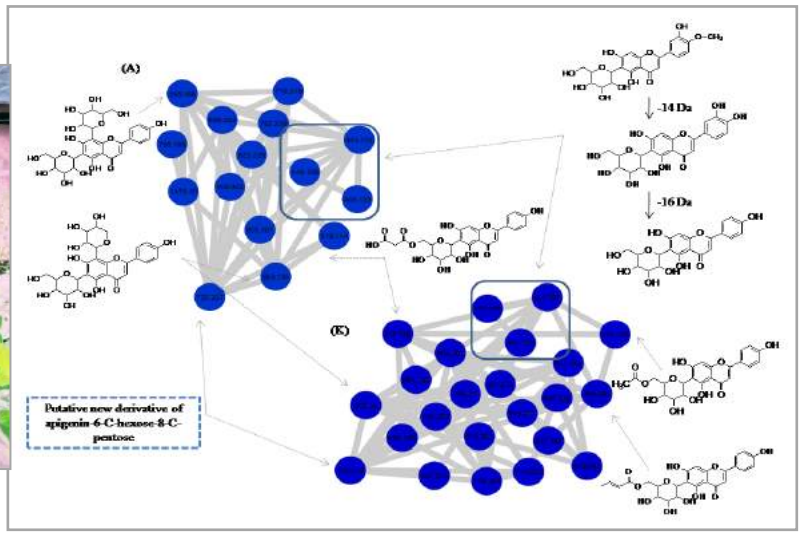

Figure 1.1: Representation of *C*-flavones glycosyl flavones clusters in (A) positive and (K) negative ionization modes

Conclusion

Untargeted tandem mass spectrometry-based molecular networking approach has been applied to profile the chemical constituents of this plant species. The putative identification of the chemical constituents was performed by comparing the MS/MS fragmentation pattern with previous reported literature along with structure hits acquired through comparison withdata in the GNPS library.The MS-targeted, semi-preparative HPLC isolation of two major constituents (isovitexin, and apigenin 6-*C*-hexose-8-*C*-pentose) and one new derivative (apigenin 6-*C*-hexose-8-*C*-pentose), identified in the flavonoid cluster, is being further persued for structural confirmation by NMR spectroscopy.

References

1) Dash, G. K. (2016). An appraisal of Christia vespertilionis (L. F.) bakh. F.: A promising medicinal plant. *International Journal of Pharmacognosy and Phytochemical Research*, *8*(6), 1037–1039.
2) Hofer, D., Schwach, G., Tabrizi-Wizsy, N. G., Sadjak, A., Sturm, S., Stuppner, H., & Pfragner, R. (2013). Christia vespertilionis plant extracts as novel antiproliferative agent against human neuroendocrine tumor cells. *Oncology Reports, 29*(6), 2219–2226.
3) Nguyen-Pouplin J, Tran H, Phan TA, Dolecek C, Farrar J, Tran TH, Caron P, Bodo B, Grellier P.(2007). Antimalarial and cytotoxic activities of ethnopharmacologically selected medicinal plants from south Vietnam. *Journal of Etnopharmacol*ogy 109: 417-427.

POSTER PRESENTATION

PHYSICS

GENERALIZED COMMUTATION RELATION IN NONCOMMUTATIVE QUANTUM MECHANICS

Nurisya Mohd Shah[1,2*], Nur Fadhillah Rahimi[3], Nadhira Abd Haris[1], Hishamuddin Zainuddin[1,2]

[1]Lab. of Computational Sciences & Mathematical Physics, INSPEM, 43400 UPM Serdang, Selangor
[2]Dept. of Physics, Faculty of Science, Universiti Putra Malaysia, 43400 UPM Serdang, Selangor
[3]Dept. of Physics, Kuliyyah of Science, IIUM Kuantan Campus, Jln. Ahmad Shah, Bandar Indera Mahkota, 25200 Kuantan, Pahang

*Corresponding author: risya@upm.edu.my

Abstract
Canonical commutation relation in quantum mechanics has become a powerful mathematical tool to describe the significant relationship of a physical measurement between the position and momentum operator. In this work, the generalized commutation relation with additional features due to noncommutative quantum mechanics (NCQM) is properly visualized discussing the case of space and phase space noncommutative quantum mechanics. Explicit results due to these commutation relations are generate and compile in the form of Mathematica Wolfram Demonstration Project and thus provide as one of a great teaching tool aid in quantum mechanics course.

Keywords: *noncommutative quantum mechanics, commutation relation*

Introduction
In quantum mechanics, the position and momentum known as canonical conjugates which are observables and are represented by an operator which satisfy the rules of canonical commutation relation. It is very fundamental for which the physical interpretation of the canonical conjugates being noncommute conclude that one could not precisely measured both position and momentum simultaneously at the same time. A decade ago, research on what is known as noncommutative quantum mechanics or NCQM for shorts was first introduced contributing features such that the commutation relation between position-position (Kang et.al, 2005; Delduc et.al, 2008) or momenta also being noncommutte if one work in two-dimensional quantum system. In this work, commutation relations are generated, compiled and visualized in the form of Wolfram Demonstration Project and the properties are related from (Kang et.al, 2006; Hasibul & Ali, 2014). Generalized states solutions with application to physics are discussed in (Balogh et.al, 2015).

Methodology
The generalized commutation relations in NCQM for space and phase space is generated and compiled in the form of Wolfram Demonstration Project using Mathematica Software Version 11.3, for which one can easily viewed them in CDF (Computable Document Format) file for interactive content. NCQM for space visualized the property where only spatial space being noncommute while NCM for phase space considered both spatial-spatial and momentum-momentum being noncommute.

Results & Discussion

The following form of generalized commutation relation in NCQM is proposed.

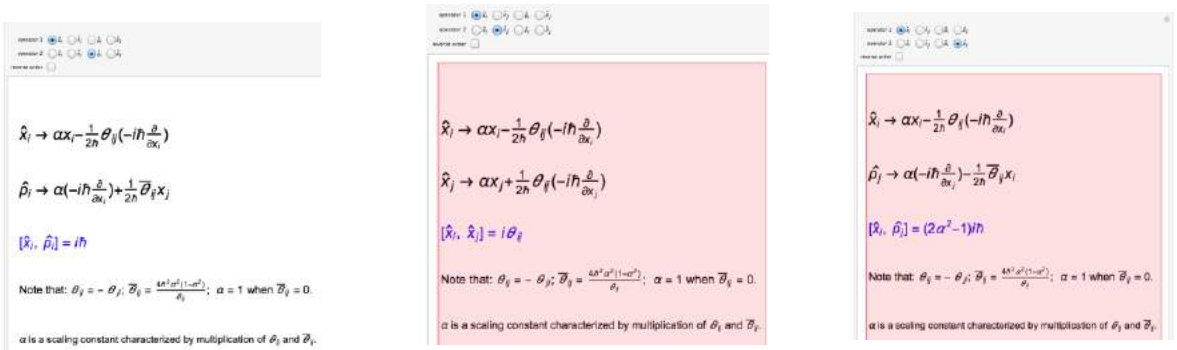

Figure 1: (From left to right) Canonical commutation rules, NC commutation rules and generalized canonical commutation rules.

Conclusion

In this work, the proper generalized commutation relation associated to the position and momentum operator due to noncommutative quantum mechanics is fully construct and compiled. Results of commutators cover both the space and phase-space noncommutative quantum mechanics case.

Acknowledgement

NMS would like to acknowledge grants from Universiti Putra Malaysia, UPM GP-IPS (9645700).

References

1. Delduc, F., Duret, Q., Gieres, F. & Lefrancois, M. (2008). *Magnetic fields in noncommutative quantum mechanics*, Journal of Physics: Conference Series, **103**, pp. 012020–26.
2. Kang, L., Xiao-Hua, C & Dong-Yan, W. (2006). *Heisenberg algebra for noncommutative Landau problem*, Chinese Physics, **15**, pp. 2236–2240.
3. Kang Li, Jianhua Wang & Chiyi Chen (2005). *Representation of noncommutative phase space*, Modern Physics Letters A,. **20**, pp. 2165–2174.
4. S Hasibul Hassan Chowdury & S Twareque Ali (2014). *Triply extended group of translations of R^4 as defining group of NCQM: relation to various gauges.* J. Phys. A: Math. Theor. **47**: 085301 (29 pg).
5. Balogh, F., Nurisya M. Shah & S. Twareque Ali (2015). *On some families of complex Hermite polynomials & their applications to physics.* Operator Theory: Advances & Applications, **247**, pp. 157-171.

COPPER REMOVAL IN AQUEOUS SOLUTION USING MAGNETITE/CARBON ADSORBENT

R.S.Azis[1,2*], I.Ismail[2], H.C.Man[3], A.H.Shaari[1], F.A.C.Isa[1], H. Halid[1], S. Sulaiman[2] and N.A.A.Nazir[2, 4]

[1] Department of Physics, Faculty of Science, Universiti Putra Malaysia, 43400 Serdang, Selangor, Malaysia.
[2] Materials Synthesis and Characterization Laboratory, Institute of Advanced Technology (ITMA), Universiti Putra Malaysia, 43400 Serdang, Selangor, Malaysia.
[3] Department of Biological and Agricultural Engineering, Faculty of Engineering, Universiti Putra Malaysia, 43400 Serdang, Selangor, Malaysia
[4] Center of Foundation Studies, Cawangan Selangor, Universiti Teknologi MARA

*Corresponding author: rabaah@upm.edu.my

Abstract
This work presents a method used for magnetic phase extraction of Copper (Cu) ions from aqueous solution. The magnetite nanoparticle (MNP) from the waste of industrial mill scales was processed to form magnetite nanoparticles by the extraction of the waste mill scales. The extraction powder were milled using the high energy ball mill (HEBM) at various milling time of 2, 4, 6 and 8 h. The formation of magnetite (Fe_3O_4) nanosized single-phase hexagonal spinel has been observed confirmed by using XRD analysis. The samples then used as an adsorbent in Copper removal of the aqueous solution. The highest adsorption capacity, q_e was contributed by MNP with 4 h milling time. Newly extracted MNP from waste mill scales is cost effective and eco-friendly process that potential in wastewater treatment.

Keywords: Copper (Cu), Waste mill scale, Adsorption, Wastewater treatment,

Introduction
Water pollution was found in source areas such as mining activities area, batteries manufacture factories, and metal-based industrial operations. Metals ions waste often found in wastewater are cadmium (Cd), zinc (Zn), copper (Cu), nickel (Ni), lead (Pb), mercury (Hg) and chromium (Cr) [1, 2]. These metals are non-biodegradable, cannot be decomposed, and are very persistent in the polluted water. These metal ions can be accumulated in living tissues, that can cause serious health problems in living cells, tissues for humans and animals. The various mechanism has been developed to manage water pollution, mainly with metal ions, such as membrane filtration, coagulation, ion exchange, adsorption, and chemical precipitation. The adsorption was found to be an excellent method for the metal ions removal from the aqueous solutions. This method is cost-effective, a wide range of applications, various types of adsorbents, reusable adsorbents and high efficiency [2]. Magnetite nanoparticles have unique physical and chemical properties that make them superior sorbents. Activated carbon has a large surface area and a well-defined pore structure that favors as excellent sorbents. In this work, the magnetite-modified activated carbon sorbent was developed to investigate the nanocomposites adsorbents capability for the removal of Copper ions from wastewater at the laboratory scale.

Methodology
The preparation of magnetite nanoparticles from waste mill scales are similar to previous report by Azis et. al [3-4] and Daud et.al [5]. The magnetite powder was milled using the SPEX 8000D milling machine with the ball to powder (BPR) ratios of 10:1 for 2, 4, 6, and 8 h. The copper solution was prepared by dissolving 1 L deionized water and copper nitrate

in a conical flask. 20 mL of copper solution in the beaker is added 0.1 g of MNPs and 0.1 g of AC. The mixture of Cu solution and MNP-AC was stirred for several minutes using a magnetic stirrer. The solution then applied a magnetic bar for the separation process. After magnetical separation of the sorbent from the solution, the residual metal concentration was determined. The percentage removal of copper was calculated using Eq. (1):

$$\%\, removal = \frac{C_0 - C_e}{C_0} \times 100\ \% \quad (1)$$

where C_o is the initial concentration and C_e is the concentration at equilibrium, after treated with adsorbant.

Results and Discussion

The magnetite nanoparticles/ activated carbon (MNP/AC) with different milling time (2,4,6 and 8h) were prepared. The percentage of Cu removal in the aqueous solution was investigated. Activated carbon (AC) was used as an efficient sorbent for wastewater treatment due to its high adsorption capacity. Activated carbon has a large surface area and highly porous. The microstructure of the MNP (4h) and AC are shown in Figure 1. The development of MNP/AC composites adsorbent shows an enhanced of the Cu removal in an aqueous solution (Figure 2). MNP/AC for 4h milling time shows the highest percent of Cu removal with the removal of 94.4%. It was observed that about 20% increment of Cu removal was achieved by the MNP/AC compared to MNP.

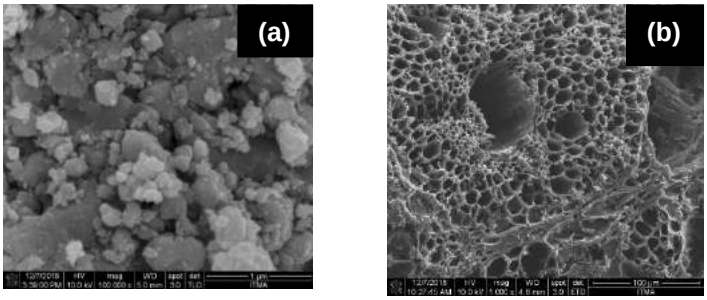

Figure 1: FESEM images of (a) magnetite nanoparticles for 4h milling time, and (b) activated carbon

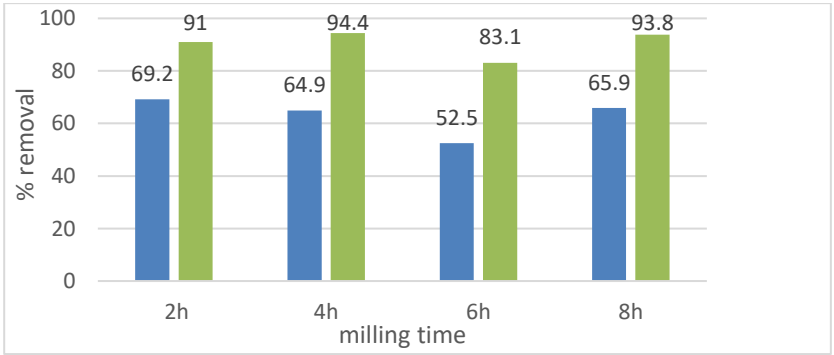

Figure 2: Percentage Cu removal against milling time for MNP (left) and MNP/AC (right)

Conclusion

The magnetite-activated carbon (MNP/AC) was tested as an adsorbent for the removal of Copper ions from the aqueous solution. The optimum adsorbent dose and contact time for metal ion removal were determined to achieve maximum removal efficiency. The maximum adsorption occurred at 20 min of contact time with the percentage removal of copper was 94.4%.

Acknowledgment

This work was supported by Universiti Putra Malaysia Grants (Putra Initiative Grants (UPM/700-1/2/GPPI/2017/954160), Impact Putra Gants (GP-IPS/2017/9580600/9533300) and the Ministry of Education Malaysia (Fundamental Research Grants Scheme (FRGS) (No. 5524942).

References

1. A. K.Gupta, M.Gupta, (2004). Synthesis and surface engineering of iron oxide nanoparticles for biomedical applications, *Biomaterials*, 26, 3995-4021.
2. A. Andelescu, M. A. Nistor, S. G. Muntean & M. E. Rădulescu-Grad, (2018), Adsorption studies on copper, cadmium, and zinc ion removal from aqueous solution using magnetite/carbon nanocomposites, Separation Science and Technology, 53(15), 2352–2364
3. R. S. Azis, M.Hashim, N. Yahya, N. M. Saiden, (2002). A study of sintering temperatures variation on microstructure developments of strontium hexaferrite millscale-derived. *Journal of Applied Sciences*, 2(12), 1092-1095.
4. R. S. Azis, M. Hashim, N. Yahya (2002), Purified iron oxide α-Fe_2O_3 from millscale using curie temperature separation technique. *Journal of Solid State Science and Technology*, 9, 87-90.
5. N. Daud, R. S. Azis, M.Hashim, K. A. Matori, J.Hassan, N. M.Saiden, N. M. M. Shahrani (2015), Preparation and characterization of $Sr_{1-x}Nd_xFe_{12}O_{19}$ derived from steel waste product via mechanical Alloying. *Materials Science Forum*, 846, 403-409.

INFLUENCE OF TUNGSTEN OXIDE ON STRUCTURAL, PHYSICAL AND ELASTIC PROPERTIES OF ZINC BOROTELLURITE GLASS SYSTEM

M.K. Halimah [1]*, M.T Nur Syahirah[1], Z. Zuhasanah[1],M.F. Faznny[1],S.N. Nazrin[1], H.A.A.Sidek[1], M.H.M. Zaid[1], A.M. Khamirul[1], A.H. Shaari[1], S.O. Baki[2] and I.S. Mustafa[3]

[1]Department of Physics, Faculty of Science, Universiti Putra Malaysia, 43400 UPM Serdang, Selangor, Malaysia.
[2] Centre of Foundation Studies for Agricultural Science, Universiti Putra Malaysia, 43400 Serdang, Selangor, Malaysia.
[3] School of Physics, University of Science Malaysia ,11800 USM, Pulau Pinang, Malaysia.

*Corresponding author: halimahmk@upm.edu.my

Abstract
Zinc borotellurite glass system doped tungsten oxide $\{[(B_2O_3)_{0.3}\ (TeO_2)_{0.7}]_{0.7}\ [ZnO]_{0.3}\}_{1-x}\{WO_3\}_x$ with x =0, 0.1, 0.02, 0.03, 0.04, 0.05 was fabricated by melt quenching method. X-ray diffraction shows that the glass samples are amorphous in nature. Density of the glass system decreases but molar volume increases with increase of WO_3. The longitudinal and shear velocity vary with WO_3. Elastic properties, mirohardness and softening temperature were calculated from measured density and ultrasonic velocity at room temperature. Elastic moduli such as longitudinal modulus, shear modulus, bulk modulus and Young's modulus show a decreasing trend with the increase of WO_3 concentration

Keywords: Elastic modulus, micohardness, ultrasonic velocity, softening temperature

Introduction
Physical and structural properties of tellurite, borate and borotellurite glasses have been widely investigated for their scientific interest and applications. Borate glasses are known as material with high thermal stability, high chemical durability, good solubility of rare earth ion. Tellurite glasses have lower phonon energy compared to phosphate and silicates glasses, large infrared transparency, good thermal and mechanical stability, good chemical durability, low melting temperature high refractive index, high dielectric constant. Addition of tellurium oxide to another glass former such as B_2O_3 can lead to an interesting unit that will affect the physical properties of the glass network [1]. Zinc oxide has high optical transparency in the visible and near infra-red region, ZnO can be considered as suitable material for electronic or optoelectronic applications [2]. Tungsten oxide as a modifier makes a good glass former for tellurite glass. Tellurite glasses containing WO_3 offered the best combination for high chemical and thermal resistance [3]. The ultrasonic non-destructing test has been found to be one of the best techniques to study the microstructure, mechanical properties and elastic constant [4]. The propagation of ultrasonic waves in solids such as glass provides valuable information regarding the solid state motion in the material. In this work, zinc borotellurite glass system doped tungsten oxide is synthesized to investigate the structure and elastic properties of the glass system.

Methodology
Conventional melt quenching technique was used to synthesize zinc borotellurite glass system $\{[(B_2O3)_{0.3}\ (TeO_2)_{0.7}]_{0.7}\ [ZnO]_{0.3}\}_{1-x}\{WO_3\}x$ with x =0, 0.1, 0.02, 0.03, 0.04, 0.05 tellurium(IV) oxide, TeO2 (99.99% Alfa Aesar, boron oxide, B2O3 (98.50%, Alfa Aesar), zinc oxide, ZnO (99.99% Alfa Aesar), tungsten oxide (99.50%, Alfa Aesar) were weighed and stirred for 30 minutes then put in crucible alumina and placed in the first furnace at 400^{o}C for one hour. After that, the crucible was transferred to second furnace at 900^{o}C for

two hours. The molten mixture was poured into the preheated mould. The molten and the mould were annealed at 400^{O}C for one hour. The furnace was switched off and the sample was allowed to cool at room temperature. The samples were polished with silicon carbide paper to obtain parallel, clear and smooth surface for characterisation.

Results and Discussion

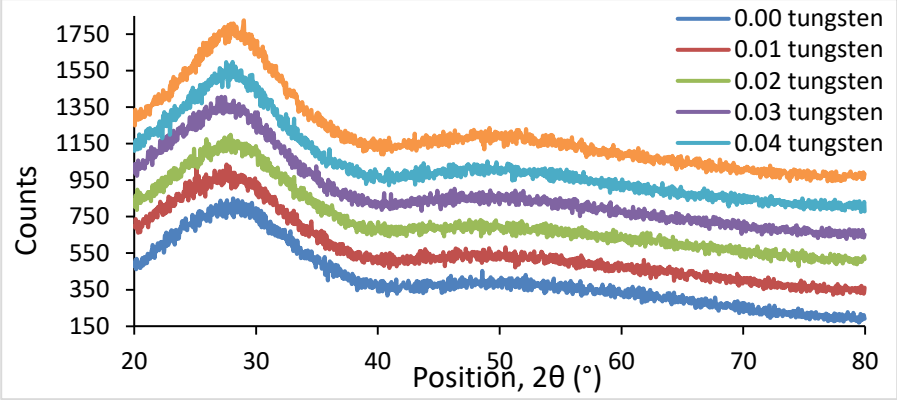

Figure 1: XRD for $\{[(B_2O_3)_{0.3}\ (TeO_2)_{0.7}]_{0.7}\ [ZnO]_{0.3}\}_{1-x}\{WO_3\}_x$ glass system

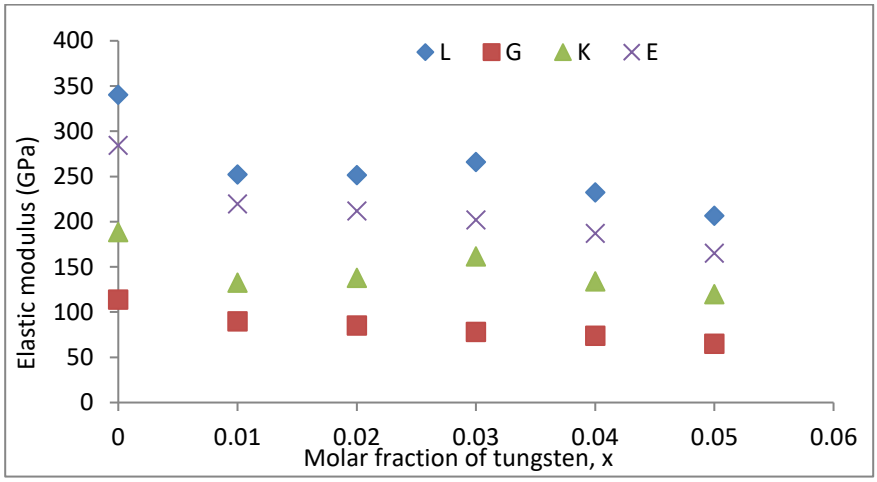

Figure 2: Elastic Moduli for $\{[(B_2O_3)_{0.3}\ (TeO_2)_{0.7}]_{0.7}\ [ZnO]_{0.3\}\ 1-x}\{WO_3\}_x$ glass system

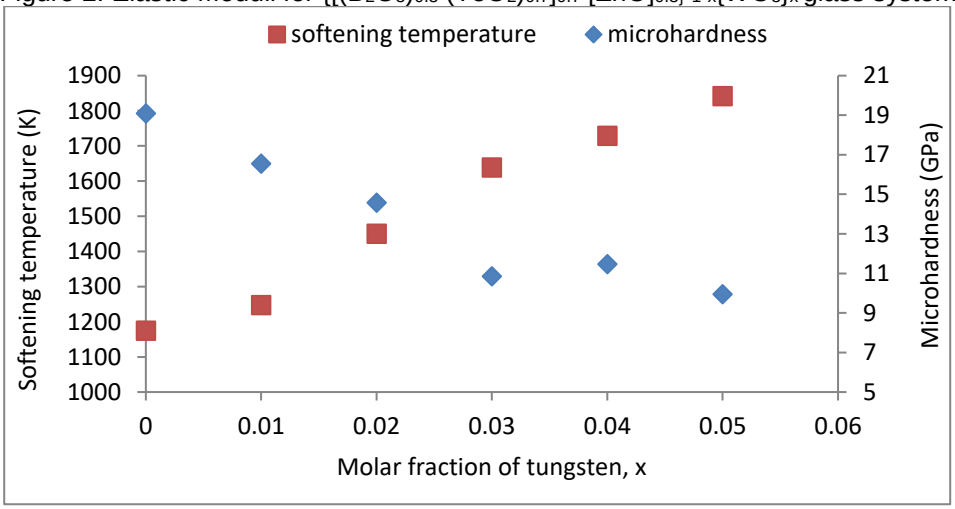

Figure 3: Softening temperature and microhardness for $\{[(B_2O_3)_{0.3}\ (TeO_2)_{0.7}]_{0.7}\ [ZnO]_{0.3}\}_{1-x}\{WO_3\}_x$ glass system

The absence of sharp peaks indicates that the glass system is an amorphous in nature [5]. The elastic moduli for longitudinal modulus (L), shear modulus (G), bulk modulus (K) and Young's modulus show a decreasing trend with WO_3. WO_3 modifies the glass structure and creates non bridging oxygen and this cause the weakening or loose packing of the glass network which influence the rigidity of the glass system. Microhardness is associated with glass rigidity as it decreases the glass will be less rigid. The decrease in glass rigidity might be due to the decrease in connectivity [6].

Conclusion

Density decreases and molar volume increases are due to the increase in non- bridging oxygen. WO_3 breaks the network glass structure and creates more non-bridging oxygen and leads to reduction of ultrasonic velocity. The decrease in rigidity of the glass system contributes to decrease in velocity and elastic moduli but increase in softening temperature.

Acknowledgement

This work was supported by Universiti Putra Malaysia, Impact Putra Gants (UPM/700-2/1/GPB/2017/9597200) and the Ministry of Higher Education Malaysia (Fundamental Research Grants Scheme (FRGS/1/2018/STG07/UPM/02/12 (No 5540136)

References

1. Paz, E.C., Dias, J.D.M., Melo, G.H.A., Lodi,T.A., CArvalho, J.O., Facanha Filho,P.F., Steimacher, A. 2016. Physical, thermal and structural properties of calcium borotellurite glass system. *Material Chemistry Physics* 178,133-138.
2. Gumus, C., Ozkendir, O.M., Kavak, H, Ufuktepe, Y. 2006. Structural and optical properties of zinc oxide thin film prepared by spray pyrolysis method. *Journal of Optoelectrinics and Advanced Materials* , 2(11), 1541-1546.
3. Fares, H., Jlassi, I.< Hraiech, S., Elhouichet, H., Ferid, M. 2014. Radiative parameter of Nd3+ doped titanium and tungsten modified tellurite glasses for 1.06 um laser materials. *Journal of Quantitative Spectroscopy and radiative Transfer*, 147,224-232.
4. Sidkey, M.A., Ghaafar, M.S. 2004. Ultrasonic studies on network structure or ternary TeO2-WO3-K2O glass system. *Physica B:Condensed Matter*,348(1-4),46-55.
5. Hasnimulyati, L., Halimah, M.K., Azmi, Z., Azlan, M.N. 2014. A comparative study of the experimental and the theoretical elastic data of Tm3+ doped zinc borotellutire glass. *Materals Chemistry and Physics*, 192,228-234.
6. Abdulbaset,A.A., Halimah, M.K., Azlan, M.N.,2017. Effect of Neodymium Ions on density and elastic properties of zinc tellutite glass system. *Solid State Phenomena*, 268,28-32.

GENERATION OF SHORT PULSE FIBER LASER UTILIZING SINGLE-POINT AND DUAL-POINTS SINGLE LAYER GRAPHENE AS SATURABLE ABSORBER

N. Mohd Radzi[1], A. Abd Latif[1]*, K. Syamim Khalid[1], N. Tamchek[1]

[1]Department of Physics, Faculty of Science, Universiti Putra Malaysia, 43400 UPM Serdang, Selangor Darul Ehsan, Malaysia.

*Corresponding author: amirahlatif@upm.edu.my

Abstract
In this work, we have experimentally demonstrated a passively mode-locked fiber laser (MLFL) based on a single-point and dual-points of single-layer graphene as saturable absorbers in a laser cavity with a total length of 15.02 m. The saturable absorbers were fabricated by sandwiching the graphene thin film between two single-mode fiber ferrules. The MLFL was operating in the L-band region employing 3 meters erbium-doped fiber (EDF) as a gain medium. The proposed fiber laser generates ultrashort pulse train with a central wavelength, pulse duration, repetition rate and average output power of 1569.07 nm, 26.0 ns,13.89 MHz and 3.430 mW, respectively. The experimental results uncover that the dual-points of single-layer graphene design configuration presents a better performance compared to a single-point of single-layer graphene by its ability to generate an ultrashort pulse with very stable operation.

Keywords: Mode-locked fiber laser, saturable absorber, L-band, graphene

Introduction
Mode locking is a technique to generate ultrashort pulses from fiber lasers. Passively mode-locked have attracted considerable attention in recent years and usually using a nonlinear passive element, namely saturable absorber (SA) to obtain much shorter pulses. Semiconductor saturable absorber mirrors (SESAMs) [1] reported as the earliest SA found by the researchers. However, SESAMs show limitation on their optical bandwidth which requires a tedious fabrication process. Years later, researchers come out with a new idea for fabricating the SA using nanomaterials, such as graphene. Graphene [2] has captured the researcher's attention due to its zero bandgap and broadband optical absorption from the ultraviolet to the far-infrared region.

In this research, we reported passively mode-locked fiber laser using graphene as SA in single-point and dual-points of single-layer graphene. The mode-locker is including graphene as SA by sandwiching the graphene thin film between two fiber ferrules. Hence, for a dual-points single layer of graphene thin film design configuration, we assembled two fiber connector which have two equal thin films of graphene into the cavity. As the results, the dual-point single-layer graphene as SA achieves more stability with a central wavelength, pulse width, repetition rate and average output power of 1569.07 nm, 26.0 ns, 13.89 MHz and 3.430 mW, respectively.

Methodology
The illustration setup of mode-locked fiber laser by using single-point and dual-points single-layer graphene is depicted as in Fig. 1. The circuit configuration includes laser diode (LD), wavelength division multiplexer (WDM), 3 m erbium-doped fiber (EDF) as a gain medium, an isolator was used to ensure the signal travels only in one direction and a coupler was used to split the signal into 2 channel where 90% portion was being looped back into the cavity and another 10% portion output was extracted out to be connected by the analyzer. In this setup, there are two SAs used during the experiment. For the

experiment of mode-locked fiber laser involving single-point of single-layer graphene, the SA2 was absent while for an experiment involving dual-point of single-layer graphene, both SA1 and SA2 were present in the configuration. The single layer of GTF was sandwiched between two fiber ferrules in each SA1 and SA2 using an optical fiber connector.

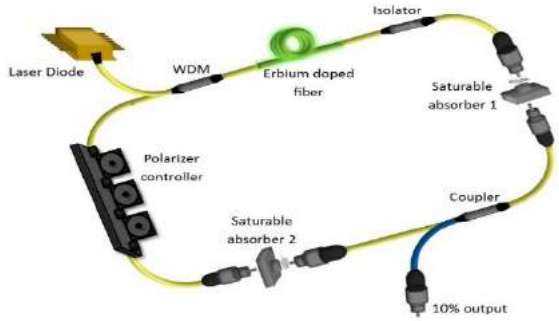

Fig. 1. Illustration circuit of graphene-based SA in a mode-locked fiber laser.

Results and Discussion

Fig. 2 demonstrates the optical spectra for both single-point and dual-points of single-layer graphene at pump power 15 mW, with their central wavelength at 1569.16 nm and 1569.07 nm respectively.

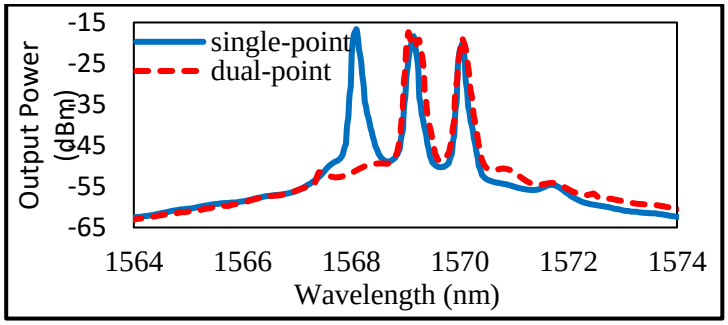

Figure 2: The results of optical spectrum for single-point and dual-points of single-layer graphene.

Conclusion

In summary, we have experimentally demonstrated a passively mode-locked fiber laser based on a single-point and dual-points single-layer graphene as saturable absorber. The experimental results reveals that a dual-points single-layer graphene present better performances compared to a single-point single-layer graphene by its ability to generate shorter pulse width and response time with a very stable operation and corresponding with length cavity of MLFL.

Acknowledgement

The authors would like to acknowledge the Ministry of Education Malaysia for the project fund No. FRGS/2/2014/SG02/UPM/02/1/5524648 for the financial support given.

References

[1] Lui, K. L. F., Tsang, K. S., Fung, M., Ho, V., Furukawa, H., Makino, T., … Man, R. (n.d.). A laser using Integrated Faraday rotator and SESAM with Amplitude Modulation stabilization, 4–6.

[2] Jia, C., Shastri, B. J., Abdukerim, N., Rochette, M., Prucnal, P. R., Saad, M., & Chen, L. R. (2016). Passively synchronized Q-switched and mode-locked dual-band Tm 3 + : ZBLAN fiber lasers using a common graphene saturable absorber. *Nature Publishing Group*, (May), 1–9. https://doi.org/10.1038/srep36071

EFFECT OF THERMAL DIFFUSIVITY ON VARIED THICKNESS OF Co DOPED ZnO USING PHOTOPYROELECTRIC TECHNIQUE

Nor Kamilah Saat*, Intan Nur Malia mohd Khalid, Ting Lee Mon, Quratul Aini Ismail

Department of Physics, Faculty of Science, Universiti Putra Malaysia, 43400 UPM Serdang, Selangor, Malaysia.

*Corresponding author: kamilah@upm.edu.my

Abstract
In this work, the effect of different thickness of Cobalt doped Zinc Oxide (CoZnO) on thermal diffusivity using photopyroelectric (PPE) method. Sample was prepared using solid state technique where the thickness of sample is controlled by different pressure in pelletizing process. The results show the increase of thermal diffusivity as the thickness of sample increase and supported with other characteriztion of sample using XRD, densimeter and Uv-Vis spectroscopy.

Keywords: photopyroelectric; CoZnO; thermal diffusivity; thickness

Introduction
Metal doped ZnO is attracted due to its potential application in microelectronics, sensing, environ-mental remediation, biomedicine and etc. There are several reports of Co doped ZnO on structural, electrical, optical, and magnetic, (Ansari et. al, Benramache et. al, Caglar et. al, and Panyajirawut et. al), but still lacking in the thermal properties particularly thermal diffusivity of the material. Photo pyroelectric is well established of non-destructive method in thermal diffusivity measurement (Noroozi et. al.) by using polyvinylidene fluoride (PVDF) films as pyroelectric sensors. Thus, this work is to study the effect thermal diffusivity on different thickness of Co doped ZnO by photo phyroelectric method.The studied samples were synthesized via solid state method where different pressures were applied from 1 to 3 tonnes/cm^2 to produce the samples with different thickness from 0.53 to1 mm. Ultimately, using PPE method shows the increase of thermal diffusivity dependence as Co doped ZnO thickness in increased which also consistent with literature review.

Methodology
Sample of Co doped Zno prepared by solid state method composed of Co 2 wt% and ZnO 98 wt %. This method was described in detail previously by Isa et. al. []. However due to higher melting temperature of Co and the sample is prepared in pallet form, the sintering temperature of 1200 ˚C for 2 h with heating and cooling rates of 5 ˚C/ min. The different thickness of sample is obtained by pressing different pressure from 1 to 3 tonne/cm^2 to give different thickness of 0.53, 0.72, 0.82, 0.93 and 1 mm. The structural, density and optical properties of the samples are investigated using XRD, densimeter and Uv-Vis spectroscopy, respectively. The thermal diffusivity measurement is obtained as shown in Figure 1 where pyroelectric (PE) output signal from PVDF are measured by varying the frequency chopping from range 5–30 Hz at room temperature of ~20 °C

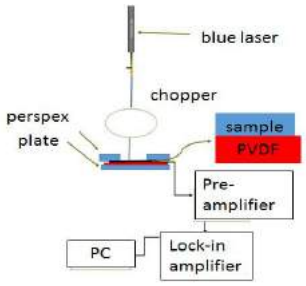

Figure 1 PPE setup to obtain thermal diffusivity.

Results and Discussion

Figure 2 shows the measured values of thermal diffusivity from PPE setup increase with specimen thickness which in a good agreement with Liu et al. and supported with result of density, XRD and well as absorption coefficient (UV-vis measurement)

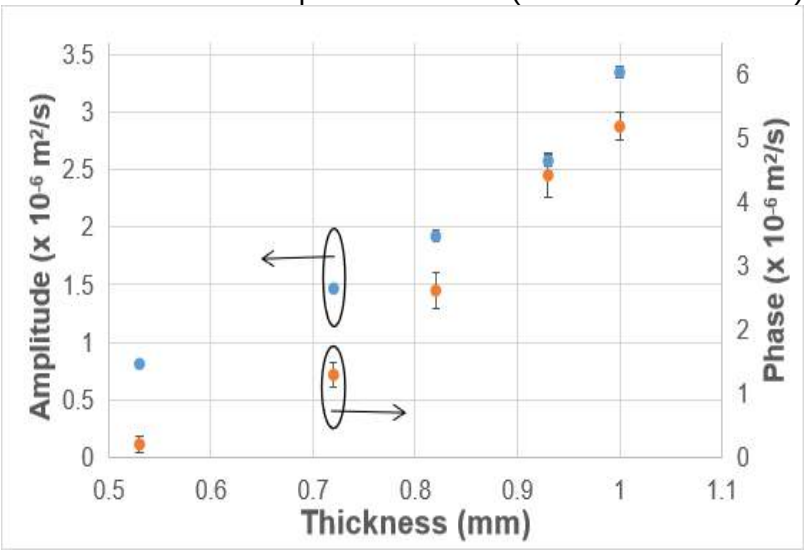

Figure 2 Effect of thermal diffusivity for amplitude and phase at different thickness of Co doped ZnO.

Conclusion

Thermal diffusivity from PPE setup increase with specimen thickness which is consistent with Liu et al which due to favorable specimen diameter to thickness ratio.

Acknowledgement

The authors are grateful to the University Putra Malaysia for supporting the work under grant no. GP-IPS/2018/9664200.

References

1. Ansari, S. A., Nisar, A., Fatma, B., Khan, W., Naqvi, A. H., 2012. Investigation on structural, optical and dielectric properties of Co doped ZnO nanoparticles synthesized by gel-combustion route, Mat. Sci. Eng: B 177, 428-435.
2. Benramache, S., Temam, H. B., Arif, A., Guettaf, A., Belahssen, O., 2014. Correlation between the structural and optical properties of Co doped ZnO thin films prepared at different film thickness, Optik. 125, 1816-1820.
3. Caglar, Y., 2013. Sol–gel derived nanostructure undoped and cobalt doped ZnO: Structural, optical and electrical studies, J. Alloys Compd. 560, 181-188.

4. Panyajirawut, P., Srithep, K.,Namsa, C., Kitcharoen, R. and, Pecharapa, W., 2016. Cobalt-doped ZnO Powders by a Simple Solid-State Method, Key Eng. Material, 675, 486-489.
5. Noroozi, M., and Zakaria, A., 2017. Measuring Nanofluid Thermal Diffusivity and Thermal Effusivity: The Reliability of the Photopyroelectric Technique, Nanofluid Heat and Mass Transfer in Engineering Problems, 62-93.
6. Liu, D.M., 1996. Effect of specimen thickness on the Thermal diffusivity of (Sr, K)Zr4(PO4)6 ceramic via a Laser-flash technique. Journal of Materials Science, 31(1), 86-89.
7. Isa, N.H., Zakaria, A., Azis, R.S., Rizwan, Z., 2017. Microstructural and Nonlinear Properties of Zn-V-Mn-Nb-O Varistor Ceramics with Gd2O3 Substitution for Low Voltage Application, Slid State Phenomena, 268, 181-185.

FRACTIONATION OF WASTE NATURAL RUBBER (NR) GLOVE AS CANDIDATE FOR CARBON NANOMATERIALS (CNMs) SYNTHESIS

M. A. Hazan[1], Y. Yaakob[1*]

[1]*Department of Physics, Faculty of Science, Universiti Putra Malaysia, 43400 UPM Serdang, Selangor Darul Ehsan, Malaysia.*

*Corresponding author: yazidakob@upm.edu.my

Abstract
Conversion of solid waste natural rubber (NR) glove into liquid was done by using fractional distillation method. The solid waste was heat at 450 °C as obtained from TGA to evaporate the waste in form of vapor and was condensed by condenser column into liquid form. The processed hydrocarbon liquid was characterized by using carbon nitrogen sulfur (CNS) analyzer, showing high carbon percentage inside the processed liquid which is 73.2010 %, nitrogen and sulfur are 0.13123 % and 0.83284 % respectively. The GCMS spectrum shows the waste contains long, short and aromatic hydrocarbon which later was used for CNMs synthesis. The morphology of the synthesized CNMs was observed under scanning electron microscope (SEM) and transmission electron microscope (TEM).

Keywords: fractional distillation, NR glove, hydrocarbon chain

Introduction
Carbon nanomaterials (CNMs) synthesis from waste materials has attract many interests as it can be a new precursor for synthesis carbon-based materials and at the same time can reduce waste from environment. One of the methods to extract the hydrocarbon compound in the liquid and solid form of waste material is by using fractional distillation. Fractional distillation is combination of fractionation and distillation method. This technique involves, repeating distillations and condensations steps to separate and purify the different compound in a mixture with different boiling point and molecular weight. In this work, we introduced the fractionation of solid waste NR glove into liquid form. The processed liquid later was used as a new carbon source to synthesis CNMs by CVD method.

Methodology
Fractional distillation was used to convert waste NR glove into liquid form. 50 g of waste NR glove was put into fractional distillation setup and heated at 450 °C. The waste then use as precursor for CNMs synthesis using CVD method at 800 °C using iron oxide catalyst. The waste NR glove was characterized by Thermogravimetric analysis (TGA) to identify the decomposition temperature of waste NR glove. Carbon, nitrogen sulfur (CNS) analyzer used to check the percentage of carbon, nitrogen and sulfur and gas chromatography mass spectroscopy (GC-MS) to check the compound in the processed liquid. The collected samples after CVD was characterized by transmission electron microscope (TEM) and scanning electron microscope (SEM).

Results and Discussion
TGA result gives information of the decomposition temperature of the waste NR glove which is at 450 °C. At this temperature, most of the compound inside the sample was liberated leaving the ash only. The processed liquid from waste NR glove shows the highest percentage of carbon thus can be used for CNMs synthesis. The chromatogram shows the compound inside the sample during the pyrolyzing process in GCMS. There are

many peaks of compound identified in the processed liquid such as xylene (C_8H_{10}), limonene ($C_{10}H_{16}$), cyclohexane ($C_{17}H_{34}$) that can be found in original NR latex. The other peaks showing the compound with long hydrocarbon chain mostly with number of carbon element above 10. Figure 2 are the CNMs synthesized from NR glove.

TABLE 1. Percentage of carbon, nitrogen and sulfur in the processed liquid.

Reps	Mass (g)	Carbon (%)	Nitrogen (%)	Sulfur (%)
Waste NR glove	0.2046	73.2010	0.13123	0.83284

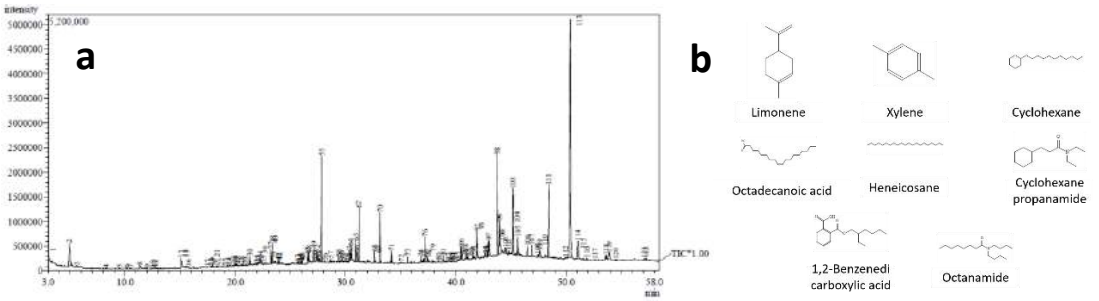

Figure 1: a) chromatogram spectrum of liquid collected from fractional distillation at 450 °C. b) compound identified at retention time.

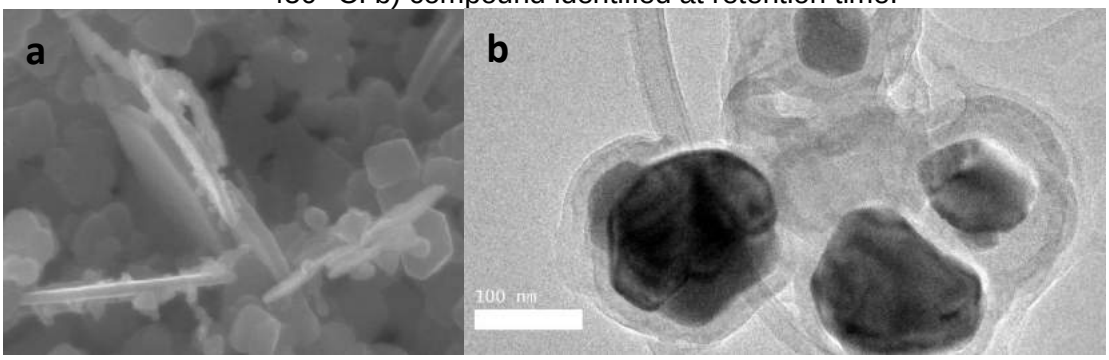

Figure 2: a) SEM image and b) TEM image of CNMs synthesis using NR glove.

Conclusion

The waste NR glove can be change into liquid by using fractional distillation method without changing the original compound. The GCMS analysis showed that waste NR glove decomposed into long hydrocarbon chain. CNMs was synthesized using waste NR glove as precursor as confirmed by TEM and SEM image.

Acknowledgement

This project has received funding from Universiti Putra Malaysia through the Geran Putra-Inisiatif Putra Muda (GP-IPM/2017/9543800).

References

[1] Deng, J., You, Y., Sahajwalla, V., & Joshi, R. K. 2016. Transforming waste into carbon-based nanomaterials. Carbon, 96

[2] Essawy, H., Fathy, N., Tawfik, M., El-Sabbagh, S., Ismail, N., & Youssef, H. 2017. Fabrication of single-walled carbon nanotubes from vulcanized scrap rubber via thermal chemical vapor deposition. *RSC Advances*, *7*(21), 12938–12944

[3] Kusch, P., & Trends, C. 2012. Identification of Organic Additives in Nitrile Rubber Materials by Pyrolysis-GC –MS". Current Trends in Mass Spectrometry, 8–15
[4] Liu, X., Zhao, J., Liu, Y., & Yang, R. 2015. Volatile components changes during thermal aging of nitrile rubber by flash evaporation of Py-GC/MS. Journal of Analytical and Applied Pyrolysis, 113, 193–201
[5] Mia, M., Islam, A., Islam Rubel, R., & Rofiqul Islam, M. 2017. Fractional Distillation & Characterization of Tire Derived Pyrolysis Oil. International Journal of Engineering Technologies IJET, 3(1), 1–10
[6] Rosmi, M. S., Shinde, S. M., Rahman, N. D. A., Thangaraja, A., Sharma, S., Sharma, K. P., … Tanemura, M. 2016. Synthesis of uniform monolayer graphene on re-solidified copper from waste chicken fat by low pressure chemical vapor deposition. Materials Research Bulletin, 83, 573–580

GREEN-BASED REDUCING AGENTS FOR REDUCTION OF GRAPHENE OXIDE

Nor Hasanah Isa[2], Raba'ah Syahidah Azis [1,2,*], Lim Hong Ngee[2,3] and Che Azurahanim Che Abdullah[1,3]

[1]Department of Physics, Faculty of Science, Universiti Putra Malaysia, 43400 UPM Serdang, Selangor, Malaysia
[2]Department of Chemistry, Faculty of Science, Universiti Putra Malaysia, 43400 UPM Serdang, Selangor, Malaysia
[3]Institute of Advanced Materials, Universiti Putra Malaysia, 43400 UPM Serdang, Selangor, Malaysia

*Corresponding author: rabaah@upm.edu.my

Abstract
Graphene has great interest for its excellent electrical, thermal, mechanical and optical properties. The main interest in the research and applications of GO nowadays is the GO reduction (rGO), which partly restores the structure and properties of the graphene. Chemical reduction of graphene oxide process is the commonly used method for mass scale production of reduced graphene oxide. Due to toxic and harmful of hydrazine which is an excellent reducing agent in chemical reduction of graphene oxide led to forward step to replace with friendly environmental and green synthesis of reduced graphene oxide. In this paper, we review the several reducing agents of the reduction of GO on both techniques and mechanisms. It also reviews the characterization of GO and its oxide reduction through the analysis of different spectroscopic and microscopic techniques such as X-ray diffraction, Fourier transform infrared spectroscopy, Raman spectroscopy, X-ray photoelectron spectroscopy, scanning electron microscopy, and transmission electron microscopy.

Keywords: Graphene Oxide, reduced graphene oxide (rGO), Green-based reducing agents, green synthesis

Introduction
Graphene has received broad interest in many areas of science and technology because of its unique physical, chemical, mechanical, thermal and optical properties [1]. Inexpensive and eco-friendly synthesis of high quality graphene is a big challenge for many researchers. Among various methods, chemical synthesis is considered the best because it is easy, scalable, facile, and inexpensive. The unique characteristics of graphene opened a new way for wide range of application such as: biosensor, solar cells, lithium-ion batteries, catalyst engineering, electromagnetic shielding application, photovoltaic devices, super capacitor, water purification, and etc [1].

Graphene oxide is produced from graphite flakes by oxidative reaction, which heavily decorates the sheets with different oxygen moieties. The presence of abundant amounts of oxygen functional groups over the carbon basal plane not only makes GO electrically insulating but also provokes thermal instability. The reduction of graphene oxide produce thermally stable graphene and regain electronic conductivity. Among all, the chemical exfoliation method is one of the most efficient methods for large scale production of reduced graphene oxide [2].

Methodology

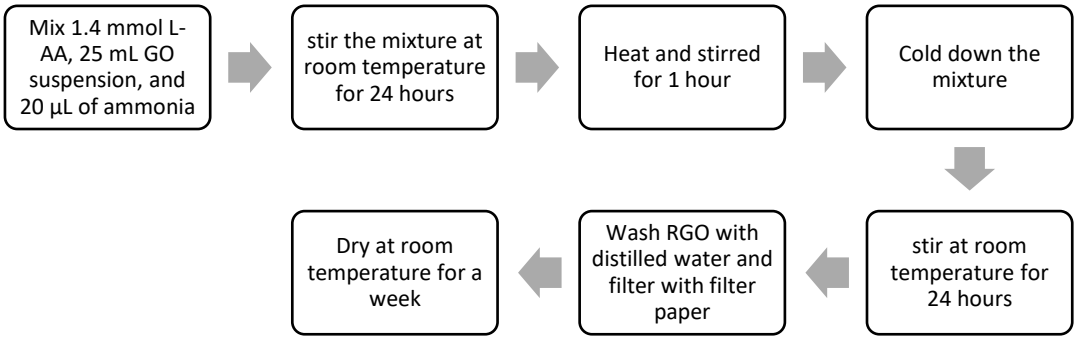

Green-Based Reducing Agents

Hydrazine ($N_2H_4 \cdot H_2O$) is the best-known reducing agent in terms of giving rGO with improved electrical and structural properties resembling pristine graphene to a large extent [3]. However, hydrazine exhibits extremely hazardous effects including DNA damage and known as a carcinogenic agent [4]. The toxic reducing agent has led to the introduction of the "green reduction" approach in this chemical exfoliation method. L-Ascorbic Acid (L-AA) or known as Vitamin C is an excellent green reducing agent compared with toxic hydrazine hydrate and glucose [5]. L-AA also efficient green reducing agent compared with D-fructose, sucrose, glucose, and Na_2SO_3 [6]. In addition, L-AA is most effective reducing agent in comparison with D-glucose and tea extract polyphenol [7].

Acknowledgement

The authors are grateful to the Universiti Putra Malaysia for supporting the project under Putra Grants (GP-IPS/9493000/9580600), Impact Putra Initiative Grants (UPM/700-1/2/GPPI/2017/954160), and the Ministry of Education Malaysia (Fundamental Research Grants Scheme (FRGS) (No. 5524942).

References

1. Aunkor, M.T.H., Mahbubul, I.M., Saidurb, R., & Metselaa, H.S.C. (2016). The green reduction of graphene oxide, RSC Adv., 6, 27807–27828
2. De Silva, K.K.H., Huang, H.H., Joshi, R.K., & Yoshimura, M. (2017). Chemical reduction of graphene oxide using green reductants, Carbon,119,190-199
3. Stankovich, S., Dikin, D.A., Piner, R.D., Kohlhaas, K.A., Kleinhammes, A., & Jia, Y., (2007) Synthesis of graphene-based nanosheets via chemical reduction of exfoliated graphite oxide, Carbon, 45 (7), 1558-1565
4. Esfandiar, A., Akhavan O., & Irajizad, A. (2011). Melatonin as a powerful bio-antioxidant for reduction of graphene oxide, *J. Mater. Chem*., 21, 10907–10914.
5. Na, Y.I., Song, Y.I., Kim, S.W., & Suh, S.J., (2017). Study on properties of eco-friendly reduction agents for the reduced graphene oxide method, Carbon Letters, 24, 1-9
6. He, D., Shen, L., Zhang, X., Wang, Y., & Bao, N. (2014). An Efficient and Eco-Friendly Solution-Chemical Route for Preparation of Ultrastable Reduced Graphene Oxide Suspensions, AIChE Journal, 60(8), 2757-2764

7. Xu, C., Shi, X., Ji,A., Shi, L., Zhou, C., & Cui, Y. (2015). Fabrication and Characteristics of Reduced Graphene Oxide Produced with Different Green Reductants, PLOS ONE, 2-15

POSTER PRESENTATION

MATHEMATICS

MODELLING OF RAINFALL VOLUME AND DURATION USING COPULA

Nur Amirah Buliah[1]*, Wendy Ling Shin Yie[1]

[1]*Department of Mathematics, Faculty of Science, Universiti Putra Malaysia, 43400 UPM Serdang, Selangor, Malaysia.*

*Corresponding author: amirah0803@yahoo.com

Abstract

A copula-based analysis is usually performed in hydrology for the purpose of water management and flood prevention. The primary goal of this study is to fit the rainfall volume and duration into copulas. Clayton, Gumbel-Hougard (GH), Frank and Joe copulas of Archimedean family are used and the parameter of the copulas is estimated using Maximum Likelihood Estimation (MLE). Three graphical methods are used to find the best parameter estimation of copulas. Results indicate that Frank copula is the best fitting copula.

Keywords: Bivariate Copulas, Dependence, Rainfall Volume, Rainfall Duration

Introduction

A copula method has been applied to construct the joint distribution with different marginal distribution to modeling multivariate distributions (Favre et al., 2004; Yee et al., 2016). Archimedean Copula allows modeling dependence in randomly high dimensions with only one parameter; control the strength of dependence. Three specific objectives of this study are (1) to estimate the correlation between rainfall volume and duration (2) to fit rainfall volume and duration into copula (3) to identify the best fitting copula.

Methodology

Hourly rainfall data from six stations namely Besut, Dungun, Sungai Tong, Ampang, Gombak, and Semenyih for the period from 1984 to 2008 were used. Rainfall in Besut, Dungun, and Sungai Tong has a longer duration compare to Ampang, Gombak, and Semenyih. The 95th percentile and six-hours of Inter-Event Time Definition (IETD) were considered. Four Archimedean Copulas were used.

Table 1. Archimedean Copula

Copula	**Copula $\mathbf{C_\alpha(u,v)}$**	**Parameter $\boldsymbol{\alpha}$**
Clayton	$[\max\{u^{-\alpha}+v^{-\alpha}-1;0\}]^{-\frac{1}{\alpha}}$	$\alpha \in [-1,\infty)\{0\}$
GH	$\exp[-((-\log(u))^{\alpha}+(-\log(v))^{\alpha})^{\frac{1}{\alpha}}]$	$\alpha \in [1,\infty)$
Frank	$-\frac{1}{\alpha}\log\left[1+\frac{(\exp(-\alpha u)-1)(\exp(-\alpha v)-1)}{\exp(-\alpha)-1}\right]$	$\alpha \in \mathbb{R}\{0\}$
Joe	$1-[(1-u)^{\alpha}+(1-v)^{\alpha}-(1-u)^{\alpha}(1-v)^{\alpha}]^{\frac{1}{\alpha}}$	$[1,\infty)$

The parameter $\hat{\alpha}$ was estimated using the MLE. Three graphical methods were presented to make a comparison of parameter estimation (1) approach using the conditional distribution function $Y|X$ (2) approach using the distribution function of the copula (3) approach using a nonparametric estimate of the distribution function of the copula.

Results and Discussions

The correlation between volume and duration is moderately high for Besut, Dungun, and Sungai Tong which are 0.5212, 0.5121, and 0.5606 respectively compare to Ampang, Gombak, and Semenyih using Kendall's tau coefficient.

Table 2. Parameter estimation of Sungai Tong

Copula	Loglikelihood	$\hat{\alpha}_3$	Valid	AIC
Clayton	54.31	1.248	Yes	-108.62
GH	103.20	2.201	Yes	-206.40
Frank	89.88	6.717	Yes	-179.76
Joe	97.44	2.802	Yes	-194.88

Next is the analysis of parameter estimation of Sungai Tong. Based on the Akaikes Information Criterion (AIC), GH copula was predicted as the best copula for Sungai Tong (refer Table 2).

Evaluating the Goodness of the Estimator $\hat{\alpha}$

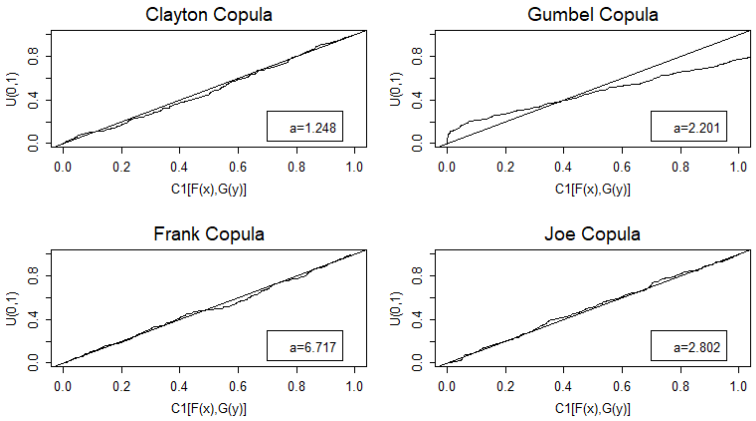

Figure 1. Graphical method 1of Sungai Tong

Using graphical method 1, Joe Copula tends to fit better but that is not obvious. For GH Copula, estimator $\hat{\alpha}_3$ does not yield a good approach. The GOF test does confirm the prediction. Considering the Kolmogorov-Smirnov (K-S) test, Joe Copula is better with high p-value 0.8043.

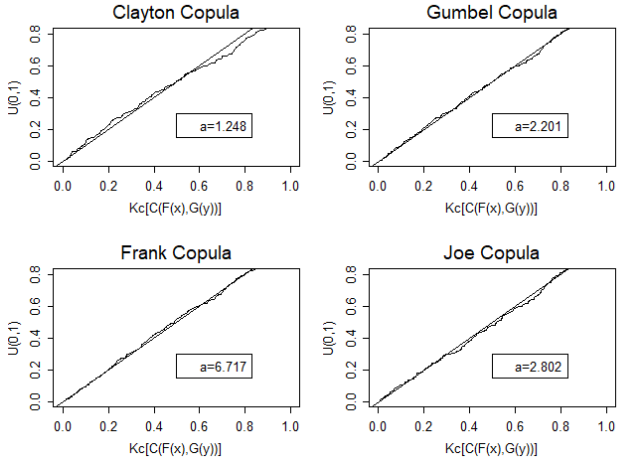

Figure 2. Graphical method 2 of Sungai Tong

For graphical method 2, all copulas seem to be a good fit. It does not reject $\hat{\alpha}_3$ of GH Copula. The K-S test does confirm this prediction. It is difficult to conclude. Clearly, graphical method 2 is not suitable for decision making in this case because there are many models that fit well. The steps were repeated for all stations. The analysis found that the graphical method 3 and the chi-square (χ^2) GOF test are not suitable for decision making. The graphical methods indicate that there is no clear favorite in most cases.

Best Fitting Copula

Overall, the best fitting copula is the Frank Copula.

Table 3. Best Fitting Copula

Station	Copula	α
Besut	Frank	5.978
	Joe	2.401
Dungun	Frank	6.023
	Joe	2.383
Sungai Tong	Frank	6.717
	Joe	2.802
Ampang	Frank	1.193
Gombak	Frank	1.067
	Clayton	0.215
Semenyih	Frank	1.686

Conclusion

Rainfall data is required to plan a hydraulic system for water supplies invention and operation, also as flood estimation and mitigation. The advantage of the proposed method is that it provides a more flexible approach to modeling multivariate distributions for which marginal distributions are not necessarily belonging to the same family of distributions. Generally, the copula is capable of modeling rainfall volume and duration well.

Acknowledgement

The present research was partially supported by the Putra Grant-Putra Young Initiative (IPM)/2017/9587800.

References

[1] Favre, A. C., El Adlouni, S., Perreault, L., Thiemonge, N. and Bobee, B. (2004). Multivariate hydrological frequency analysis using copulas. Water Resources Research 40: 1-12.

[2] Yee, K. C., Suhaila, J., Yusof, F. and Mean, F. H. (2016). Bivariate copula in johor rainfall data. AIP Conference Proceedings, Vol. 1750 (AIP Publishing, 2016) p. 060019.

RELATION BETWEEN REPRESENTATIONS OF FIGURATE NUMBERS INDUCED BY PARTITIONS 8

M.A.M. Johari[1]*, S.H. Sapar[1], N.A. Zaini[1]

[1]*Department of Mathematics, Faculty of Science, Universiti Putra Malaysia, 43400 UPM Serdang, Selangor, Malaysia*

*Corresponding Author: mamj@upm.edu.my

Abstract
The relation between the number of representations of an integer *n* as a sums of squares induced by λ, $s_\lambda(n)$ and the number of representations of an integer *n* as a sums of centred pentagonal numbers induced by λ , $c_\lambda(n)$ for $\lambda = (\lambda_1, \dots, \lambda_m)$ be a partition of 8 is given by

$$s_\lambda(8n) - s_\lambda(2n) = \beta_\lambda c_\lambda(5n+3)$$

for all non-negative integers *n* where $\beta_\lambda = 2^m + 2^{m-1}\left(\binom{i_1}{4} + \binom{i_1}{2}\binom{i_2}{1} + \binom{i_1}{1}\binom{i_3}{1}\right)$ for i_j denote the number of parts of λ which are equal to *j*. There are 22 partitions of 8. This relation is proved for all partitions of 8 by using the generating function method.

Keywords: Number of representations, Squares, Centred Pentagonal Numbers, Partitions

Introduction

Figurate numbers are positive numbers that can be represented by geometric patterns as regular geometrical arrangement of equally spaced points. A plane figurate numbers are also called polygonal numbers. They are defined as positive integers that can be represented by regular polygons in a systematic fashion. The most common types of polygonal numbers are the triangular numbers, square numbers and pentagonal numbers.

Let $\lambda = (\lambda_1, \dots, \lambda_m)$ be a partition of *k*. That is, $\lambda_1, \dots, \lambda_m$ are integers satisfying $\lambda_1 \geq \dots \geq \lambda_m \geq 1$ and $\lambda_1 + \dots + \lambda_m = k$. For any non-negative integer *n*, define $s_\lambda(n)$ is the number of integer solutions of the equation

$$\lambda_1 x_1^2 + \lambda_2 x_2^2 + \dots + \lambda_m x_m^2 = n$$

and $t_\lambda(n)$ is the number of non-negative integer solutions of the equation

$$\lambda_1 \frac{x_1(x_1+1)}{2} + \lambda_2 \frac{x_2(x_2+1)}{2} + \cdots + \lambda_m \frac{x_m(x_m+1)}{2} = n.$$

For partition $\lambda = (\lambda_1, \dots, \lambda_m)$ and $1 \leq k \leq 7$, Adiga *et al.* (2005) obtained a relation

$$s_\lambda(8n+k) = \beta_\lambda t_\lambda(n)$$

where

$$\beta_\lambda = 2^m + 2^{m-1}\left(\binom{i_1}{4} + \binom{i_1}{2}\binom{i_2}{1} + \binom{i_1}{1}\binom{i_3}{1}\right) \dots\dots\dots\dots (1)$$

and i_j denote the number of parts in λ which are equal to *j*.They provided the proof for the result by using the generating functions and combinatorial method.

Next, Baruah (2008) continued the research on the relationship between $s_\lambda(n)$ and $t_\lambda(n)$ for partition of 8. They obtained

$$s_\lambda(8n+8) - s_\lambda(2n+2) = \beta_\lambda t_\lambda(n).$$

They proved for this relation by using the generating function method.

Let $c_\lambda(n)$ denote the number of representations of an integer *n* as a sums of centred pentagonal numbers induced by λ. In other words, $c_\lambda(n)$ is the number of non-negative integer solutions of the equation

$$\lambda_1 \frac{5x_1^2 + 5x_1 + 2}{2} + \cdots + \lambda_m \frac{5x_m^2 + 5x_m + 2}{2} = n.$$

Johari et al. (2012) gave a relation between $s_\lambda(n)$ and $c_\lambda(n)$) as

$$\beta_\lambda c_\lambda(n) = s_\lambda\left(\frac{8n-3k}{5}\right)$$

for $\lambda = (\lambda_1, \ldots, \lambda_m)$ is a partition of *k* and $1 \leq k \leq 7$. They proved this relation by using the generating function method. Later, the combinatorial proof was given by Johari et al. in 2013.

Result

A relation between sum of squares and sums of centred pentagonal numbers induced by partitions of 8

In this section, we extend our discussion to the relation between the number of representations of an integer *n* as sums of squares and number of representations of n as sums of centred pentagonal numbers induced by partitions of 8. The relation is given by following theorem:

Theorem 1

Let $\lambda = (\lambda_1, \ldots, \lambda_m)$be a partition of 8. Then for any non-negative integer n, we have

$$(8n) - s_\lambda(2n) = \beta_\lambda c_\lambda(5n+3)$$

where $\beta_\lambda = 2^m + 2^{m-1}\left(\binom{i_1}{4} + \binom{i_1}{2}\binom{i_2}{1} + \binom{i_1}{1}\binom{i_3}{1}\right)$

and i_j denote the number of parts in λ which are equal to j.

This theorem has been proved by using generating functions method where there are 22 partitions of 8 to be considered.

References

[1] Adiga, C., Cooper, S.and Han, J. H., (2005). A general relation between sums of squares and sums of triangular numbers. International Journal of Number Theory 1(02) 175-182.

[2] Baruah, N. D., Cooper, S. and Hirschhorn, M. (2008). Sums of squares and sums of triangular numbers induced by partitions of 8. International Journal of Number Theory, 4(04) 525-538.

[3] Johari, M. A. M., Atan, K. A. M. and Sapar, S. H., (2012). Relation between Square and Centered Pentagonal Numbers. Malaysian J. Math. Sci. 6(02),165-175.
[4] Johari, M. A. M., Atan, K. A. M. and Sapar, S. H. (2013). A Combinatorial Proof For a Relation Between Certain Types of Integers.JP Journal of Algebra, Number Theory and Applications 28(02) 129-139.

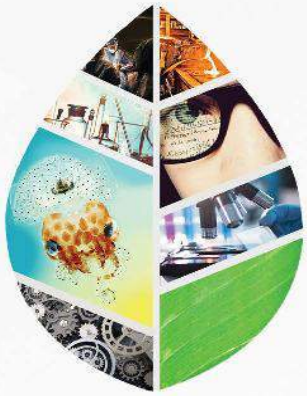

IFSC2019

'Fortifying Fundamental Sciences
for Translational Impact'